

A Theoretical Study of Disorder and Decomposition in Multinary Nitrides Hard Coatings Materials

THÈSE N° 4430 (2009)

PRÉSENTÉE LE 18 JUIN 2009

À LA FACULTÉ SCIENCES DE BASE

LABORATOIRE DE NANOSTRUCTURES ET NOUVEAUX MATÉRIAUX ÉLECTRONIQUES

PROGRAMME DOCTORAL EN PHYSIQUE

ÉCOLE POLYTECHNIQUE FÉDÉRALE DE LAUSANNE

POUR L'OBTENTION DU GRADE DE DOCTEUR ÈS SCIENCES

PAR

Björn ALLING

acceptée sur proposition du jury:

Prof. G. Meylan, président du jury
Dr A. Karimi, Prof. I. Abrikosov, directeurs de thèse
Prof. P. Muralt, rapporteur
Prof. J. Neugebauer, rapporteur
Dr J. Patscheider, rapporteur



ÉCOLE POLYTECHNIQUE
FÉDÉRALE DE LAUSANNE

Suisse
2009

Abstract

The development of multinary nitrides materials has revolutionised the hard coatings industry over the last 20 years. Especially important materials systems in this matter have been TiAlN and CrAlN which shows higher hardness, better oxidation resistance and can perform at higher temperatures as compared to TiN. When synthesised through physical vapour deposition techniques these system form cubic rock salt structured $\text{Ti}_{1-x}\text{Al}_x\text{N}$ and $\text{Cr}_{1-x}\text{Al}_x\text{N}$ solid solutions as a metastable phase over a large part of the concentration range. One of the main objectives during the optimisation of the coatings has been to increase the amount of Al in the coating while still keeping the rock salt structure, avoiding phase separation and the formation of hexagonal wurtzite AlN. However, in Al-rich TiAlN coatings it was found that *isostructural* decomposition within the cubic phase was in fact beneficial for the coatings performance at working temperatures just below 1000 °C. The reason was that the formation of strained coherent c-AlN domains within the grains initiated a age-hardening of the coating. In the CrAlN coatings it is possible to solve a larger amount of Al in the cubic phase. Possibly connected to this fact is that no isostructural decomposition and in principle no age hardening has been observed in rock salt structured $\text{Cr}_{1-x}\text{Al}_x\text{N}$.

Although large series of experimental investigations have been performed on these systems, no systematic theoretical study has yet been undertaken. This theoretical work is an attempt by means of first-principles calculations together with thermodynamics considerations within the framework of alloy theory, to close or decrease the knowledge gap between experimental observations of cutting performance of various coatings and the fundamental quantum mechanical and thermodynamics processes that governs it.

We first consider the structural properties of the treated mixed nitride systems. The concept of atomic misfit or volume difference, which is well known in the community is studied and the physics that leads to a positive deviation from Vegard's rule is revealed. Then the TiAlN and CrAlN systems are studied in detail. A clear connection between the development of the electronic structure with composition and the mixing enthalpy of the alloys, and thus the tendency for decomposition, is found for TiAlN. The importance of magnetic effects on the thermodynamics of mixing in CrAlN is established leading to a qualitative lower tendency for decomposition. Since the nitrogen composition can deviate substantially from perfect stoichiometry in these systems, a study of the influence of nitrogen vacancies on the decomposition pattern of TiAlN in the cubic phase is performed. The results imply that a presence of nitrogen sub-stoichiometry in Al-rich TiAlN will enhance the tendency for isostructural decomposition. The achieved results including those for the systems ScAlN and HfAlN are compared and discussed especially by considering volume misfit and electronic bandstructure effects as driving forces for coherent and incoherent decomposition.

Keywords

Transition metal nitrides, aluminium nitride, TiAlN, CrAlN, Density Functional Theory, first-principles, solid solutions, random alloys, disordered phases, phase separation, electronic structure, volume misfit, mixing enthalpy, defects.

Version abrégée

Le développement des nitrures multi composés a profondément changé l'industrie des revêtements durs au cours de ces 20 dernières années. Les matériaux les plus importants dans ce domaine ont été en particulier TiAlN et CrAlN qui démontrent une grande dureté, meilleures résistances à l'oxydation, et qui peuvent supporter plus haute température du travail que TiN. La déposition par des méthodes PVD assure une phase cubique à face contrée $\text{Ti}_{1-x}\text{Al}_x\text{N}$ et $\text{Cr}_{1-x}\text{Al}_x\text{N}$, qui reste une solution solide métastable pour un large intervalle de la composition. L'un des objectifs principaux dans le développement de ces revêtements a été d'augmenter la teneur en Al tout en conservant la structure cubique et empêchant la séparation des phases et formation de l'AlN hexagonale würtzite. Cependant, il a été observé que la décomposition iso structurale avait un effet bénéfique jusqu'à la température du travail d'environ 1000°C. Ceci a été attribué à la formation des domaines cohérent c-AlN dans la matrice ternaire due au vieillissement dynamique des revêtements. Les observations expérimentales ont montré qu'on peut incorporer plus d'Al dans la phase cubique de CrAlN, probablement due au fait que ni la décomposition iso structurale et ni le vieillissement dynamique se produisent dans la phase cubique de ce nitrure.

Malgré une grande nombre des travaux expérimentaux consacrés à ces familles des nitrures, aucune étude théorique systématique n'a pas encore été entreprise. Ce travail théorique est un effort d'utilisation de simulation numérique basé sur des principes primaires et les considérations thermodynamiques, afin de réduire l'écart de connaissance entre les observations expérimentales de la performance de ces revêtements et les processus thermodynamiques et principes quantum mécaniques qui gouvernent le comportement de ces matériaux. Nous allons tout d'abord étudier les propriétés structurales de ces nitrures. Le concept de différence volumique et atomique, bien connu dans la communauté scientifique, sera ensuite considéré et la déviation par rapport à la loi de Vegard sera expliquée. Ensuite, les systèmes TiAlN et CrAlN seront étudiés. Une relation directe entre l'évolution de la structure électronique avec la composition, ainsi que l'enthalpie de mélange autrement dit la tendance à la décomposition sera proposée pour TiAlN. L'importance de l'effet magnétique sur la thermodynamique de CrAlN sera établie qui démontrera l'origine de sa faible capacité à la décomposition. Étant donné que la concentration de l'azote dans ces systèmes peut dévier de la stoechiométrie, le rôle des lacunes de N_2 sur la figure de la décomposition dans TiAlN sera évalué. Les résultats démontrent que le sou stoechiométrie de l'azote dans TiAlN riche en aluminium, augmente la tendance à la décomposition iso structurale. Les résultats obtenus pour les systèmes ScAlN et HfAlN seront comparés et discutés en termes de l'effet de la différence volumique et la structure électronique, considérés comme les forces motrices de la décomposition.

Mots clés

Nitride des métaux de transition, nitride d'aluminium, TiAlN, CrAlN, Théorie de la Fonctionnelle de la Densité (DFT), Principes primaires de la thermodynamique, solutions solides, alliages à répartition aléatoire, phases désordonnées, séparation des phases, structure électronique, volume incohérence, enthalpie de mélange, défauts cristallins.

Contents

Introduction	1
1 Scientific background	5
1.1 Thin film synthezis of materials	5
1.2 Thermodynamics and kinetic stability concepts	6
1.3 Hardening mechanisms in coatings materials	9
1.4 The building blocks of nitride coating materials	10
1.5 Alloying of transition metal nitrides with AlN	14
1.5.1 TiAlN	14
1.5.2 CrAlN	21
1.5.3 Other MAIN systems	25
1.6 Insights from theory	26
1.6.1 Why first-principles?	26
1.6.2 The bonding picture in transition metal nitrides and carbides . .	26
1.6.3 Electronic structure and hardness in $\text{TiC}_{1-x}\text{N}_x$	27
1.6.4 AlN	28
1.6.5 Alloys of III-V nitride semiconductors	28
1.6.6 Early theoretical work on mixed transition metal nitride materials	28
1.6.7 Recent publications	28
2 Calculational methods	31
2.1 A Quantum Mechanics description of solids	31
2.2 Density Functional Theory	33
2.2.1 The Hohenberg-Kohn theorem	33
2.2.2 The Kohn-Sham equations	34
2.2.3 The exchange and correlation energies	34
2.2.4 Solving the equations	38
2.2.5 The Projector Augmented Wave method	39
2.2.6 Green's-function methods	40
2.3 The treatment of disordered systems	40
2.3.1 The Special Quasi-random Structures method	44
2.3.2 The Coherent Potential Approximation	46
3 Structural properties of $\text{M}_{1-x}\text{Al}_x\text{N}$ systems	51
3.1 Volumes and lattice spacings	51
3.1.1 The polymorphs of AlN	51
3.1.2 Pure nitrides with B1 structure	52

3.1.3	Lattice spacings of c-M _{1-x} Al _x N alloy systems	53
3.2	Bulk modulus	60
3.3	Formation energies	61
4	Mixing and decomposition thermodynamics of Ti_{1-x}Al_xN	63
4.1	Mixing enthalpies of competing phases in Ti _{1-x} Al _x N	63
4.2	Local lattice relaxations	65
4.3	Electronic structure	70
4.4	Thermodynamics of c-Ti _{1-x} Al _x N	72
4.4.1	Mixing enthalpy	72
4.4.2	Mean field phase diagram of c-Ti _{1-x} Al _x N	75
4.4.3	Thermodynamics beyond the mean field approximation	77
5	Cr_{1-x}Al_xN - the effect of magnetism	83
5.1	Magnetic structure of Cr _{1-x} Al _x N	83
5.2	Electronic structure	85
5.3	Thermodynamics	87
5.4	Beyond the LDA and GGA: Effects of strong electron correlation	91
5.4.1	Lattice spacing	92
5.4.2	Electronic structure	92
5.4.3	Magnetism	93
5.4.4	Mixing energy of ordered CrAlN compounds	94
6	Point defects and off-stoichiometry	97
6.1	Vacancy formation energies in binary nitrides	97
6.2	Local environment effects for V _N in Ti _{0.5} Al _{0.5} N	99
6.3	Nitrogen sub-stoichiometry in c-Ti _{1-x} Al _x N _{1-y}	101
7	Discussion	107
7.1	Methodological discussion	107
7.2	The effects of alloying elements	110
8	Conclusions	115
	Bibliography	119
	Acknowledgements	131

Introduction

Since the dawn of mankind the usage of cutting tools has been a prime necessity. The oldest findings of manufactured cutting tools are dated to 2.5 to 2.6 millions years before present and since then the development and research on cutting tools materials has challenged the creativity of more than 100 000 generations of hunters, farmers, metal workers, craftsmen, industrial workers, and scientists.

Today the most critical challenge for cutting tools performance is no longer cutting trees, carving in bone or ploughing heavy loam. Instead it is high speed machining (HSM) of hard metals such as steels and various alloys under dry conditions that puts the cutting tools to the test. The bulk material of use in present days cutting tools are mostly WC-Co and TiCN-Co cemented carbides and cermets. Although rather hard in themselves those bulk materials on their own show unsatisfactory performance in modern days HSM operations, primary with respect to wear rate.

In the 1970's the industrial usage of hard protective coatings of the tools began, primary focusing on materials systems such as TiN, TiC and Al_2O_3 . These hard ceramics coatings can improve the life time of tools by orders of magnitude in many applications. The demands from the users however, in terms of tool lifetime and cutting speed are constantly increasing. The demand on higher cutting speeds are equivalent with higher temperatures on the rake of the tool during operation and one of the main shortcomings of TiN hard coatings is their rapid drop in hardness as well as oxidation resistance when subjected to temperatures above 500 °C. Thus the main line of research in this area over the last 30 years has been the search for more advanced coatings materials system that are able to withstand such deteriorating conditions. In this effort the combinations of several elements forming ternary or multinary coatings systems such as Ti-C-N, Ti-Al-N, Cr-Al-N and Ti-Si-N has been investigated. Especially the addition of Al to transition metal nitrides has been successfully used in large scale industrial applications.

In the system Ti-Al-N, coatings synthesised with physical vapour depositions techniques and sufficient access to nitrogen typically form $\text{Ti}_{1-x}\text{Al}_x\text{N}$ solid solutions in the cubic rock salt structure, at least as the majority phase and for $x \leq 0.67$. This is somewhat surprising since TiN and AlN shows extremely limited solubility in bulk even at very high temperatures indicating that the solid solution phase is only metastable. Extensive experimental investigations have been conducted on these solid solutions systems and they have been shown to drastically increase the oxidation resistance of the coatings as compared to TiN. Furthermore they show higher hardness in the as-deposited state. More recently it has been demonstrated that such coatings with high Al content show retained or even enhanced hardness after annealing at for cutting operations relevant temperatures around 1000 °C. This has been suggested to be due to alleged isostructural spinodal decomposition into cubic AlN and TiN or Ti-rich $\text{Ti}_{1-x}\text{Al}_x\text{N}$. Taken together

the effect is a drastic increase in tool lifetime and possible maximum working temperature of TiAlN, as compared to TiN, coated cutting tools. In the related system Cr-Al-N the solid solutions also form but with the possibility to include a larger amount of Al in the rock salt phase thus possibly further increasing the oxidation resistance. On the other hand, no isostructural decomposition has been shown and no age hardening has been unambiguously observed for the cubic phase domain. These observations clearly demonstrate the high importance of phase stabilities and instabilities on the mechanical behavior of the materials.

A certain understanding of these materials systems has been obtained through intense experimental research. However, experimental investigations have important limitations. First of all the experimentalists are limited to observe phases and processes that do occur, possible competing phases and processes that are not observed can not be analysed and thus not the reason why they are not seen. Further more, it is often difficult or impossible to study the effect of different internal and external conditions independently. For instance, the influence of Al-content, cubic or hexagonal structures, configurational pattern in the solid solution and the temperature can not be separated in the experiments thus limiting the basic understanding of their respectively influence on materials properties. And knowledge about these factors are indeed of utmost importance in the attempt to develop new coatings materials systems in which several stable and metastable phases exist.

An alternative approach to experimental procedures is to apply the basic rules of quantum mechanics and statistical physics and study the systems theoretically from first-principles. Such an approach allows for the study of both stable, metastable and even unstable phases, an independent investigation of the role of composition, structure and configuration, and is able to give important information about the origin of different experimentally observed phenomena.

The basic equations governing quantum systems were developed in the early and mid 1900's, but first-principles procedures were for a long time anyway practically impossible to apply to realistic systems due to the computational costs. But today efficient methods to solve quantum mechanics problems within the framework of density functional theory are well established. Owing also to the drastic improvement of computational resources over the last decades numerous important discoveries within solid state physics have been made through the application of first-principles calculations.

However, the system of interest in the present study includes several challenges for a first-principles approach. First of all the treatment of the solid solution phases. These phases characterised by substitutional disorder has puzzled theoretical physicists for a long time. The basic problem is that the statistical distribution of atoms brakes the translational symmetry of the lattice making it impossible to handle the calculations within traditional unitcell or supercell calculations. Within alloy theory instead a number of different tools have been developed to handle this situation in terms of both specifically designed supercells, cluster expansions as well as effective medium approaches. Secondly, the exact stoichiometry of the materials is often only approximately controlled, at least at high temperatures and considerable influence on physical properties can be expected from the presence of point defects e.g. nitrogen vacancies. Further complications arise when both defects and substitutional disorder are present simultaneously.

The objectives and structure of this work

Although being well known and widely used in practise, the coatings systems TiAlN and CrAlN have not before been subject to a systematic theoretical study from first-principles. Thus the fundamental quantum mechanics and thermodynamics governing the phase stabilities and experimentally observed transformation processes in these systems are still largely unknown. This is unsatisfying on the level of fundamental physics research, but perhaps more importantly also a limitation on the ongoing experimental development work of new coatings materials. In the absence of a fundamental understanding of the processes at work on the atomic scale in the presently used systems, the choice of new alloying materials and other coating parameters are done more or less at chance.

The scope of the present work is to use, and if necessary further develop, state of the art alloy theory and first-principles calculations in a study of a number of important multinary nitride hard coatings materials systems. The systems studied are transition metal nitrides alloyed with aluminium nitride, TiAlN, CrAlN, ScAlN, and HfAlN. They are chosen both on the basis of direct practical importance (TiAlN and CrAlN) as well as with respect to novelty (ScAlN and HfAlN). ScAlN has not been considered at all in the literature while only very few experiments have been reported for the HfAlN system. Furthermore the combination of the four different systems allows for the critical investigation of different possible explanations for phase stabilities or decomposition behaviour such as lattice mismatch and electronic band structure effects in this class of materials systems.

The objective is to reach an understanding of structural and electronic properties of the solid solution nitride systems, stoichiometric and non-stoichiometric, as well as the possible driving force for phase separation.

First a scientific background is given (chapter 1) discussing some important physical concepts as well as a background to the different treated materials systems. Then the theoretical framework of this thesis in terms of first-principles calculations is presented, together with some crucial methodological questions regarding the theoretical treatise of disordered systems (chapter 2). Structural properties and deviation from Vegard's rule in the B1 structured systems $\text{Ti}_{1-x}\text{Al}_x\text{N}$, $\text{Cr}_{1-x}\text{Al}_x\text{N}$, $\text{Sc}_{1-x}\text{Al}_x\text{N}$, and $\text{Hf}_{1-x}\text{Al}_x\text{N}$ are studied and compared with experimental results (chapter 3) providing also a test of the reliability of the theoretical methods. The electronic structure effects and thermodynamics in the systems TiAlN (chapter 4) and CrAlN (chapter 5) are investigated. The effects of point defects in terms of nitrogen vacancies with focus on nitrogen sub-stoichiometric $\text{Ti}_{1-x}\text{Al}_x\text{N}_{1-y}$ (chapter 6) are presented followed by a general discussion (chapter 7) and a chapter with conclusions and outlooks (chapter 8).

Chapter 1

Scientific background

In this chapter a scientific background is given to the topic of the thesis. First the experimental background to the formation of solid solutions in thin film synthesis is given followed by a discussion of certain stability concepts, such as *metastability*, used throughout this work. It is followed by a discussion about *hardness* in nitrides materials. Then a presentation of the most important building blocks of the hard coatings materials covered in this work is made followed by a more extensive presentation of the experimental research on TiAlN and CrAlN thin films. In the final part, previous theoretical works aiming to understanding these materials are presented. The research leading up to this thesis was initiated 2006. The important publications that have appeared since then, including publications directly related to this thesis, is briefly covered in the final section: Recent publications. Those works are instead covered and discussed in detail in the following chapters where the results are presented as well as in the Discussion chapter.

1.1 Thin film synthesis of materials

The hard coatings materials treated in this work are typically prepared through thin film growth using physical vapour deposition techniques such as arc evaporation or reactive magnetron sputtering. These methods are very different from equilibrium bulk synthesis in the way the materials are formed and thus have dramatic consequences for the materials properties. The metals are supplied through sputtering or arc evaporation of elemental or alloy targets while the nitrogen is present as a reactive gas in the chamber typically together with an inert working gas such as argon. The vaporised and ionised metal and nitrogen atoms condense and react on the chamber walls and on the substrate growing the film. In some cases the attraction to the substrate can be increased through the application of a negative bias. The substrate temperature is rather low, in industrial applications $T \leq 500^\circ \text{C}$ is typical, which in general means that when the atoms from the plasma impinge on the substrate their mobility due to thermal activity is quite restricted. Even if the mobility is enhanced by collisions with other energetic ions, this process does not drive the system towards thermodynamic equilibrium. Instead, if the kinetic energy of the incoming ions are sufficient, recoil implantation and cascade mixing of the atoms already present in the film may occur [1]. Thus two simultaneous effects promotes the formation of high entropy material phases: The limited mobility of the

surface atoms prohibits long range diffusion to form phase separated domains and rather stochastic impact of high energy ions on the film causes additional phase mixing. These are the basic reason why many multinary nitrides thin film systems grow in the form of solid solutions [2].

1.2 Thermodynamics and kinetic stability concepts

One of the main purposes of this work is to investigate the stability of different hard coatings nitride materials, as well as their tendency for phase separation and decomposition, using theoretical calculations and analysis. It is therefore necessary to clarify what is meant with different concepts of stability. First of all, two systems in *thermodynamic equilibrium* with each other are characterised by having both temperature, pressure and chemical potentials equal. Such a state is characterised by the presence of *thermodynamically stable* phases. In principle, thin films can hardly be in thermodynamic equilibrium with bulk substrates at normal temperatures due to the huge entropy gain it would give to solve the thin film material in the bulk. However, in practise the thin film itself can often be considered as a bulk material and thermodynamic considerations can be done for the thin film alone¹. One example of a hard coating system that could be considered as a thermal equilibrium system is a TiN coating on a WC-Co tool present in a N₂ atmosphere at room temperature.

However, the coating materials being the subject for this thesis are mixed nitrides, especially transition metal nitrides mixed with AlN. As will be apparent these system typically do not constitute systems in thermal equilibrium, thus possessing a potential for phase change. Nevertheless, they are any way created with thin film deposition techniques and persist under ambient condition for timespans long enough for being useful in practical applications. The term *metastable* has been introduced to describe such systems. The term is not uniquely defined for just one certain situation, instead it is in general use for all situations matching the combination of one positive and one negative stability criteria. The system should be stable with respect to a small change in state parameters while at the same time being unstable with respect to a larger change in parameters. Another way to say it is that the metastable state should constitute a local energy or free energy minima but not a global minima. This means that there should exist an energy barrier, or free energy barrier that can confine the system to the metastable state rather than transforming to the equilibrium.

Such barriers can be of different kinds. *Kinetic barriers* might lock atoms into certain crystal positions, constituting local energy minima, during the growth of the thin film nitride materials. This prevents the atoms to diffuse enough to form separate de-mixed nitrides domains. Kinetic barriers might also prevent changes of crystal structure such as the transition from cubic B1 AlN to hexagonal B4 AlN since such a change needs the overcoming of a rather high energy barrier.

The barriers can also be of thermodynamic rather than kinetic character. This situation can be illustrated by the following example. Consider a system of a binary A_{1-x}B_x alloy

¹Of course it is necessary to be aware of the possibility for diffusion of different components to and from the substrate, and also loss of light elements to the vacuum or reaction with i.e. oxygen from an atmosphere.

where the equilibrium mixing and de-mixing process is governed by the minimisation of the Gibb's Free energy,

$$G = H - TS, \quad (1.1)$$

of the system under the condition that the global composition x is kept constant. In Eq. 1.1, G is the Gibbs free energy, H is the enthalpy, T is the absolute temperature, and S is the entropy of the system. This problem can be solved graphically by calculating the Gibbs free energy as a function of composition and temperature and then perform a common tangent construction as is schematically illustrated in Fig. 1.1.

This figure illustrates in the top panel the free energy curves for a hypothetical $A_{1-x}B_x$ alloy, with a strictly positive mixing enthalpy, at different temperatures. As temperature increases the free energy of the alloy decreases as a consequence of the increased impact of entropy. The equilibrium phase diagram can be derived through a common tangent construction at each temperature illustrated for $T = T_2$ in the figure ($T = T_1$ in the inset). This gives the binodal line shown in solid black in the phase diagram of the bottom panel. In this case with a positive mixing enthalpy it results in a miscibility gap. This corresponds to a region in the composition-temperature space where no mixed single phase configuration can exist in equilibrium. A close investigation of the figure reveals that two separate regions can be identified within the miscibility gap. Depending whether the curvature of $G(x, T)$ is positive or negative, the system either gains or loses Free energy by a small decomposition into phases of composition $x - \delta$ and $x + \delta$ respectively. The criteria where the second concentration derivative is zero,

$$\frac{d^2G(x, T)}{dx^2} = 0, \quad (1.2)$$

is defining the boundary between the *spinodal* ($\frac{d^2G}{dx^2} < 0$) and *binodal* ($\frac{d^2G}{dx^2} > 0$) domains shown by a dashed red line in the bottom panel of the figure. In the spinodal region any fluctuation in composition will lower the free energy and the system will decompose through *spinodal decomposition* given that there is no kinetic barriers prohibiting diffusion of alloy components. Such decomposition might give raise to very complicated concentration profiles. One binary alloy system where spinodal decomposition is observed is fcc-AlZn [3]. In the binodal region the system can still decompose but it requires that a large enough *nucleus* is formed with a sufficiently large offset in composition. This means that there exists a thermodynamic barrier in form of an obstacle for atomic diffusion until the nucleus is formed. It should be noticed that even though these two concepts might be well defined in the ideal continuum thermodynamic analysis, in real systems where the discrete lattice set limits for the smallest possible concentration deviations, the picture is less clear. Especially it is unclear if it is possible to experimentally distinguish a process of spinodal decomposition from a isostructural decomposition through nucleation and growth without studying the kinetics of the decomposition process.

Figs. 1.2 to 1.4 give a schematic illustration of these concepts for the system TiAlN. Fig. 1.2 illustrates the energy curve in phase space of the TiAlN-system at 0K. The cubic $Ti_{1-x}Al_xN$ solid solution constitutes a local energy maximum and is unstable in the thermodynamic sense with respect to an isostructural decomposition into c-TiN and c-AlN. The latter situation in turn being unstable with respect to a phase change

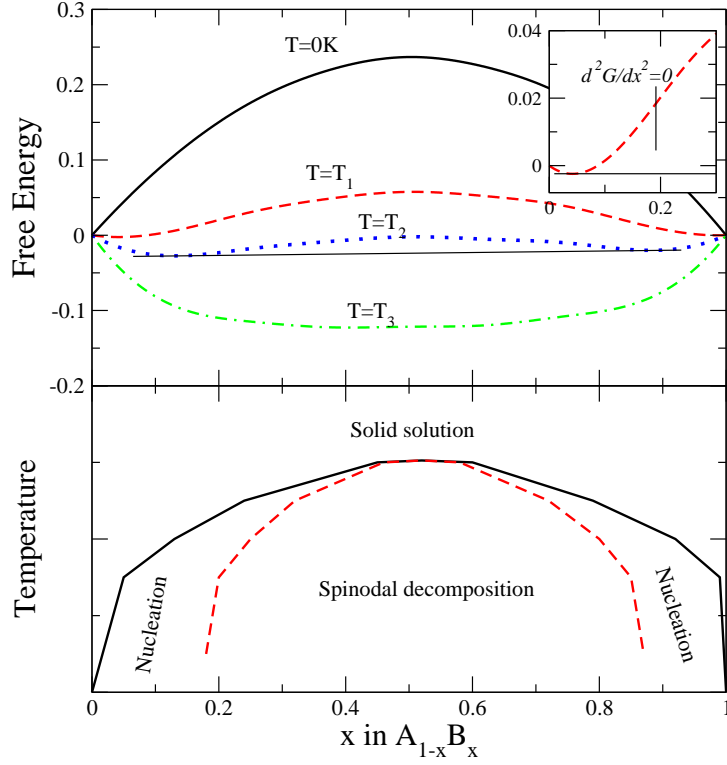


Figure 1.1: Schematic illustration of how phase equilibria in a $A_{1-x}B_x$ alloy system can be found by means of common tangent construction of the corresponding Gibbs free energy curves. The inset in the top panel shows how the change of sign of the second concentration derivative decides the position of the spinodal line.

of cubic AlN to hexagonal AlN. However two distinct types of energy barriers called ΔE_k and ΔE_B in the figure illustrates the reason why both the solid solution and the isostructural cubic two-phase situation can be viewed as metastable. If the cubic solid solution is achieved, diffusion of Ti and Al atoms on the cubic lattice are prohibited due to kinetic energy barriers ΔE_k which can not be overcome by the atoms without considerable thermal activity. The cubic isostructural phase separated system can also be considered as metastable since an energy barrier, ΔE_B , prohibits the transformation of AlN to its thermal equilibrium hexagonal structure.

Fig. 1.3 shows the schematics of the system at a finite temperature. Since the mixed alloy system has a considerable configurational entropy it will be gradually more favourable, or less unfavourable, compared to the phase separated systems. On the other hand, at elevated temperatures atomic diffusion on the lattice is initiated, thus possibly promoting the alloy state to phase separate into almost pure components. For certain compositions however, the system might be metastable with respect to phase separation in the thermodynamic sense. This would correspond to a situation where the system is between the spinodal and the binodal line in the composition-temperature phase diagram. Since the formation of stable nucleus might require long range diffusion in the lattice, the alloy system could possibly still persist for extended time spans and being considered as metastable. Please notice that the placing of energy (such as the value of the kinetic barriers) and the free energy on the same axis is strictly speaking not correct, but it serves an illustrative purpose in this example.

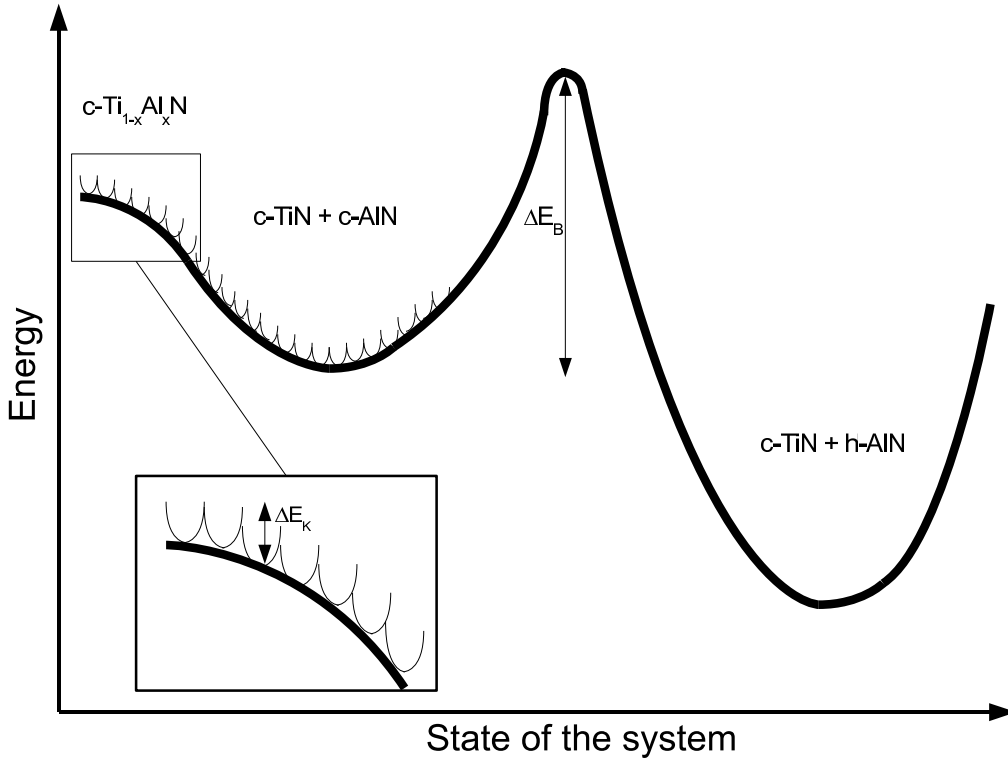


Figure 1.2: Schematic illustrations of the energetics of different phases in the TiAlN system at $T = 0K$.

Fig. 1.4 illustrate the situation at an even higher temperature. The cubic solid solution is now favoured over the isostructural phase separation but still less favourable than a mixed system consisting of c-TiAlN and h-AlN. Even though the energy barrier $\Delta E'_B$ might be higher than at lower temperatures consisting of a combination of the thermodynamic barrier to de-mix AlN and the energy barrier to transform c-AlN to h-AlN, in reality small nuclei of h-AlN can be present in i.e. grain boundaries etc. and are likely to grow due to the high mobility in the system. A mixed system in the hexagonal structure is possibly also important but not shown here. The present work is a theoretical attempt to find, characterise, and quantify the underlying quantum mechanical driving forces that guide the processes illustrated above.

1.3 Hardening mechanisms in coatings materials

Hardness is a macroscopic property describing the resistance of a material against deformation. Typically in hard coatings materials the most important factor is the resistance against plastic deformation, a process mediated through dislocation motion through the grains, but possibly also grain boundary sliding. Since the hardness itself is practically impossible to directly derive using first principles calculations, one ought to study the different mechanisms that are the origin of this macroscopic property. Of relevance for the present work are the mechanisms that can work hardening in nitride coatings materials. To increase the hardness of a material the resistance against dislocation motion should be increased. Mechanisms that work in this direction are e.g. grain refinement,

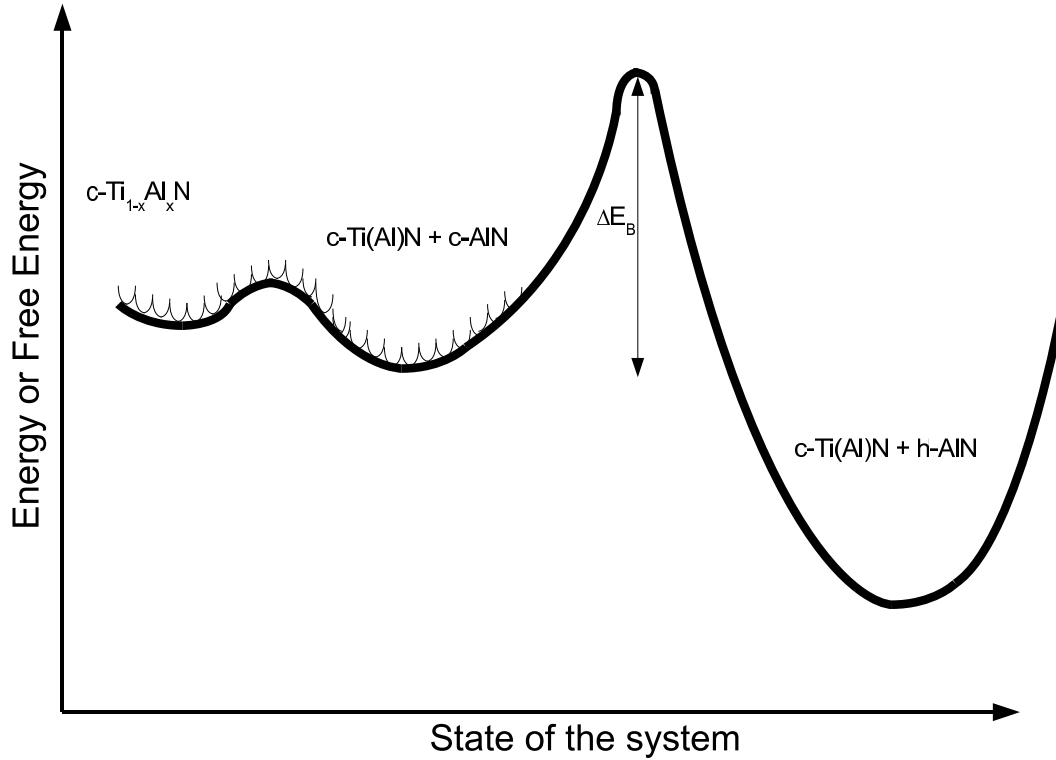


Figure 1.3: Schematics of the free energy and energy relations in the TiAlN system at a higher temperature, $T_1 > 0K$.

bond strengthening, solid solution hardening, defects hardening, build-up of residual stress, and phase boundary creation. In this work the phenomena of phase separation is studied and this is closely related to the development of the hardness of the subject material through multiple of the above mechanisms, as will be illustrated below for $Ti_{1-x}Al_xN$. Solid solution hardening will also be discussed as well as the presence of point defects in the form of nitrogen vacancies. The phenomena of hardening through bond strengthening was illustrated for the TiCN system [4] and is briefly described below.

1.4 The building blocks of nitride coating materials

The by far most investigated transition metal nitride system is titanium nitride. TiN crystallises in the cubic B1 NaCl (Rock Salt) structure shown in Fig. 1.5. The phase is stable over a large range of N content ranging from about 30-50 at.% as can be seen from the phase diagram presented in Fig. 1.6. The usage and development of TiN as a coating material began in the 1960's. Due to favourable properties TiN has been and still is, used as a coating material for wear resistant purposes on cutting tools, as a diffusion barrier in electronic components [5,6], for decorative purposes [7] and as a corrosion resistant material [8].

Although the bulk modulus of TiN is believed to be highest for stoichiometric compounds, an interesting idea was presented by Shin *et al.* [10]. They found that the hardness of understoichiometric TiN_x increased with decreasing N content. This hap-

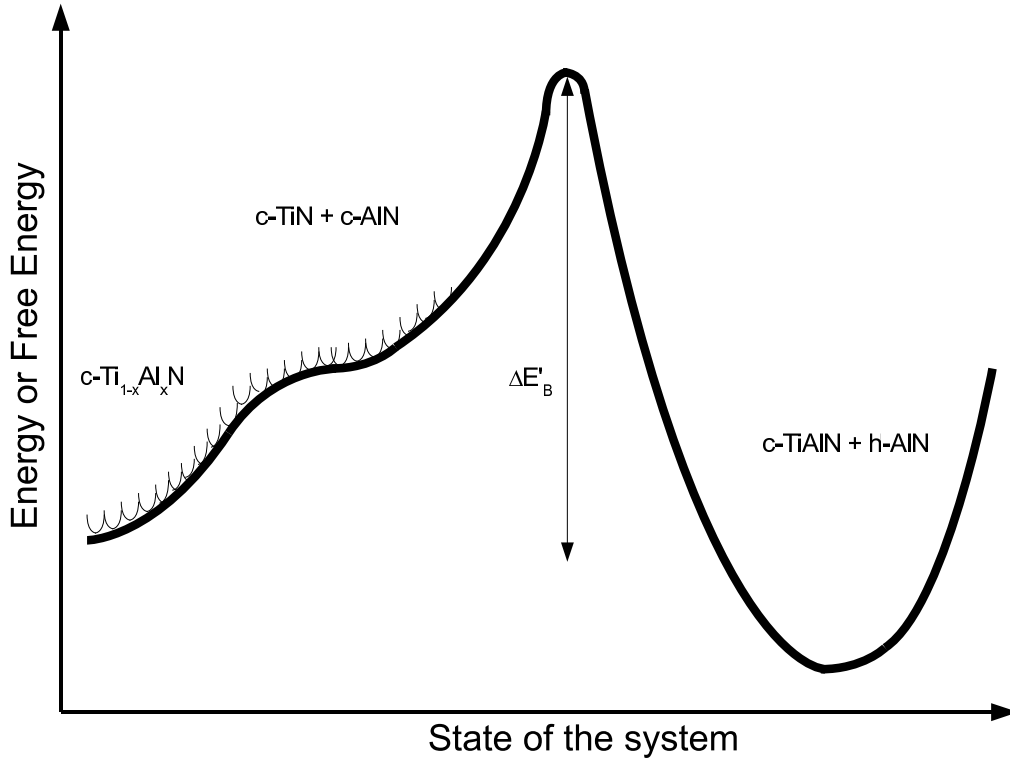


Figure 1.4: Schematic illustrations of the free energy and energy relations in the TiAlN system at an even higher temperature $T_2 > T_1 > 0K$.

pened for TiN_x films at the same time as the elastic modulus decreased. This observation lead the authors to conclude that the presence of point defects in the form of N vacancies in TiN_x caused an increased resistance against dislocation movements on average due to the increase in bond-strength for some atoms at particular configurations of N and N vacancies overtaking the softening effect of a slightly lower bond density.

Another important transition metal nitride is chromium nitride. CrN can be grown as thin films by different deposition techniques and is used in industrial applications in metal forming and plastic moulding [11, 12]. However, pure CrN is not as hard as TiN and it starts to lose nitrogen at much lower temperatures making it a less attractive choice for most hard coatings applications. However, as will be shown below CrN has also very important properties as an alloying material.

The low temperature ground state structure of CrN is not ideal B1 but an orthorhombic structure with one of the angles of the underlying B1 lattice being not 90° , but slightly smaller 88.23° . [13]. The reason for this distortion has been explained as a magneto-structural induced strain due to a double layer antiferromagnetic configuration with a Néel temperature around room temperature [13, 14]. Above this temperature the system forms a paramagnetic state with the ideal cubic B1 lattice structure. However, it has been shown that the cubic structure could be stabilised by means of epitaxial strain in thin films down to at least 20K [15, 16]. In those experiments no signs of a magnetic phase transition was observed. Moreover, the experiment presented in Ref. [15] showed that B1 CrN at low temperatures exhibited semiconductor behaviour, being explained as a Mott-type insulator [15]. In subsequent measurements it was concluded that the

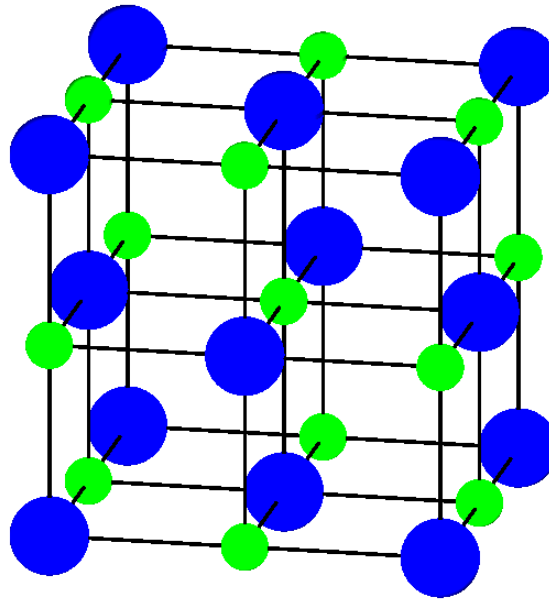


Figure 1.5: The cubic B1 structure of TiN. Ti atoms sit on a fcc-sublattice with the N atoms octahedrally coordinated forming a second fcc-sublattice

electric conductivity and magnetic properties were very sensitive to off-stoichiometry and defects [16].

AlN is a wide-bandgap semiconductor that crystallises in the hexagonal Wurtzite structure, designated B4 under ambient conditions. AlN has a lower hardness compared to transition metal nitrides and is not used on its own as a hard coating material. About twenty years ago it was shown by Vollstädt *et al.* that AlN transformed into the B1 cubic phase under high pressure and temperature [17]. The cubic phase was shown to be metastable under ambient conditions. Cubic B1 AlN has also been synthesised by means of pulsed laser deposition [18]. The finding of pure c-AlN actually came several years after the research on Al inclusion in B1 structure transition metal nitrides began. Also the tetrahedrally coordinated cubic, zinc blende B3, prototype of AlN has been synthesised, stabilised by epitaxial forces [19].

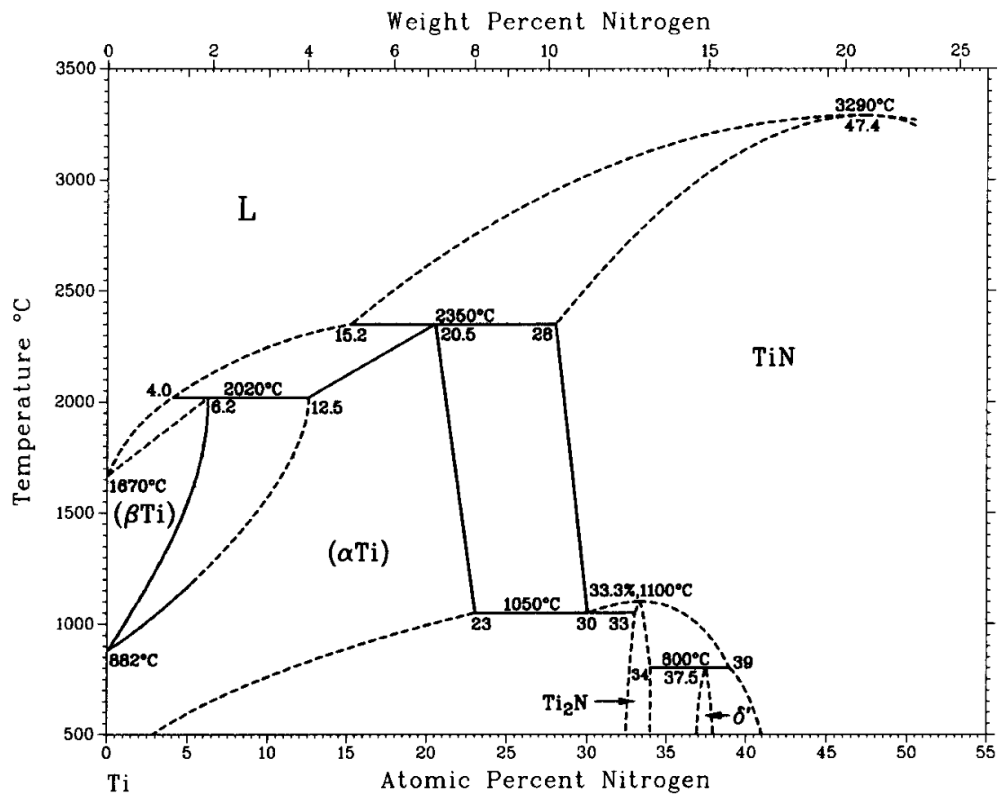


Figure 1.6: The Ti-N equilibrium phase diagram. Redrawn from Ref. [9].

1.5 Alloying of transition metal nitrides with AlN

1.5.1 TiAlN

Following a long time of development of TiN coatings, improvements of coating processes and fine-tuning of coating parameters during the 1970's the stage was set to go beyond the binary nitrides and introduce more complicated materials system into the coatings. During the 1980's the addition of aluminium into TiN coatings forming Ti-Al-N coatings was introduced and found to give considerable or in some cases drastic improvement of cutting performance compared to TiN coated tools [20–24]. This improvement in performance was manifested as a decrease in flank wear and corresponding life time of the tool, in drilling and cutting tests in different materials [21, 24].

Structurally it was realised that for low or moderate Al content, the structure of the Ti-Al-N coatings was predominantly cubic B1 [20]. The gradual change in lattice spacing indicated that Al was substituting Ti on the metal sublattice of the B1 structure [25]. The formation of these c-Ti_{1-x}Al_xN alloys, in spite of the fact that the equilibrium phase diagram shows no miscibility of TiN and AlN for bulk phases, showed clearly the potential of thin film deposition techniques such as PVD to explore and make use of metastable phases. At higher Al content the coatings displayed a mixed structure of the cubic B1 and hexagonal B4 structure [25]. In most works such mixed phases results in worse cutting performance compared to single phase cubic TiAlN films [26].

One key property for the performance of cutting tools under normal conditions is the resistance against oxidation. It was this property for which the addition of Al was first identified and studied. It was shown in an early stage of the development of TiAlN that the addition of Al into TiN coating created a superior oxidation resistance and also an improved maximum working temperature [21, 22, 27]. The oxidation of TiAlN films in hot air was found to take place through the formation of an almost pure Al₂O₃ top layer, followed by an Al-depleted oxy-nitride layer between the oxide and the TiAlN film [28]. The increased oxidation resistance of the Al containing films should thus be attributed to the formation of such a protective oxide layer. The oxidation experiments above show the drastic influence on the coatings when heat treated in air for time periods of a few hours. However, it has not been made clear in these works to what extent the crucial contact area between the cutting inset and the work piece is exposed to oxygen during typical cutting operations. Thus although important, the increased resistance of the coating against oxidation is not the only relevant parameter for the design of coatings for cutting tools.

Another vital parameter is the development of the hardness of the coating with change in composition. It has been shown by means of nanoindentation that the addition of Al increase the hardness of as-deposited coatings [25, 26, 29]. Fig. 1.7 shows the measured Hardness of thin Ti_{1-x}Al_xN films of different compositions for three different experiments. Please note that the details of the hardness measurements might differ so a direct comparison of absolute values might be misleading. The hardness increase with increasing Al-content and reaches a maximum around x=0.60. At higher Al-content, the hardness drops rather quickly, a phenomena that has been explained by the initiation of h-AlN formation during growth.

The attempt to increase the Al-content in order to promote oxidation resistance and

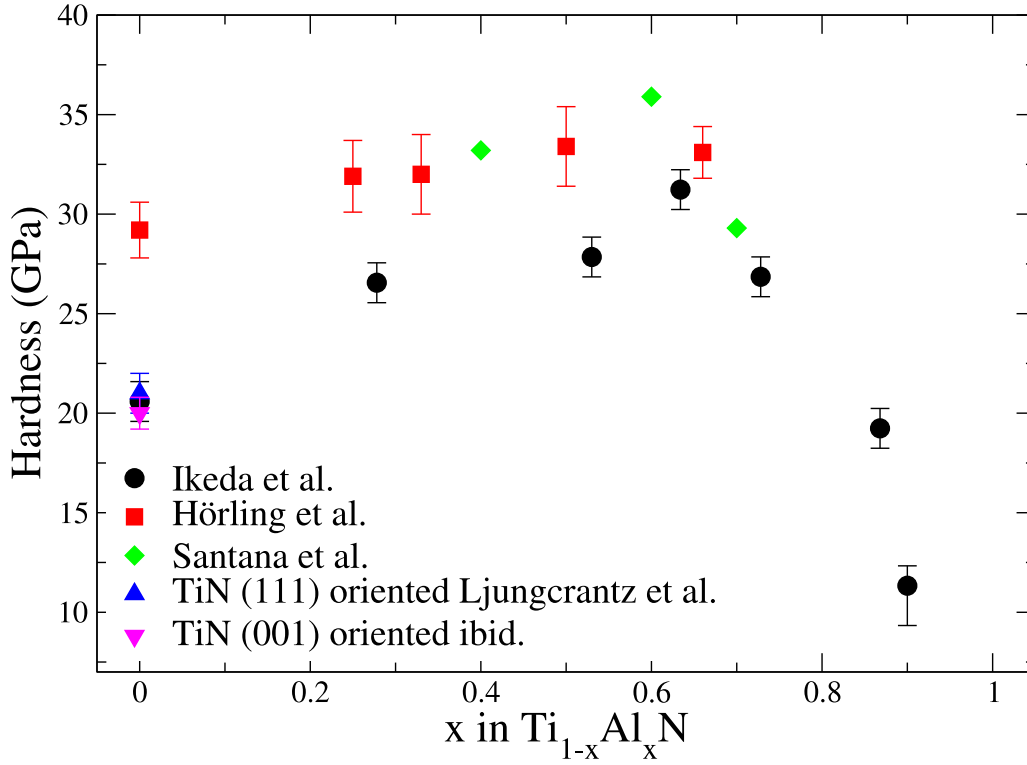


Figure 1.7: The measured hardness of as-deposited $\text{Ti}_{1-x}\text{Al}_x\text{N}$ thin films of various composition compared to pure TiN values. Redrawn from Ikeda *et al.* [25], Hörling *et al.* [26], Santana *et al.* [29], and Ljungcrantz *et al.* [30].

increased hardness, while at the same time avoiding the nucleation of h-AlN during growth in Al-rich films has governed a large numbers of studies of the properties of Al-rich TiAlN films and different deposition techniques relevant for their syntheses. A recent review of the subject is presented in Ref. [31].

However, more recently a new mechanism was suggested to play a very important role in TiAlN based hard coatings: *age hardening* [32]. Since the cutting tool and its coating is subject to very high temperatures, easily above 800°C in applications such as high speed machining, and that the driving force of productivity is to continuously increase cutting speed and thus temperature, the thermal stability of the hard coating materials is of crucial interest. The development of the hardness of the coating with temperature is of special interest. A usual behaviour of TiN hard coatings is a decrease in hardness upon annealing. This is so since structural defects created during growth, such as stacking faults and point defects, are annealed away leading to a more relaxed lattice with less obstacles for dislocation motion. So even though it is possible to achieve rather high hardness in as-deposited TiN samples such as the one in Ref [26], there is a sharp drop in hardness of such coatings already at temperatures around 500°C. However, in $\text{Ti}_{0.34}\text{Al}_{0.66}\text{N}$ coatings it was shown that the hardness could be retained, or even increased after annealing for 2 hours at temperatures as high as 950°C [32]. A corresponding age hardening was also found in a $\text{Ti}_{0.30}\text{Al}_{0.70}\text{N}$ coating after annealed at 1000°C [29] for 30 minutes. Similar results, although less extensive, were found in the same work for $\text{Ti}_{0.40}\text{Al}_{0.60}\text{N}$ coatings, while the hardness of $\text{Ti}_{0.60}\text{Al}_{0.40}\text{N}$ films decreased

almost in a similar manner as TiN films. Fig. 1.8 shows the hardness of different TiAlN coatings [26, 29] after annealing at different temperatures as compared to as-deposited values, shown with open symbols, as well as an illustrative TiN example [33].

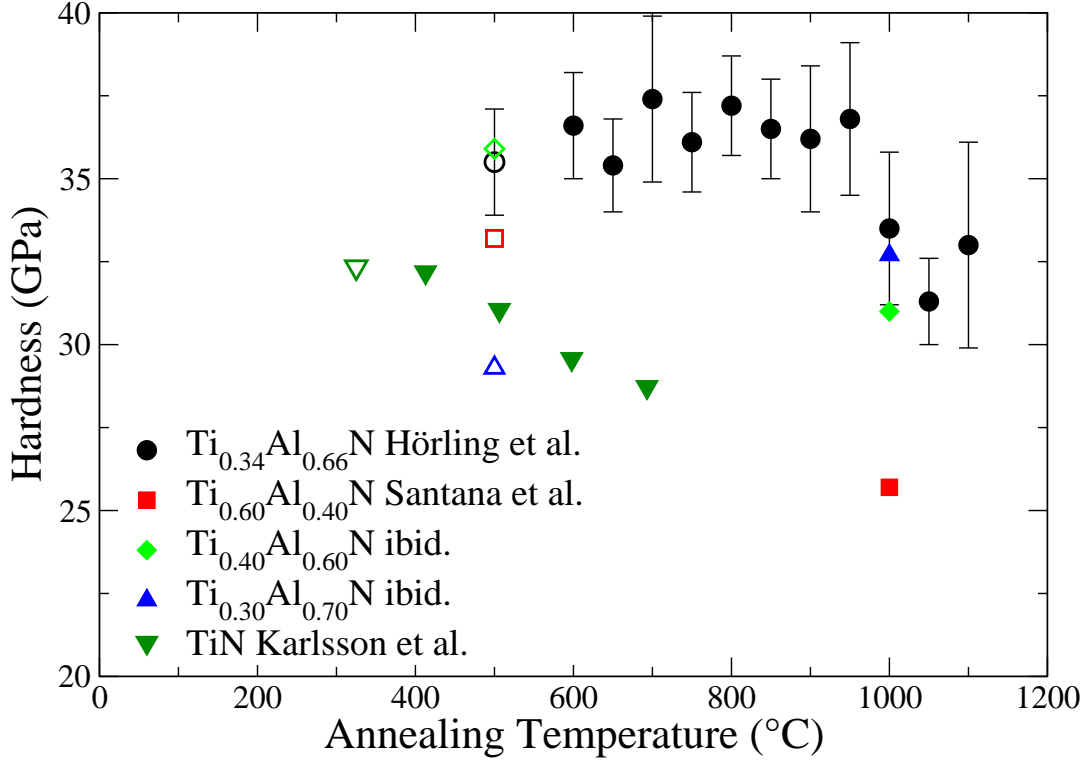


Figure 1.8: The measured hardness of $\text{Ti}_{1-x}\text{Al}_x\text{N}$ thin films of various composition, annealed at different temperatures, as compared to as-deposited values (open symbols) and TiN values. Redrawn from Hörling *et al.* [26], Santana *et al.* [29], and Karlsson *et al.* [33].

Since the relaxation of defects leading to a softening in TiN should be present also in these materials, another mechanism counteracting the softening at least partially should be present in these TiAlN coatings displaying age hardening or at least reduced softening. Mayrhofer *et al.* [32] explained their findings of age hardening of $\text{Ti}_{0.34}\text{Al}_{0.66}\text{N}$ thin films by the formation of coherent domains of c-AlN and TiN in the c-TiAlN matrix through alleged spinodal decomposition. They identified three qualitatively different stages in the transformation of the as-deposited samples by means of differential scanning calorimetry (DSC), x-ray diffraction (XRD) and transmission electron microscopy (TEM) studies. Fig. 1.9 shows the results of DSC measurements during annealing of $\text{Ti}_{0.34}\text{Al}_{0.66}\text{N}$ and $\text{Ti}_{0.50}\text{Al}_{0.50}\text{N}$ thin films. Fig. 1.10 shows XRD measurements of the same films after subject to different temperatures of annealing. The first transformation was initiated at around 600-700°C and was supposed to be recovery process of lattice point defects since it was also visible in pure TiN samples. Around 800-1000°C another process is visible resulting in a peak broadening of the XRD-spectrum. This is interpreted as a spinodal decomposition of the film into first c-AlN and Ti-enriched TiAlN matrix and then also TiN domains.

The authors actually interpret the experiments by separating this process into two sub-processes, first the coherent decomposition process which induces strain fields in the

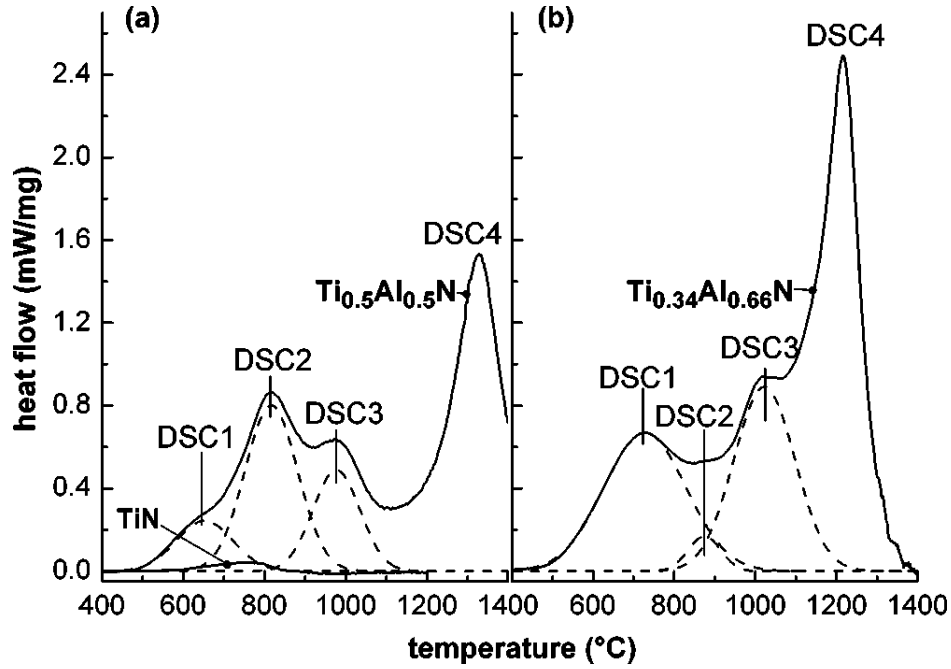


Figure 1.9: Differential scanning calorimetry measurements of heat treated $\text{Ti}_{0.34}\text{Al}_{0.66}\text{N}$ and $\text{Ti}_{0.50}\text{Al}_{0.50}\text{N}$ thin films. Redrawn from Mayrhofer *et al.* [32].

film leading to hardening (800-950°C) and then the relaxation of these strained domains by the introduction of dislocations, leading to softening (above 1000°C). Finally at around 1200°C the c-AlN is transformed into its stable counterpart h-AlN. A schematic illustration of these ideas together with a TEM-micrograph of a $\text{Ti}_{0.34}\text{Al}_{0.66}\text{N}$ showing dislocations due to relaxation of coherency strain is displayed in Fig. 1.11 [32].

Hörling extended this work in his PhD-thesis [34], also including a study of $\text{Ti}_{0.75}\text{Al}_{0.25}\text{N}$ films. For these films thermal annealing by 50°C per minute increase up to 1050°C showed no change of the XRD pattern, and only after the same type of annealing up to 1400° a faint shoulder of the peaks was visible and suggested to be c-AlN. On the other hand, an exothermic reaction between 500°C and 1000°C was identified by DSC measurements but was not explained.

Santana *et al.* [29] investigated the thermal stability of $\text{Ti}_{1-x}\text{Al}_x\text{N}$ thin films with compositions $x = 0.40, 0.60, \text{ and } 0.70$. It was found that the hardness of the $\text{Ti}_{0.60}\text{Al}_{0.40}\text{N}$ films decreased by 7.5 GPa after annealing at 1000°C for 30 minutes, from 33.2 GPa to 25.7 GPa. $\text{Ti}_{0.40}\text{Al}_{0.60}\text{N}$ thin films only decreased by 4.9 GPa from 35.9 to 31.0 GPa while the $\text{Ti}_{0.30}\text{Al}_{0.70}\text{N}$ actually showed age hardening from 29.3 GPa as-deposited to 32.7 GPa after the thermal load. The two films with lower Al content were in cubic phase while the $\text{Ti}_{0.30}\text{Al}_{0.70}\text{N}$ showed a nano-composite structure of mixed cubic and hexagonal structure. The low Al sample, $\text{Ti}_{0.40}\text{Al}_{0.60}\text{N}$ showed no phase transitions after annealing according to the authors, however a minute broadening of the XRD-peaks visible in the figure in the paper might anyway indicate a redistribution of Ti and Al atoms within the B1 lattice. The sample with $\text{Ti}_{0.40}\text{Al}_{0.60}\text{N}$ composition showed appar-

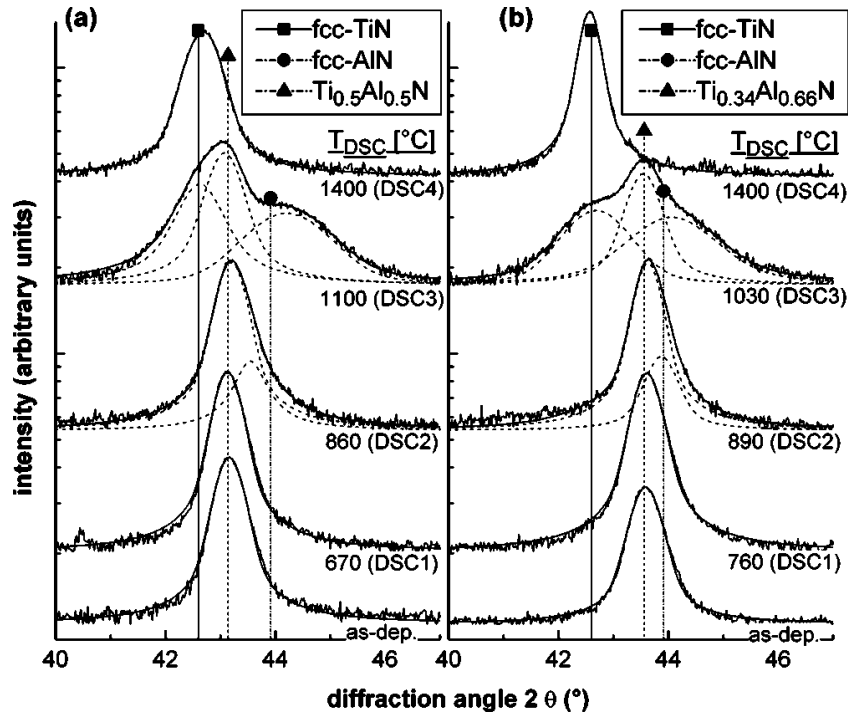


Figure 1.10: X-ray diffraction measurements of $\text{Ti}_{0.34}\text{Al}_{0.66}\text{N}$ and $\text{Ti}_{0.50}\text{Al}_{0.50}\text{N}$ thin films after being subject to annealing at different temperatures. Redrawn from Mayrhofer *et al.* [32].

ent decomposition into c-AlN and a small amount of h-AlN. The $\text{Ti}_{0.30}\text{Al}_{0.70}\text{N}$ showed phase changes for both the cubic and hexagonal phases with the appearance of c-AlN and a change in lattice parameters for the hexagonal phase.

Different individual properties like oxidation resistance and hardness of as-deposited and thermally treated films can be used to understand their properties on a fundamental level. However, at the end of the day it is the actual performance in cutting operations that benchmarks the usability of the coating materials. Fig. 1.12 shows the tool lifetime as a function of Al content in $\text{Ti}_{1-x}\text{Al}_x\text{N}$ coated cutting tools redrawn from [26]. It is directly obvious that the lifetime increase with increasing Al content up to a threshold around $x=0.66$ above which the performance deteriorates, in good agreement with the discussion above.

In summary there is profound experimental evidence that $\text{Ti}_{1-x}\text{Al}_x\text{N}$ thin films when grown using physical vapour deposition techniques forms a cubic B1 solid solution phase (when $x < 0.67$) and a mixed cubic and hexagonal structure when the Al content is higher. When cubic phase films with medium or high Al-content are heat treated at temperatures between 800-1000°C, temperatures where diffusion on the metal sublattice of the cubic B1 phase is likely to have been initiated, an isostructural decomposition, possibly spinodal in nature, into c-AlN and Ti-enriched $\text{Ti}_{1-x}\text{Al}_x\text{N}$ or even TiN takes place. Following this decomposition at higher annealing temperatures there is a transformation of c-AlN into its stable h-AlN polymorph. Films with lower Al-content also shows a tendency for isostructural decomposition. However, it seems to be weaker than for higher Al-content films. This is manifested through higher activation temperatures

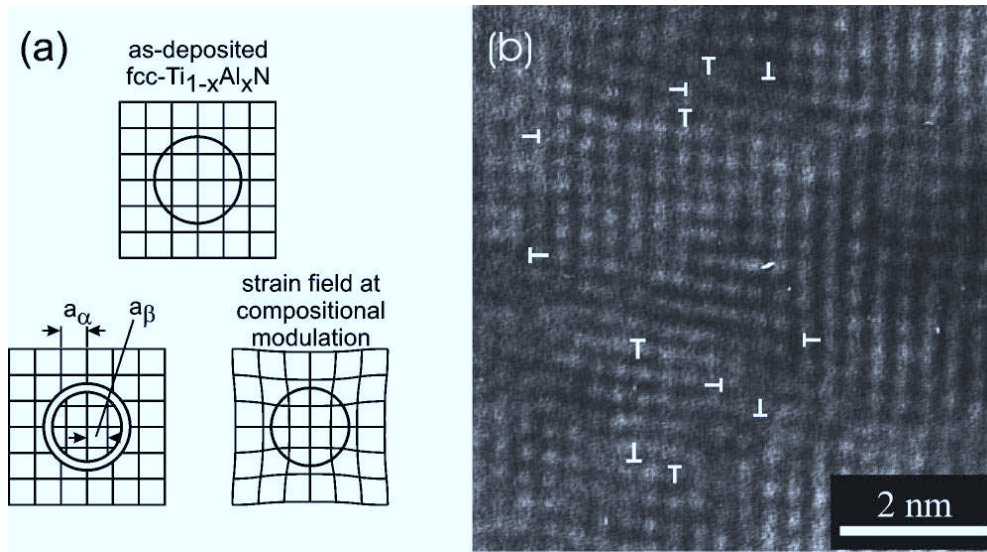


Figure 1.11: (a) Schematic illustration of the explanation in Ref. [32] for the phenomena of age hardening in $\text{Ti}_{0.34}\text{Al}_{0.66}\text{N}$ thin films. The strain fields induced by coherent isostructural decomposition at moderate temperatures are relaxed through introduction of dislocations at temperatures around 1000°C . (b) A TEM photograph of such dislocations. Reprinted from Mayrhofer *et al.* [32]

for the decomposition, weaker signs of decomposed phases in XRD and also absence of age hardening behaviour.

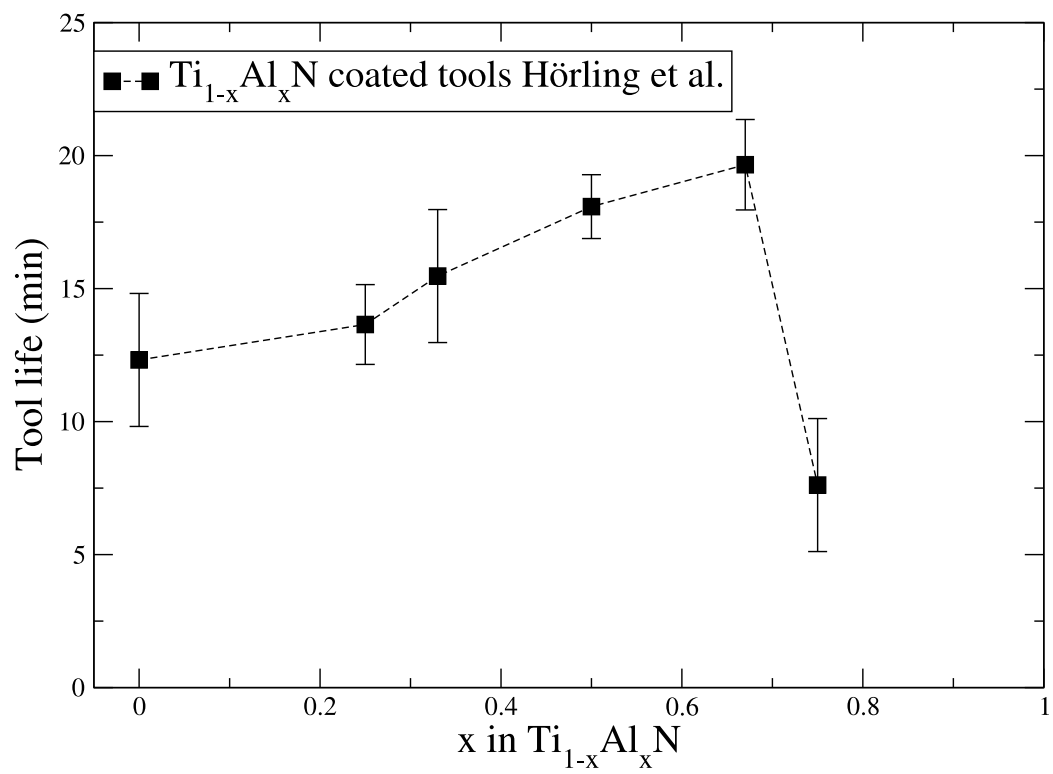


Figure 1.12: Tool lifetime for a TiAlN coated drill as a function of Al-content. Redrawn from Hörling *et al.* [26].

1.5.2 CrAlN

Following the success of adding Al to TiN coatings, the corresponding alloying between AlN and other transition metal nitrides has been explored. Due to the increased oxidation resistance with increasing AlN content in the film, the amount of AlN that can be incorporated into the coating while still keeping the single phase B1 structure has become one of the key issues of cutting tool coating design. One of the absolutely most promising systems in this respect is $\text{Cr}_{1-x}\text{Al}_x\text{N}$ [35–38] where single cubic phase or almost single cubic phase was synthesised with an AlN content higher than 0.70. The solid solution between CrN and AlN was first synthesized in the very end of the 1980's [39, 40] following on the recent development of TiAlN based coatings discussed above. Also in $\text{Cr}_{1-x}\text{Al}_x\text{N}$ solid solutions the lattice spacing decreased with inclusion of AlN compared to CrN indicating a substitutional disorder on the metal sublattice [39].

The general trend in the $\text{Cr}_{1-x}\text{Al}_x\text{N}$ system as compared to $\text{Ti}_{1-x}\text{Al}_x\text{N}$ is that the hardness is somewhat lower for corresponding values of Al-content. The oxidation resistance on the other hand is better compared to $\text{Ti}_{1-x}\text{Al}_x\text{N}$. This can be attributed to two reasons. Primarily the possibility to solve a larger amount of Al in the cubic phase but also due to a better oxidation resistance in CrN where oxidation initiates between 700 and 800°C [37, 41] compared to TiN coatings where oxidation is initiated already at 600°C [22].

The isostructural decomposition within the B1 phase which was discussed above for $\text{Ti}_{1-x}\text{Al}_x\text{N}$ has this far not been observed in the system $\text{Cr}_{1-x}\text{Al}_x\text{N}$ [37, 38]. This absence might actually be a prerequisite for the possibility to create cubic $\text{Cr}_{1-x}\text{Al}_x\text{N}$ phases with x higher than 0.7 or possibly even as high as 0.81 [42]. The absence of isostructural decomposition in the cubic phase would suggest that the age hardening present in the TiAlN system at temperatures between 600 and 950°C would be absent in CrAlN. This is also what is seen experimentally. However, instead a series of phase transformations including several phases related to nitrogen deficiency occurs at temperatures above 900-1000°C. Such transformations might also induce a hardening of the film. Fig. 1.13 shows a schematic diagram illustrating which phases appear when CrAlN coatings of different compositions are annealed to different temperatures [37].

Reiter *et al.* performed an extensive study of the structural, thermal, and mechanical properties of CrAlN coatings [37]. One result that is striking and also different from the TiAlN system is the low temperatures at which the system starts to lose nitrogen to the vacuum or atmosphere. This is manifested in Al-free CrN ($x=0$) coatings through the formation of the nitrogen poor hexagonal Cr_2N phase already at temperatures around 800°C followed by further nitrogen loss and appearance of bcc-Cr at temperatures of 1000°C. When Al is added to the system this temperature is pushed upwards being interpreted as a strengthening of the Cr-N bonds by inclusion of Al. $\text{Cr}_{0.79}\text{Al}_{0.21}\text{N}$ coatings begins to lose nitrogen and transform into Cr_2N phase at 900°C while $\text{Cr}_{0.54}\text{Al}_{0.46}\text{N}$ and $\text{Cr}_{0.29}\text{Al}_{0.71}\text{N}$ films remains in a single B1 phase up to 1000°C where they start to transform. In the Al-containing films the onset of Cr_2N formation is accompanied by the appearance of the hexagonal AlN phase, possibly with a solved amount of Cr [37].

Fig. 1.14 shows the measurement of the hardness of different $\text{Cr}_{1-x}\text{Al}_x\text{N}$ thin films after annealing up to different temperatures as measured in Ref. [37]. The hardness of as-deposited $\text{Cr}_{1-x}\text{Al}_x\text{N}$ thin films was found [37] to raise with increasing Al content from

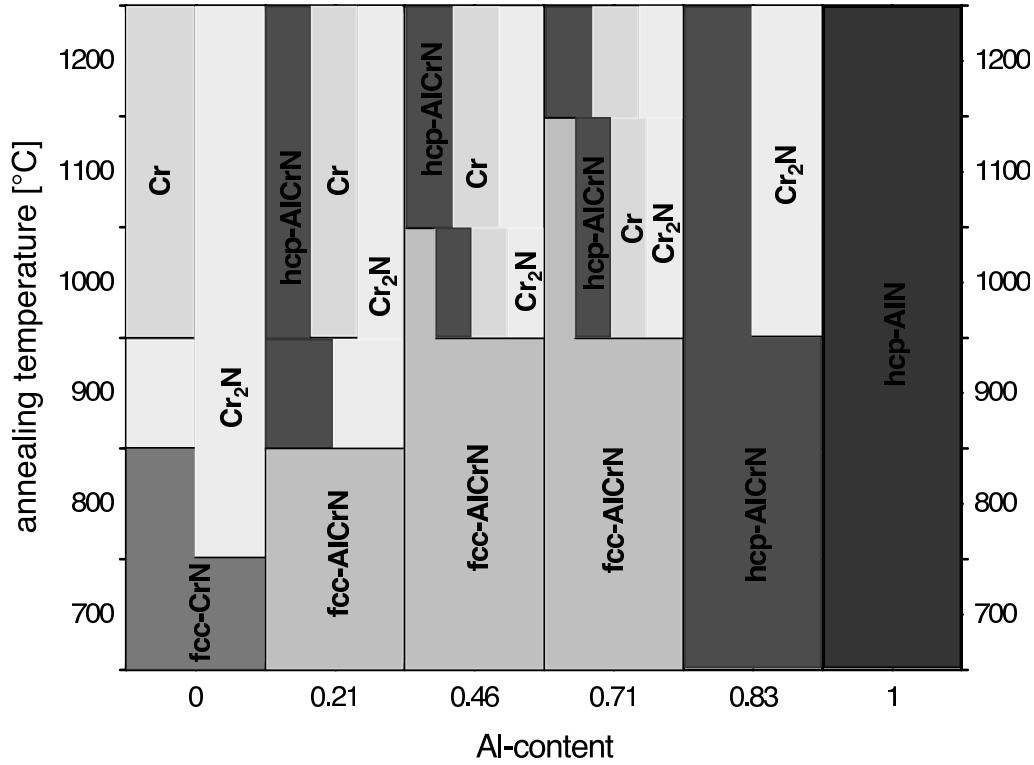


Figure 1.13: A schematic illustration of how the phases of CrAlN coatings of various compositions develop following annealing at different temperatures. Reprinted from Reiter *et al.* [37].

21 GPa for $x=0.00$, CrN to 38.8 GPa to $x=0.46$. The value for $x=0.71$ films was almost as high, 38.4 GPa. The $\text{Cr}_{0.17}\text{Al}_{0.83}\text{N}$ film which shows a hexagonal structure, has a lower hardness, 21.2 GPa. Pure AlN films, has a hardness of 29 GPa.

The hardness of the pure CrN films shows an interesting development with annealing temperatures. The phase transformation from B1 CrN to hexagonal Cr₂N phases increases hardness from 15.2 GPa in the relaxed CrN film to 22.4 GPa in the film annealed to 900°C. This is attributed to the fact that the hexagonal Cr₂N phase in it self is harder compared to the cubic CrN phase [43]. This value is then more or less stable during the continued nitrogen losing process up to temperatures around 1200°C.

The $\text{Cr}_{0.79}\text{Al}_{0.21}\text{N}$ and $\text{Cr}_{54}\text{Al}_{0.46}\text{N}$ coatings show a more expected gradual decrease in hardness without any positive effects of the phase transformations initiated at 900 and 1000°C respectively. With the exception of one data point the $\text{Cr}_{0.29}\text{Al}_{0.71}\text{N}$ coatings show similar behaviour although with a slower decrease in hardness compared to the coatings with lower Al content. The hexagonal $\text{Cr}_{0.17}\text{Al}_{0.83}\text{N}$ film on the other hand shows a steady *increase* in hardness starting from annealing temperatures of 900°C. This could suggest a good performance of such coatings in applications connected with very high temperatures.

As was discussed for $\text{Ti}_{1-x}\text{Al}_x\text{N}$ based coatings above, hardness and oxidation resistance, although extremely important, are only two out of many factors influencing the usability of the coatings. A real benchmarking test for tool lifetime was also done in Ref. [37] and the result is redrawn in Fig. 1.15. This test showed a superior lifetime for tools with the $\text{Cr}_{0.29}\text{Al}_{0.71}\text{N}$ coating. They displayed an almost six-fold increase in tool lifetime

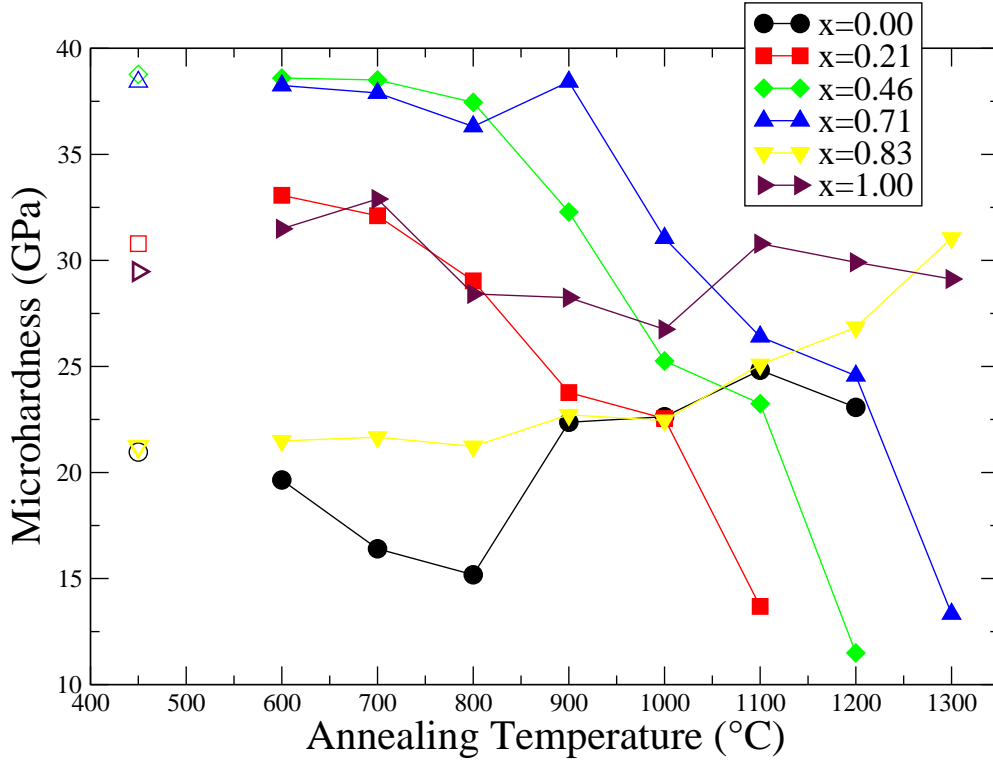


Figure 1.14: The measured hardness of $\text{Cr}_{1-x}\text{Al}_x\text{N}$ thin films of various composition, annealed at different temperatures, as compared to as-deposited values. Redrawn from Reiter *et al.* [37].

as compared to tools coated with CrN and almost the double lifetime compared to $\text{Cr}_{0.54}\text{Al}_{0.46}\text{N}$ and $\text{Cr}_{0.17}\text{Al}_{0.83}\text{N}$ coated tools. Interestingly, also tools coated with pure AlN showed reasonable tool life.

The electronic properties of various $\text{Cr}_{1-x}\text{Al}_x\text{N}$ thin films were measured at room temperature by Sanjines *et al.* [16] using x-ray photo-emission spectroscopy (XPS). Fig. 1.16 shows a redrawing of their valance band measurements. For pure CrN it is in general agreement with the measurement of Gall *et al.* When Al is added to the system the Cr d-state signatures naturally decreases in intensity but also an increased localisation of Cr states are observed.

In summary, CrAlN coatings in the form of B1 $\text{Cr}_{1-x}\text{Al}_x\text{N}$ solid solutions show as high or higher potential than TiAlN for serving as a hard coatings materials on cutting tools. Especially its high thermal stability and oxidation resistance is outstanding. However in certain applications they are inferior compared to TiAlN and the suitable coating material should be chosen with respect to each cutting purpose.

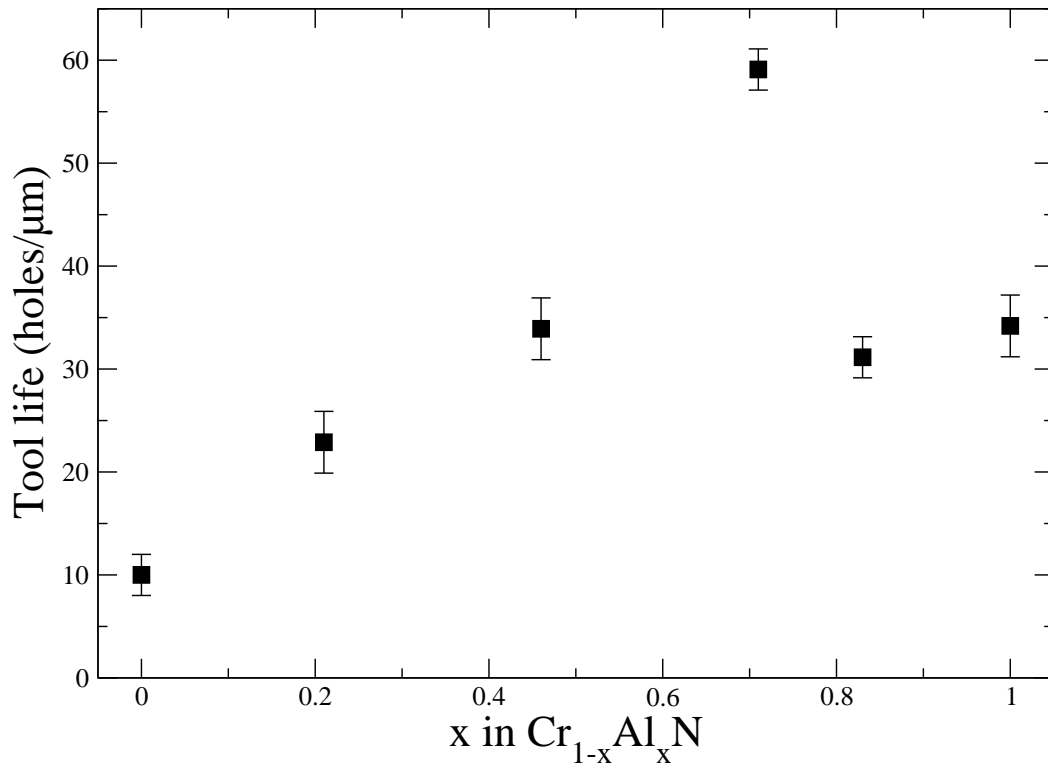


Figure 1.15: The measured lifetime of $\text{Cr}_{1-x}\text{Al}_x\text{N}$ coated tools in drilling tests in steel as a function of the AlN-content x . Redrawn from Reiter *et al.* [37].

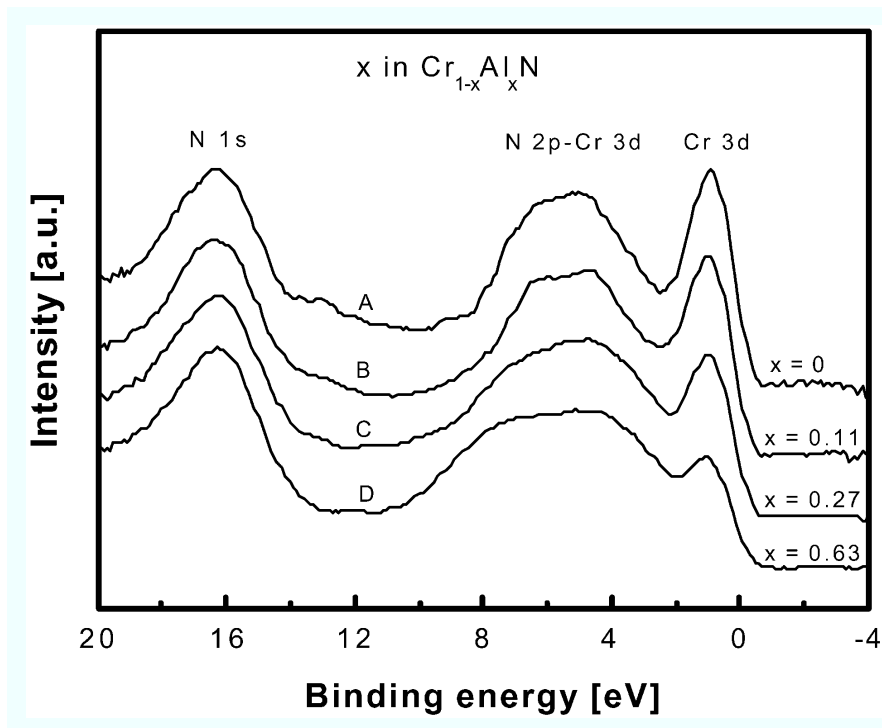


Figure 1.16: The XPS valence band spectra for different $\text{Cr}_{1-x}\text{Al}_x\text{N}$ thin films. Redrawn from Sanjinés *et al.* [16].

1.5.3 Other MAIN systems

Besides TiAlN and CrAlN, several other transition metals have been alloyed with AlN for hard coatings purposes. ZrAlN [44,45] as well as HfAlN [2,46] coatings have been synthesised and investigated. Naturally also multi-component combinations of different transition metals and aluminium nitride have been investigated such as the TiAlZrN [21], TiAlVN [21,47], and TiCrAlN [48] systems.

Hf and Zr are isovalent to Ti and especially HfN is a promising hard coatings material since it has the highest known melting point of all transition metal nitrides, 3310°C [49]. ZrN melts at slightly lower temperatures, 2930-2980°C similar to TiN, 2930-2950°C [49], although these melting temperatures are rather uncertain as can be realised from examining the value given in Fig. 1.6. Further more the alloying of HfN or ZrN with AlN forming HfAlN and ZrAlN coatings offers the possibility to study the effect of a large size mismatch between the alloying components. The downside with HfN is of course the high cost of Hf on the market.

Sanjinés *et al.* studied the thermal stability of $\text{Zr}_{0.65}\text{Al}_{0.35}\text{N}$ and $\text{Zr}_{0.57}\text{Al}_{0.43}\text{N}$ coatings and found that the metastable films started to decompose into Al-poor $\text{Zr}_{1-x}\text{Al}_x\text{N}$ and AlN domains at temperatures above 600°C leading to age hardening. The initial part of this process was interpreted in terms of bulk spinodal decomposition.

Howe *et al.* investigated magnetron sputtered $\text{Hf}_{1-x}\text{Al}_x\text{N}$ thin films with $0 \leq x \leq 0.50$ [46]. They observed single phase B1 structure although an onset of spinodal decomposition was traced in the samples with high AlN content. The hardness of the films increased with addition of AlN by ~30% from 24.7 ± 0.8 GPa in HfN to 32.4 ± 0.7 GPa in $\text{Hf}_{0.71}\text{Al}_{0.29}\text{N}$ above which the hardness of the samples was more or less stable with composition.

Only just recently thin films of the solid solution between ScN and AlN has been synthesised by reactive magnetron sputtering, partly motivated by the present theoretical work [50]. These thin films open the possibility to achieve semiconducting coatings with wear properties possibly similar to the metallic TiAlN coatings.

A large number of different mixed nitride systems based on the alloying of transition metal nitrides with aluminium nitride have thus been synthesised. The control of the phase separation process in these systems is one of the key issues in their usage in hard coatings applications since it can result in both age hardening and film failure. It is clear that a fundamental understanding of the physical origins of these decomposition processes is desirable in order to accelerate the development of new and better hard coatings materials. This is a strong motivation for the present work.

In the current research of hard protective coatings, the synthesis of nano-composites of nitrides materials is perhaps the most hot topic. By refining the grain size of e.g. TiN, TiAlN, or CrAlN phases embedded in e.g. a SiN_x matrix phase, extreme hardness as well as thermal stability has been reported [51,52]. The understanding of these phenomena naturally demands that the physics of the constituting phases like TiAlN or CrAlN are first resolved.

1.6 Insights from theory

1.6.1 Why first-principles?

Solid state physics as well as material science are at the end of the day experimental sciences. The work of a theoretical scientist in this field must be governed by the simple fact that what actually counts is the properties of the materials that can be synthesised. With this perspective in mind it might seem a bit odd to perform a theoretical study from first-principles of hard coatings materials. However, the ideology of the first-principles approach is not to disregard experimental results, only to avoid fitting of any input parameters to experimental values. This gives the calculations that are done using first-principles an extraordinary capability to explain and predict material properties, including phase stabilities, structural, electronic, and magnetic properties independently of previous existing experiments. By comparing such results with the experimentally observed values a confidence about interpretations and conclusions can be reached that would not have been possible with experimental research alone. Furthermore, in calculations using first-principles the effect of different external and internal conditions, such as structure, composition, disorder and pressure can be studied independently, something that is not always the case for the experimentalist. When carried out properly and in close contact with the experimental community, first-principles calculations have the ability to predict new materials guiding the experimental work that must follow.

1.6.2 The bonding picture in transition metal nitrides and carbides

The electronic structure, guiding the bondings of transition metal nitrides and carbides, has been studied for more than 25 years using first-principles approaches [53,54]. In the cubic B1 structure, shown in Fig. 1.5, Ti-atoms form a face centred cubic (fcc) sublattice while the nitrogen or carbon atoms form another fcc-sublattice with an offset of half the cubic lattice parameter along the axis's placing them in an octahedral coordination to Ti. The electronic structure for this atomic arrangement has been presented in Ref.s [54–57] and several later publications. In Fig. 1.17 the valence electronic density of states calculated using a KKR-ASA scheme, described further bellow, is presented. It is very similar to the structure shown in i.e. Ref. [56]. The main features consists of the following: A N 2s semicore state at about 15 eV bellow the Fermi energy (E_F). At about 7-3 eV below E_F a state is present consisting of N-2p and Ti-3d electrons with e_g symmetry as well as a small in-mixture of Ti-4s states. This state is called the bonding state since it is the result of the hybridisation between nearest neighbouring Ti and N atoms. Since N has a higher electronegativity than Ti, these bonding states are mostly of N-character. Slightly above E_F , but with a low energy shoulder overlapping with the bonding states are the so called non-bonding states consisting of Ti-3d electrons with t_{2g} symmetry which can only hybridise weakly with N 2p states but instead also with next-nearest neighbouring Ti-states with the same symmetry. These states also overlap slightly with the anti-bonding states mostly of Ti-3d e_g character. This picture is generally accepted in the literature although Häglund *et al.* [55] suggested that anti-bonding and bonding states should be in reversed order, a picture not supported by

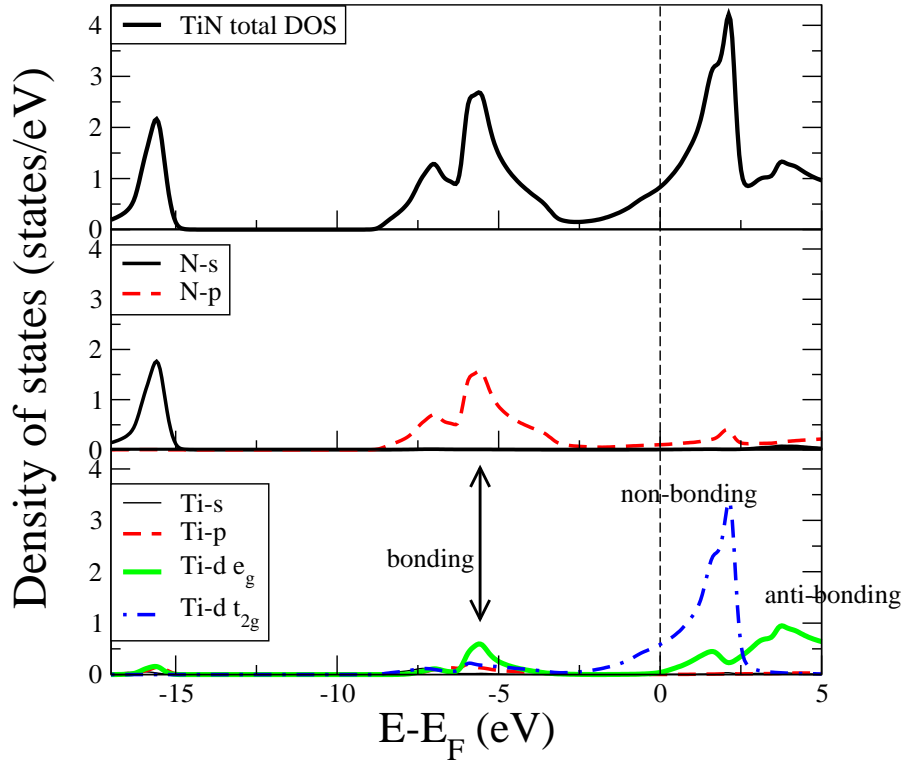


Figure 1.17: The electronic density of states in TiN. Shown are both total DOS and site and orbital projected DOS.

earlier or later works.

1.6.3 The connection between electronic structure and hardness in $\text{TiC}_{1-x}\text{N}_x$

One example of how first-principles calculations might be used to understand the properties of hard coatings materials is the work by Jhi *et al.* [4] explaining the observed hardness maximum at intermediate C/N composition in $\text{TiC}_{1-x}\text{N}_x$ by means of band-filling arguments. In the case of TiC the splitting of bonding and non-bonding states are smaller compared to TiN. TiC also has one less valence electron giving a number of 6 (not counting C-2s semicore states) exactly matching the number of states in the bonding states. Due to the overlap between bonding and non-bonding states, TiC has a substantial part of the bonding states unoccupied. Upon alloying with N, and following a rigid band argument, gradually the high energy tail of the bonding states are filled leading to stronger Ti-C and Ti-N bonds which tends to oppose shear of the cell. However, simultaneously the low energy tail of the non-bonding states are gradually more occupied. These states tends to favour shear of the cell. Thus Jhi *et al.* showed by means of first-principles calculations that the elastic modulus c_{44} of $\text{TiC}_{1-x}\text{N}_x$ alloys reaches a maximum at a composition around $\text{TiC}_{0.60}\text{N}_{0.40}$ in approximative agreement with hardness experiments [4].

1.6.4 AlN

The electronic structure [58–60], as well as structural [61, 62], and vibrational [63, 64] properties of the different prototypes of AlN has been investigated by means of first principles calculations. In general and with the exception of band gap values the results are in good agreement with the experimental measurements.

1.6.5 Alloys of III-V nitride semiconductors

Although semiconductor alloys for electronic applications are far from the main topic of this work, the huge amount of theoretical efforts laid down in this field must be acknowledged due to the role it has played in developing the alloy theory for multicomponent systems, not the least for group III-V nitrides [65]. The group led by A. Zunger has used cluster expansion techniques for predicting and "designing" band gaps, lattice spacing etc. from first-principles [66]. What is striking in this type of material is the central role played by volume misfit of the components and the connected strain relations in the thermodynamics relations of the systems [67].

1.6.6 Early theoretical work on mixed transition metal nitride materials

It is now almost exactly 20 years since the appearance of the first publication of electronic structure calculations of the TiAlN system [68]. However the bands structure calculation was performed non-selfconsistently and no attempts to discuss any properties depending on the total energy was done. In a following work, Vogtenhuber *et al.* performed self-consistent calculations of the band structure of small ordered $\text{Ti}_{0.75}\text{Al}_{0.25}\text{N}$ and $\text{Ti}_{0.50}\text{Al}_{0.50}\text{N}$ systems [69]. Some interesting conclusions were reached regarding a strengthening of Ti-N and Ti-Ti bonds upon Al addition. However, the consequences were not discussed and no total energies were presented. The bandstructure of these compositions was also analysed using the CPA [70]. Ivanovsky *et al.* calculated a series of different systems based on Ti-Al-Si-C-N [71] and concluded, among other things, that it could be ruled out that Al could substitute N instead of Ti. In a more recent study Hugosson *et al.* studied the effect of metal and non-metal substitutions on the relative phase stabilities of the rock salt and wurtzite phases in $\text{Ti}_{1-x}\text{Al}_x\text{N}$. The explicit aim of the study was to come up with substitution suggestions that could make it possible to include more Al in the cubic phase. Unfortunately, the conclusions that higher valent metal substitutions and different non-metal substitutions might be useful [72], are questionable due to the usage of small ordered structures in the calculations, the neglect of the possibility of isostructural decomposition as well as the non-magnetic treatment of Cr and Mn substitutions.

1.6.7 Recent publications

In this section the theoretical work published during the period of this thesis work is briefly presented. It will be discussed in detail in connection to the relevant parts of the results and in the discussion part later in this thesis.

Following the experimental findings of alleged spinodal decomposition and age hardening in Al-rich TiAlN thin films, Mayrhofer *et al.* used first-principles calculations to predict the isostructural binodal and spinodal lines of the B1 cubic $\text{Ti}_{1-x}\text{Al}_x\text{N}$ system [73] as well as other structural properties of the system [74]. Although going beyond the use of small ordered structures such as the ones used in i.e. [72], the method for treating the solid solution can anyway be questioned, as is describe below. Furthermore an unfortunate unit mistake was done leading to an underestimation of all temperatures in the phase diagram by a factor of 2 [75]. Another attempt to connect a few ab initio calculations with thermodynamics modelling of the $\text{Ti}_{1-x}\text{Al}_x\text{N}$ system was made by Zhang *et al.* [76]. Alling *et al.* showed that both a supercell and an effective medium approach could be used to calculate mixing enthalpies as well as related properties for $\text{Ti}_{1-x}\text{Al}_x\text{N}$ in a manner consistent with state of the art alloy theory [77]. In that work conclusions were made connecting the thermodynamics behaviour of the mixed system with the development of the electronic structure with composition. Mayrhofer *et al.* combined the first-principles analyses with thermodynamics and continuum mechanics simulations to predict growth kinetics of AlN and TiN nuclei in TiAlN [78]. The CrAlN system was investigated by Alling *et al.* [79], showing the importance of taking magnetism into consideration when calculating thermodynamic and other properties of the system also above the Neél temperature, a result later supported by calculations of Mayrhofer *et al.* in contrast to Zhang *et al.* who argued that such considerations was unnecessary and performed nonmagnetic calculations [80].

Sheng *et al.* used *ab initio* calculations of small ordered compounds as input to thermodynamics simulations of the system $\text{Zr}_{1-x}\text{Al}_x\text{N}$ [81]. However the large error that could arise from approximating a solid solution with ordered compounds was clearly demonstrated by Alling *et al.* for the case of c- $\text{Ti}_{1-x}\text{Al}_x\text{N}$ together with a general analysis of the effects of electronic structure variations with AlN content in several $\text{M}_{1-x}\text{Al}_x\text{N}$ systems [82].

In common for all these work are that they consider the nitrogen sublattice in the B1 structure as completely occupied. However the B1 phase of TiN is well known to be stable also with considerable amounts of nitrogen vacancies as is indicated in Fig. 1.6. Tsetseris *et al.* considered point defects in TiN, ZrN and HfN, both N vacancies, metal vacancies and different configurations of N and metal interstitials theoretically and found intriguing relations between repulsion and attraction among them [83, 84]. The coupling between composition on the metal sublattice and N sublattice occupation in $\text{Ti}_{1-x}\text{Al}_x\text{N}_{1-y}$ was studied by Alling *et al.* [85]. A coupling was established leading to an increased tendency for decomposition in the nitride in the presence of a small amount of nitrogen vacancies.

Chapter 2

Computational methods

In this chapter the theoretical foundation of this work is presented. The basic equations from quantum mechanics are introduced together with the framework used in this and most present day simulations of the electronic structure of solid state systems, the density functional theory (DFT). In the second part of the chapter the problems and challenges related to simulations of disordered systems such as solid solutions are discussed.

2.1 A Quantum Mechanics description of solids

The understanding of the behaviour of systems at the atomic scale was developed within the framework of quantum mechanics during the beginning of the 20th century. It was manifested through the presentation of the Schrödinger equation, governing non-relativistic quantum systems of particles, and the Dirac equation being the relativistic counterpart for fermionic systems. The calculations performed in this work are based on the scalar form of the relativistic Dirac equation but for simplicity and without losing any of the key features of the theory, the formalism is presented below based on the Schrödinger equation.

The motion of the particles of a non-relativistic quantum mechanical system is governed by the time-dependent Schrödinger equation

$$i\hbar\frac{\partial\Psi}{\partial t} = H\Psi \quad (2.1)$$

where Ψ is the many-body wave function and H is the Hamiltonian of the system. In the case of normal matter consisting of atomic nuclei and electrons, the wave function

$$\Psi = \Psi(\mathbf{r}_1, \mathbf{r}_2, \dots, \mathbf{r}_n, \mathbf{R}_1, \mathbf{R}_2, \dots, \mathbf{R}_N, t) = \Psi(\bar{\mathbf{r}}, \bar{\mathbf{R}}, t) \quad (2.2)$$

depends on the coordinates of all n electrons (spin is assumed to be included in the coordinates \mathbf{r}_i and \mathbf{R}_i), all N nuclei, and the time. In the absence of any external perturbation like a magnetic or electric field, the Hamiltonian is given by¹

¹Neglecting the weak gravitational interaction between particles and considering the nuclei as single particles.

$$H = -\frac{1}{2} \sum_{i=1}^n \frac{\hbar^2}{m_e} \nabla_i^2 - \frac{1}{2} \sum_{I=1}^N \frac{\hbar^2}{M_I} \nabla_I^2 - \frac{1}{2} \sum_{i,I} \frac{Z_I e^2}{|\mathbf{r}_i - \mathbf{R}_I|} + \frac{1}{2} \sum_{i \neq j} \frac{e^2}{|\mathbf{r}_i - \mathbf{r}_j|} + \frac{1}{2} \sum_{I \neq J} \frac{Z_I Z_J e^2}{|\mathbf{R}_I - \mathbf{R}_J|} \quad (2.3)$$

where the first term on the right hand side is the kinetic energy for the n electrons, the second term is the kinetic energy of the N nuclei, the third term is the coulomb interaction between electrons and nuclei, the fourth term is the electron-electron interaction, and the fifth term is the nuclei-nuclei interaction.

Due to the three potential energy terms in Eq. 2.3 the degrees of freedom connected to the position of all electrons and all nuclei becomes coupled and one readily realises that to solve Eq. 2.1 directly is impossible for systems with more than just a few particles and definitely for macroscopic systems containing in the order of 10^{23} nuclei and an additional order of magnitude number of electrons. The first approximation that can be done to simplify the problem is the separation of the motion of the electrons from the motion of the nuclei. One can argue that the mass of the electrons are so small in comparison with the mass of the nuclei so that their acceleration in response to changes in the system are orders of magnitude larger. This would mean that the electrons effectively move in the potential field from fixed nuclei resulting in a so called electronic structure problem. Furthermore if the motion of the nuclei is of interest their equation of motion can be solved iteratively for each step resolving the electronic structure resulting in a new potential surface for the nuclei. This is the famous Born-Openheimer approximation which has been shown to be extremely accurate in most systems of relevance for this work. The rest of this section will treat the electronic structure problem considering the potential from the nuclei as a fixed external potential. The problem regarding specific distributions of atoms and thus different potentials will be discussed in the next part.

It is easily shown that in the absence of an explicit time dependence of the Hamiltonian the wave function can be separated into a product of time and space dependent functions

$$\Psi(\bar{\mathbf{r}}, t) = \Phi(\bar{\mathbf{r}})\chi(t) \quad (2.4)$$

where the space part satisfy the time independent Schrödinger equation

$$H\Phi(\bar{\mathbf{r}}) = E\Phi(\bar{\mathbf{r}}) \quad (2.5)$$

which is an eigenvalue problem with the solutions, the eigenfunctions or eigenstates $\phi_n(\bar{\mathbf{r}})$ being the standing waves corresponding to their respectively energy eigenvalue E_n . Since electrons are fermionic particles their wave function must be antisymmetric with respect to change of any two coordinates.

In solid state systems the atoms typically form crystals with a periodic repetition of atomic positions in space². This translation symmetry also gives rise to a periodicity of the external potential felt by the electrons. According to Bloch's theorem [86] a wave-function solving the Schrödinger equation in such a periodic potential can be expressed as

²Neglecting for the time displacements due to thermal vibration, defects and disorder.

$$\phi_{n\mathbf{k}}(\bar{\mathbf{r}}) = e^{i\mathbf{k}\cdot\mathbf{r}} u_{n\mathbf{k}}(\bar{\mathbf{r}}) \quad (2.6)$$

where \mathbf{k} is a reciprocal vector, $e^{i\mathbf{k}\cdot\mathbf{r}}$ is a plane wave and $u_{n\mathbf{k}}(\bar{\mathbf{r}})$ is a function with the periodicity of the lattice. This implies that we only have to solve the problem of the wave function in the crystal for one unit cell, corresponding in reciprocal space to the first Brillouin zone.

Even though simplified the task of solving Eq. 2.5 for real materials systems is still unmanageable due to the coupling of the electrons through the Coulomb repulsion term in the Hamiltonian. Different approximative methods are in use to handle this problem but in materials modelling of today, one method, the density functional theory is completely dominating.

2.2 Density Functional Theory

The basic ideas behind density functional theory (DFT) is to move away from the terribly complicated many-body wave function $\Phi(\bar{\mathbf{r}})$ depending on all $3n$ variables (not counting spin) of the included electrons and consider instead the electron density $n(\mathbf{r})$ depending on only 3. Attempts with density functional theories are almost as old as quantum mechanics itself with important examples such as the Thomas-Fermi theory [87, 88]. However it was only with the publication of the Hohenberg-Kohn theorems [89] in 1964 and the development of the Kohn-Sham approach [90] the year after that the theory reached a level where quantitative predictions of materials properties came within reach.

2.2.1 The Hohenberg-Kohn theorem

Hohenberg and Kohn presented the cornerstones of exact DFT in two important theorems. The first theorem states that for any system of interacting particles in an external potential $V_{ext}(\mathbf{r})$, the potential is uniquely determined up to a constant by the ground state particle density $n_0(\mathbf{r})$.

This statement might not be completely intuitive since the normal procedure in solving the Schrödinger equation is to start with the external potential, solve the equation to obtain all eigenstates, find the eigenstate with the lowest energy (the ground state), and from this construct the ground state density. However the theorem is easily proven with contradiction [89]. Following directly from this first theorem is the fact that since the external potential is determined, all properties, ground state and excited state properties alike, are also determined.

The second theorem states that there exists a universal functional for the energy, $E[n(\mathbf{r})]$ that is valid for any external potential which has its global minima, equal to the exact ground state energy, for the exact ground state density $n_0(\mathbf{r})$.

These theorems clearly show that a density functional approach has the potential for success, however the problem is that the functional $E[n]$ is not known.

2.2.2 The Kohn-Sham equations

The year after the publication of the Hohenberg-Kohn theorems, Kohn and Sham published a paper [90] where they suggested a practical approach to this problem. They proposed that the properties of the real many-body problem could be obtained by calculations of an auxiliary system of independent particles moving in an effective external potential V_s , chosen in such a way that the density of the auxiliary system equals that of the real system. This turned out to be a great improvement on earlier density functional approaches that tried to directly find approximate functionals for the energy using for instance a local density functional approximation for the kinetic energy.

Instead in the Kohn-Sham approach the independent particles are the solutions to Schrödinger-like equations

$$\left(\frac{-\hbar^2}{2m_e} \nabla^2 + V_s(\mathbf{r}) \right) \varphi_i = \epsilon_i \varphi_i \quad (2.7)$$

where the effective potential is given by

$$V_s(\mathbf{r}) = V_{ext} + e^2 \int \frac{n(\mathbf{r}')}{|\mathbf{r} - \mathbf{r}'|} d\mathbf{r}' + \frac{\delta E_{xc}[n(\mathbf{r})]}{\delta n(\mathbf{r})} \quad (2.8)$$

Where $E_{xc}[n(\mathbf{r})]$ is the exchange-correlation energy to be discussed below. The total energy of the Kohn-Sham system is given by the functional

$$E_{KS} = T_s[n] + \int d(\mathbf{r}) V_{ext}(\mathbf{r}) n(\mathbf{r}) + E_{Hartree}[n] + E_{xc}[n] + E_{II} \quad (2.9)$$

Where the first term on the right hand side is the kinetic energy of the non-interacting system

$$T_s[n] = -\frac{\hbar^2}{2m_e} \sum_{i=1}^n \langle \varphi_i | \nabla^2 | \varphi_i \rangle \quad (2.10)$$

the second term is the interaction with the external potential, the third term is the classical electrostatic or Hartree-term

$$E_{Hartree}[n] = \frac{1}{2} \int d\mathbf{r} d\mathbf{r}' \frac{n(\mathbf{r}) n(\mathbf{r}')}{|\mathbf{r} - \mathbf{r}'|} \quad (2.11)$$

the forth is the exchange-correlation energy and the fifth is the nuclear-nuclear repulsion energy. The latter only adds a energy constant but is of course essential to include if optimal nuclei coordinates are searched for.

2.2.3 The exchange and correlation energies

The only term in Eq. 2.9 which can not be exactly calculated is the exchange-correlation energy term $E_{xc}[n(\mathbf{r})]$. In this term all the delicate physics of the many-body effects originating from the Schrödinger equation is included and good approximations have to be applied in order to achieve reasonable results from the Kohn-Sham procedure. Before

going into this details we note that one, although definitely not the only, reason why the Kohn-Sham ansatz turns out to work very well is that an approximative treatment is used only for a term in Eq. 2.9 which is rather small as compared to the other terms. In Fig. 2.1 the energy terms of the TiN system as calculated with the Local Density Approximation (LDA) and the Koringa-Kohn-Rostocker (KKR) framework within the atomic sphere approximation (ASA) to be described below are shown. One realises, although the numbers would not be exactly the same, that one of the main reasons for the failure of the earlier Thomas-Fermi theory was that it attempted to approximate also the much larger kinetic energy term within the a local approximation for the density.

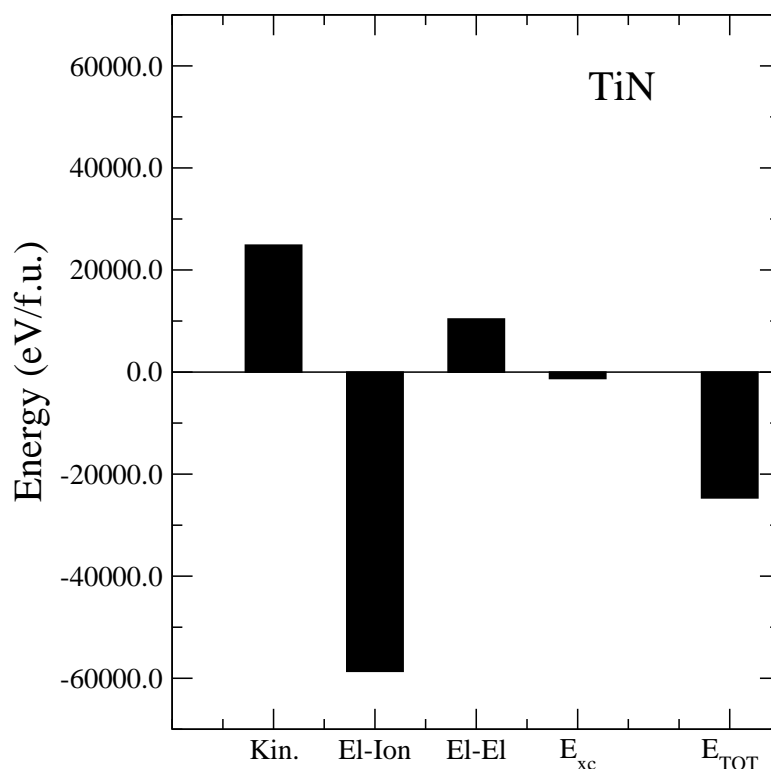


Figure 2.1: The calculated different energies of the TiN system using KKR-ASA method and the Local Density Approximation. The kinetic energy of the electrons, the potential energy due to electron-ion attraction, electron-electron repulsion as well as exchange-correlation energy is shown together with the total energy.

However, the exchange-correlation energy is anyway large enough to be of utmost importance for the energy scale governing bonding, mixing, structural stability and other important properties of solid state matter.

The local density approximation

Already in their 1965 paper Kohn and Sham proposed the Local Density Approximation (LDA) for treating the exchange-correlation energy functional. However, the subsequent success of that particular approximation was probably surprising for them. In the LDA the exchange-correlation energy is given by

$$E_{xc}^{LDA}[n] = \int \epsilon_{xc}^{hom}(n(\mathbf{r}))n(\mathbf{r})d\mathbf{r} \quad (2.12)$$

where $\epsilon_{xc}^{hom}(n(\mathbf{r}))$ stands for the exchange-correlation energy per unit charge in a homogeneous electron gas with the same density as the considered point in space in the system. The exchange-correlation energy of the homogeneous electron gas has been calculated with extreme accuracy using quantum Monte Carlo simulations [91] for different densities and is implemented in most electronic structure codes using reasonable parametrisations [92,93]. It is not completely obvious why the LDA gives such reasonable results for a large number of properties and materials. In real atomic systems the density is far from homogeneous and it is not even specifically slowly varying. However, in the region of space far from the nuclei in crystals, the region mainly responsible for the bonding, the gradients of the density are not so large. Furthermore, it turns out that what enters into the exchange-correlation energy is the system-average, spherical-average of the so called exchange-correlation hole, (in general) depletion in the charge density around an electron. Or more correctly the interaction between the charge density and the exchange-correlation hole. Even though the detailed behaviour of this hole can be rather different for real systems as compared to the homogeneous electron gas, the averaged values are not. This is so since all exchange correlation holes of real electronic Hamiltonians, including the one corresponding to the homogeneous electron gas, obeys certain limiting condition such as sum rules, which heavily reduces the possible differences in averaged values [94].

The Generalized Gradient Approximation

Nevertheless the LDA has certain limitations especially when treating atoms and molecules naturally showing quite substantial density gradients. Also in the case of 3d transition metals and their alloys, the LDA underestimates the volume quite substantially. The latter problem can give rise to rather profound errors in prediction, for instance Fe is predicted to be of fcc rather than bcc crystal structure. A natural attempt to improve on the LDA is to include the effect of density gradients. However it turns out that it is not an easy task to construct a functional which systematically improves the LDA results. The reason is that when different gradient correction schemes, such as for instance the gradient expansion approximation (GEA) also suggested by Kohn and Sham [90], is introduced, the functional does not any longer have the foundation of a real electron Hamiltonian. The results are that certain limiting conditions for the exchange-correlation hole may no longer be fulfilled leading to unphysical behaviour for some situations. An approach that has proven to be very useful is the class of functionals named generalised gradient approximations (GGA). In these functionals, some limiting values of the exchange-correlation hole are fixed by hand so that the down side of the GEA are corrected. A number of different GGA's have been proposed [95,96], the one used most frequently throughout this work is the functional according to Perdew, Burke, and Enzerhof (PBE) from 1996 [97].

The GGA functionals are usually formulated based on an enhancement factor of the LDA exchange energy

$$E_{xc}^{GGA}[n] = \int d\mathbf{r} \epsilon_x^{hom}(n(\mathbf{r})) F_{xc}(n(\mathbf{r}), s(\mathbf{r})) \quad (2.13)$$

where $s(\mathbf{r}) = \frac{|\nabla n(\mathbf{r})|}{2k_F n(\mathbf{r})}$ is the reduced gradient and $F_{xc}(n(\mathbf{r}), s(\mathbf{r}))$ is an enhancement factor regulating both correlation and gradient dependent terms.

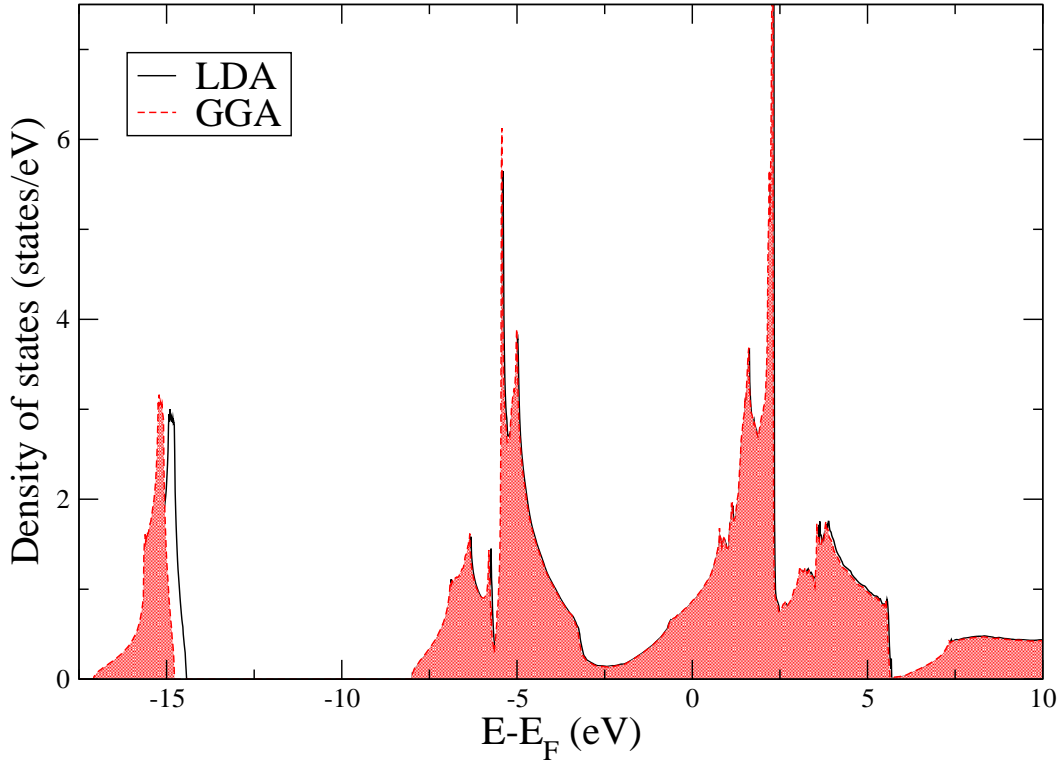


Figure 2.2: The calculated electronic density of states for TiN at the experimental lattice spacing of 4.24 Å, using both LDA and the PBE-96 GGA approximations for exchange and correlation effects. For clarity the area under the GGA curve has been shaded. Note that the two approximations give almost identical results for the valence states. For the N 2s semicore states where the density gradients are somewhat larger, a difference can be seen.

The main reason why GGA outperforms the LDA in many systems based on 3d elements is the improved results for equilibrium volumes and lattice parameters. However, this result is not mainly due to an improved description of the valence states as one would believe. Fig. 2.2 shows the calculated valence density of states for TiN using both LDA and GGA-PBE96 for a fixed lattice spacing corresponding to the experimental value 4.24 Å. For clarity the GGA curve has been shaded. It is clear that for the valence band, the difference is very small. Instead, for the N 2s semi-core state where density gradients are larger, an effect can be seen. This indicates that given that the volume is treated correctly, the LDA-based and GGA-based calculation of physical properties of solid state systems are likely to give similar results [98]. It should be noted that both the LDA and the GGA functionals can easily be generalized to account for spin polarisation, i.e. magnetism.

Strong electron correlation beyond the LDA and GGA

There are other situations where the LDA shows qualitative errors which are in principle not improved at all by the GGA. One such error is the well known underestimation of band gaps in semiconductors. The main reason for this problem is that the self interaction of the charge density through the Hartree-term is only approximately cancelled by the exchange-correlation energy in non homogeneous systems. This leads to a shift to higher energies for occupied states thus decreasing band gaps. This is not necessarily a problem if only relative energy differences of ground state structures are of interest since the total energy only depends on the occupied states. It might be a problem if disturbances in the system, such as defect introduced states, are predicted to be above the conduction band edge due to the band gap underestimation.

Another problem is the treatise of systems where strongly localised states are present together with delocalised states. Examples of such systems are f-electron systems with partially filled f-bands as well as 3d-metal oxides. In these systems the LDA is likely to get a result where also the f- and d-states are itinerant. The research on this type of systems with strong correlation effects is actually one of the most hot topics in electronic structure theory of today.

A rather blunt but still quite successful approach to strong correlation is the so called LDA+U approach. It is based on the idea that the on-site, intra-band electron-electron interaction of localised states in the LDA should be substituted with a Hubbard type Hamiltonian. Assuming that the total coulomb energy of these states are given correctly by the LDA and subtracting this term to avoid double counting one arrives, using the rotationally invariant scheme according to Dudarev *et al.* [99] in the formula:

$$E_{LDA+U} = E_{LDA} + \frac{U - J}{2} \sum_{\sigma} \left[\left(\sum_i \rho_{i,i}^{\sigma} \right) - \left(\sum_i \sum_j \rho_{i,j}^{\sigma} \rho_{j,i}^{\sigma} \right) \right] \quad (2.14)$$

where ρ^{σ} is the density matrix of the correlated states, U and J are the screened averaged Coulomb and exchange parameters. The two latter parameters could in principle be calculated using e.g. constrained LDA calculations but could also be used as fitting parameters to experimental data. Note that in Eq. 2.14 there is only one free parameter in terms of the difference $U - J$. The effective result of this approach is that occupied states are shifted down while unoccupied states are shifted up in energy.

Of relevance for the present work is the realisation that band gaps in e.g. B1 AlN are probably underestimated by the calculations. However, this is not likely to influence the total energy calculations of the alloys and are not crucial. In the case of CrN it seems possible that strong correlations play some role and an investigation using the LDA+U approach is performed.

2.2.4 Solving the equations

When the Kohn-Sham equations are to be solved two qualitatively different classes of methods exist. The first one relies on the direct treatment of the Hamiltonian and works with wave functions. The other class is based on multiple scattering theory and has the electron Greens-function as the central property. In this work both classes of methods

have been applied. To do calculations for ordinary supercells mainly a wave function based method, the projector augmented wave method (PAW) has been applied while two different approaches to Green's-functions formalism have been applied to treat disorder in an analytical way.

2.2.5 The Projector Augmented Wave method

To solve the electronic structure problem numerically one needs to expand the independent particle wave functions in a basis set.

$$\varphi_{n\mathbf{k}}(\mathbf{r}) = \sum_i c_{n\mathbf{k},i} \psi_{n\mathbf{k},i}(\mathbf{r}) \quad (2.15)$$

where $\psi_{n\mathbf{k},i}(\mathbf{r})$ are the basis functions and $c_{n\mathbf{k},i}$ are the expansion coefficients. Due to the periodicity of the lattice (unit cell or supercell) and the corresponding periodicity of the wave functions, Eq. 2.6, a practical approach in many aspects is to use plane waves as the basis set. This is a nice set of functions from a computational point of view due to the numerical machinery for treating this kind of problems such as fast Fourier transforms.

The periodic function in Eq. 2.6 can then be expressed

$$u_{n\mathbf{k}}(\mathbf{r}) = \sum_{\mathbf{G}} c_{n\mathbf{k},\mathbf{G}} e^{i(\mathbf{G} \cdot \mathbf{r})} \quad (2.16)$$

and thus

$$\phi_{n\mathbf{k}}(\mathbf{r}) = \sum_{\mathbf{G}} c_{n\mathbf{k},\mathbf{G}} e^{i(\mathbf{k} + \mathbf{G}) \cdot \mathbf{r}} \quad (2.17)$$

where the problem now is to find the Fourier coefficients $c_{n\mathbf{k},\mathbf{G}}$. In practise one has to use a finite set of plane waves so an energy cut-off is applied including in Eq. 2.17 only plane waves with kinetic energy $\frac{\hbar^2}{2m_e} |\mathbf{k} + \mathbf{G}|^2 < E_{cut}$. The problem with a plane wave expansion of the wave functions is the treatment of the core region where electrons have high kinetic energy due to the strong Coulomb interaction from the nucleus and the Pauli principle. An alternative to include huge numbers of plane waves in the expansion is to use so called pseudopotentials. The pseudopotential method aims to replace the potential of the core region, including the effect of the nucleus and core electrons, with an effective smooth potential. This pseudopotential is constructed in such a way that the valence electron wave functions as well as the potential, although being replaced by smooth pseudo wavefunctions and potentials inside a specified radius from the nucleus, are still identical to those in a real all-electron problem outside this radius [94, 100, 101]. An extension to this method is the projector augmented wave method (PAW) introduced by Blöchl [102]. This method keeps the wave function of the core electrons in the calculations but applies the frozen-core approximation where they are unaffected by the behaviour of the valence states. In this work an implementation of the PAW method in the Vienna *ab-initio* simulation package (VASP) [103, 104] is used.

2.2.6 Green's-function methods

The alternative to the Hamiltonian approach to the Kohn-Sham equations is the Green's-function formalism. This formalism is computationally slower when doing calculations for ordered systems but, as we will see, has a big advantage when it comes to treating systems with disorder.

The one-particle Green's-function describes the propagation of a particle of energy E from point \mathbf{r} to another point \mathbf{r}' . It solves the Schrödinger-like equation of energy E

$$\left(-\frac{\hbar^2}{2m_e}\nabla^2 + V_s(\mathbf{r}) - E\right) G(\mathbf{r}, \mathbf{r}', E) = -\delta(\mathbf{r} - \mathbf{r}'). \quad (2.18)$$

The natural formalism for the electron Green's function is the multiple scattering theory in the Korringa-Kohn-Rostocker method [105,106]. Considering non-overlapping muffin-tin spheres centred at each nuclei position as scattering centres and solving the scattering problem the Green's-function can be obtained as

$$G(\mathbf{r} + \mathbf{R}_i, \mathbf{r}' + \mathbf{R}_j, E) = \sum_{LL'} R_{il}(\mathbf{r}, E) g_{LL'}^{ij}(E) R_{j'l'}(\mathbf{r}', E) - \delta_{ij} \sum_L R_{il}(\mathbf{r}, E) H_{jl}(E) \quad (2.19)$$

where the coordinates \mathbf{r} and \mathbf{r}' are inside the spheres centred at \mathbf{R}_i and \mathbf{R}_j respectively, E is the energy relative the potential in between the spheres, L is the combination of angular-momentum quantum numbers, and $R_{jl'}(\mathbf{r}', E)$ and $H_{jl'}(\mathbf{r}', E)$ are the regular and irregular solutions to the Schrödinger like equation in the sphere i for orbital angular-momentum l and energy E .

The central object is the scattering path operator $g_{LL'}^{ij}(E)$ which in a simple monoatomic case it is given by

$$g_{LL'}^{ij}(E) = \frac{1}{V_{BZ}} \int_{BZ} d\mathbf{k} [m(E) - B(\mathbf{k}, E)]_{LL'}^{-1} e^{i\mathbf{k}(\mathbf{R}_i - \mathbf{R}_j)} \quad (2.20)$$

where $m(E)$ is the potential function and $B(\mathbf{k}, E)$ is the Fourier transformed structure constant matrix. This separation of the atomic part and structural part is general for multiple scattering methods and a great advantage when one is to develop schemes for treating disordered system as will be shown below. In this work two different Green's function methods, the Korringa-Kohn-Rostocker-atomic sphere approximation (KKR-ASA) [107–110] as implemented in the bulk Green's-function method (BGFM) [111] and in the order- N locally self-consistent green's-function method (LSGF) [112,113], as well as the exact muffin-tin orbitals method (EMTO) [114,115] were used. They differ in the particular representation of the potentials as well as wave functions with the latter in principle giving a possible accuracy in level with full-potential methods.

2.3 The treatment of disordered systems

The objective of this work is to study materials systems which display disordered phases. In condensed matter there are two distinct types of disorder. First there are topologically

disordered systems, where atomic positions can not be associated with a lattice i.e. liquid and amorphous materials. Then there are random alloys. In the latter case, which is treated here, the positions of the atoms are connected to lattice points but the distribution of atomic species over them is stochastic. The fact that the atoms in an alloy in general show a non-periodic displacement from the ideal lattice points due to thermal vibration and local lattice relaxations do not change the analysis. Point defects, such as vacancies, can also be counted to this kind of disordered system.

The perfect random alloy, where the distribution of components is completely stochastic and uncorrected is of course an idealisation for equilibrium systems. In principle this would be the situation when $V/T \rightarrow 0$ where V corresponds to the strongest effective interaction in the system. In principle this argument is true also for non-equilibrium systems such as thin films synthesised using PVD. Instead the materials are likely to show some degree of short ranged tendencies towards either ordering or clustering, also in the alleged random alloy state. Nevertheless, the ideal random state is a good starting point for a theoretical analysis, especially when the tendencies are unknown. In any case the systems are non-periodic and the calculations of properties of such systems from first-principles are not trivial.

The atomic configuration on a lattice can be described by occupation numbers

$$c_{i:p} = \begin{cases} 1 & \text{if component } p \text{ occupies site } i, \\ 0 & \text{otherwise.} \end{cases} \quad (2.21)$$

For a quasi-binary alloy such as Ti and Al on the metal sublattice of $\text{Ti}_{1-x}\text{Al}_x\text{N}$, there is only one independent occupation number. The set of all occupation numbers uniquely determines the configuration of the whole crystal but gives large amount of excessive information. Instead a statistical representation is of interest. Such a representation are occupation correlation functions which can be defined as

$$\zeta_f^{(n)-pq\dots r} = \langle c_{i;p} c_{j;q} \dots c_{k;r} \rangle - c_p c_q \dots c_r \quad (2.22)$$

where $\langle \dots \rangle_f$ is the ensemble average over all n -site clusters of type f that are equivalent due to the symmetry of the crystal. c_p is the concentrations of component p in the alloy. It is easily seen that in the ideally random alloy with uncorrelated distribution, $\zeta_f^{(n)-pq\dots r} = 0$. A usual way to describe the correlation function for pair clusters is the Warren-Cowley short range order (SRO) parameters defined for a binary alloy as

$$\alpha_n^{AB} = -\frac{\zeta_n^{(2)-AB}}{c_A c_B} \quad (2.23)$$

where n gives the coordination shell. The values of these parameters can be measured by e.g. diffuse neutron scattering experiments. A schematic 2D representation of $\text{A}_{0.5}\text{B}_{0.5}$ square lattice systems with different values of short range order can be seen in Fig. 2.3. In panel (a) a supercell is presented that is strongly clustered, well on its way to complete phase separation (which would correspond to $\alpha_i^{AB} = 1$ for all coordination shells). In panel (b) a cell is shown where there is short range clustering present with a value of $\alpha_1^{AB} = 0.4$. Panel (c) shows a cell which actually is a very good representation of an ideal random situation for this 2D square lattice. The value of α_i^{AB} is very close to 0 for the first 6 coordination shells. Panel (d) shows instead the opposite trend with a short

range order of $\alpha_1^{AB} = -0.4$. Panel (d) and (e) shows two different types of order with different values of the SRO-parameters.

From this schematics and especially the panel (c) in Fig. 2.3 it seems plausible that i.e. the total energy of any configuration, including ideally random distribution, could be calculated using a large enough supercell. At least this is the case as long as effective interactions in the system are not infinitely ranged. However, it is not clear how large the supercell needs to be, or how it should look. The answer can be found through a cluster expansion of the alloy energetics. The foundation for this theoretical framework, briefly described below for the case of a binary alloy, was worked out by Sanchez, Ducastelle, and Gratias [116] and was recently reviewed in Ref. [98].

An alternative to the occupation numbers introduced above is the so called spin variables σ_i which is +1 if site i is occupied by atom A and -1 if it is occupied by atom B. Then for a crystal with N sites a characteristic function

$$\Phi_d^{(n)}(\bar{\sigma}) = \prod_{i \in d} \sigma_i. \quad (2.24)$$

can be defined for every cluster d of order n in the crystal, where $\bar{\sigma}$ is the N -dimensional vector describing the configuration of the crystal. It was shown that, applying the proper inner product [116], these functions form a complete orthonormal set for any given crystal and thus can be used as basis functions to expand any property $G(\bar{\sigma})$ which is a function of the configuration:

$$G(\bar{\sigma}) = \sum_d g_d^{(n)} \Phi_d^{(n)}(\bar{\sigma}) \quad (2.25)$$

The expansion coefficients are simply the projections

$$g_d^{(n)} = \langle G(\bar{\sigma}), \Phi_d^{(n)}(\bar{\sigma}) \rangle, \quad (2.26)$$

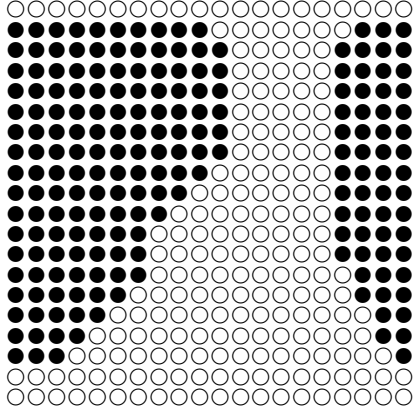
and when the alloy total energy is the function of interest the coefficients are the so called effective cluster interactions,

$$V_d^{(n)} = \langle E_{tot}(\bar{\sigma}), \Phi_d^{(n)}(\bar{\sigma}) \rangle \quad (2.27)$$

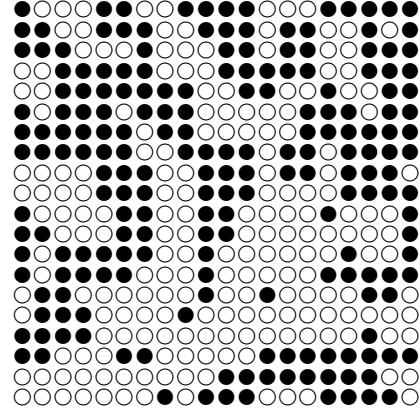
which plays a central role in the alloy theory. Due to the symmetry of the lattice, all $V_d^{(n)}$ of clusters connected through symmetry operations to the same figure $d \in f$ must be the same and if they are known one can easily and quickly calculate the total energy of any configuration as

$$E_{tot}(\bar{\sigma}) = \sum_f V_f^{(n)} m_f^{(n)} \xi_f^{(n)}(\bar{\sigma}) \quad (2.28)$$

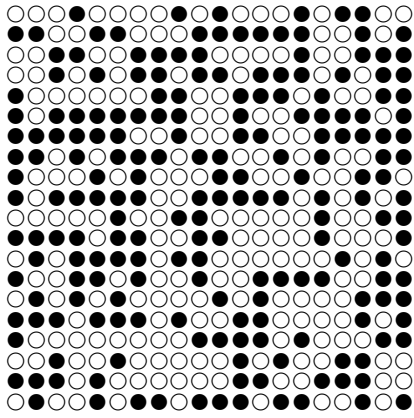
where the sum now runs over all distinct figures f of the lattice and $\xi_f^{(n)}(\bar{\sigma})$ is the correlation function for the figure f , the average value of the corresponding characteristic functions, $\xi_f^{(n)}(\bar{\sigma}) = \langle \Phi_{d \in f}^{(n)} \rangle$, $m_f^{(n)}$ is just the weight factor for the figure f on the lattice. For instance, on the fcc-lattice each atom has 12 nearest neighbours but only 6 next-nearest neighbours which is manifested through different values of $m_f^{(n)}$.



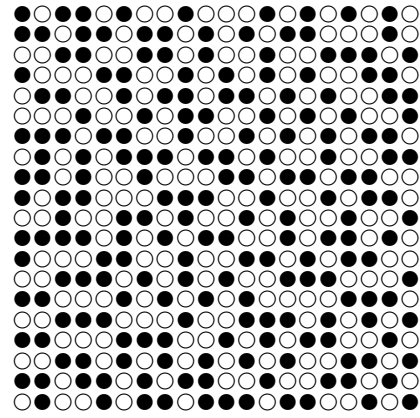
(a) Clustering, $\alpha_1 = 0.8$



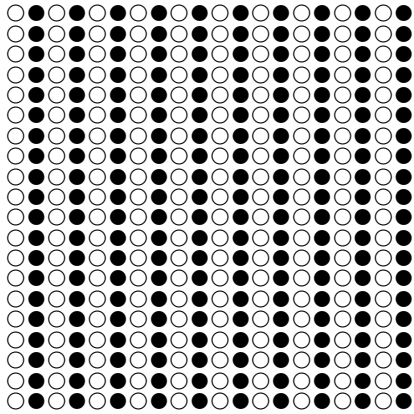
(b) Short-range clustering, $\alpha_1 = 0.4$



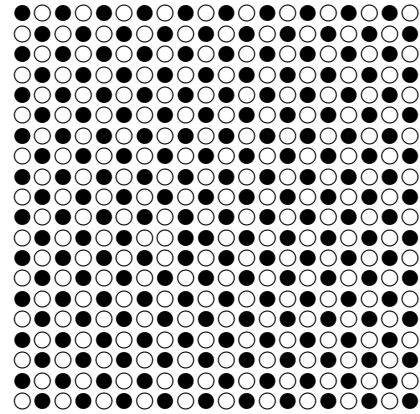
(c) Random, $\alpha_{1,2,\dots,6} = 0.0$



(d) Short-range order, $\alpha_1 = -0.4$



(e) Order 1, $\alpha_1 = 0.0, \alpha_2 = -1.0$



(f) Order 2, $\alpha_1 = -1.0, \alpha_2 = 1.0$

Figure 2.3: Schematic illustration of systems with different short range order parameters.

Inspecting Eq. 2.28 one can see that if a supercell is to represent the energy of a random alloy, with or without any degree of short range order, the supercell must be constructed in such a manner to mimic the correlation functions $\xi_f^{(n)}(\bar{\sigma})$ above for all figures f where the effective interactions $V_f^{(n)}$ are non-negligible.³ This is obviously a non-trivial task.

2.3.1 The Special Quasi-random Structures method

The method in use in this work to model solid solution systems using supercells is the so called special quasirandom structure (SQS) method. The method was introduced by Zunger *et al.* [117] as a reaction on attempts to create random like supercells by random number generated configurations. They noted the general qualitative situation that short ranged pair interactions was the most important interactions in alloys. Building on this idea rather small supercells were created in order to resemble the correlation functions of the random alloy for the first couple of nearest neighbour pairs. Of course, the larger the supercell, the more correlation functions can be made to mimic the random alloy [118].

In this work SQS supercells were designed for the fcc-structure (corresponding to the rock salt B1 structure if the nitrogen sublattice is kept ideally completely occupied) and the hcp-structure (corresponding to the wurtzite B3 structure) for $A_{1-x}B_x(N)$ systems with composition $x = 0.125, 0.250, 0.375, 0.500, 0.625, 0.750$, and 0.875 . The accuracy of the SQS method must be weighted against the computational time associated with large supercells with low symmetry. The fcc SQS structures has 24 metal sites ($x=0.25, 0.50, 0.75$) and 32 metal sites ($x=0.125, 0.375, 0.625, 0.875$) while the hcp SQS structures all has 64 metal sites.

The Warren-Cowley SRO-parameters for the seven nearest neighbour shells of pairs on the metal sublattice of the fcc based structures are shown in Tab. 2.1.

Table 2.1: Short-range order (SRO) parameters for the supercells used to model different compositions of Al on the metal sublattice of the B1 structure. The SRO parameters are given for the metallic coordination shells.

composition x	shell						
	1	2	3	4	5	6	7
0.125, 0.875	0.00	-0.04	-0.04	0.04	0.00	0.14	-0.04
0.25, 0.75	0.00	-0.03	-0.03	0.00	0.00	0.05	-0.04
0.375, 0.625	0.00	-0.02	-0.02	0.02	0.00	0.06	-0.02
0.50	0.00	0.00	0.00	0.00	-0.05	0.00	0.00

The creation of "good" SQS supercells are not a completely trivial task even in the sense expressed in Ref. [117]. Although codes using a Monte Carlo-like simulated annealing algorithm can be used [119] to optimise the atomic configurations on the lattice, e. g. the finding of an optimal supercell geometry often takes a certain amount of trial-and-error. The large uncertainty with the method is however the fact that the values of the effective cluster interactions $V_f^{(n)}$ of Eq. 2.27 can not be known *a priori* and thus, the effect of the

³Although it could happen by chance that the effect of deviations for several figures could cancel.

interactions corresponding to the uncontrolled correlation functions of the supercells are not known. Of course the values of the ECI are completely system specific although the judgement made in Ref. [117] about the prime importance of the closer pair interactions is generally true. In order to illustrate the SQS method, a series of calculations of mixing energies in the B1 $\text{Ti}_{0.25}\text{Al}_{0.75}\text{N}$ system is performed using gradually larger SQS supercells and shown in Fig. 2.4. All supercells are created trying to approach SRO values as close as possible to 0 for increasingly numbers of shells. As a comparison the values of calculations for random number generated supercells with the same geometries are shown as well as the value using the CPA+ISM method to be described below.

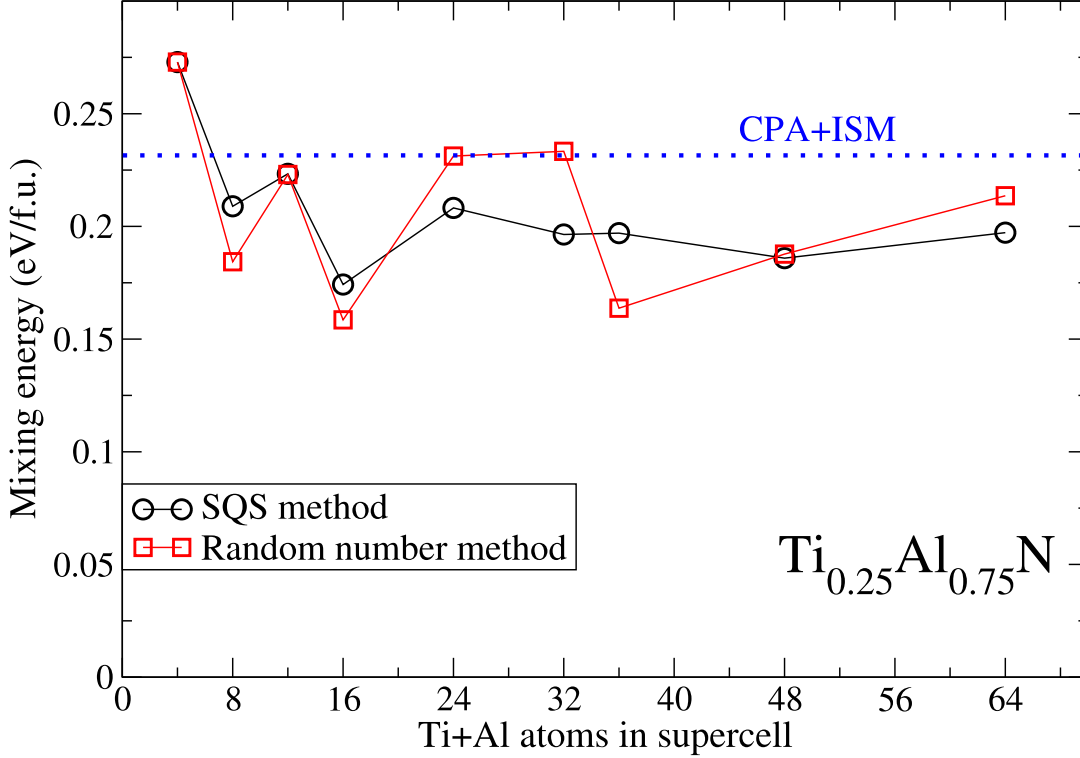


Figure 2.4: The calculated mixing energy for different $\text{Ti}_{0.25}\text{Al}_{0.75}\text{N}$ supercells as a function of the number of Ti+Al atoms in the cells. Both random number generated structures and structures obtained with the SQS philosophy is presented. The CPA-ISM value is shown with a dotted line for comparison.

One can see in the figure that the mixing energy of this particular system tends towards a value around 0.2 eV/f.u. when the SQS method is applied. From the usage of 24-site (48 atoms in the supercell including N) and larger SQS the value does not change much. For the random number method on the other hand, the convergence is much slower. It seems likely that an accurate description of the energetics of the $\text{Ti}_{1-x}\text{Al}_x\text{N}$ system can be given by the SQS method. However, one should realise that this example corresponds to a concentration where the creation of random-like SQS cells are particularly manageable. For less "symmetric" compositions, that could be for instance $x=0.67$, the task is much more delicate. Further more, if the second concentration derivative of the mixing energetics is of interest, for instance in a discussion about spinodal decomposition, even the small fluctuations between the 24 and 64 metal-site SQS in Fig. 2.4 can be of importance. Thus the SQS method can with favour be complemented with other

treatments of the disordered systems.

2.3.2 The Coherent Potential Approximation

A completely alternative to the supercell based approach above is the coherent potential approximation (CPA) first suggested by Soven [120] and developed for the KKR-framework by Györffy [121]. The CPA is the most promising out of many effective medium approaches which aim at replacing the real problem of stochastically distributed atoms on a lattice with a homogeneous effective medium. The main idea of the CPA is to create this effective medium so that it has the same scattering properties as the real random alloy. This is done through a self-consistent derivation where the effective medium is designed to have the averaged scattering properties of the components embedded in this effective medium. The effective medium within the CPA is given by a coherent potential function \tilde{m} and the on-site coherent path operator is given by

$$\tilde{g}(E) = \frac{1}{V_{BZ}} \int_{BZ} \frac{d\mathbf{k}}{\tilde{m}(E) - B(\mathbf{k}, E)} \quad (2.29)$$

which in a $A_{1-x}B_x$ alloy according to the above condition should fulfill

$$\tilde{g}(E) = (1-x)g^A(E) + xg^B(E) \quad (2.30)$$

where the on-site path operators of the i :th component is derived self-consistently through a single-site Dyson equation

$$g^i(E) = \frac{\tilde{g}(E)}{1 + \tilde{g}(E)[m^i(E) - \tilde{m}(E)]}. \quad (2.31)$$

With the path operators of the components known, one can easily calculate the physical properties of the system according to the equations of the multiple scattering theory.

An interesting application of the CPA theory is the so called disordered local moments (DLM) method suggested by Györffy [122]. This is a method aimed at describing a magnetically disordered system with finite magnetic moments. This is a quite usual situation in nature in magnetic materials above the critical magnetic ordering temperature. One example is CrN which is of importance for this work. In the DLM method such a system is modelled using the CPA as a $\text{Cr}_{0.5}^{\uparrow}\text{Cr}_{0.5}^{\downarrow}\text{N}$ alloy between spin up and down magnetic components.

There are also problems with the CPA. The most striking challenges for the successful application of CPA to real systems are all directly related to the fact that the CPA is a single-site theory:

Firstly the electronic structure of the CPA is not including local environment effects which are present also in random alloys without any short-range order. One drastic example is the spin-flip phenomena of Fe magnetic moments on lattice sites heavily surrounded by other Fe atoms in fcc-FeNi alloys demonstrated to be of importance for the invar-effect [123]

Secondly electrostatics is not correctly described since the effective medium surrounding the components is forced to be electro-neutral while in real systems, charge transfer between components leads to non-negligible electrostatic interactions.

Thirdly local lattice relaxations can not be directly included since the framework assumes translational symmetry of the lattice sites and besides the environment of all atoms are the same effective medium suppressing any displacements.

The first of these three problem is something one has to live with within the single site CPA. If such effects are thought to be of importance, and in a wide range of systems they are not, one has to go beyond this approximation, either to supercells or so called non-local CPA calculations. The second of the problems, the electrostatics, has been intensively discussed but today an efficient scheme of accounting for this effect within the so called screened impurity model [124, 125] exists, relying on only a few additional supercell calculations. The third issue, the local lattice relaxations, are a somewhat larger problem but different models exist for treating also this problem as an additional contribution to the energy upon the value from the ideal lattice CPA calculations, for instance the effective tetrahedron model (ETM) designed for the fcc and bcc lattices [126]. For the structure of primary interest in this work, the rock salt B1 structure with two separate sublattices, a new model, the independent sublattice model (ISM) [77], needed to be designed.

The independent sublattice model

The local lattice relaxation energy is defined as

$$E_{rel}(x_1, x_2, \dots) = E_{tot}(x_1, x_2, \dots) - E_{unrel}(x_1, x_2, \dots) \quad (2.32)$$

where $E_{tot}(x_1, x_2, \dots)$ is the total energy for a system with the concentrations x_1, x_2 etc. of the different alloy components and with fully relaxed ionic positions while $E_{unrel}(x_1, x_2, \dots)$ is the total energy calculated for the same system when all atoms are placed on ideal lattice positions.

In the ETM model for e.g. fcc-systems, one considers the effect of a local volume relaxation of small clusters of different composition in the alloy. In the B1-case however, one needs to consider the additional effect of the relaxation of the nitrogen and metal atoms relative to each other. For this purpose, the independent sublattice model is proposed.

In order to understand the mechanism behind the local relaxations in for instance c-Ti_{1-x}Al_xN we note that it is only one of the two sublattices, the metal sublattice, that shows a random distribution of atoms. This is true as long as the nitrogen sublattice is considered as completely homogeneous. The treatise of nitrogen vacancies will be covered below. This means that the metal atoms all have chemically equivalent nearest neighbor nitrogen atoms, while the latter have different nearest neighbor environments. For this reason, nitrogen atoms are more likely to show considerable displacement from their ideal B1 positions than the metal atoms. We therefore divide the relaxation energy into two parts, corresponding to independent relaxations of the two sublattices in the B1 structure:

$$E_{rel}^{ISM}(x_1, x_2, \dots) = E_{Nrel}(x_1, x_2, \dots) + E_{metalrel}(x_1, x_2, \dots). \quad (2.33)$$

where $E_{Nrel}(x_1, x_2, \dots)$ is the energy gained by relaxing the positions of the nitrogen atoms in the alloy with concentration x_1 of the first metal component, x_2 of the second,

etc., assuming that the metal atoms occupy ideal fcc lattice positions. The second term, $E_{metal\,rel}(x_1, x_2, \dots)$, is the energy that the system gains by relaxing the positions of the metal atoms, which can be calculated following the ETM scheme [126].

Let us consider the first term on the right-hand side of Eq. (2.33). The nitrogen atoms occupy octahedral positions and have two metal atoms in opposite directions along the x, y and z axes (see Fig. 1.5). If one assumes that the relaxation of N atoms are only effected by their nearest neighbors one can show by spring model arguments that in a random alloy with moderate dicplacements

$$E_{N\,rel}(x_1, x_2, \dots) = 3 \sum_{i=M_1, M_2, \dots} \sum_{j=M_1, M_2, \dots} v_{ij} p_{ij}(x_i, x_j). \quad (2.34)$$

The factor 3 comes from the three dimensions in which the atom can move. The sums are taken over the different metallic alloy components (denoted as M_1, M_2 above), which can occupy the two metal-sites neighboring N in each direction, so that all possible Metal-N-Metal triplets present in the alloy are included in the summation. v_{ij} is the relaxation energy gained by shifting an N-atom positioned between one metal atom of sort i and one of sort j , while $p_{ij}(x_i, x_j)$ denotes the probability that the neighboring metal on one side of the nitrogen atom is of sort i and the metal on the opposing side is of sort j . Due to the symmetry of the B1 crystal lattice $v_{ii} = 0$ and $v_{ij} = v_{ji}$ in the nearest neighbor approximation. Of course $p_{ij}(x_i, x_j) = p_{ji}(x_i, x_j)$. In the case of a ternary alloy with two metal components like c-Ti_{1-x}Al_xN, equation (2.34) is simplified to

$$E_{N\,rel}(x) = 6v_{12}x(1 - x). \quad (2.35)$$

The energies v_{ij} can be calculated by considering relaxation energies in an *ordered* structure on the underlying B1 lattice. In this work we used the structure shown in Fig. 2.5. In this structure metal atoms occupy positions corresponding to a “double L1₀”, also called Z2, structure. The relaxation energy can be calculated by the PAW method, as is done in this work, or with any method that allows for the geometry optimization. Of course the method used for the geometry optimization should be consistent with the method in which the CPA is implemented. This is the case with EMTO and PAW as will be shown in the next chapter.

When $E_{N\,rel}(x_1, x_2, \dots)$ and $E_{metal\,rel}(x_1, x_2, \dots)$ have been calculated one can easily obtain the total relaxation energy by Eq. 2.33, and then calculate the total energy of the alloy as:

$$E_{tot}(x_1, x_2, \dots) = E_{unrel}(x_1, x_2, \dots) + E_{rel}^{ISM}(x_1, x_2, \dots) \quad (2.36)$$

In this work this model has been investigated and used for the c-Ti_{1-x}Al_xN-system and also applied to the c-Cr_{1-x}Al_xN system and with slight modification to the c-Ti_{1-x}Al_xN_{1-y} system.

Locally self-consistent Green’s-function method

The CPA approximation has also been implemented as a part in a combined CPA+supercell methodology to treat random alloys using the order-N scaling locally self-consistent

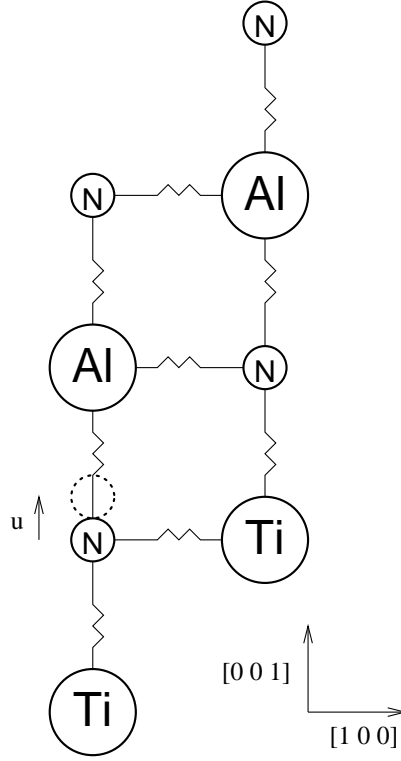


Figure 2.5: The structure used to calculate the parameters of the independent sublattice model v_{ij} , Eqs. (2.34) and (2.35), in the case of $c\text{-Ti}_{1-x}\text{Al}_x\text{N}$. It is an ordered structure on the B1 underlying crystal lattice, in which the metal atoms in the $[001]$ -planes follow the ordered sequence Ti-Ti-Al-Al-Ti-Ti-Al-Al etc. The (exaggerated) displacement of a nitrogen atom by vector \mathbf{u} from its ideal B1-position is also shown.

Green's function (LSGF)-method [112, 113] where a very large supercell, created using the SQS (or in another way) method is treated with the following calculational framework: For each lattice site the exact atomic distribution in a certain number of neighbouring shells is fully considered, the so called local interaction zone (LIZ), while the distribution outside this zone is considered using the CPA. In this way short range order effects can also be included. The LSGF code is used in this work to calculate the system $c\text{-Ti}_{1-x}\text{Al}_x\text{N}_{1-y}$ where two sublattices are simultaneously disordered.

The screened generalized perturbation method

The CPA framework is not only an efficient way to calculate properties of the random alloy. It is also a suitable reference frame for deriving the effective cluster interactions, V_f^n discussed above. This can for instance be done within the framework of the screened generalised perturbation method [118, 127, 128]. By a close inspection of the meaning of V_f^n in Eq. 2.27, and noting that the spin product $\Phi(\bar{\sigma})$ takes on the value +1 if there is an even number of B-atoms in the cluster and -1 if there is an odd number of B-atoms in the cluster, one can see that it corresponds to

$$V_f^n = E_{B\text{-even}} - E_{B\text{-odd}} \quad (2.37)$$

but the way how to calculate these energies is not obvious. Using the CPA as an effective medium one can however derive the one-electron part of those terms by considering the change in integrated density of states caused by the embedding of the clusters in the effective medium. The electrostatic contribution for the effective cluster interactions can also be calculated, e.g. with a method consistent with Ref. [124]. The SGPM method was recently reviewed by Ruban and Abrikosov [98]. In this work the SGPM method together with the ISM method for local relaxations are used to derive ECI for the $\text{c-Ti}_{1-x}\text{Al}_x\text{N}$ system.

Chapter 3

Structural properties of $M_{1-x}Al_xN$ systems

In this chapter the initial results for the structural properties of the pure transition metal nitrides (MN) systems TiN, CrN, ScN and HfN are presented together with the different polymorphs of AlN as well as the mixed c- $M_{1-x}Al_xN$ systems. The calculated lattice parameters are presented and compared with the experimentally measured values. This procedure indicates, if agreement is found, that the theoretical methods are accurate and give reliable descriptions of the studied systems. This means that even the results for the pure nitride systems are of interest, although the results of similar calculations have been presented many times before. Furthermore, since volume or lattice mismatch is a widely known limiting factor for alloy formation, the famous first Hume-Rothery rule, and since it has been used to explain segregation in mixed semiconductor nitride systems [67], a detailed discussion of the lattice spacings and volumes of the mixed $M_{1-x}Al_xN$ systems is presented and compared to Vegard's rule. Thereafter the results for bulk modulus as well as formation energies for the binary nitrides are given.

3.1 Volumes and lattice spacings

3.1.1 The polymorphs of AlN

Aluminium reacts with nitrogen to form a stoichiometric AlN semiconductor. The ground state crystal structure of this system is the hexagonal wurtzite structure, B4. However, under pressures of 14.5-16 GPa and temperatures of about 1100 K the cubic rock salt structure, B1, is formed [17]. The B1 structure is also metastable under ambient conditions. Also the tetrahedrally coordinated cubic zinc-blende structure, B3, has been synthesised, stabilised by epitaxial forces [19].

Figure 3.1 shows the calculated equation of states (the term is used for the energy-volume curve in this work) for wurtzite, zincblende and rock Salt AlN.

The theoretical calculations shown in Fig. 3.1 are in good agreement with previous first-principles calculations using the LDA functional and the pseudopotential method [64]. The equilibrium volume per formula unit of h-AlN is calculated to $21.3 \text{ \AA}^3/\text{f.u.}$ to be compared to the experimental value of $20.86 \text{ \AA}^3/\text{f.u.}$ [129].

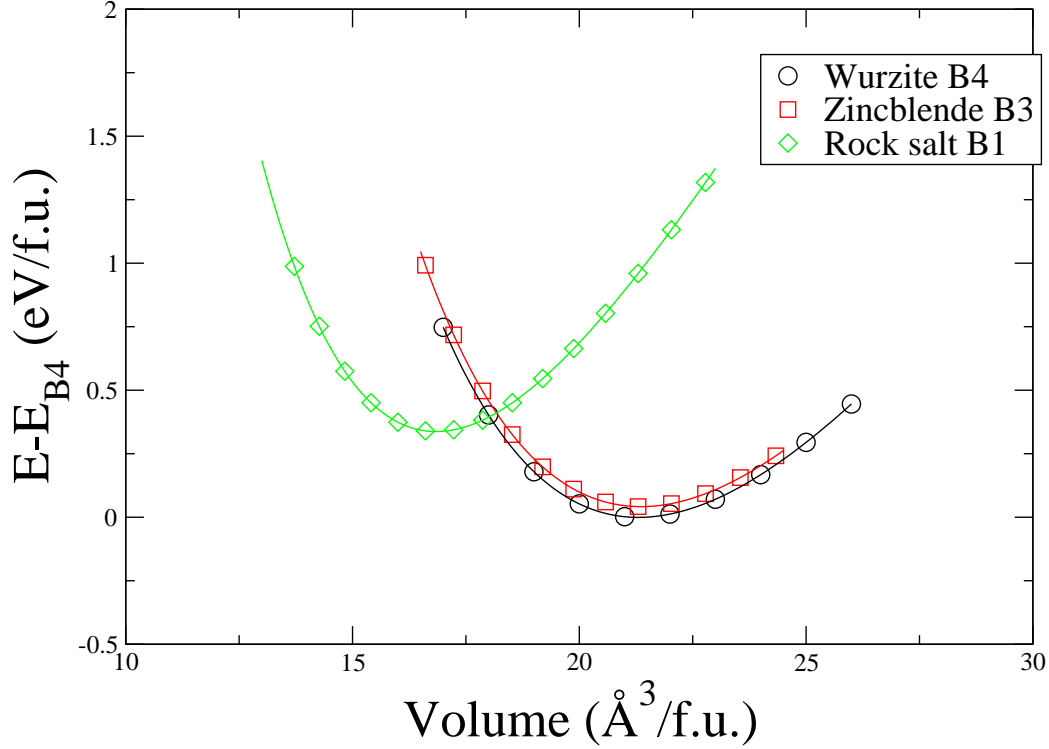


Figure 3.1: The binding energy curve of the three known polymorphs of AlN: The ground state hexagonal wurtzite structure (B4) together with the cubic zincblende (B3) and cubic rock salt (B1) structures which both are metastable at ambient conditions.

3.1.2 Pure nitrides with B1 structure

The calculated lattice parameters of the B1 structure of TiN, CrN, ScN, HfN, and c-AlN are presented in Table 3.1 together with experimental data. All calculations are done within the DFT framework using the GGA-PBE96 [97] functional for exchange-correlation effects. Three different schemes to describe the one-electron wave functions and to expand the density have been used: the Projector Augmented Wave (PAW) method, the Exact Muffin-Tin Orbitals (EMTO) method and the Korringa-Kohn-Rostocker Atomic Sphere Approximation (KKR-ASA). These are all explained in more details in chapter 2.

From Table 3.1 one can see that all the methods reproduce the experimental lattice spacings well. The small systematic overestimation of about 1% or below is usual for the usage of the GGA functional. This agreement is a necessary condition if the results for more intricate properties such as mixing enthalpies are to be trustworthy on a quantitative scale.

Since the main topic discussed in this work is the mixing of the transition metal nitrides with aluminium nitride in the cubic phase, it is of interest to study differences in lattice spacing between the transition metal nitrides and aluminium nitride and how these

Table 3.1: Calculated lattice spacing for transition metal nitrides and c-AlN compared with experimental values. All calculations are performed using the GGA-PBE96 [97] functional for exchange-correlation effects.

System	calculated a_0 [Å]	measured a_0 [Å]	deviation
TiN	4.255 ^{PAW} , 4.29 ^{EMTO}	4.239 [130]	+0.4%, +1.1%
CrN	4.196 ^{KKR-ASA}	4.162 [15]	+0.8%
ScN	4.521 ^{PAW}	4.50 [131]	+0.5%
HfN	4.535 ^{PAW}	4.519 [46]	+0.4%
c-AlN	4.068 ^{PAW} , 4.10 ^{EMTO} , 4.094 ^{KKR-ASA}	4.045 [17]	+0.6%, +1.4%, +1.2%

differences are described by the theoretical calculations. In Table 3.2 the relative differences in lattice parameters and volumes (per formula unit) between the four different transition metal nitrides and cubic AlN are presented and compared with experimental values. CrN shows the smallest lattice mismatch with c-AlN of the considered MN systems. The difference in lattice parameters between these two systems is only 2.5% (calc.) or 2.9% (expt.). This corresponds to a difference in volume per formula unit of 7.7% (calc.) or 9% (expt.). TiN has a slightly larger difference in lattice spacing compared to CrN, 4.6% (calc.) or 4.8% (expt.), corresponding to 14% (calc.) or 15% (expt.) differences in volume. The situation is different when considering the systems ScN and HfN which have considerably larger differences in lattice spacing and volumes. The difference is 11.1% (calc.) or 11.2% (expt.) in lattice spacing for ScN corresponding to a 37.1% (calc.) or 37.7% (expt.) difference in volumes. For HfN the values are 11.5% (calc.) or 11.7% (expt.) for difference in lattice spacing and 38.6% (calc.) or 39.4% (expt.) difference in volume per formula unit.

Table 3.2: Differences in lattice parameters and volumes between transition metal nitrides and c-AlN.

Systems	Δa^{calc} [%]	ΔV^{calc} [%]	Δa^{expt} [%]	ΔV^{expt} [%]
TiN-AlN	4.6 ^{PAW} , 4.6 ^{EMTO}	14 ^{PAW} , 14 ^{EMTO}	4.8	15
CrN-AlN	2.5 ^{KKR-ASA}	7.7 ^{KKR-ASA}	2.9	9
ScN-AlN	11.1 ^{PAW}	37.1 ^{PAW}	11.2	37.7
HfN-AlN	11.5 ^{PAW}	38.6 ^{PAW}	11.7	39.4

The results show that the error in differences of the calculated lattice spacings and volumes between MN and c-AlN with respect to experimental values are even lower than the absolute errors discussed above. Thus one can expect that the change in lattice spacing as a function of concentration in the mixed systems should be very well described by the present methods, even if there is a small systematic overestimation of the absolute values.

3.1.3 Lattice spacings of c-M_{1-x}Al_xN alloy systems

We now turn to the results of lattice parameters for the mixed c-M_{1-x}Al_xN systems. Fig. 3.2 shows the lattice parameter values obtained for the B1 structure using the PAW-

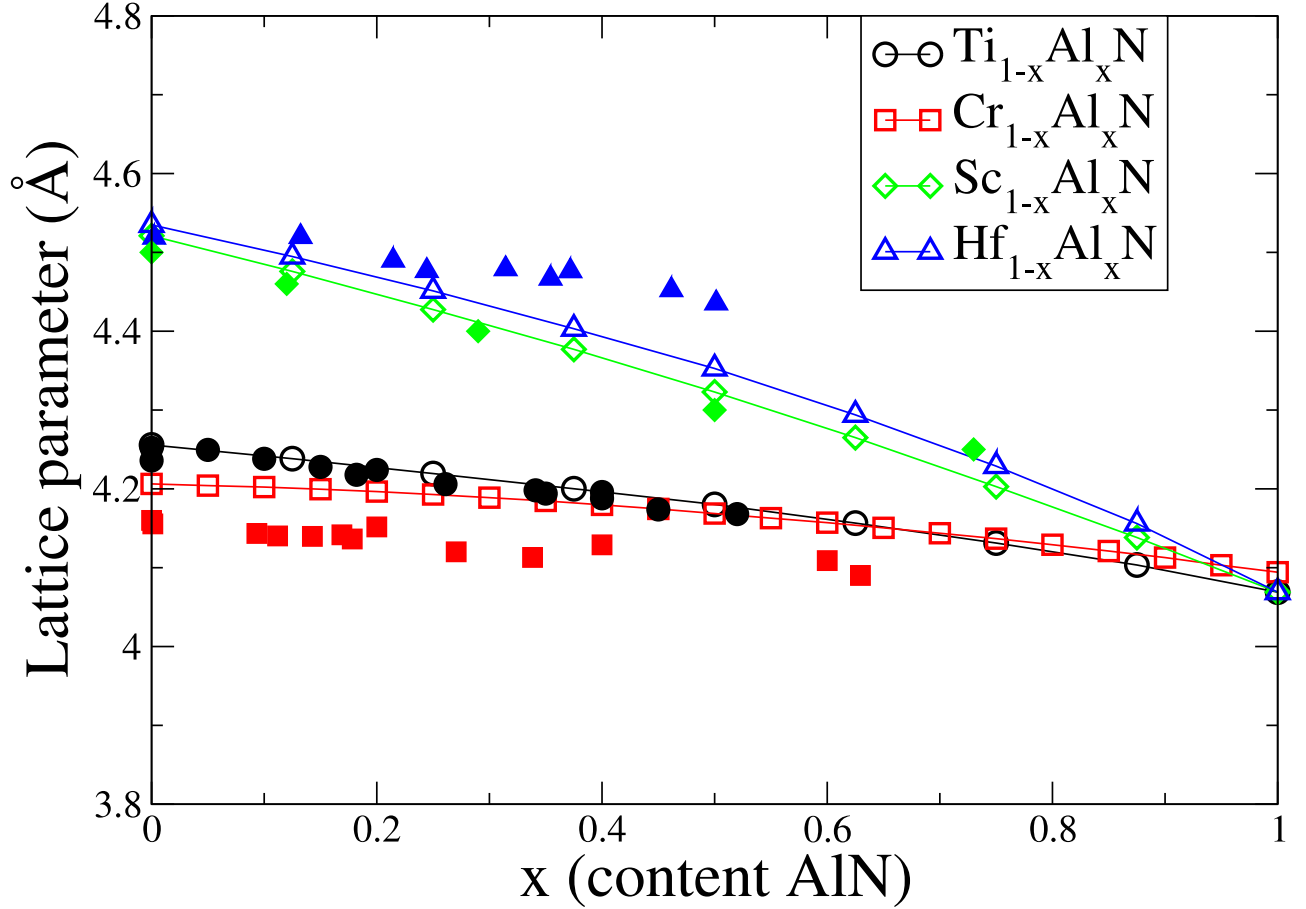


Figure 3.2: The calculated lattice parameters of the conventional cubic cell of the B1 phase of $Ti_{1-x}Al_xN$, $Cr_{1-x}Al_xN$, $Sc_{1-x}Al_xN$, and $Hf_{1-x}Al_xN$. Experimental thin film values are shown by solid symbols: $Ti_{1-x}Al_xN$ [132, 133], $Cr_{1-x}Al_xN$ [16, 134], $Sc_{1-x}Al_xN$ [50], $Hf_{1-x}Al_xN$ [46]. The $Cr_{1-x}Al_xN$ system is calculated for the disordered magnetic phase using the KKR-ASA-CPA framework while the other three systems are calculated using a PAW-SQS framework.

SQS method for the systems $Ti_{1-x}Al_xN$, $Sc_{1-x}Al_xN$, and $Hf_{1-x}Al_xN$ taking local lattice relaxation into full account, and KKR-ASA-CPA method for the disordered magnetic configuration of $Cr_{1-x}Al_xN$. Note that the usage of two different methods leads to a small but finite difference in lattice spacing for pure c-AlN ($x=1.00$). The reason why the KKR-ASA method is needed for the $Cr_{1-x}Al_xN$ system is that it can be used to model a disordered magnetic state as is described in chapter 2 and to be discussed in depth in chapter 5. The figure also shows experimental thin film results with solid symbols: $Ti_{1-x}Al_xN$ [132, 133], $Cr_{1-x}Al_xN$ [16, 134], $Sc_{1-x}Al_xN$ [50], $Hf_{1-x}Al_xN$ [46]. In general, the theoretical calculations reproduce the experimental findings well for the systems $Ti_{1-x}Al_xN$ and $Cr_{1-x}Al_xN$ although there is a small systematic overestimation in the case of $Cr_{1-x}Al_xN$, most likely due to the slightly lower accuracy of the KKR-ASA method as compared to PAW calculations. For the $Sc_{1-x}Al_xN$ system there is a good agreement for the compositions with $x \leq 0.50$ while the experimental data point for $x = 0.73$ differs considerably. This is explained in Ref. [50] by the presence of a AlN-rich phase in the film, possibly pure AlN, with grain size so small that it is

practically invisible in XRD. The presence of such a phase would indicate that the global composition of $x=0.73$ do not correspond to the local composition in the cubic phase for which the measurement is done. Instead, this cubic phase might have a composition close to $x=0.60$ [50].

In the $\text{Hf}_{1-x}\text{Al}_x\text{N}$ system the experimental data points show somewhat less good agreement with the calculated values. This can be attributed mainly to two reasons. Firstly the experimental films show a small but finite overstoichiometry of nitrogen: $\text{N}/(\text{Hf}+\text{Al}) = 1.05 \pm 0.05$ while the calculations consider structures with a perfect 1:1 metal to nitrogen stoichiometry. Secondly the experimental analysis indicates an onset of decomposition already during film growth for samples with AlN content $x \geq 0.29$ [46]. The result of such a process might very well be that the XRD measurement gives lattice spacings for regions slightly richer in Hf compared to the global concentration. However further studies are needed to fully understand the lattice spacing and related issues in the $\text{Hf}_{1-x}\text{Al}_x\text{N}$ system.

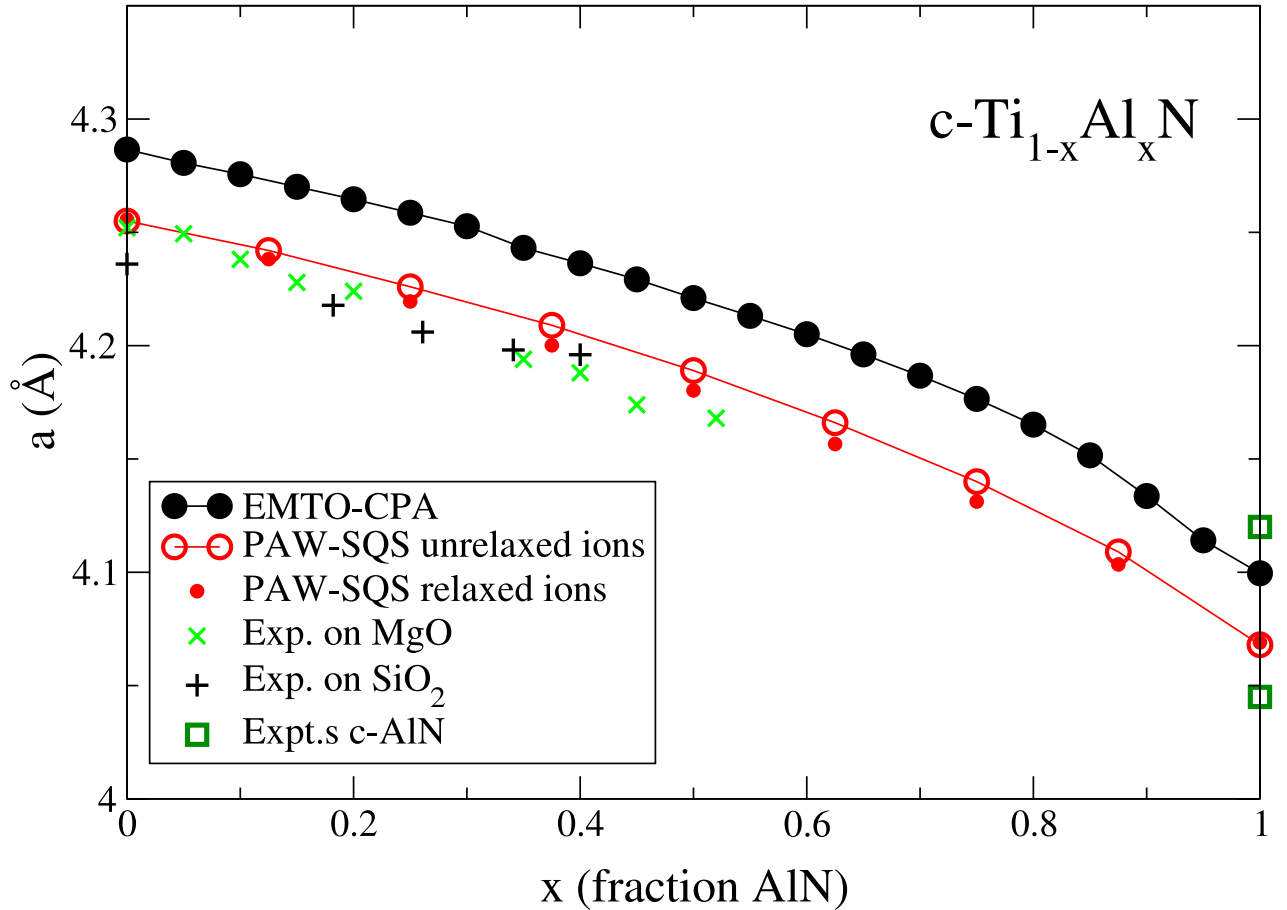


Figure 3.3: The calculated lattice parameters for $\text{c-Ti}_{1-x}\text{Al}_x\text{N}$ alloys using the EMT0-CPA and PAW-SQS method together with two experimental thin films series grown on MgO [132] and SiO_2 [133]. Also shown are the two different reported values of the lattice spacing of c-AlN, 4.12 Å [135] and 4.045 Å [17]. SQS calculations using ideal B1-lattice spacings are shown with open circles while calculations of fully relaxed supercells are shown with small solid circles.

The $\text{Ti}_{1-x}\text{Al}_x\text{N}$ system has been analysed using two different calculational schemes, the

EMTO-CPA method and the PAW-SQS method. It is therefore important that both frameworks give an accurate description of the equilibrium lattice parameters of the system. Fig. 3.3 shows the results for lattice spacings of the two methods together with experimental values. The EMTO calculations, which assume an ideal B1 lattice also for the alloys, consistently overestimate the lattice spacing with about 0.7% as compared to PAW-calculations of the unrelaxed structures. This is the case both for pure components and alloys. The inclusion of the effect of local lattice relaxation in the PAW-SQS calculations further decreases the calculated lattice spacing slightly, about 0.2% at the maximum at $x=0.50$, bringing the calculations very close to the experimentally measured values. This latter minute effect, the coupling between local lattice relaxations and the equilibrium lattice spacing, is not likely to influence calculated physical properties significantly. Instead, if there is any effects of the differences in lattice spacing it should originate in the constant slight shift to larger values for the EMTO-calculations. From these calculations it is also possible to conclude that the value of the equilibrium lattice spacing of c-AlN are more likely to be in accordance with the value in Ref. [17], 4.045 Å, rather than the larger value in Ref. [135]. There is no reason to believe that the calculations using the GGA functional, which shows a slight overestimation of the experimentally measured value for all other considered nitride systems should instead underestimate the value of c-AlN.

The composition dependence of lattice spacing or volumes are often discussed in comparison with Vegard's rule [136]. This rule simply predicts that the lattice spacings of alloys follows the line decided by the compositional weighted arithmetic average of the lattice spacing of the pure components. There is of course no reason why any alloy system should strictly obey this rule, but a distinct deviation is anyway often discussed in terms of changes in the electronic bonding of the system. The systems studied in this work turn out to show a systematic positive deviation from Vegard's rule, at least in the theoretical calculations. Fig. 3.4 shows the deviation from Vegard's rule for the calculated lattice spacings of the four systems treated here. For comparison the experimental deviation from Vegard's rule are also shown with solid or semi-solid symbols calculated with respect to each series own value for the transition metal nitride and from the experimental reference values of the pure c-AlN in Tab. 3.1. For $Ti_{1-x}Al_xN$, the maximum deviation from Vegard's rule is about 0.018 Å at a composition of about $x=0.55$. The results of the experiment in Ref. [133] shown with solid circles, have slightly larger deviations from Vegard's rule while the experiments by [132], shown with semi-solid circles, are in rather good agreement with the calculated deviation. The previous interpretation in several works, that the lattice spacing of $Ti_{1-x}Al_xN$ follows Vegard's rule [133] can be attributed to the choice of the larger reference value (4.12 Å) for lattice spacing of pure c-AlN and to the fact that $Ti_{1-x}Al_xN$ thin films can be prepared only with $x \leq 0.67$ where the curvature of the lattice parameter curve is less distinct.

In the case of $Cr_{1-x}Al_xN$, the calculated deviation is also about 0.018 Å at its maximum at about $x=0.45$. In the case of this system, the two experiments in Ref.s [16, 134] give different results. While Kimura *et al.* measures deviations from Vegard's rule similar to the calculations, Sanjines *et al.* gets a very small or even negative deviation from the rule. Possibly this difference might be connected to the usage of two different substrates in those two experiments, WC in [134] and SiO_2 in [16], or to other differences in deposition conditions. The error bars for the experimental points given in Ref. [16] but not shown in the figure corresponds to about ± 0.005 Å.

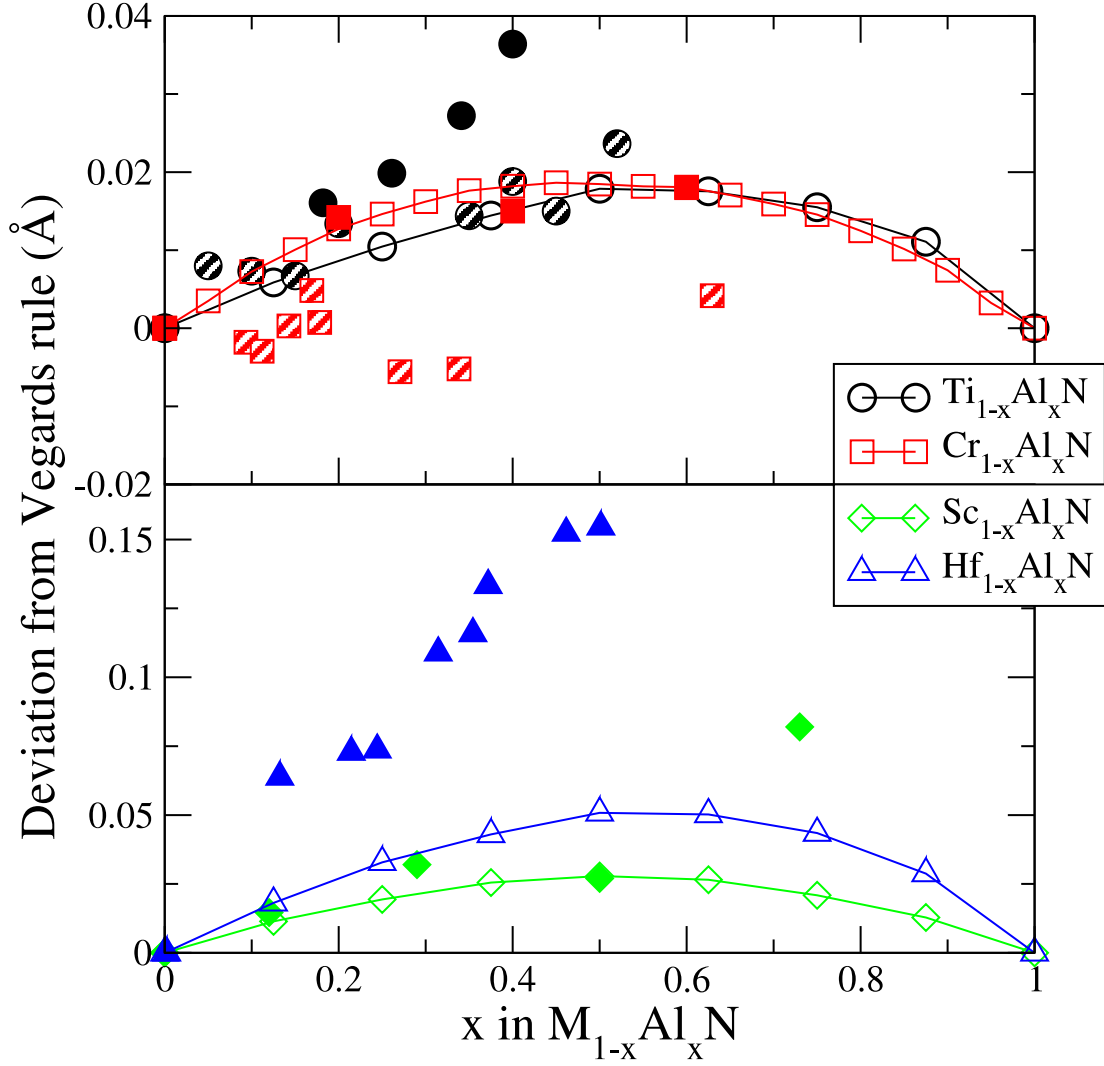


Figure 3.4: The deviation from Vegard's rule for the four systems $\text{Ti}_{1-x}\text{Al}_x\text{N}$, $\text{Cr}_{1-x}\text{Al}_x\text{N}$, $\text{Sc}_{1-x}\text{Al}_x\text{N}$, and $\text{Hf}_{1-x}\text{Al}_x\text{N}$. The calculated values are shown with open symbols while experiments are marked with solid and semi-solid symbols: $\text{Ti}_{1-x}\text{Al}_x\text{N}$: solid [133], semi-solid [132], $\text{Cr}_{1-x}\text{Al}_x\text{N}$: solid [16], semi-solid [134], $\text{Sc}_{1-x}\text{Al}_x\text{N}$ [50], $\text{Hf}_{1-x}\text{Al}_x\text{N}$ [46]. Please note the different scales in the top and bottom panels.

In the lower panel of Fig. 3.4 the deviations from Vegard's rule for the systems $\text{Sc}_{1-x}\text{Al}_x\text{N}$ and $\text{Hf}_{1-x}\text{Al}_x\text{N}$ are shown. The scale on the y-axis in this panel is larger compared to the upper panel. $\text{Sc}_{1-x}\text{Al}_x\text{N}$ shows a positive deviation from Vegard's rule that is somewhat larger as compared to the $\text{Ti}_{1-x}\text{Al}_x\text{N}$ and $\text{Cr}_{1-x}\text{Al}_x\text{N}$ system with a maximum deviation of 0.025 \AA for the composition $x=0.50$. The deviation curve is symmetric with respect to equiatomic compositions. The experimental values from Ref. [50] are shown with solid diamonds. As was discussed above the results for composition with $x \leq 0.50$ is in very good agreement with the predicted curve while the data point for $x=0.73$ has a substantial positive deviation likely due to the offset in composition for the measured cubic phase as compared to the global composition in that sample.

In the $\text{Hf}_{1-x}\text{Al}_x\text{N}$ case the calculated deviation from Vegard's rule is the largest among the studied systems. The maximum deviation is about 0.05 \AA which is reached at a

composition of about $x=0.55$. The experimental points show a much stronger positive deviation, up to three times as large compared to the calculations, which however is not surprising considering the discussion above about the experimental situation with off-stoichiometry and initiated decomposition.

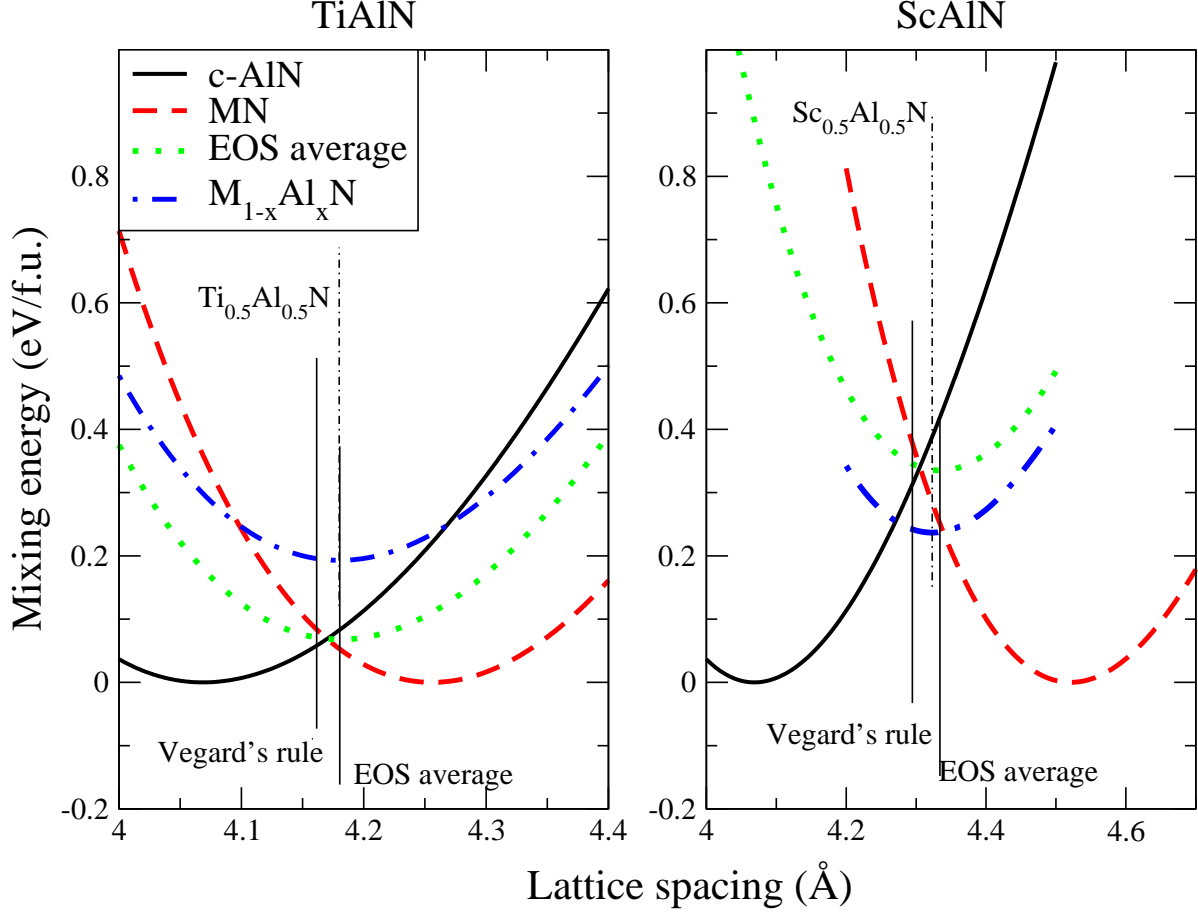


Figure 3.5: Left panel: The calculated and normalised equations of state for TiN , c-AlN as well as for $Ti_{0.5}Al_{0.5}N$. The EOS average of the curves of TiN and c-AlN is also shown. Right panel: Same but for the ScAlN system.

Even though there is a certain spread in experimental values, the overall picture and the definite results from the calculations are that there exists a systematic positive deviation from Vegard's rule in these c- $M_{1-x}Al_xN$ systems. In order to understand this behaviour one should first note that unlike binary metallic alloys, where the A-B nearest neighbour bonds are present in the mixed $A_{1-x}B_x$ alloy, but not present in the pure components, the nearest neighbour bonds in a $M_{1-x}Al_xN$ system are still the M-N and Al-N bonds present in the binary nitrides. Since these strong M-N and Al-N nearest neighbour bonds are likely to govern the equation of states of the system to a large extent, this fact suggests that an insight to the systematic positive deviation from Vegard's rule can be gained from a rather simple analysis of the included binary systems.

Let us first make the crude assumption that the equation of states for both pure transition metal nitrides and AlN as well as the alloys between them is completely determined by the nearest neighbour M-N and Al-N bonds and their length. Let us then make another crude approximation that the components of the alloys are fixed on an ideal B1

lattice with one common bond length. In such a situation the equation of states of the alloys would be nothing else but the concentration weighted arithmetic average of the equation of states of the binary nitrides. Whether the equilibrium lattice spacing of such a hypothetical system is larger or smaller compared to the Vegard's rule depends on the particular properties of each equation of states of the constituents. One might for instance think that the equilibrium parameter would tend in the direction of the stiffest of the included systems, the system with the highest bulk modulus. However, the bulk modulus describes only the second derivative of the EOS at the equilibrium. A common behaviour of the binding energy curves of all types of electronic bonds is the anharmonicity favouring expansion rather than compression when a substantial deviation is made from the equilibrium. This is a property which would indicate a tendency for larger lattice spacings compared to Vegard's rule.

To investigate these properties for the systems studied in this work Fig. 3.5 shows the situation for $\text{Ti}_{0.5}\text{Al}_{0.5}\text{N}$ and $\text{Sc}_{0.5}\text{Al}_{0.5}\text{N}$. Shown in the left panel of the figure are the EOS for pure TiN and pure c-AlN, normalised to $E=0$ at their equilibrium. Furthermore the EOS average calculated as

$$E^{average}(a) = \frac{E_{norm.}^{TiN}(a) + E_{norm.}^{c-AlN}(a)}{2} \quad (3.1)$$

is shown with a dotted line. The self consistent fully relaxed EOS for the real $\text{Ti}_{0.5}\text{Al}_{0.5}\text{N}$ alloy as modelled with a SQS structure is shown with dash-dotted line (also normalised to the mixing energy by subtracting the proper amount of equilibrium TiN and c-AlN energies). Vertical lines show the Vegard's rule value, the equilibrium of the EOS average curve, and with a dash-dotted line, the equilibrium of the self-consistent calculations. It is obvious that the EOS average curve has its minimum value at a lattice spacing considerably above the Vegard's rule value as a consequence of the fact that it is more easy to extend the Al-N bonds in c-AlN compared to compressing the Ti-N bonds in TiN. In fact, despite the crude approximations made in this model, it reproduces almost exactly the value of the equilibrium lattice spacing for the self-consistent calculations of the c- $\text{Ti}_{0.5}\text{Al}_{0.5}\text{N}$ alloy. It is likely that this agreement is due to a cancelation of the effects of the two main approximations made, the effect of local lattice relaxations leading to a smaller lattice spacing compared to fixed lattice, while the inclusion of real electronic structure effects in the alloy tends to increase lattice spacing in this system.

The right panel of Fig. 3.5 shows the same construction for the $\text{Sc}_{0.5}\text{Al}_{0.5}\text{N}$ system. In this system the difference in lattice spacing is larger between the constituting binary nitrides but the results are qualitatively the same with the EOS average giving a better estimate of the true lattice spacing compared to Vegard's law. In fact the usage of the EOS averaging method might be considered as a modified Vegard's rule.

In summary the calculations show that all the four treated c- $\text{M}_{1-x}\text{Al}_x\text{N}$ alloy systems show a systematic positive deviation from Vegard's rule. This can be qualitatively explained by the anharmonicity of the M-N and Al-N nearest neighbour bonds making it more easy to extend the Al-N bonds than to compress the M-N bonds. The somewhat surprising accuracy of the proposed modified Vegard's rule approximation to equilibrium lattice spacing, at least in the case of $\text{Ti}_{1-x}\text{Al}_x\text{N}$ and $\text{Sc}_{1-x}\text{Al}_x\text{N}$, is likely due to the fact that, opposite to the binary metallic alloy case, no new types of nearest neighbour bonds appear in these alloyed systems compared to the pure binary nitrides and to

smaller degree to a cancellation of errors from the approximations made. That the physics of the real mixed systems are much more complicated will be apparent in the following chapters.

The experimental thin films picture is somewhat more complicated due to various reasons. Epitaxial strain from substrates, internal stress, compositional uncertainty and off-stoichiometry as well as incomplete mixing or even phase separation makes the judgement of the reliability of the calculations based on a direct comparison with the experimental results impossible. On the other hand, it appears that a qualitative disagreement between the theoretical prediction and the experimental values of lattice parameters can be used as an indication that some sort of phase change process driving the system away from ideal B1 solid solution has appeared in the experimental samples. This is valuable knowledge in its own right and can be exemplified with the experimental deviation from theoretical result for the $Sc_{0.27}Al_{0.73}N$ sample in Ref. [50].

3.2 Bulk modulus

We now turn to the calculated bulk modulus of the transition metal nitrides, aluminium nitride and their alloys. The bulk modulus defined as

$$B = V \frac{d^2 E}{dV^2} \quad (3.2)$$

has been calculated numerically by fitting a modified Morse function [137] to the calculated energy values. The values for pure nitrides as well as for the equiatomic alloys, $c-M_{0.5}Al_{0.5}N$ are presented in Tab. 3.3. Since the bulk modulus depends on the second derivative of the energy the value of this quantity is much more sensitive to numerical noise as compared to i.e. total energies or equilibrium lattice spacing. This makes it difficult to obtain perfectly converged values, with respect to i.e. number of k-points in the Brillion zone sampling or even configurational distribution of atoms, of the bulk modulus for the large SQS calculations. The results presented here are converged to an accuracy of 0.1GPa for the binary nitrides and 0.5 GPa for the alloys with respect to k-points.

The bulk modulus is a measure of the resistance of a material against isotropic compression. As such it gives a certain although limited insight in the bonding strength of the material. It must be stressed that although hard materials often have a high bulk modulus, diamond is one example, there is no direct relation between the bulk modulus and the hardness of a system.

The calculated values of the bulk modulus for the pure nitrides are in good agreement with previous DFT calculations using the GGA functional as well as with experimental values where such are present, see for instance Ref. [140] and references therein. One important exception is CrN. Non-magnetic calculations, such as the one in Ref. [140] give considerably higher values of the Bulk modulus, around 320 GPa, compared to value presented here 237.5 GPA resulting from a calculation of the disordered magnetic state. The latter is as expected closer to the value in Ref. [141], 245 GPa obtained for antiferromagnetic calculations using the PAW method. One can expect that the values of bulk modulus calculated using the more approximate KKR-ASA method are somewhat lower compared to PAW values connected to the fact that the lattice spacings

Table 3.3: Calculated bulk modulus in GPa for transition metal nitrides, c-AlN, as well as c-M_{0.5}Al_{0.5}N alloys. All calculations are performed using the GGA-PBE96 [97] functional for exchange-correlation effects.

System	B [GPa]	Alloy	B [GPa]	System	B [GPa]
TiN	292.7 ^{PAW} , 318 ^{expt.} [138]	Ti _{0.5} Al _{0.5} N	262.1 ^{PAW}	c-AlN	255.5 ^{PAW}
ScN	198.8 ^{PAW} _expt.	Sc _{0.5} Al _{0.5} N	207.5 ^{PAW}		
HfN	285.5 ^{PAW} 306 ^{expt.} [139]	Hf _{0.5} Al _{0.5} N	243 ^{PAW}		
CrN	237.5 ^{KKR-ASA} _expt.	Cr _{0.5} Al _{0.5} N	239.8 ^{KKR-ASA}		242.0 ^{KKR-ASA}

achieved are slightly higher. This is illustrated in Table 3.3 with the two values for c-AlN: 255.5 GPa (PAW) and 242 GPa (KKR-ASA). For the three systems Ti_{1-x}Al_xN, Sc_{1-x}Al_xN, and Hf_{1-x}Al_xN the calculated bulk moduli for the equiatomic alloys are below the arithmetic mean value of the MN and c-AlN. This is connected to the positive deviation from Vegard’s rule discussed above since the bulk modulus in general depends heavily on the volume. The Cr_{1-x}Al_xN system seem to have a bulk modulus that is almost concentration independent.

3.3 Formation energies

Finally we report the formation energies of the pure binary nitrides. The formation energies calculated as

$$E_f^{XN} = E(XN) - E(X) - \frac{1}{2}E(N_2) \quad (3.3)$$

where X is Sc, Ti, Cr, Hf, and Al respectively are shown in Tab. 3.4. Since the value of the nitrogen chemical potential is difficult to obtain within the KKR-ASA or EMTO framework, also the CrN system is calculated with the PAW method using the 001 antiferromagnetic configuration. As reference state for the metal chemical potential, hcp-Sc, hcp-Ti, 001-antiferromagnetic bcc-Cr, hcp-Hf, and fcc-Al is used. For the nitrogen chemical potential, a N₂ molecule is used. It should be noted that the GGA (or even more LDA) are not as exact in treating molecular systems as compared to solid state systems thus introducing an uncertainty in the predictions of absolute formation energies for these systems. However, when comparisons are made between the different nitrides, this error of course cancels.

Since the nitrogen chemical potential is the same for all systems, the difference in formation energies between the systems are governed by the difference between the cohesive energies of the nitrides and pure metal systems respectively. One can see that ScN has the largest (negative) formation energy, -3.861 eV/f.u., showing the strong chemical driving force of metal Sc to react with nitrogen. Adding one more valence electron to the system, HfN, -3.589 eV/f.u., and TiN, -3.383 eV/f.u., show lower formation energies

compared to ScN. Hf with 5d instead of 3d valence electrons has a higher affinity for N compared to Ti. The AlN phases has still lower formation energies than TiN, h-AlN has -2.851 eV/f.u. and c-AlN has -2.513 eV/f.u., while the CrN phase has the lowest formation energy, only -0.856 eV/f.u. Similar calculations using the LDA approximation was presented by Hugosson *et al.* [72]. In comparison to the present results the LDA results was lower (more negative) in formation energy, most likely due to the better treatment of the N_2 molecule in the GGA approximation used here. However comparing the values for CrN with TiN in Ref. [72] giving a considerably larger difference, 3.094 eV/f.u. one can see the impact of the magnetic treatment of CrN (and bcc-Cr) present in this work but neglected in [72]. The difference presented here is 2.527 eV/f.u. The reason for the difference in formation energies will be discussed in the following chapters.

Table 3.4: Calculated formation energies of the pure nitrides.

Systems	E_f^{XN} [eV/f.u.]
ScN	-3.861
HfN	-3.589
TiN	-3.383
h-AlN	-2.851
c-AlN	-2.513
CrN	-0.856

It has been showed in this chapter that the calculational frameworks used throughout this thesis give reliable results in terms of lattice spacing, bulk moduli for pure nitrides as well as the evolution of the lattice parameter with composition. Further more an understanding of the background to the general property of positive deviation from Vegard's rule displayed in the systems has been given in terms of a modified Vegard's rule. We now turn to the more intricate properties related to electronic structure and thermodynamics.

Chapter 4

Mixing and decomposition thermodynamics of $\text{Ti}_{1-x}\text{Al}_x\text{N}$

In this chapter the important hard coating material system TiAlN is studied in depth. First the calculated mixing enthalpies for the competing cubic and hexagonal phases of the random $\text{Ti}_{1-x}\text{Al}_x\text{N}$ alloys are presented. The results of this study motivates together with experimental reports the focus on the cubic phase in the rest of the chapter. Then the effects of local lattice relaxations in c- $\text{Ti}_{1-x}\text{Al}_x\text{N}$ are investigated, both in terms of energetics and static atomic displacements. The former is directly coupled with the possibility to use the CPA based approach to describe the random alloy using the independent sublattice model for lattice relaxations, and the latter is discussed in relation to bond strength and the concept of solid solution hardening. The electronic structure of the system is investigated with focus on the evolution of the Ti d-states with composition. This is followed by the thermodynamics chapter. The mixing enthalpy and its second concentration derivative is calculated and compared to different ordered structures. The mean-field phase diagram is constructed and the initial results of thermodynamic simulations beyond the mean-field are presented.

4.1 Mixing enthalpies of competing phases in $\text{Ti}_{1-x}\text{Al}_x\text{N}$

It was discussed above that the thin films deposition techniques of relevance for hard coatings materials has an inherent tendency to favour the formation of high entropy solid solutions. In a system such as $\text{Ti}_{1-x}\text{Al}_x\text{N}$, where the pure binary nitrides have different ground state structures one should consider the possibility of the formation of solid solutions in both these phases [2]¹.

However, the experimental evidence points in the direction that the cubic phase wins the competition over the hexagonal phase over the major part of the composition range. While there are plenty of evidence of the formation of cubic $\text{Ti}_{1-x}\text{Al}_x\text{N}$ phases with x as high as 0.67 there are only a few reports of hexagonal B4-based $\text{Ti}_{1-x}\text{Al}_x\text{N}$ phases [29,

¹In principle also possible but not considered in this work, yet other structures could form either as solid solutions or ordered phases. One example is CuZn which can form bcc-based solid solutions or B2 ordered compounds at intermediate compositions while Cu crystallises in the fcc structure and Zn in the hcp structure.

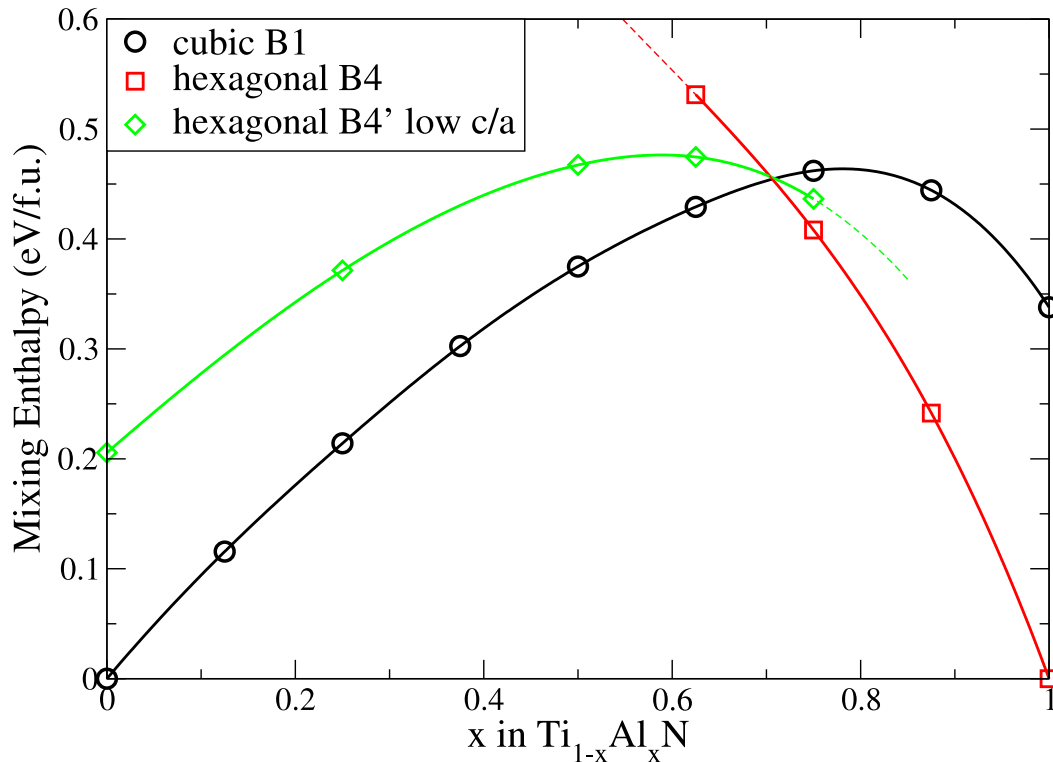


Figure 4.1: Mixing enthalpy for cubic B1 and two different hexagonal wurtzite B4 structures for $Ti_{1-x}Al_xN$.

134,142,143]. Since the main focus of the vast majority of the experimental studies of this system have been on the cubic phase, it is also difficult to know to what extent the h-AlN phases often reported in the literature have in fact a small amount of Ti solved into it. In order to investigate the competition between cubic and hexagonal phases the calculated mixing enthalpy with respect to c-TiN and h-AlN is presented in Fig. 4.1 for the B1 phase as well as for two prototypes of hexagonal phases. The first B4 phase is based on the h-AlN cell parameters, and is shown with squares in the figure. The second is based on the hexagonal ScN phase predicted as metastable by Farrer and Bellaiche [144] here called B4' shown by diamonds.

While both these phases are based on the same unit cell, their cell-parameters in terms of their c/a-ratio and internal parameter u, are rather different. While the B4 phase of AlN has a calculated c/a-ratio of 1.614, the B4'-phase of TiN has a c/a-ratio of 1.20. Of course, the cell parameters are relaxed for each concentration x in h- $Ti_{1-x}Al_xN$, and the c/a-ratio of the B4 phase does decrease with inclusion of Ti, but there is still a significant difference between the two phases. Furthermore, the B4' phase has a considerably lower volume as compared to the B4 phase, at least for comparable compositions. For two compositions, x=0.625 and x=0.75 they are in fact separated by an energy barrier with respect to both c/a-ratio and volume. For other compositions no such barriers exist and one of the phases transforms into the other upon simple static relaxations. Fig. 4.1 shows however that the cubic phase is the most favourable, or rather least unfavourable, solid solution for compositions as high as about $x \leq 0.71$. This is close to the values predicted by Hugosson *et al.* [72] and Mayrhofer *et al.* [74]. The B4' phase

is never found below both the B1 and B4 phases in mixing enthalpy. Furthermore, no calculations investigating the dynamical stability of the Ti-rich B4'-phase has been performed. This means that no conclusions regarding the possibility of existence of this phase can be drawn from these results. However, taking also into account this phase, which has been neglected in previous attempts [72, 74], further strengthen the conclusion of the importance of the study of the cubic phase and cubic isostructural phase transformations.

The energy or enthalpy relations between the different alloy phases might be one part of the explanation why certain phases are or are not formed during thin film growth. However also other factors are very important. For instance pure AlN has been shown to be possible to grow in the cubic phase under certain deposition conditions suggesting that the kinetic mechanism of growth itself can favour the cubic phase [18]. If the growth is epitaxial, the substrate structure, acting as a template is also likely to influence the phase balance. Taken together the experimental reports and these calculations clearly indicate that for the compositional range $0 \leq x \leq 0.67$ the cubic phase should be the main object of study when as-deposited related properties are of interest. Of course, upon heat treatment during annealing or cutting tool operations the system will start to transform towards thermodynamic equilibrium. Hexagonal AlN should be included in such considerations but since the starting material in most cases have the cubic structure the isostructural cubic decomposition, if present, is likely to be activated first. This is also in line with the experimental observations discussed in Chapter 1. The rest of this chapter is devoted to the study of isostructural phenomena in c-Ti_{1-x}Al_xN.

4.2 Local lattice relaxations

As has been described above, in a solid solution the translational and other symmetry operations are only valid on average due to the different chemical environment of each atom. One consequence of this fact is that the atoms do not sit on ideal lattice points of the underlying lattice. Instead they relax locally in a manner that lowers the energy of the system. This effect, although present in all alloys, is typically more important in systems with a considerable size mismatch between the alloy components such as Cu_{1-x}Au_x [126] while it is very small in some size-matched systems such as Ag_{1-x}Au_x [145]. Due to the moderate size mismatch in the c-Ti_{1-x}Al_xN system, 4.6% in lattice parameter compared to more than 11 % in Cu_{1-x}Au_x, one would expect that the effect in this system would be rather small. However, the situation turns out to be much more complicated in these nitride cases.

Fig. 4.2 shows the isostructural mixing enthalpy at zero pressure of c-Ti_{1-x}Al_xN calculated with respect to c-TiN and c-AlN,

$$H(x) = E(c\text{-Ti}_{1-x}\text{Al}_x\text{N}) - (1-x)E(c\text{-TiN}) - xE(c\text{-AlN}), \quad (4.1)$$

using the PAW method and SQS supercells and with the EMTO-CPA method, for both cases where the atoms are placed at ideal B1 lattice positions and when local relaxations are considered. In the case of EMTO-CPA calculations, the local lattice relaxations are considered using the independent sublattice model as described in the chapter Computational methods. The relaxation energies themselves are also shown.

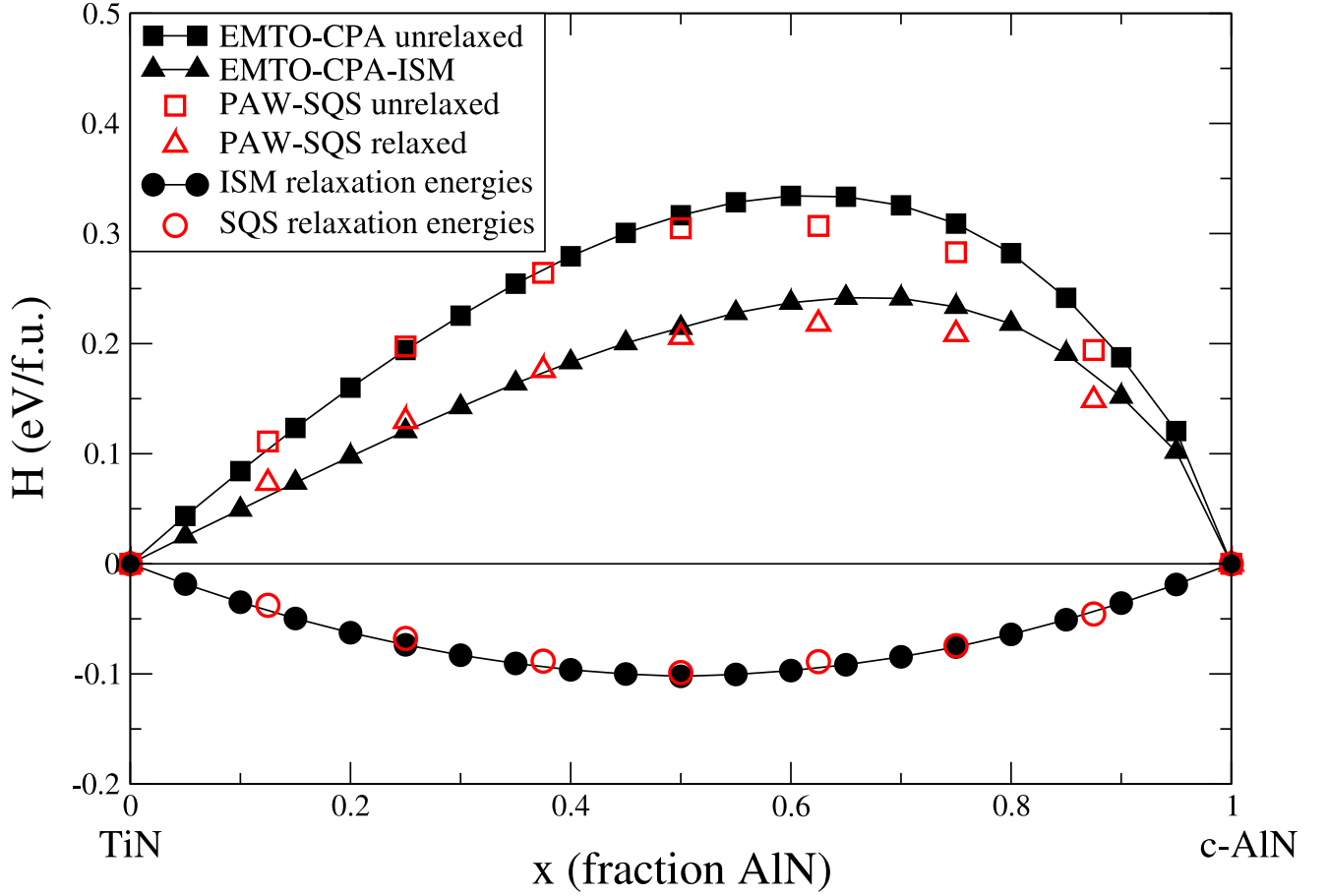


Figure 4.2: The isostructural mixing enthalpy of $c\text{-}Ti_{1-x}Al_xN$ as calculated with the PAW-SQS method (open symbols) and the EMT0-CPA method (solid symbols). Results are shown both for ideal B1 lattice positions (squares) and including local relaxation (triangles). The relaxation values themselves are shown with circles.

One can clearly see in Fig. 4.2 that including local relaxations lowers the mixing enthalpies by up to one third or about 0.1 eV/f.u. for the $x=0.50$ composition. Thus, it is obvious from an energetics point of view that one can not approximate substitutional disorder in this system by considering random occupation at sites of an ideal underlying B1 lattice. In order to anyway be able to use the fast and accurate CPA framework for the treatment of disorder, the Independent Sublattice Model (ISM) as described in the Computational methods chapter is used.

The parameter v_{TiAl} in eq. 4.1 is calculated to 0.060 eV/f.u. For the alloy with $x = 0.5$, this gives $E_{Nrel}(0.5) = 0.090$ eV/f.u. Using the Effective Tetrahedron Model (ETM) for the local cluster volume relaxation energy of the metal sublattice we get $E_{metalrel}(0.5) = 0.01$ eV/f.u. which adds up to $E_{rel}^{ISM}(x) = 0.10$ eV/f.u. in excellent agreement with the supercell value for this concentration, 0.098 eV/f.u. As can be seen in Fig. 4.2 the ISM model for local relaxations works extremely well for all concentrations where the supercell energies have been calculated.

In Fig. 4.3 the displacement of the atoms from the ideal B1 positions in the fully relaxed supercell which models $Ti_{0.75}Al_{0.25}N$ alloy are shown. We show the values of the

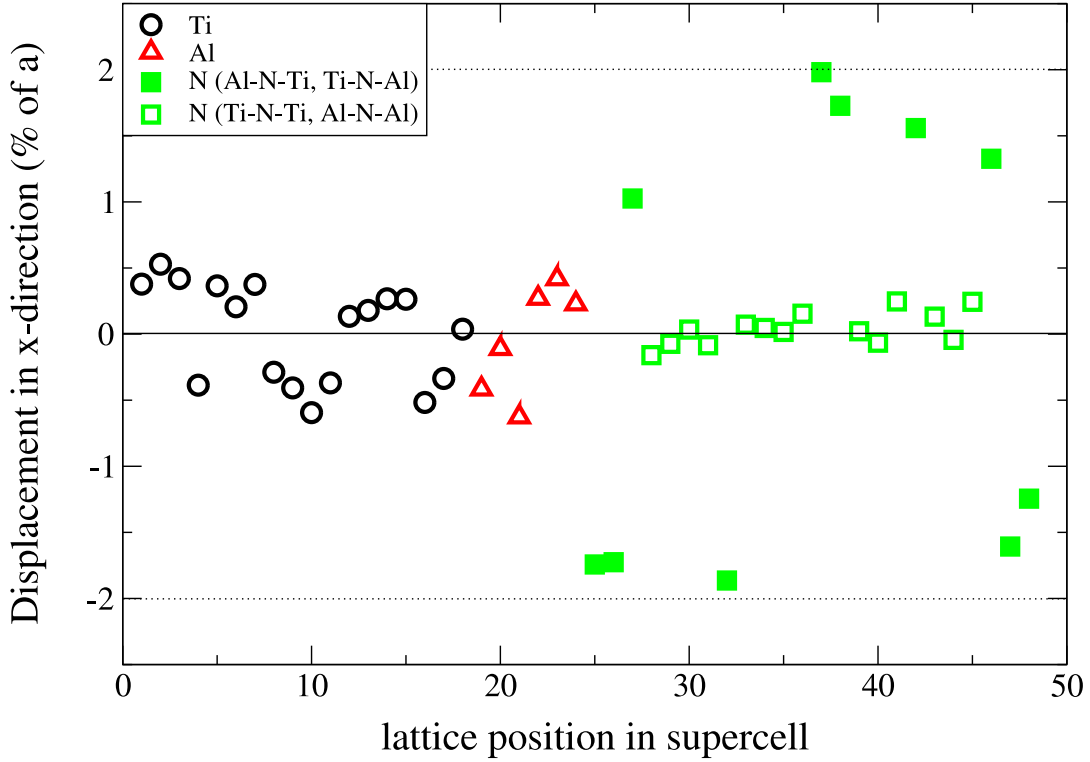


Figure 4.3: Relaxation pattern in the x direction for the atoms in the $\text{Ti}_{0.75}\text{Al}_{0.25}\text{N}$ supercell. Ti atoms are marked with circles (position 1-18), Al atoms with triangles (position 19-24). N atoms surrounded by one Al and one Ti atom along the x direction are marked with solid squares while N atoms surrounded by two chemically equivalent metal atoms are marked with open squares

displacements projected in the x -direction. One can clearly see that N-atoms that are surrounded along the x -axis by two metallic atoms of different kinds (solid green squares in Fig. 4.3) show the largest displacements, 1-2 % of the average lattice parameter. Note that the values are in agreement with the displacements of the N-atom in the pseudo Z2 ordered compound used for the determination of the parameters of the ISM (shown by the dotted lines in Fig. 4.3). At the same time, the N-atoms that are surrounded along the x direction by two chemically equivalent atoms show negligible displacements (0.1 - 0.3 % of the average lattice parameter). The metal atoms themselves show small displacements that are consistent with the small values of local cluster volume relaxations obtained within our ETM calculations.

From these considerations, it is obvious that the approximations made in deriving the ISM model above are justified and that the model itself captures the relevant physics behind the local relaxation phenomenon in this system very well. The relaxation energies for all concentrations are in good quantitative agreement with the supercell calculations and the actual relaxation patterns are qualitatively captured. It can therefore be expected that this is the case also in other metal nitrides with the B1-structure.

The pattern of relaxations in the $c\text{-Ti}_{0.5}\text{Al}_{0.5}\text{N}$ and $c\text{-Ti}_{0.25}\text{Al}_{0.75}\text{N}$ systems shown in Figs. 4.4 and 4.5 are qualitatively similar to the $c\text{-Ti}_{0.75}\text{Al}_{0.25}\text{N}$ case although especially the $c\text{-Ti}_{0.5}\text{Al}_{0.5}\text{N}$ system shows larger displacements of the metal atoms.

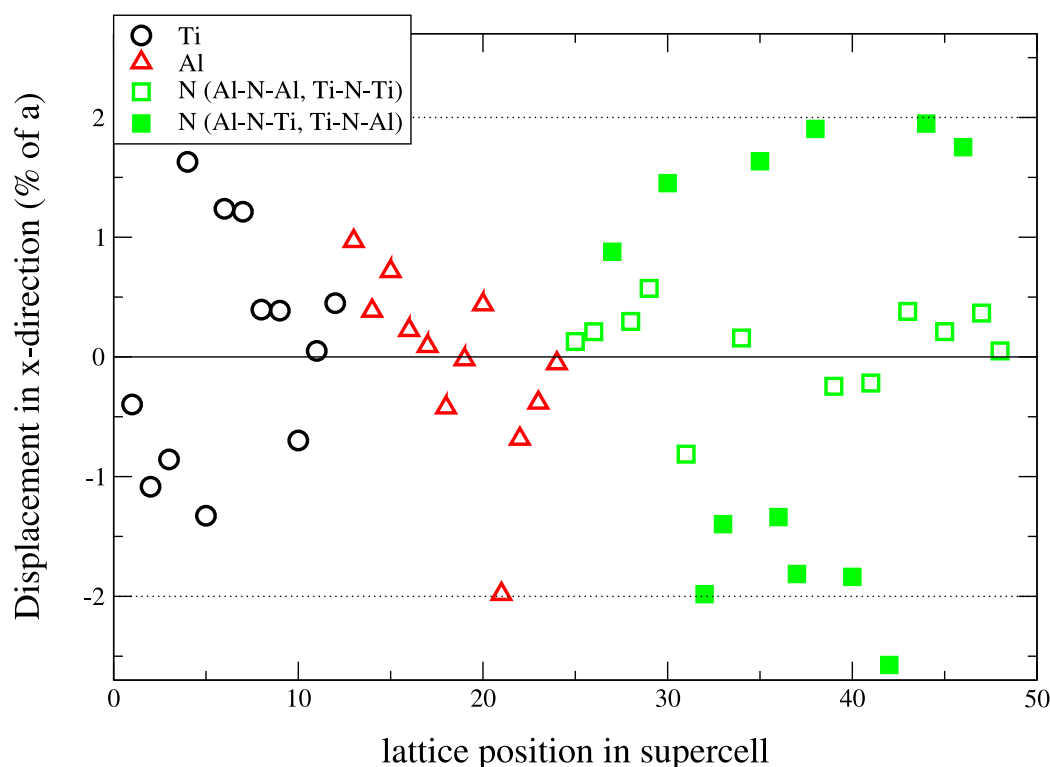


Figure 4.4: Relaxation pattern in the x direction for the atoms in the $Ti_{0.5}Al_{0.5}N$ supercell. Ti atoms are marked with circles (position 1-12), Al atoms with triangles (position 13-24). N atoms surrounded by one Al and one Ti atom along the x direction are marked with solid squares while N atoms surrounded by two chemically equivalent metal atoms are marked with open squares

The consequences for the nearest neighbour bond lengths can be seen in Fig. 4.6. The three panels show the fraction of nearest neighbour Ti-N (up) and Al-N (down) bonds as a function of bond length for the three compositions $x=0.25$, 0.50 , and 0.75 . The bars show the fraction rounded to each 0.01 \AA . One can see that there is a substantial spread in the NN Al-N and even more drastically Ti-N distances. Interestingly and perhaps unexpected there are Ti-N bonds that become both longer than in pure TiN, and although very rare also shorter than c-AlN distances. The same phenomena can be seen for the Al-N distances although to a lesser extent. The spread in NN bond lengths are to a large extent due to the relaxation of the nitrogen atoms surrounded by different metal atoms along the cartesian axis' as shown above but also the relaxation of metal atoms contribute to this spread especially for the composition $x=0.50$.

This spread in the bond length of nearest neighbour atoms are likely to have a certain impact on various properties of the material and can be discussed in terms of solid solution hardening: The spread corresponding to more than 10% of the average nearest neighbour bond length is a clear indication that the local environment affects the strength of the bonds considerably. Further more, the offset in position itself might influence some aspects of the bond strength. Although these atomic positions correspond to a stress-free state in the sense that the net forces acting on all atoms are zero, the resistance of the material against plastic deformation is most likely affected. This is so since such plastic deformations require the breaking of a number of bonds through

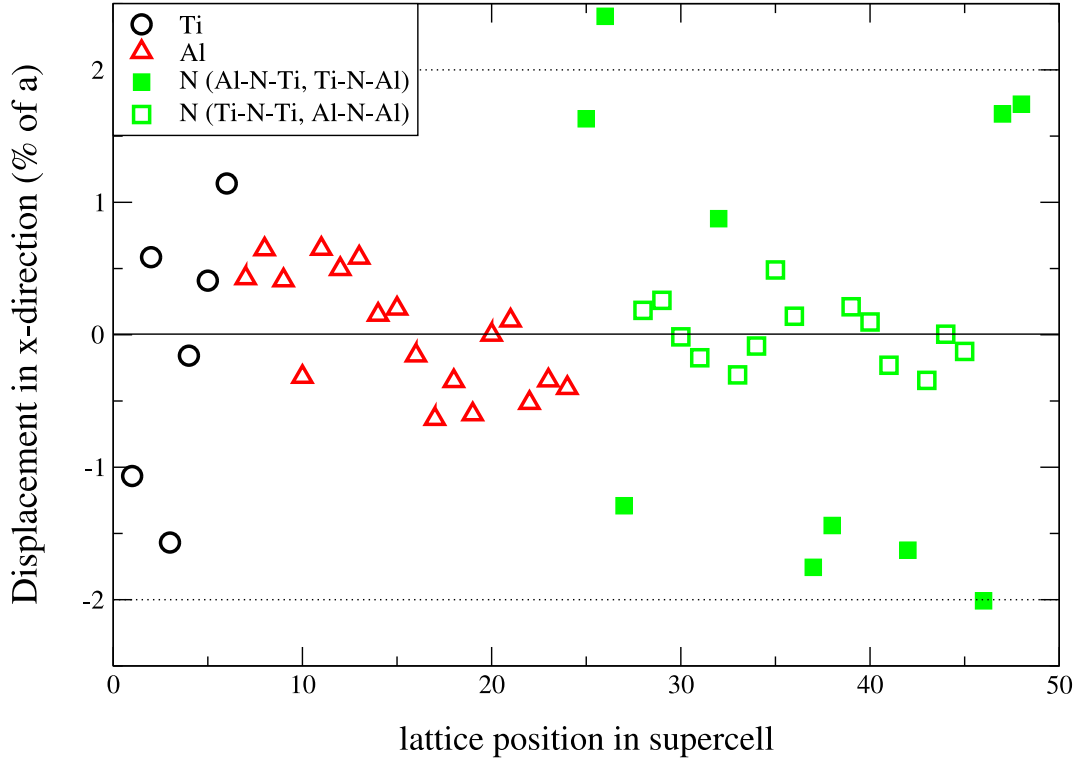


Figure 4.5: Relaxation pattern in the x direction for the atoms in the $\text{Ti}_{0.25}\text{Al}_{0.75}\text{N}$ supercell. Ti atoms are marked with circles (position 1-6), Al atoms with triangles (position 7-24). N atoms surrounded by one Al and one Ti atom along the x direction are marked with solid squares while N atoms surrounded by two chemically equivalent metal atoms are marked with open squares

cation (or cation vacancy) hopping during for instance dislocation nucleation or motion throughout grains. Although the explicit individual bond strength with respect to different deformation processes are not directly extractable from these results, it is very likely that at least some of these bonds that differ so much in bond length are considerably more resistant against atomic displacements compared to the situation in pure TiN and c-AlN where all bonds are equal in length and strength. This will create a higher maximum value of the energy potential (E_k) to overcome for cations during migrating. At the same time many of the bonds are likely to be weaker. However since the probability of migration is proportional to $e^{-E_k/k_B T}$ the motion of dislocations are to a large extent limited by the highest values of E_k and not the average value. This would lead to a slower dislocation movement in the alloyed samples and might in fact be one part of the explanation to the phenomena of solid solution hardening attributed to Al addition to TiN in c- $\text{Ti}_{1-x}\text{Al}_x\text{N}$ with $x \leq 0.60$ [25, 26, 29] as shown in Fig. 1.7. A similar discussion was made for the case of nitrogen vacancies in TiN_x in Ref. [10] although in that case electronic redistribution rather than change in bond length was the main point for hardening effects. It should be stressed again that the spread in bond lengths can be seen more as an evidence that the bonds really do have different strengths, rather than being the main reason behind the differences.

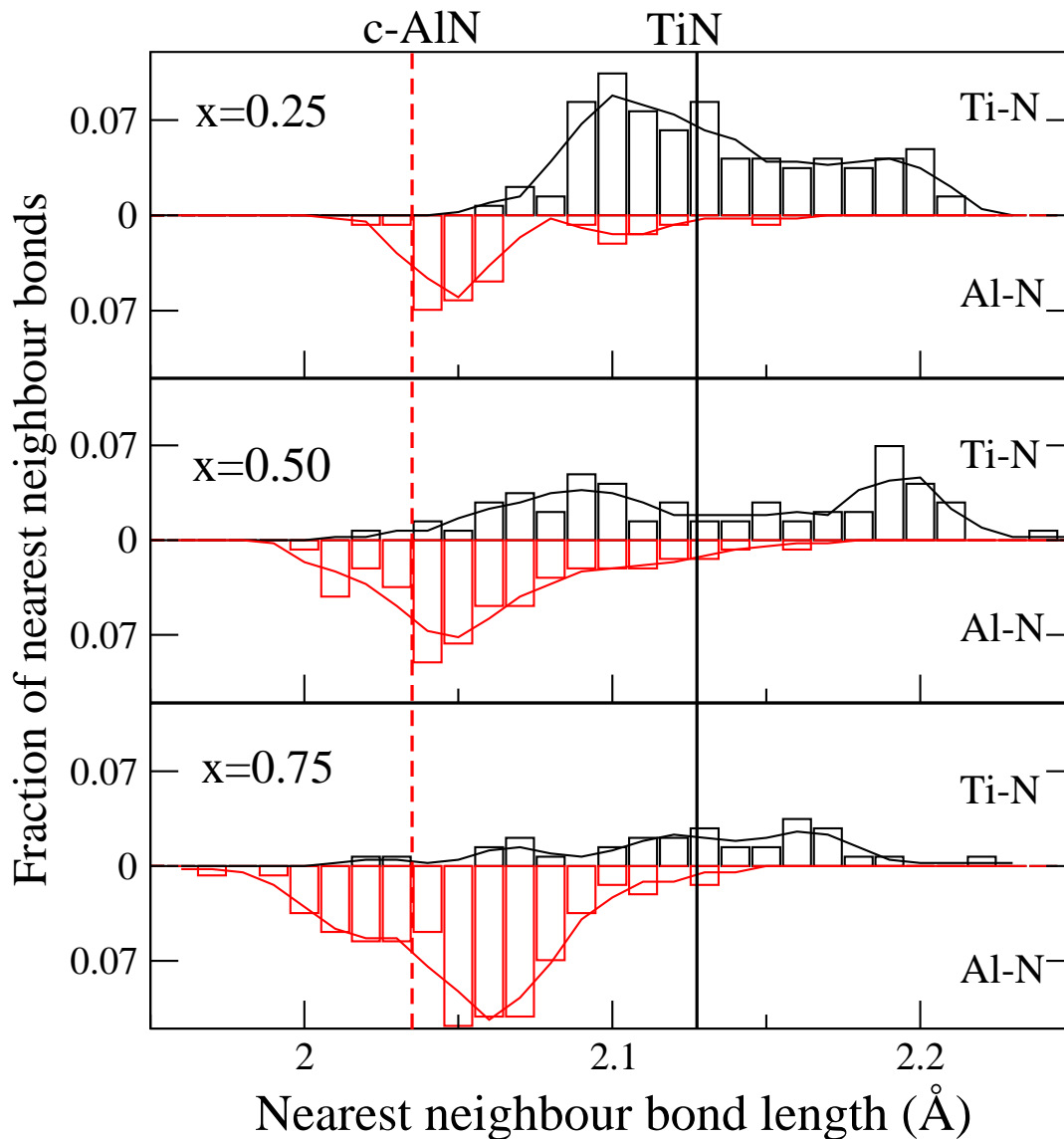


Figure 4.6: The distribution of nearest neighbour Ti-N (bars up) and Al-N (bars down) bond lengths in the relaxed c - $Ti_{1-x}Al_xN$, $x=0.25, 0.50, 0.75$, supercells. The bars show the fraction of NN-bonds that are rounded to each 0.01 \AA while the lines are the running average over 0.03 \AA . Note the considerable spread in bond lengths, especially in the $Ti_{0.5}Al_{0.5}N$ composition. The bond length in pure c -AlN is shown with a dashed vertical line and the value for pure TiN is shown with a solid vertical line.

4.3 Electronic structure

It is well established that the bonding in TiN as well as in the related compound TiC has a mixed character of both covalent, ionic, and metallic bonds [53–55,57]. N $2p$ -Ti $3d$ hybridization leads to the formation of covalent bonding and anti-bonding states. The following discussion is illustrated in Figs. 1.17 and 4.7. However, the symmetry of the B1-structure only allows Ti $3d$ -states with e_g symmetry to hybridize with the N $2p$ -states while the d -states with t_{2g} symmetry form so called non-bonding states and account for weak hybridization between next-nearest neighbor Ti atoms [55]. Even though the

extent of overlap between Ti-*d*-states for the next-nearest neighboring Ti-atoms have been shown to be small for states below the Fermi level [57] this hybridization broadens the non-bonding state to form a shoulder at the DOS curve [56] that in TiN is occupied. Due to the difference in electronegativities a large charge transfer occurs from Ti to N leading to an ionic admixture to the bonding.

In cubic AlN on the other hand the ionic bonds have been shown to dominate [146]. This is different to the case of wurtzite AlN where covalent bonding is also present [146]. Due to the differences between TiN and c-AlN one can expect that the electronic structure effects will give strong variation of the properties of metastable c-Ti_{1-x}Al_xN as a function of composition. In Fig. 4.7 we show the EMTO-CPA calculated density of states for the system Ti_{1-x}Al_xN as a function of energy (in eV relative to the Fermi energy E_F) and fraction of AlN, x . In the case of pure TiN one can clearly see the peaks corresponding to the bonding (-8 to -3 eV) and non-bonding (-2 to 2 eV) states separated by a pseudo-gap. The N 2s-states at about -15 eV are clearly separated from the rest of the valence band and play no significant role in the bonding for this system. Since the bonding states can only accommodate 6 valence electrons and there are totally 7 present (4 Ti + 3 N) in the unit cell (not counting N-2s) one electron has to occupy the non-bonding states and the Fermi level is shifted above the minimum of the pseudo-gap.

In the case of pure c-AlN, the semiconducting character is clearly visible. The calculated bandgap is 3.42 eV while no experimental value has been found in the literature. It should be noted that bandgaps in semiconductors are generally underestimated within GGA (and LDA) calculations, mainly due to the fact that self-interaction is not perfectly cancelled by these exchange correlation functionals pushing all occupied states to higher values in contrast to unoccupied states. It should also be considered that the measurement of band gap energies correspond to a dynamical process not exactly described by differences of the one-electron eigenvalues of the Kohn-Sham Hamiltonian. For comparison, the calculated value of the band gap of h-AlN using the PAW-method is 4.01 eV as compared to the experimental value 6.2 eV [147]. When gradually increasing the Al content in Ti_{1-x}Al_xN one can see that up to $x=0.50$ there is a gradual, smooth change in the DOS. However, for the composition $x=0.75$ one can see that the DOS shows clear similarities with the one for pure AlN, but with an isolated Ti state within the band gap. This result can be explained by the fact that substitution of Ti by Al is destroying the hybridization between next-nearest neighbor metal atoms, as there are no Al *d*-states which could participate in the bonding. This localizes the non-bonding Ti *d*-states in the band gap of the material with predominantly ionic bonds. Since Ti has one valence electron more than can be accommodated by the AlN valence band, the impurity state at E_F becomes populated.

In Fig. 4.8 the Ti-site projected DOS at E_F (in states per eV) is plotted as a function of fraction of AlN. It is obvious that above $x=0.50$ the decrease of Ti-Ti hybridization leads to a dramatic increase of the local DOS at the Fermi level at the Ti-sites. The destabilizing effect of a high DOS at the Fermi level is well known [148] and the increase of Ti-site projected DOS at E_F is an indication of increased tendency towards decomposition in the Ti_{1-x}Al_xN system.

The above results also underline the importance of local environment effects, as is illustrated in Fig. 4.9. The figure shows the Ti-site PDOS (in states per eV and unit cell)

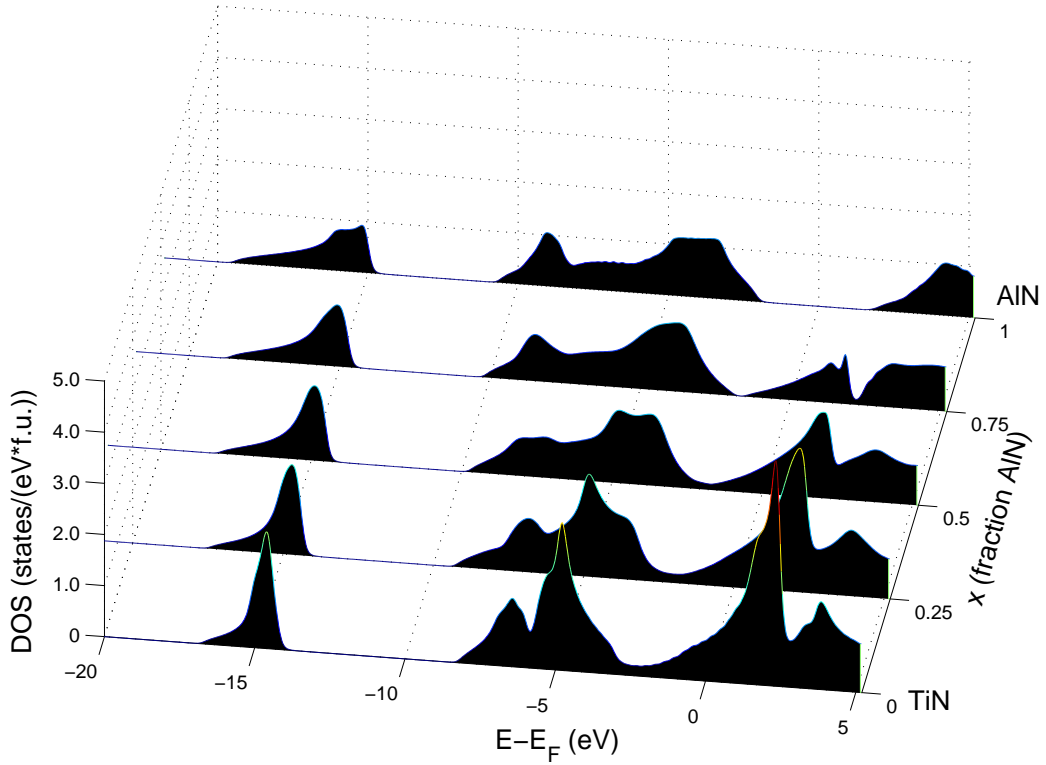


Figure 4.7: The total electronic density of states of c- $Ti_{1-x}Al_xN$ as calculated with the EMTO-CPA method. The DOS are shown for different fractions x of AlN: 0.00, 0.25, 0.50, 0.75, and 1.00 and are presented as a function of energy with respect to the Fermi energy. Note the band gap present in the semiconductor c-AlN.

calculated for the the supercell with $x=0.50$. The PDOS at two different Ti-atoms with different local environments are shown together with the Ti PDOS in pure TiN. One of the Ti atoms has next-nearest neighbors consisting of 3 Al atoms and 9 Ti atoms (thick solid line) while the other atom has 9 Al and 3 Ti atoms (dashed line). There are clear differences, in particular the increase of the PDOS at E_F for the Ti-atom in the Al-rich environment.

Considering these results and the relatively small lattice mismatch discussed in the previous chapter, we suggest that electronic structure effects are responsible for both the high mixing enthalpy as such and its strongly asymmetric concentration dependence, c.f. Fig. 4.2.

4.4 Thermodynamics of c- $Ti_{1-x}Al_xN$

4.4.1 Mixing enthalpy

Using the EMTO-method we have calculated the total energy with composition intervals of 5% as seen in Fig. 4.2. This gives a fine mesh in terms of alloy concentration that makes it possible to calculate accurately the second derivative of the mixing enthalpy with respect to composition. This is important in order to obtain information about alloy compositions that are likely to show spinodal decomposition.

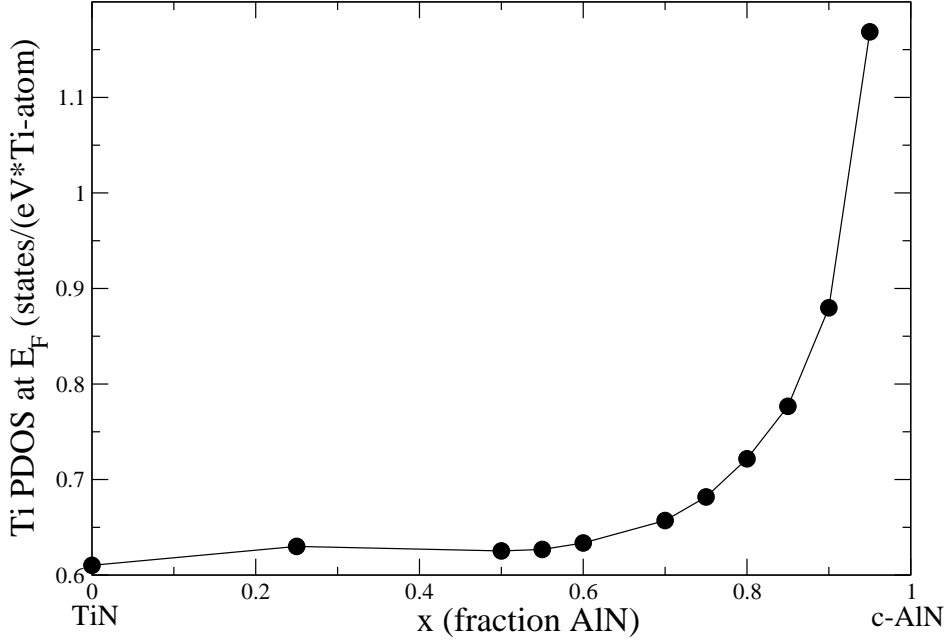


Figure 4.8: The Ti site projected electronic density of states of $\text{Ti}_{1-x}\text{Al}_x\text{N}$ at the Fermi level as a function of AlN content as calculated using the EMTO-CPA method.

In order to avoid numerical noise in the evaluation of the second concentration derivative, Eq. 1.2, a fifth order polynomial fit to $H(x)$ was used in the derivation. A convergence test with respect to polynomial order was performed and the fifth order of the polynomial fit was found to give a relatively accurate description of the second concentration derivative. However, if a polynomial fit with lower order is used, such as the third order used in Ref. [73], some important structure of the second derivative is lost. In Fig. 4.10 the mixing enthalpy and its second concentration derivative is shown together with the enthalpy of four different ordered $\text{Ti}_{0.5}\text{Al}_{0.5}\text{N}$ compounds.

The mixing enthalpy of $\text{Ti}_{1-x}\text{Al}_x\text{N}$ is found to be positive for all values of x . The curve is not symmetric, but has its highest value, 0.24 eV/f.u., at about $x=0.68$. This shows that the energy needed to solve a small amount of AlN in TiN is smaller than the energy required to solve an equal amount of TiN in c-AlN. This is a clear manifestation of the complex evolution of the electronic structure as discussed in the previous section.

$d^2H(x)/dx^2$ has a strong concentration dependence. It is only for low AlN content, with $x < 0.15$, that the spinodal condition is not fulfilled at 0 K. It should be pointed out that the value of $d^2H(x)/dx^2$ at very low x is difficult to derive numerically and the true value might actually be very close to 0 or just below. In any case since the value is small, at finite temperature the entropy contribution with positive second derivative (large in this region) will rule out spinodal decomposition in this concentration regime.

At large x the second derivative goes to very large negative numbers. This is a consequence of the non-symmetric shape of the mixing enthalpy curve which at 0K is the same as the free energy and indicates an extreme instability towards decomposition at high fractions of AlN. The plateau of $d^2H(x)/dx^2$ at intermediate concentrations on the

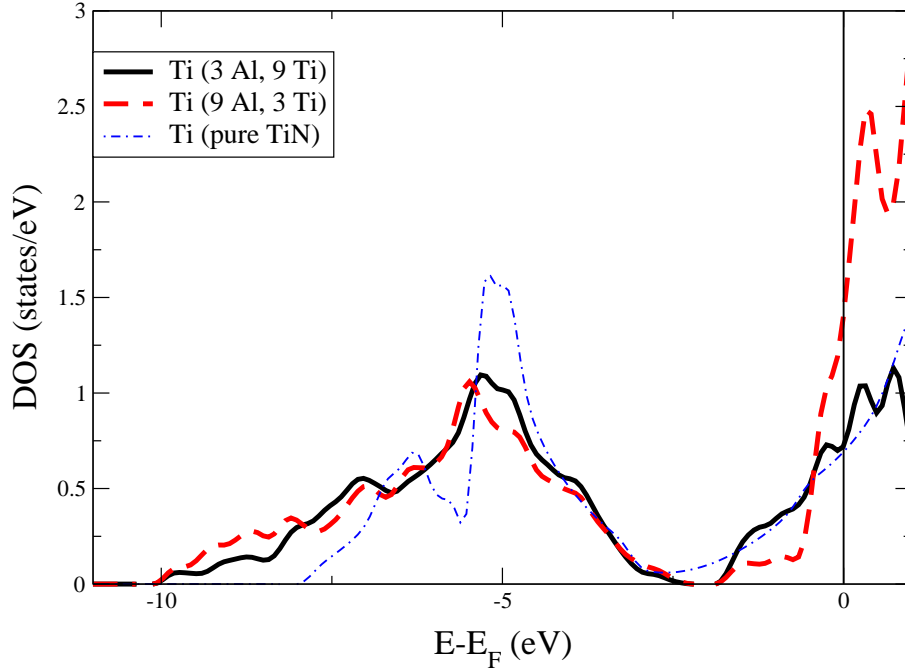


Figure 4.9: The Ti site projected electronic density of states of two differently coordinated Ti-atoms in $Ti_{0.5}Al_{0.5}N$ compared to a Ti-atom in pure TiN. The legends show the number of Ti and Al next-nearest neighbours of the studied atoms.

other hand indicates that there might be a quite limited temperature intervall where a large part of the concentration range is moved out of the spinodal regime.

The four ordered $Ti_{0.5}Al_{0.5}N$ compounds shown in Fig. 4.10 are the B1 counterparts to the fcc based structures $L1_0$, $L1_1$, double layer $L1_0$ and double layer $L1_1$. $L1_0$ consist of a fcc lattice where 001-planes are alternatively occupied by the two alloy components. $L1_1$ is similar but with the alternating planes stacked in the 111-direction. The double layered $L1_0$ is the structure shown in Fig. 2.5 while the double layered $L1_1$ has 111-planes of the same alloy component in the sequence A-A-B-B. In our B1 case it means that the metal sublattice is ordered according to the corresponding fcc based structure while the nitrogen sublattice is kept homogenous. The large dispersion in mixing enthalpy of these different ordered compounds, despite the fact that they have the same composition and underlying lattice, shows that there are strong local interactions in the system. This shows the importance of treating the substitutional disordered solid solution in a correct way if properties of the random state is to be calculated. It should be stressed that there exist ordered compounds that, even though they have positive mixing enthalpy, are considerably below the disordered phase in total energy. Their existence are likely to effect the decomposition thermodynamics and kinetics of the system and will be further analysed below.

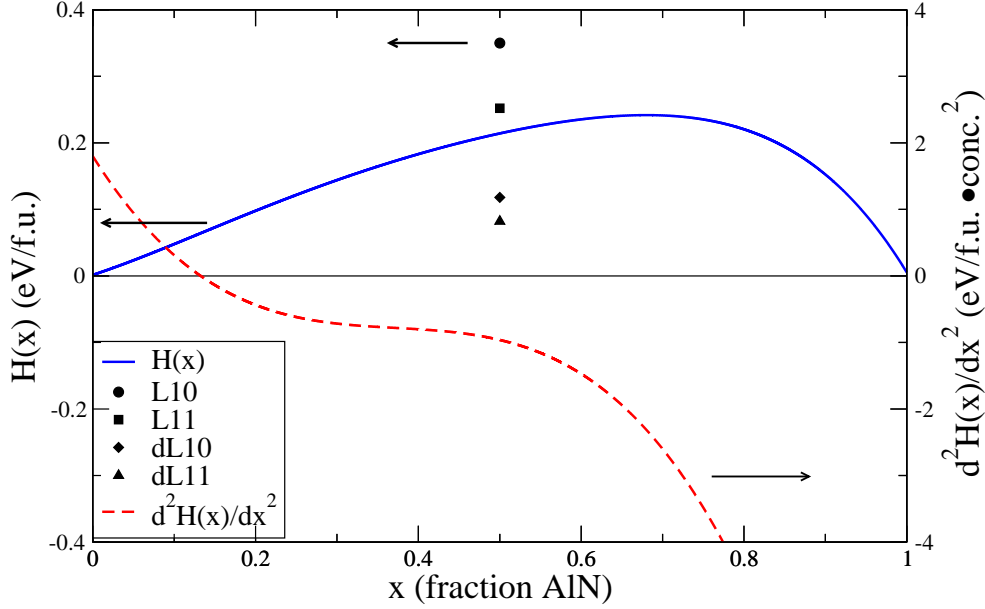


Figure 4.10: Mixing enthalpy of a random solid solution of $c\text{-Ti}_{1-x}\text{Al}_x\text{N}$ as a function of fraction of AlN together with its second concentration derivative. Also shown are the enthalpies of four different ordered $\text{Ti}_{0.5}\text{Al}_{0.5}\text{N}$ compounds. See text for discussion.

4.4.2 Mean field phase diagram of $c\text{-Ti}_{1-x}\text{Al}_x\text{N}$

In order to perform a first simulation of the effect of increasing temperature on the thermodynamic stability of the mixed $c\text{-Ti}_{1-x}\text{Al}_x\text{N}$ state we estimate the free energy per formula unit

$$G(x, T) = H(x) - TS(x) \quad (4.2)$$

where $H(x)$ is the mixing enthalpy per formula unit and T is the absolute temperature within the mean-field approximation for the entropy

$$S_{mf}(x) = -k_B[x\ln(x) + (1-x)\ln(1-x)] \quad (4.3)$$

where x is the fraction of AlN. In our case the mixing takes place only on one of the two sublattices and the contribution to the entropy from the ordered nitrogen sublattice is equal to zero. The use of common tangent analysis of the free energy curves and the sign of the second concentration derivatives of the free energy allows us to estimate the phase diagram which is shown in Fig. 4.11.

This formula in Eq. 4.3 is a drastic simplification of the real finite temperature situation and is used only to get a first idea of the relevant temperature scales for the thermodynamics of this system and as a guideline for further experiments or more realistic theoretical calculations. Especially in a system with strong local interactions like the one in the present study we expect the mean field approximation to give an overestima-

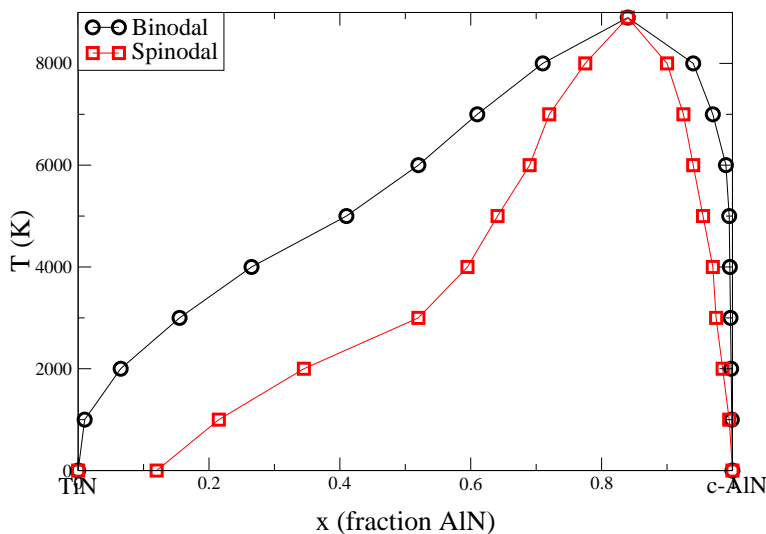


Figure 4.11: The mean-field estimate of the composition-temperature phase diagram of $c-Ti_{1-x}Al_xN$. The binodal is shown with circles and the spinodal with squares.

tion of transition temperatures. Indeed short range order (or clustering) lowers the free energy for the solid solution phase. The latter is neglected in the mean field approach. Vibrational entropy is also neglected. This simplification is probably of less importance than the configurational one at relevant temperatures since the difference in lattice parameter between the phases is so small. On the other hand further investigations would be welcome since the spread of nearest neighbour bond lengths in the alloys shown above raises some doubts.

The mean field phase diagram suggests that $c-Ti_{1-x}Al_xN$ possesses a miscibility gap up to very high temperatures, around 6000 K for equiatomic composition and above 8000 K for compositions around $x=0.80$. In this context one can note that the melting temperature is around 3000 K for TiN and 2500 K for h-AlN. Further more, the phase diagram predicts that solid solutions should be subject to spinodal decomposition over a large range of the concentrations. At temperatures around 1273K, often used in annealing experiments the spinodal region goes from about $x=0.25$ to $x=0.99$.

Even though the phenomena of age hardening have been experimentally reported only for AlN fractions higher than 50 percent, there are weak signs of isostructural decomposition in experiments with AlN content as low as 40 and even 25 percent [29,34], however the mechanism of this decomposition is not characterised and can, at least in the case of Ref. [34] be nucleation and growth.

Our results differ significantly from the mean-field phase diagram in Ref. [73]. We attribute the major part of this difference to the fact that in Ref. [73] the entropy contribution was originally overestimated leading to a corresponding underestimation of transition temperatures with a factor of 2 [75]. However also our mixing enthalpies are different and we believe that this is because of the inconsistent treatment of substitutional disorder in Ref. [73] as will be apparent below. Also the usage of a low order polynomial fit of the enthalpy values influences the results in Ref. [73].

4.4.3 Thermodynamics beyond the mean field approximation

In the results above the mechanism behind the decomposition has been discovered and a first simulation of the phase diagram has been performed by means of the mean-field approximation to configurational entropy. However, in order to be more confident in the actual quantitative values of temperatures in the phase diagram one can not be satisfied by the mean-field treatment. The crucial point neglected in the MF-approximation is the fact that the short range order of the distribution of metal atoms on the corresponding sublattice of the system could considerably influence the transition temperature of the $\text{Ti}_{1-x}\text{Al}_x\text{N}$ system from solid solution (with short range clustering) to phase separation. This is so since the short range clustered system above the transition temperature decreases the configurational energy with respect to ideal random solid solution much more than the corresponding decrease in entropy thus lowering the free energy.

In order to go beyond the mean field approximation one would like to apply a Monte Carlo scheme for the thermodynamics simulations for the $c\text{-Ti}_{1-x}\text{Al}_x\text{N}$ system. However the number of energy evaluations and the size of the simulation box needed to perform such a simulation makes direct first-principles calculations impossible, at least within a reasonable time frame. Instead the coarse-graining procedure in terms of a cluster expansion of the configurational energetics has been performed within the Screened Generalized Perturbation Method (SGPM) in conjunction with the Independent Sublattice Model (ISM) for local lattice relaxations as described in Chapter 2. This procedure reduces the computational costs for the energy evaluation by several orders of magnitude and makes the Monte Carlo simulation possible.

The concentration dependent effective cluster interactions (ECI) of the configurational Hamiltonian in Eq. 2.28 has been calculated for concentration steps of $\Delta x = 0.10$. Effective 2-site (pairs), 3-site, and 4-site interactions have been considered. It turns out that the most important terms are the pair interactions on the first two fcc-shells of the metallic sublattice. Fig. 4.12 shows the value of these two interactions as a function of the AlN content x . As an inset the first 10 pair interactions of the $\text{Ti}_{0.50}\text{Al}_{0.50}\text{N}$ system are shown.

The pair interactions of the Hamiltonian can be written as the energy relation

$$V_{ij}^2 = E(\text{Ti}_i, \text{Ti}_j) + E(\text{Al}_i, \text{Al}_j) - 2E(\text{Ti}_i, \text{Al}_j) \quad (4.4)$$

in line with Eq. 2.37.

Thus the sign of the potential parameter V determines if the system has a tendency towards ordering (positive) or clustering (negative) on that certain coordination shell. In our system the first interaction is strong and negative showing a clear impact of the electronic structure effect described above as Ti-atoms strive to neighbour other Ti atoms and similar for Al atoms on the first coordination shell. On the other hand the second nearest neighbour interaction is positive, with the exception of $x \geq 0.80$. This is the result of the local lattice relaxation of N atoms situated in between Ti-Al and Al-Ti pairs. If bare SGPM-interactions on a fixed B1-lattice were considered, this interaction would also be negative, although smaller as compared to the first coordination shell. Longer ranged pair interactions, 15 shells are considered here, show alternating signs and gradually decreasing intensities as can be seen from the inset of Fig. 4.12. The 3 and 4-site interactions on the first couples of coordination shells are relatively less important

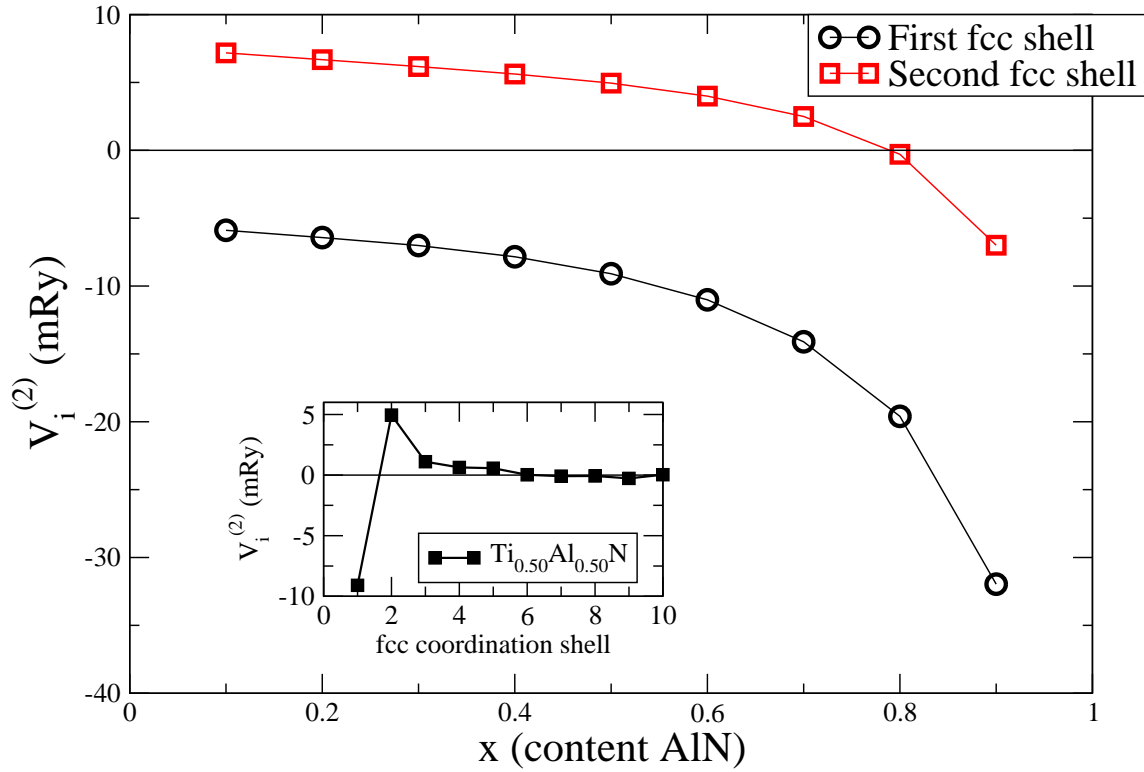


Figure 4.12: The first two pair interactions as a function of concentration calculated using the SGPM method and including the ISM-relaxation effect. Inset: the first ten pair interactions in $Ti_{0.5}Al_{0.5}N$.

but should be included for quantitative predictions. The leading 3-site interactions favours the formation of pure c-AlN domains rather than pure TiN domains.

The leading two pair-interactions has a profound non-linear concentration dependence. For Ti-rich compositions there is a linear gradual decrease of both V_1^2 and V_2^2 but for compositions with $x \geq 0.50$ the decrease accelerates. For the composition $x=0.90$ the magnitude of V_1^2 is five times larger compared to $x=0.10$. This development is directly related to change in electronic structure with composition as is described in a previous section. Especially remaining Ti-Ti nearest neighbour bonds become gradually stronger as they become fewer as Ti is substituted by Al.

When the ECI's of the system are known one can perform a Monte Carlo simulation to achieve thermodynamic properties such as i.e. specific heat, which can be used to determine critical temperatures for phase separation.

The concentration dependent ECI obtained with the SGPM-method describe the chemical interactions as perturbations on the solid solution state with a specific concentration. As such they are most likely describing very well the first few steps of redistribution of atoms when a frozen-in solid solution are subjected to temperatures where diffusion is allowed or the short range order at very high temperatures (hypothetical in the present case). However in phase separating systems such as $Ti_{1-x}Al_xN$, a profound problem is present when one tries to simulate the critical phase separating temperatures. The reason is that in order for such a simulation to be accurate, the set of ECI used must accurately describe the energetics of the systems on both sides of the critical temperature. The high temperature disordered phase is rather well described while the low

temperature clustered phase is much more problematic. The reason can be understood by first considering the mean-field phase diagram in Fig. 4.11. If we start with a solid solution $\text{Ti}_{0.5}\text{Al}_{0.5}\text{N}$ system at very high temperatures and decrease it the binodal phase separation line is hit at about $T=6000\text{K}$, but might in reality be lower. If the equilibrium phase separated system below this point had consisted of a mixture of $\text{Ti}_{0.5+\delta}\text{Al}_{0.5-\delta}\text{N}$ and $\text{Ti}_{0.5-\delta}\text{Al}_{0.5+\delta}\text{N}$ the usage of concentration dependent interactions would probably be acceptable. However, as can be seen in Fig. 4.11 the resulting compositions right below the critical temperature are closer to $\text{Ti}_{0.5+\delta}\text{Al}_{0.5-\delta}\text{N}$ and pure $c\text{-AlN}$. This means that the ECI derived at $x=0.50$ are not sufficient to accurately describe all parts of the Monte Carlo simulation box. Instead all compositions $0.50 \leq x \leq 1.00$ needs to be accurately described in this case. Due to the strong concentration dependence, especially in the AlN-rich side of the composition space, the use of fixed ECI derived from $x=0.50$ will not yield a reliable result.

Fig. 4.13 shows the resulting atomic configurations of simulated isothermal annealing of the initially random $\text{Ti}_{1-x}\text{Al}_x\text{N}$ systems with different compositions and 108000 metal atoms in each simulation box derived using the method discussed above. Ti atoms are shown light grey while Al atoms are shown in red. N atoms are not shown and are actually only present in this part of the simulation through their fundamental effect on the ECI's. A Monte Carlo scheme where only nearest neighbouring atoms are allowed to change places has been used to qualitatively simulate distribution pattern possibly developing in real systems. In each simulation at least 10000 atomic swaps per metal atom in the cell is tested, Ti-Ti and Al-Al "swaps" are not counted. No qualitative difference in appearance is visible in the simulation boxes during the last 1000 steps per metal atom meaning that the pattern are either equilibrium or effectively frozen-in. The latter effect is not due to kinetic energy barriers stopping diffusion, because such barriers are neglected in this simulation, but rather due to local thermodynamic barriers effectively hindering for instance Ti atoms to migrate through large $c\text{-AlN}$ clusters at low temperatures. This is a phenomenon that should also be present in real systems but possibly being dominated as limiting factor of the kinetic energy barriers connected to vacancy hopping guided atomic diffusion.

The effects of both temperature and concentration dependence of the ECI's can readily be seen in Fig. 4.13. For instance, this simulation predicts that $\text{Ti}_{0.60}\text{Al}_{0.40}\text{N}$ forms a disordered state although with a certain short range clustering tendency at 1100 K while at the same temperature $\text{Ti}_{0.40}\text{Al}_{0.60}\text{N}$ forms a clearly phase separated state with large homogenous areas of almost pure $c\text{-AlN}$. This prediction could be in line with reality but an example of the problem of using concentration dependent ECI's for phase separating systems can be seen when studying the compositions $x=0.50$, 0.60 , and 0.70 at $T=1100$ K. All three compositions are clearly within a two-phase region and having the same temperature, the composition of the two respective phases should be the same, only differing in the relative amount. However, this is not the case which is easily seen as more Al is solved in the Ti-rich phase in $\text{Ti}_{0.50}\text{Al}_{0.50}\text{N}$ as compared to $\text{Ti}_{0.30}\text{Al}_{0.70}\text{N}$. Another interesting result can be seen in the Ti-rich compositions at lower temperatures. The resulting ground state structures are predicted to be not completely phase separated but rather a form of superstructure ordering, built of alternating Ti-Ti and Al-Al bi-layers along the 111-direction also considered and called "dL11" above. This is the result of the competing interactions on the first two coordination shell that have different signs. The finding of such structures as the equilibrium phase is a result of the simulations where

AlN-rich phases are poorly described with the used ECI's. However their appearance show that this type of ordering is low in energy and configurational patterns related to them could be considered as possible metastable states since they can be formed from a disordered matrix with only short range diffusion of atoms. In contrast, the formation of homogenous c-AlN clusters requires long range diffusion of a large amount of Al atoms. In order to investigate the possibility of super-structure formation we have calculated the total energy of multi-layered superstructures ordered both in the [111] and [001] crystallographic directions with different numbers of layers, the results shown in Fig. 4.14. Two conclusions can be drawn from these results. Firstly, [111] oriented structures are energetically favoured over [001] oriented structures. Secondly, the double layer [111]-structure reduces the mixing enthalpy by more than 60% compared to a random distribution modelled with a SQS-structure, but thicker multi-layers changes the energy only slightly, -13 meV/f.u. from double to quadruple layers. This indicates that if such layered superstructures would be formed, the driving force for complete phase separation would be significantly weakened and a large amount of long range atomic diffusion with limited energetic driving force would be required to perform it.

Thus this kind of structural pattern might be considered as metastable, especially in large coherent grains where incomplete volume relaxation limits the energy gain by complete phase separation. At the end of the day also completely phase separated Ti(Al)N+c-AlN systems are only metastable with respect to formation of h-AlN.

What is interesting is to know if a certain configuration or phase can be reached through any synthesis route, and if there are specific experimental conditions under which they can persist. From the present results one is led to the conclusion that such superstructures should be looked for in samples with low to medium AlN content, rather large grains and that has been subject only to a short post-growth annealing at a temperature just enough for the onset of bulk diffusion.

With these preliminary results and with certain important questions raised rather than answered we turn to another important hard coatings material system.

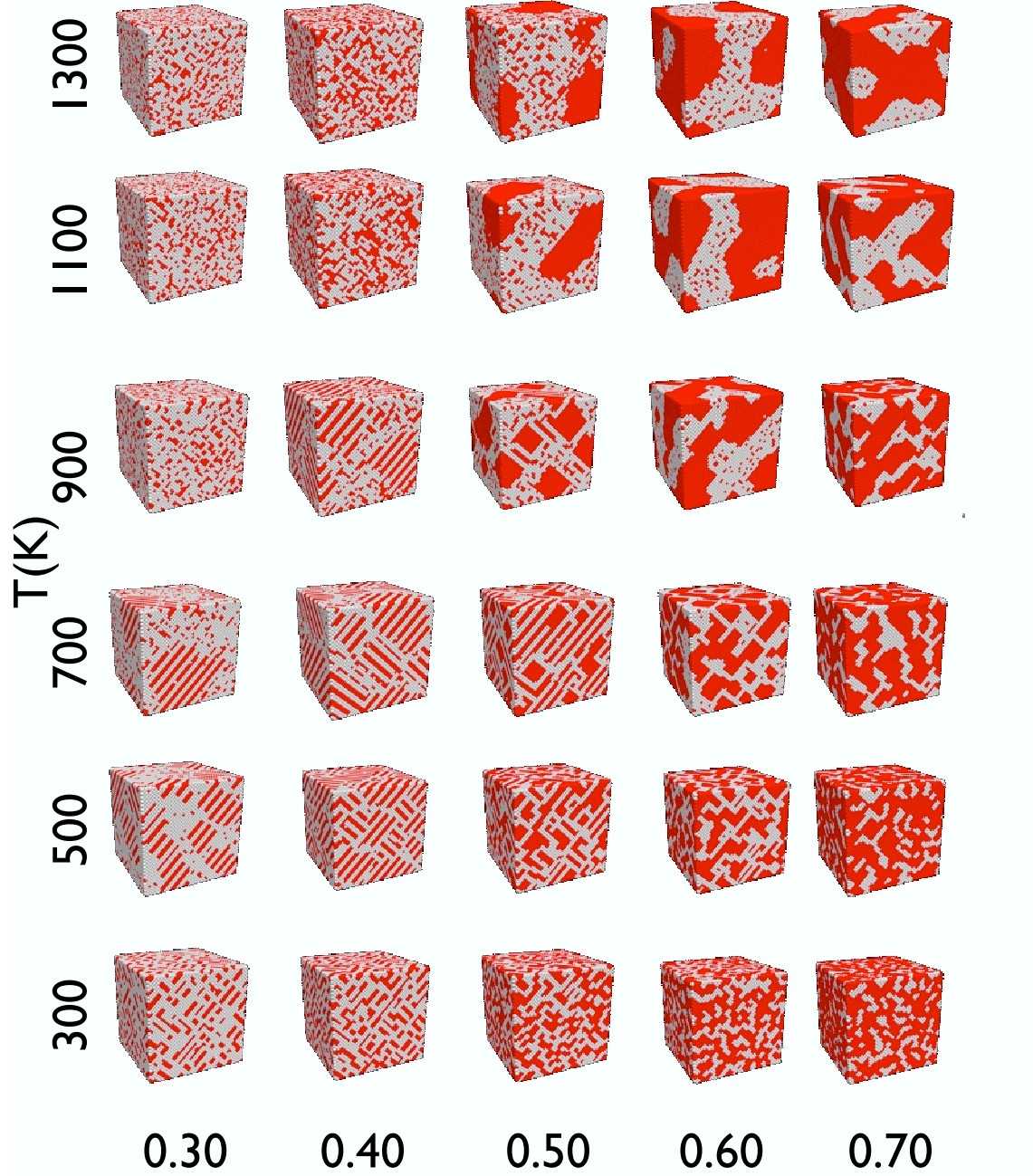


Figure 4.13: The resulting atomic configurations after a simulated annealing at different temperatures of $c\text{-Ti}_{1-x}\text{Al}_x\text{N}$ systems ($x=0.30, 0.40, 0.50, 0.60$, and 0.70 on the x-axis) using a Monte Carlo procedure and the effective cluster interactions derived with the SGPM-ISM method.

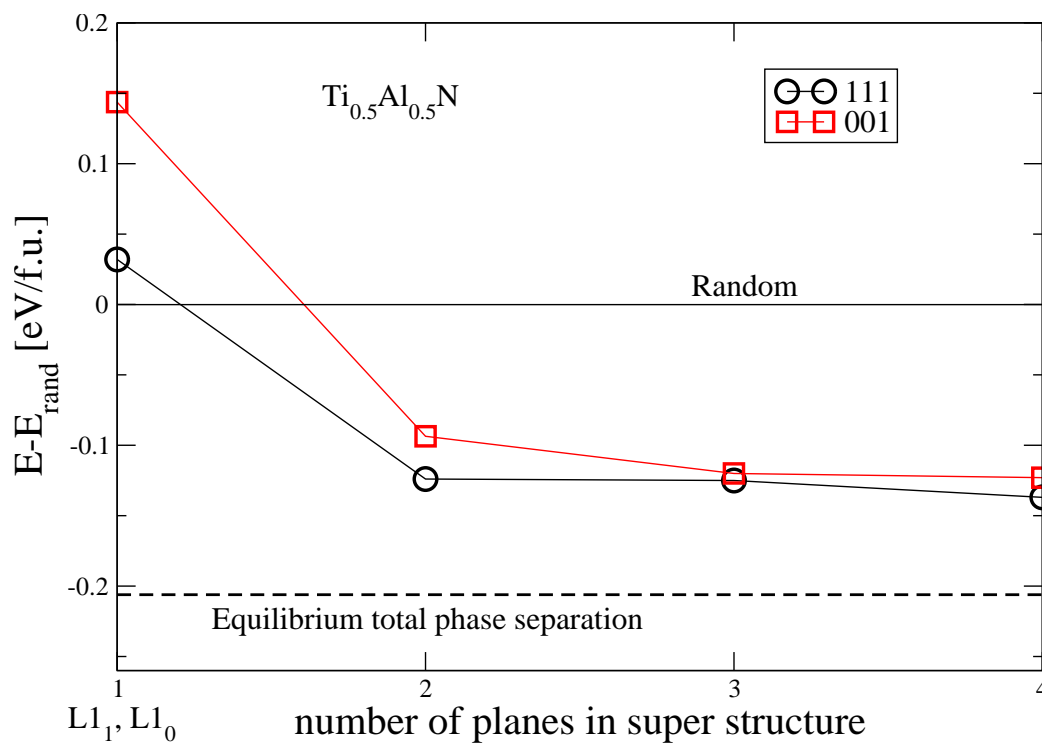


Figure 4.14: Total energy of layered superstructures in $Ti_{0.5}Al_{0.5}N$. Shown is the energy of [111] and [001]-stacking sequences as a function of the number of sequential Ti(Al) layers. The energy of fully relaxed, phase separated TiN and c-AlN is shown for comparison.

Chapter 5

$\text{Cr}_{1-x}\text{Al}_x\text{N}$ - the effect of magnetism

In this chapter the $\text{Cr}_{1-x}\text{Al}_x\text{N}$ system is investigated theoretically using the KKR-ASA-CPA-ISM method as described above. Similar topics as in the previous $\text{Ti}_{1-x}\text{Al}_x\text{N}$ chapter are covered such as the electronic structure and mixing enthalpies. However an important difference between $\text{Cr}_{1-x}\text{Al}_x\text{N}$ and $\text{Ti}_{1-x}\text{Al}_x\text{N}$ is that the former displays a magnetic behaviour. This chapter starts with an investigation of the magnetic structure of $\text{Cr}_{1-x}\text{Al}_x\text{N}$, continues with a discussion of the electronic structure and mixing enthalpy and ends with a discussion about the possible effects of strong electron correlation on the properties of the system.

5.1 Magnetic structure of $\text{Cr}_{1-x}\text{Al}_x\text{N}$

The magnetic ground state of orthorhombic CrN with $\alpha = 88.23^\circ$ has a double-layer antiferromagnetic configuration. However, since the main purpose of this work is to investigate materials of relevance for operations at room temperature and above, the B1 phase present above T_N is studied. This structure has also been shown to be possible to stabilise epitaxially at lower temperatures [15,16]. We are not aware of any experiments which show the magnetic ordering transition for epitaxially stabilised B1 structure CrN. In Ref. [149] DFT calculations carried out for B1 CrN found the single layer [110]-oriented antiferromagnet to be lower in energy than both the double layer [110], single layer [111] and the ferromagnetic configuration. The single layer [110] ordering in the B1 structure is equivalent to the [001] layered antiferromagnet considered in this work. Also considered here is the ferromagnetic state, the non-magnetic state as well as a disordered magnetic state modelled with the disordered local moments (DLM) method as described Chapter 2.3.2.

The calculated equations of state (EOS) curves for the four different configurations of pure CrN considered are shown in Fig. 5.1. Since the main subject of this work is to describe the properties of $\text{Cr}_{1-x}\text{Al}_x\text{N}$ at elevated temperatures above the Néel temperature, the electronic structure in those cases must be calculated for a disordered magnetic structure. It has been proven [150,151] that the DLM model, rather than an ordered magnetic configuration, should be used to accurately calculate thermodynamic properties of magnetic materials with finite local moments above the ordering temperature. It was suggested that CrN has localized moments on the Cr sites [149]. It will be apparent

from this work that the magnetic degree of freedom, also above the ordering temperature, is crucial to understand the thermodynamics of chemical mixing in $\text{Cr}_{1-x}\text{Al}_x\text{N}$. The DLM approximation uses the CPA to model a system with randomly oriented local magnetic moments. Thus it is a model which allows one to simulate the alloy energetics in the paramagnetic state.

Fig. 5.1 shows that the antiferromagnetic configuration is the lowest in energy among those considered in this work. This result is in agreement with previous calculations on the CrN system [149]. The calculated lattice parameter is 4.196 Å, in good agreement with the experimental one 4.162 Å [15]. While the ferromagnetic and the non-magnetic configurations are considerably above the antiferromagnetic configuration in energy, the DLM solution is only 15 meV per Cr atom higher than the latter. This indicates a stability of the local magnetic moments at the Cr-sites while the ordering between them is rather weak. The local moments at Cr-sites are $2.20 \mu_B$, $2.32 \mu_B$ and $2.19 \mu_B$ in the antiferromagnetic, DLM and ferromagnetic cases respectively.

Before considering the development of the magnetic properties with concentration, we note that the local relaxation energies in the $\text{Cr}_{1-x}\text{Al}_x\text{N}$ system are considerably smaller than in the system $\text{Ti}_{1-x}\text{Al}_x\text{N}$ reflecting the smaller difference in equilibrium metal-nitrogen bond length between the components but possibly also a difference in electronic structure to be considered below. In DLM $\text{Cr}_{0.50}\text{Al}_{0.50}\text{N}$ the local relaxation energy is 0.022 eV/f.u. compared to 0.100 eV/f.u. in $\text{Ti}_{0.50}\text{Al}_{0.50}\text{N}$ as discussed above.

Fig. 5.2 shows the magnetization energy as a function of AlN content. The figure shows the difference in energy between the three different magnetic configurations and the non-magnetic solution expressed in eV per Cr atom. The inset shows a magnification of the energy difference between the [001] ordered antiferromagnetic configuration and the DLM solution (in eV per Cr-atom). Since cubic AlN is a non-magnetic semiconductor the energy differences *per formula unit* goes to zero as x in $\text{Cr}_{1-x}\text{Al}_x\text{N}$ approaches 1, i.e. when the Cr atoms are more and more diluted. However, to understand thermodynamic properties, such as mixing enthalpy or magnetic ordering energies, it is important to consider magnetisation energies *per Cr-atom* as is shown in the main plot of Fig. 5.2. One can see that the driving force for magnetisation of the Cr atoms increases with increasing Al content. At the same time, as can be seen in the inset, the difference between the antiferromagnetic and the DLM configuration decreases. At the AlN-concentration of 20% the DLM solution becomes lower in energy than the [001]-oriented antiferromagnetic configuration. This indicates that there should exist another antiferromagnetic-configuration that becomes the ground state at higher AlN content. However in systems with chemical disorder such as $\text{Cr}_{1-x}\text{Al}_x\text{N}$ one can expect strong effects of the local environment on the orientation of the local magnetic moments [152,153]. A complete ground-state search for the low-temperature magnetic order in $\text{Cr}_{1-x}\text{Al}_x\text{N}$ is beyond the subject of this work since it is focused on high temperature applications. In the Cr-poor regime, where the Cr-atoms are quite far away from each other, the different magnetic configurations, including the ferromagnetic one, approach each other in terms of magnetization energy per Cr-atom. At the same time the magnitude of the magnetisation energy increases rapidly. It is obvious that the system, regardless of AlN-content (except the endpoint $x=1$) needs to be treated within a framework that allows for the spin polarisation of the Cr-atoms. From this point forward, the results of the calculations carried out for the DLM model are reported except when otherwise is

explicitly specified.

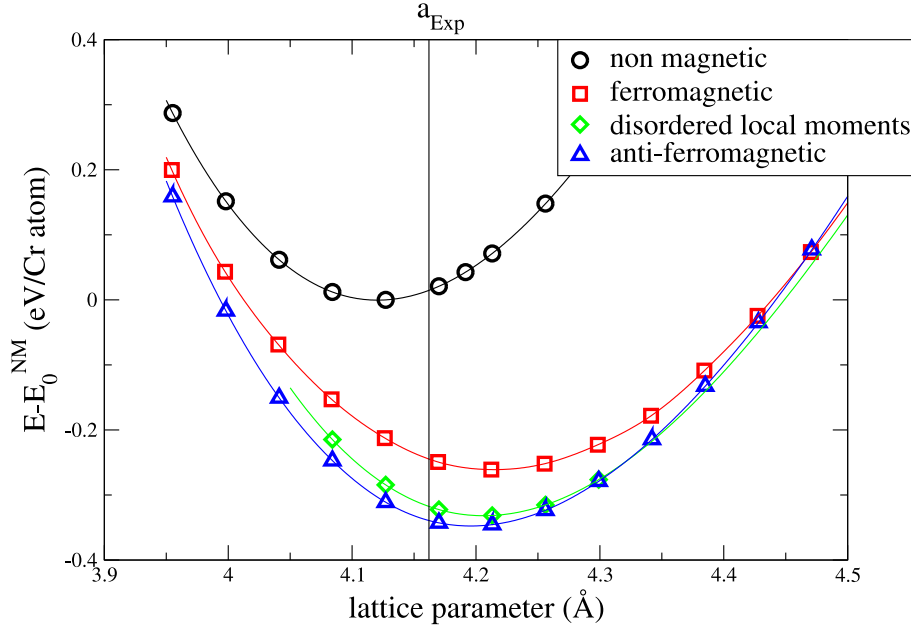


Figure 5.1: Equation of states for four different magnetic configurations of B1 CrN. A [001]-stacked antiferromagnetic configuration (triangles), a configuration with disordered local moments (diamonds), a ferromagnetic configuration (squares), and a nonmagnetic solution (circles) are shown. Energies are given relative to the minimum energy for the nonmagnetic solution E_0^{NM} . The experimental lattice parameter [15] is shown by a vertical line.

5.2 Electronic structure

Fig. 5.3 shows the $\text{Cr}_{1-x}\text{Al}_x\text{N}$ total density of states (DOS) for the valence band at five different compositions, $x = 0.00, 0.25, 0.50, 0.75, 1.00$, as a function of energy relative to the Fermi level. For clarity the curves of composition $x = 0.25, 0.50, 0.75$ and 1.00 are shifted by 1.5, 3.0, 4.5 and 6.0 states/eV respectively. Total DOS for the spin up and spin down channels are the same since the magnetic moments are randomly distributed up and down with equal probability. It should be noted that even though the spin channels are globally degenerate this does not mean that there is no magnetism in the system, since there is a local magnetic splitting of spin up and down electrons at each Cr-atom. The latter effect is shown in Fig. 5.4.

The DOS of pure CrN, i.e. $x = 0.00$, is shown as the bottom plot in Fig. 5.3. The state positioned at about -15 eV is the N-2s semi-core state that does not participate significantly in the bonding in the system. From about -8 eV to about -3 eV there is a two-peak bonding state which is formed due to the hybridization between the 3d and 2p states of nearest neighbor Cr and N atoms, respectively. A pseudo-gap separates the bonding states from the so called non-bonding states. They consist of Cr 3d states with t_{2g} symmetry that, opposite to the 3d states with e_g symmetry cannot hybridise strongly with the N-2p states. However, they form a weak hybridisation with next-nearest neighbouring Cr states of the same symmetry. If we do not count the N-2s electrons there are nine valence electrons per unit cell in CrN (3 N + 6 Cr). Six

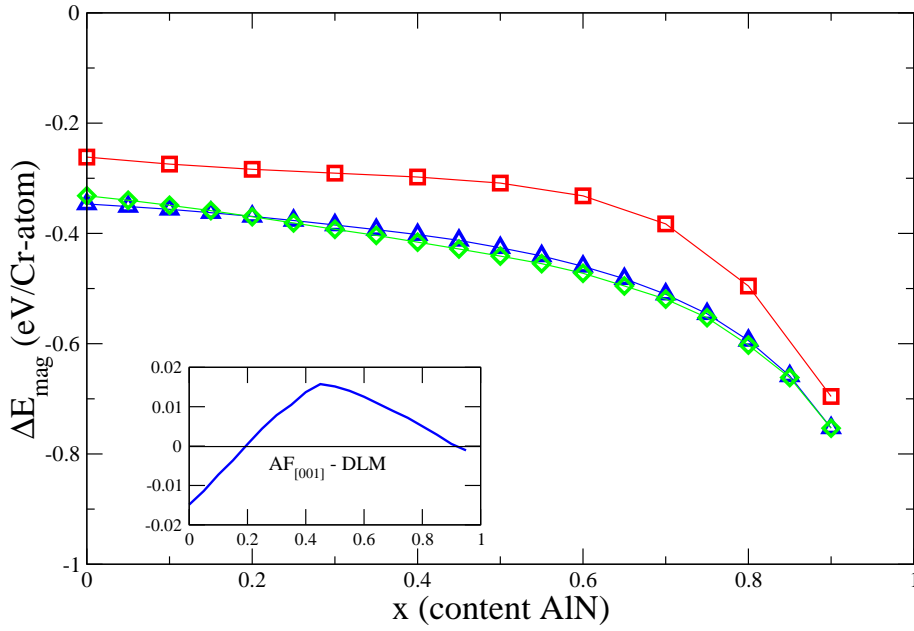


Figure 5.2: The magnetization energy $E-E_0^{\text{NM}}$ per Cr atom (in eV per Cr atom) as a function of AlN content in $\text{Cr}_{1-x}\text{Al}_x\text{N}$. As the content of AlN increases, the magnitude of the magnetization energy of the Cr atoms increases which underlines the importance of a magnetic treatment also in the Cr-poor regime. Inset: The total energy difference per Cr atom between the antiferromagnetic [001] ordered state and the disordered local moments solution (in eV per Cr atom).

electrons can be fitted in the bonding Cr-N states while the remaining three have to be accommodated in the non-bonding Cr-states that could hold six electrons in total. If there had been no magnetism in the system, the Fermi level should be located almost at the maximum of the non-bonding peak. This indicates that the Stoner criteria is fulfilled, resulting in a magnetic splitting. One can clearly see this effect in Fig. 5.4 where the density of states at the Cr-site is shown for pure CrN (solid line) and $\text{Cr}_{0.25}\text{Al}_{0.75}\text{N}$ (dashed line). The Cr majority spin (in the local magnetic framework) non-bonding states are almost entirely filled (-2 to 0 eV) and there is only a small overlap with minority spin non-bonding and majority spin antibonding (0 to 2 eV) states. The hump at about 4 eV corresponds to minority spin antibonding states. The bonding states (-8 to -3 eV) show a negligible magnetic split.

The obvious effect when Al is added to the system is that the Cr-states gradually decrease in intensity. The hybridization between Cr 3d and N-2p states is reduced and the ionic bonding between Al-3p and N-2p becomes more dominant. More interestingly the Cr-Cr next-nearest neighbor hybridization is weakened, resulting in a transformation of the non-bonding Cr-3d states into atomic-like impurity states which can be seen both in Fig. 5.3 and Fig. 5.4.

However, in contrast to the system $\text{Ti}_{1-x}\text{Al}_x\text{N}$, where the formation of such a sharp state leads to a drastic increase of the Ti site-projected DOS at the Fermi level as seen in the previous chapter, the opposite effect happens in $\text{Cr}_{1-x}\text{Al}_x\text{N}$. The magnetic splitting of the non-bonding state leads to a situation where the non-bonding spin up state becomes more and more occupied approaching the maximum of three electrons while the spin down counterpart is pushed above the Fermi level. Thus the Fermi level is shifted

down the slope of the majority spin state as Cr-Cr hybridisation decreases and with high enough Al content the system shows semiconducting behaviour. In the $\text{Ti}_{1-x}\text{Al}_x\text{N}$ -case the system stays non-magnetic over the whole concentration range, possibly with the exception of a minimal splitting in the extreme case of a single Ti-impurity in semiconducting AlN. This is so since in $\text{Ti}_{1-x}\text{Al}_x\text{N}$ there is only one electron per Ti-atom that needs to be accommodated by the non-bonding states. Regardless if this state is magnetically split or not, the Fermi level falls onto the peak, minimising the energy which could be gained due to magnetization. Pure B1 AlN is predicted within the KKR-ASA framework to be a semiconductor with a band gap of about 3 eV. Both concentration dependent trends and the relative intensity of different peaks of the calculated DOS of $\text{Cr}_{1-x}\text{Al}_x\text{N}$ show reasonable agreement with the X-ray photoelectron spectroscopy experiments in Ref. [16].

In summary, the electronic structure effects, that destabilise AlN rich $\text{Ti}_{1-x}\text{Al}_x\text{N}$ is absent in the case of $\text{Cr}_{1-x}\text{Al}_x\text{N}$ due to the magnetic split of the non-bonding Cr-3d states. The consequences for the mixing enthalpies will be apparent in the next section.

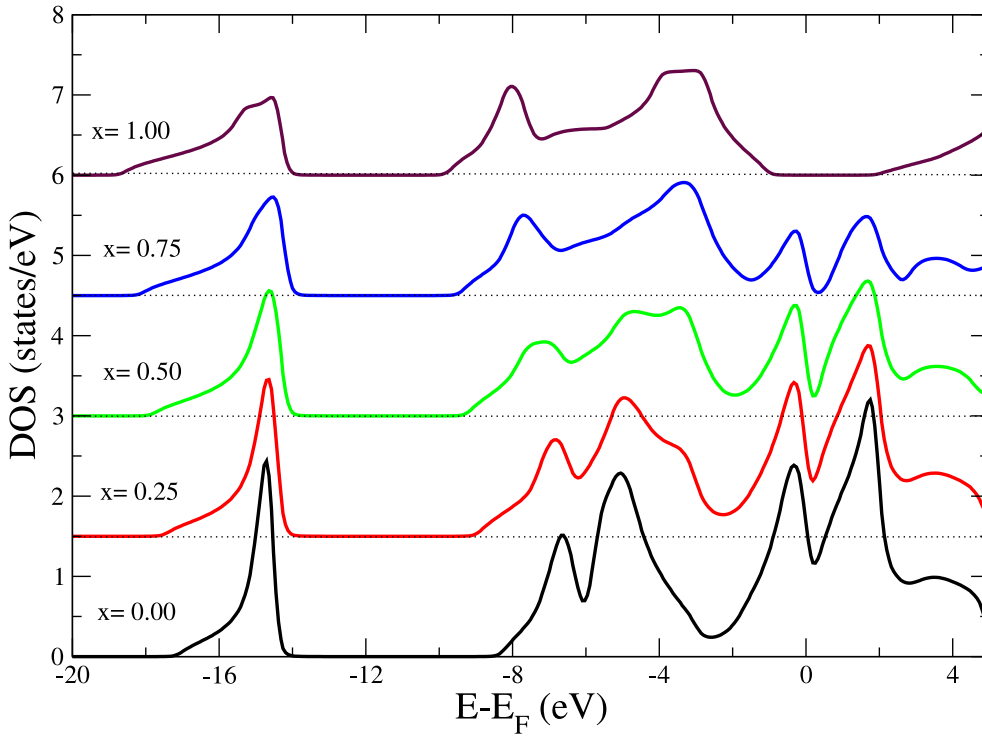


Figure 5.3: The total density of states for five different compositions of $\text{Cr}_{1-x}\text{Al}_x\text{N}$ calculated within the disordered local moment model. For clarity the curves, $x=0.25, 0.50, 0.75$, and 1.00 , are shifted up by $1.5, 3.0, 4.5$, and 6.0 states/eV, respectively. The magnetic split of the Cr 3d non-bonding state is clearly seen at the Fermi level.

5.3 Thermodynamics

The isostructural mixing enthalpy

$$H(x) = E(\text{Cr}_{1-x}\text{Al}_x\text{N}) - (1-x)E(\text{CrN}) - xE(\text{c-AlN}), \quad (5.1)$$

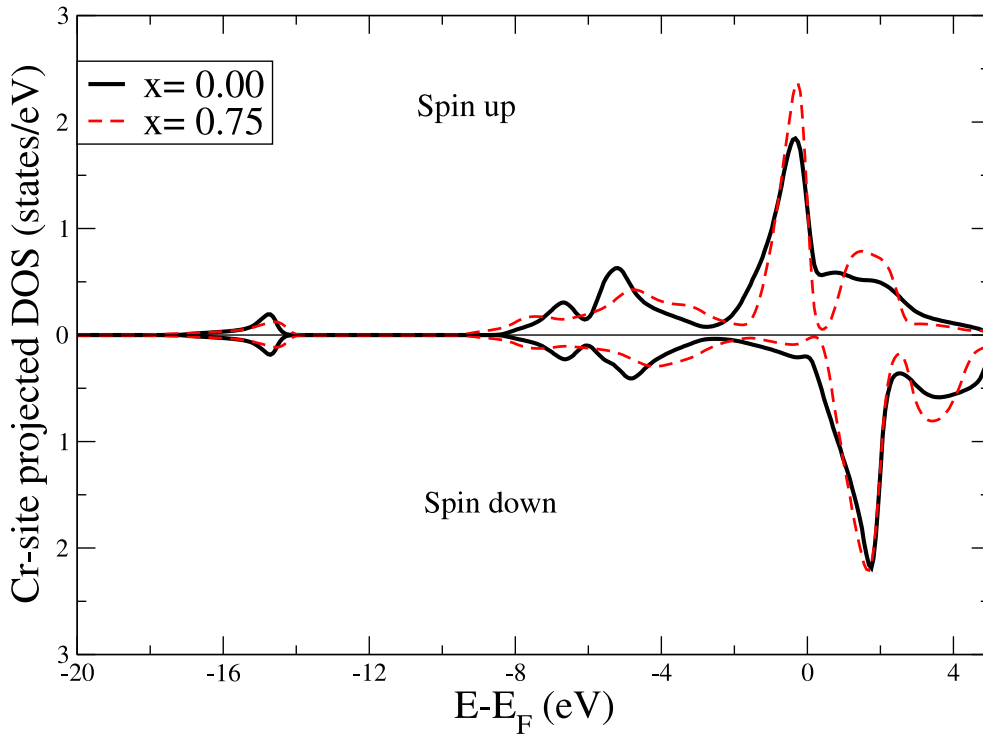


Figure 5.4: The spin polarized site projected DOS at the Cr site for CrN (solid line) and $\text{Cr}_{0.25}\text{Al}_{0.75}\text{N}$ (dashed line), calculated within the DLM model.

has been calculated for $\text{Cr}_{1-x}\text{Al}_x\text{N}$ with concentration steps of $x = 0.05$. The energies are taken for the calculated equilibrium volume for each specific concentration, thus setting the PV-term of the enthalpies to zero. This gives a total of 21 points on the mixing enthalpy curve. The magnetic state relevant for thin film growth and applications at elevated temperatures is the DLM state as has been shown in the first section of this chapter. It has been shown [150,151] that the mixing enthalpies calculated for the ordered and disordered magnetic states can differ qualitatively. However, also a non-magnetic calculation gives qualitatively different results compared to the DLM description of the paramagnetic phase of $\text{Cr}_{1-x}\text{Al}_x\text{N}$ as can be seen in Fig. 5.5. The figure shows the mixing enthalpy calculated for the DLM state and the non-magnetic state of $\text{Cr}_{1-x}\text{Al}_x\text{N}$ in eV per formula unit as a function of AlN content. The mixing enthalpy calculated for the DLM state is very symmetric with respect to equiatomic composition with its maximum 0.074 eV/f.u. at about $x=0.50$. On the other hand, the mixing enthalpy of the non-magnetic system shows a non-symmetric curve shifted to the AlN-rich side and with a maximum of 0.130 eV/f.u. The difference underlines that only a model that allows for disordered magnetism, like the DLM, could be used to accurately calculate the thermodynamic properties of $\text{Cr}_{1-x}\text{Al}_x\text{N}$ at relevant temperatures. It should be noted again that the ground state structure of AlN is wurtzite. The structural energy difference between B1 (cubic rock-salt) and B4 (hexagonal Wurtzite) AlN is 0.338 eV/f.u. This indicates that at almost all temperatures and fractions of AlN, the cubic mixture can at the most be metastable, which however is sufficient for a successful use of $\text{Cr}_{1-x}\text{Al}_x\text{N}$ in hard coatings applications.

Fig. 5.6 shows a comparison between the mixing enthalpies of $\text{Cr}_{1-x}\text{Al}_x\text{N}$ (bold dashed line) and $\text{Ti}_{1-x}\text{Al}_x\text{N}$ (bold solid line) as well as their second concentration derivatives

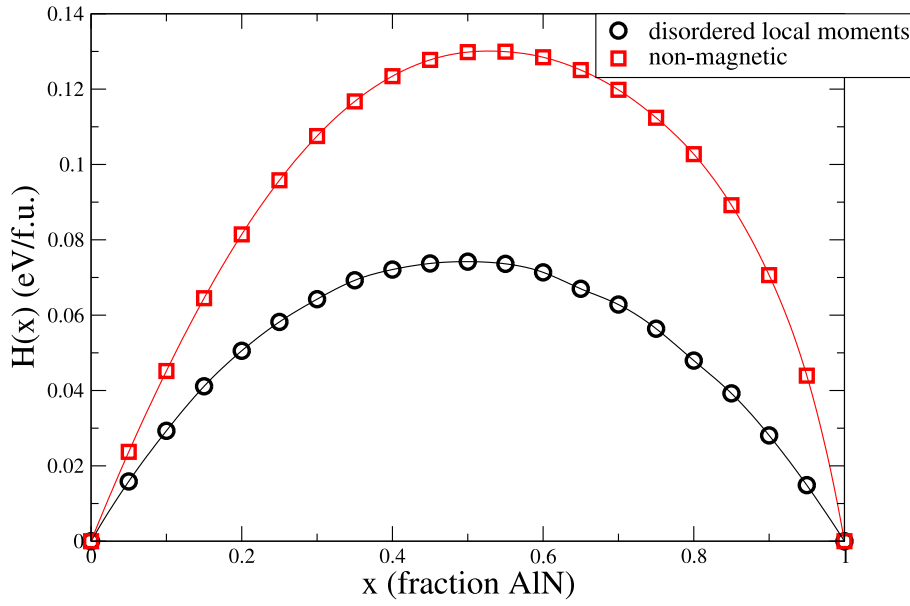


Figure 5.5: The isostructural mixing enthalpy of $\text{Cr}_{1-x}\text{Al}_x\text{N}$ calculated for a non-magnetic (squares) and disordered magnetic (circles) state.

($\text{Cr}_{1-x}\text{Al}_x\text{N}$: thin dashed line, $\text{Ti}_{1-x}\text{Al}_x\text{N}$: thin solid line). As seen in Fig. 5.6 there are both striking qualitative and quantitative differences between the mixing enthalpies of the $\text{Cr}_{1-x}\text{Al}_x\text{N}$ and the $\text{Ti}_{1-x}\text{Al}_x\text{N}$ systems. Firstly the mixing enthalpy of $\text{Ti}_{1-x}\text{Al}_x\text{N}$ is about two to three times larger than that of $\text{Cr}_{1-x}\text{Al}_x\text{N}$ for all concentrations except for the regime with very low fraction of AlN. Secondly the shape of the $\text{Ti}_{1-x}\text{Al}_x\text{N}$ enthalpy curve is highly asymmetric in contrast to $\text{Cr}_{1-x}\text{Al}_x\text{N}$ which shows a very symmetric behaviour with respect to equal fractions of CrN and AlN. This difference becomes more striking when considering the second concentration derivative. While the second derivative of the $\text{Cr}_{1-x}\text{Al}_x\text{N}$ -curve shows a smooth parabola, the second derivative of $\text{Ti}_{1-x}\text{Al}_x\text{N}$ -curve goes to very large negative numbers as the content of AlN increases above $x=0.50$. The latter is a direct result of the electronic structure variations with alloy composition, as described above. Indeed an atomic like Ti-d state is formed at the Fermi level at high AlN-content while there is no such counterpart in the Cr-case due to the magnetic splitting. Since the second concentration derivative of the free energy is directly related to the tendency for a mixture to decompose through the spontaneous spinodal mechanism, the results shown in Fig. 5.6 can be used to predict the hypothetical 0 K limit of regions of metastability and instability in the systems. More importantly it is the starting-point for finite temperature predictions.

A first approximation for the entropy contribution to the alloy free energy is the mean field approximation used above for $\text{Ti}_{1-x}\text{Al}_x\text{N}$. If the same approximation is applied to the $\text{Cr}_{1-x}\text{Al}_x\text{N}$ system the spinodal region at 1000 °C would be from $x=0.23$ to $x=0.70$. However those numbers should be taken as an upper limit of the extent of the spinodal region since the mean field approximation is known to generally overestimate transition temperatures and that vibrational entropy and strain effects are not considered. In any case, coatings with medium or high AlN content, which have large potential for industrial applications, are predicted to show much weaker tendency towards decomposition in $\text{Cr}_{1-x}\text{Al}_x\text{N}$ compared to $\text{Ti}_{1-x}\text{Al}_x\text{N}$. The unusual effect in $\text{Ti}_{1-x}\text{Al}_x\text{N}$, that

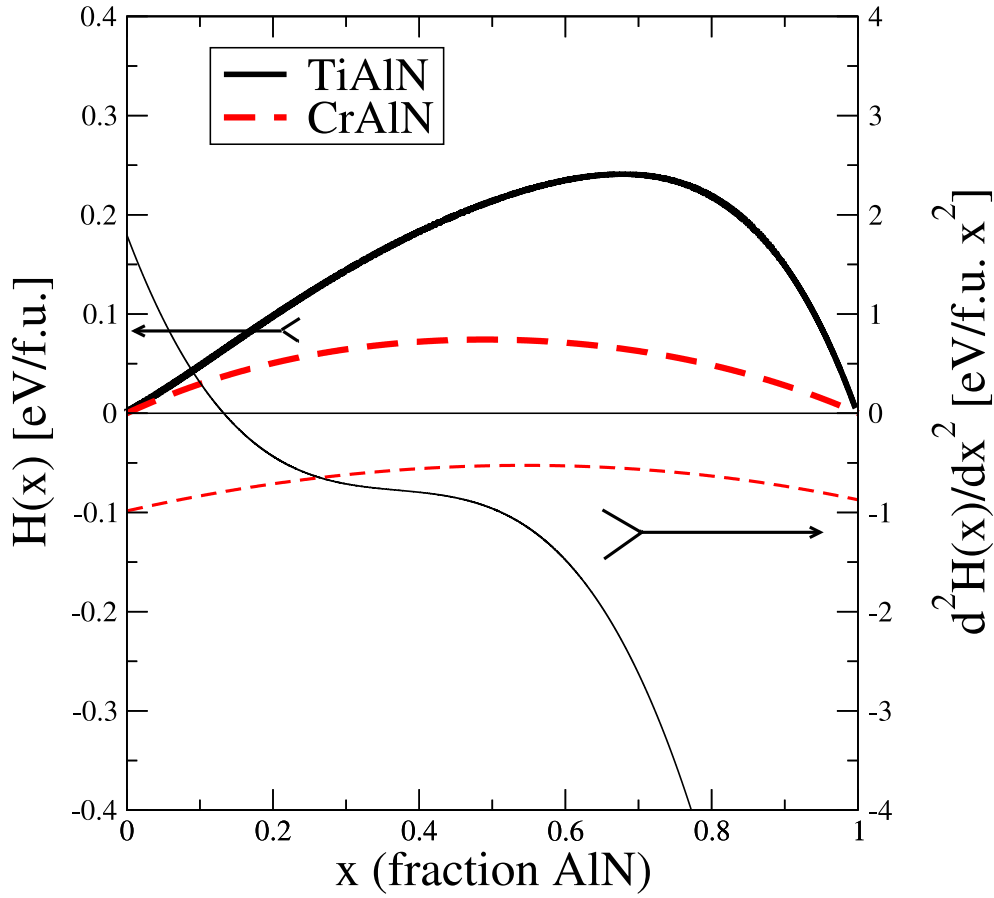


Figure 5.6: The spin polarized site projected DOS at the Cr site for CrN (solid line) and $\text{Cr}_{0.25}\text{Al}_{0.75}\text{N}$ (dashed line), calculated within the DLM model.

the endpoint of the isostructural decomposition are samples with regions of almost pure c-AlN, is absent in the case of $\text{Cr}_{1-x}\text{Al}_x\text{N}$. If isostructural decomposition anyway do occur in the latter system it should end with regions of Cr- or Al-enriched $\text{Cr}_{1-x}\text{Al}_x\text{N}$. Since the composition difference between such domains would be smaller and since the concentration dependence of the lattice parameter is rather weak, see Fig. 3.2, the strain fields induced by iso-structural decomposition in $\text{Cr}_{1-x}\text{Al}_x\text{N}$ are expected to be much weaker than in the $\text{Ti}_{1-x}\text{Al}_x\text{N}$ -system. Since such strains are thought to be the reason for the age hardening in the Ti containing system [32] we expect no, or a minimal, age hardening effect for the B1 structure of $\text{Cr}_{1-x}\text{Al}_x\text{N}$. On the other hand, at even higher temperatures where the strained domains of $\text{Ti}_{1-x}\text{Al}_x\text{N}$ are relaxed by the introduction of dislocations the loss of coherency leads to a drastic loss in hardness. In $\text{Cr}_{1-x}\text{Al}_x\text{N}$ coherency in the material should be able to survive higher temperatures.

Experimentally the thermal stability of the $\text{Cr}_{1-x}\text{Al}_x\text{N}$ has been explored in Refs. [37,38]. It was found that the single phase cubic B1 structure is obtained for samples with $x \leq 0.71$. Pure CrN starts to lose nitrogen already at 750°C but this process is shifted to higher temperatures, between 900 and 1000°C , with AlN fraction of 0.46 and 0.71 . This is likely to be connected to the larger affinity for Al to form nitrides as compared to Cr as was shown in calculations of the formation energies in chapter 3. However, even more relevant are the nitrogen vacancy formation energies that will be considered below. Above the nitrogen release temperature a series of phase transformations take

place, resulting in the formation of Cr_2N , bcc-Cr and hcp-Al(Cr)N. Below the nitrogen release temperature the B1 cubic phase is totally dominating, but in the coating with $x=0.71$ small amounts of hexagonal AlN nucleates already at temperatures below 800°C .

For the matter of comparison with the present study, the XRD-evidence of isostructural decomposition within the cubic phase present in the $\text{Ti}_{1-x}\text{Al}_x\text{N}$ system at temperatures between 600 and 950°C [26, 32], is absent in the case of $\text{Cr}_{1-x}\text{Al}_x\text{N}$. Also the age hardening effect seen at temperatures between 600 and 950°C in the $\text{Ti}_{1-x}\text{Al}_x\text{N}$ films is not seen in the B1 structured Cr-based coatings [37, 38] with the exception of one unexplained observation point in [37]. Instead it was suggested that nucleation and growth of h-AlN in grain boundaries at high temperatures as well as transformation from CrN to h- Cr_2N which is harder might have positive effects on the coatings during operation at high temperature [37, 38].

5.4 Beyond the LDA and GGA: Effects of strong electron correlation

Although the LDA and GGA approximations turn out to work very well for a large number of solid state systems there are also well known cases where they work less well. Such systems are typically transition metal oxides and f-electron systems, both with considerably localised states. Such bands are not very well described within the LDA since this approximation over-emphasises the minimisation of the kinetic energy and underestimates the on-site Coulomb interaction. Transition metal nitrides should in general be more weakly correlated and consequently better described by LDA and GGA calculations, which also were shown above c.f. Chapter 3. However, CrN is a border case with its half-filled non-bonding 3d-state. Epitaxial stabilised B1 CrN has been experimentally shown to be a semiconductor at low temperatures [15]. Zero temperature first-principles calculations of the ordered AFM magnetic state on the other hand shows an overlap of the spin up non-bonding and the combined spin down non-bonding and spin up anti-bonding states leading to a metallic behaviour [149], similar to the disordered situation discussed above. This discrepancy seems to be due to the result that the GGA calculations put the spin up non-bonding states at too high energies creating a small overlap with the spin down non-bonding states. For instance the DLM-calculations above put the peak of the spin up state at about -0.3 eV with respect to E_F while both the experiments in Ref. [15] and [16] measure this peak at about -1.0 eV. The reason for this discrepancy might be due to strong correlation effects for the rather localised non-bonding 3d-states in Cr. In order to test this hypothesis and explore possible influence of such effects on thermodynamic properties, calculations using the LDA+U and GGA+U frameworks are presented below. The LDA+U, and similarly GGA+U, are based on the method to replace the LDA (GGA) on-site electron-electron interaction of electrons in a state which is believed to be rather localised with a term described by a Hubbard type Hamiltonian as described in Chapter 2.2.3. One problem with this approach is that the parameter U can be seen as a fitting parameter to experimental values thus moving away from the first-principles idea. However such a procedure can be motivated in order to study qualitative effects before making the effort to deduce the U-value from complex theoretical schemes which is also possible in

principle. Note that in the following discussion the term U is used for the combined (U-J) term in Eq. 2.14.

First the effect of different choices of the value of the Hubbard- U parameter on the lattice spacing and electronic structure of CrN is presented, followed by calculations of magnetic energy differences and magnetic moments in this system. It is followed by the calculation of mixing enthalpies of two ordered CrAlN-compounds. The PAW method is used in this investigation and the magnetic state is modelled with antiferromagnetic ordered magnetic moments. This is so since the LDA+ U method is currently not implemented in the available KKR-ASA-CPA and EMT-CPA codes where the DLM magnetic state can be addressed. Further more the calculation of two ordered $Cr_{0.5}Al_{0.5}N$ compounds are not an attempt to model the energy of the random state. However this test is likely to revile if there are qualitative effects on the mixing energetics of the system when strong correlation is considered.

5.4.1 Lattice spacing

The value of the U -parameter influences the calculated equilibrium lattice spacing for AFM CrN as can be seen in Fig. 5.7. The experimental value of the so called relaxed lattice spacing of epitaxial B1 films of CrN at room temperature¹ 4.162 Å, is shown with a horizontal line. This is most likely slightly but not much higher, due to thermal expansion, as compared to the 0 K value of relevance for a direct comparison with the calculations. If the value of U was to be chosen in order to reproduce this value, a U between 4 and 5 eV should be chosen in a LDA+ U calculation and between 0 and 1 eV in a GGA+ U calculation. However, since on-site interactions are not the only reason why lattice spacings are slightly off target in GGA and LDA calculations, this would be an unsafe procedure. Instead, one can compare the calculated valence density of states with available experiments to see the effect of the U -parameter on the electronic structure directly.

5.4.2 Electronic structure

In Fig. 5.8 the calculated electronic DOS of CrN using the LDA+ U framework is presented. The chosen lattice spacing is the experimental value 4.162 Å. The calculations are performed for a series of values of U ranging from $U=0$ (pure LDA) to 6 eV. Also present in all pictures is the experimental valence band of CrN redrawn from Ref. [16]. Please note that these experimental values show a small gradual offset with decreasing energy and that they are given in arbitrary units. Comparison between the calculations and the experiments should be made with respect to peak positions rather than absolute intensities. In the case of $U=0$, that is pure LDA calculations, one can see that the calculation puts the spin up Cr-3d non-bonding state very close to the Fermi level. Actually even closer as compared to the GGA calculations at a slightly larger lattice spacing and using a disordered magnetic state shown in Fig. 5.3. The experimental value for this peak is about -1.0 eV in line also with the value in Ref. [15]. The bonding states presenting peaks at about -5 and -6.5 eV are better describing the experimental situation. As the value of U is increased the spin up Cr-3d non-bonding state is shifted down while

¹Room temperature is assumed since no other information of the XRD measurement is given in [15].

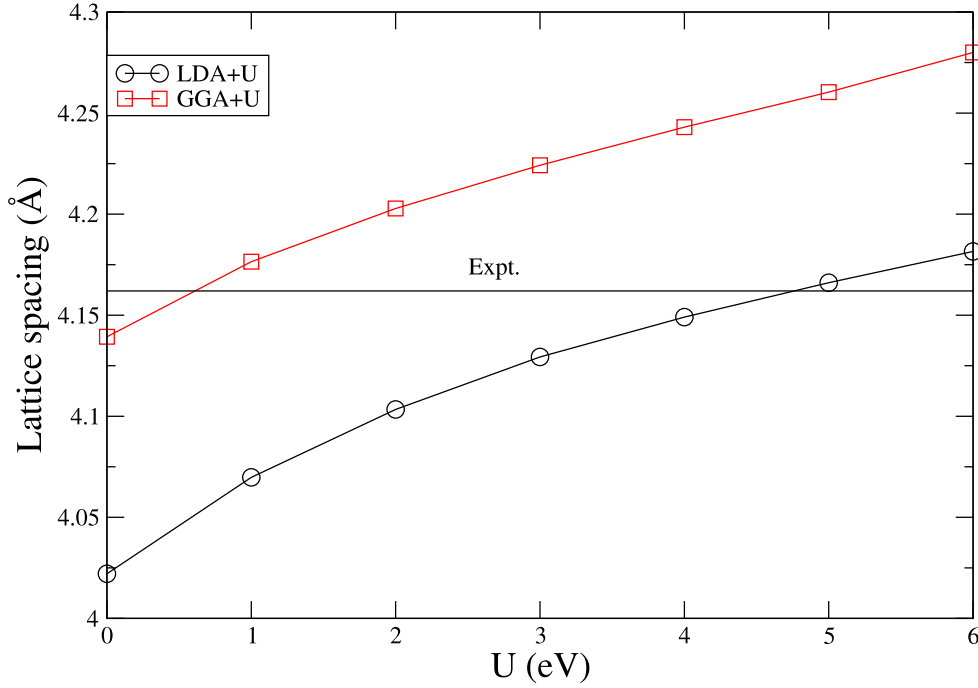


Figure 5.7: The calculated equilibrium lattice spacing of B1 001-AFM CrN using the LDA+U and GGA+U methods respectively. The horizontal line is the experimental results from Ref. [15].

the (largely) non-occupied spin down counterpart is shifted up above E_F . There is also a small shift upwards in energy relative E_F of the bonding states. At a value of $U=2-3$ the calculated DOS seems to be best describing the experimental values. At higher values of U the spin up non-bonding peak is present at too low values while the bonding states are too high. From this analysis it seems reasonable to perform calculations using the experimental lattice spacing together with the LDA+U method with the U parameter around 2-3. One can note that the calculations using $U=3$ still presents a non-zero but very small DOS at E_F while $U=4$ gives semiconducting behaviour in line with Ref. [15].

5.4.3 Magnetism

The tendency for ordering of the Cr local moments in CrN is rather weak as shown by the quite low Néel temperature around 0°C [13]. Further more, in the epitaxially stabilised B1 structure no magnetic ordering has been observed at all [15,16]. The tendency for magnetic ordering can qualitatively be related to the energy difference between anti-ferromagnetic configurations and the ferromagnetic configuration of Cr moments. The left panel of Fig. 5.9 shows the energy difference between the AFM [001] order and the FM order calculated using LDA+U and the experimental lattice constant 4.162 Å for different values of U . The right panel shows the size of the total and local Cr-moments in FM and local Cr-moments in AFM CrN as function of U . The 001-oriented AFM state is lower in energy as compared to the FM state regardless of U -value. With the introduction of a small value of U the energy difference first increases from -0.11 eV/Cr-atom to -0.16 eV/Cr-atom, but then it decreases again and at $U=3$ it is back at about -0.11 eV/f.u. At higher values of U the difference decreases further. This behaviour

can be understood by consideration of the size of the magnetic moments and the electronic structure. The magnetic moments increase with increasing U since the gradual localisation of the Cr-3d states makes the spin up non-bonding state more and more occupied on expense of the spin down non-bonding state. Larger absolute values of the spin polarisation is a definite factor in strengthening magnetic interactions. However, this localisation also gradually decrease the overlap of next nearest-neighbour Cr-atoms thus diminishing the coupling between Cr-moments. These competing processes leads to the energetic behaviour seen in the left panel of Fig. 5.9.

5.4.4 Mixing energy of ordered CrAlN compounds

Finally, to get an insight in whether or not strong electron correlations beyond LDA and GGA can influence the configurational thermodynamics of $\text{Cr}_{1-x}\text{Al}_x\text{N}$ the mixing energy of two ordered $\text{Cr}_{0.5}\text{Al}_{0.5}\text{N}$ phases, the $L1_0$ and $L1_1$ structures have been calculated in antiferromagnetic states corresponding to alternating up and down spins within the Cr planes (001 for $L1_0$ and 111 for $L1_1$). These calculations are done with the lattice spacing of 4.11 Å, which corresponds to a linear regression fit of the experimental $\text{Cr}_{1-x}\text{Al}_x\text{N}$ values in Ref.s. [16, 134]. As reference states the 001 ordered antiferromagnetic CrN and c-AlN at their respectively experimental lattice parameters have been used. The results of LDA+ U and GGA+ U calculations as a function of the U -parameter are presented in Fig. 5.10. The value of the mixing energy of these ordered structures decreases with increasing U . The mixing energy of the $L1_0$ phase, which is higher than the $L1_1$ -phase for all values of U decreases from 0.125 eV/f.u. in the LDA calculation (0.09 eV/f.u. with GGA) to about 0.05 eV/f.u. (0.055 eV/f.u. with GGA+ U) at the value $U=3$ eV concluded to be reasonable above. Interestingly, the mixing energy of the $L1_1$ -structure goes to negative values although with a small magnitude when U is above 1 eV both with LDA+ U and GGA+ U calculations. The latter fact is also true if all calculations are instead performed at the calculated equilibrium GGA+ U lattice spacings. This analysis indicates, although no direct quantitative conclusions regarding the magnetically and chemically disordered phases can be done, that the inclusion of strong electron correlation into the picture slightly decreases the mixing enthalpies in the cubic $\text{Cr}_{1-x}\text{Al}_x\text{N}$ system.

The reason for this effect, as well as the effect on the energy differences between AFM and FM magnetic ordering in pure CrN described above, can be understood from the development of the electronic structure when strong correlation is taken into account. A certain part of the rather weak isostructural decomposition tendency in the c- $\text{Cr}_{1-x}\text{Al}_x\text{N}$ system in the GGA calculations above arises from the cutting of the Cr-Cr next nearest neighbouring bonds when Al is introduced in the system. However, when the non-bonding states are further localised as U increases, this bond becomes weaker and weaker giving a lower effect on mixing properties.

Thus the important effect of magnetism observed above is likely to be further enhanced when the theoretical analysis goes beyond the LDA and GGA approximations for exchange and correlation effects, possibly leading to a situation where c- $\text{Cr}_{1-x}\text{Al}_x\text{N}$ alloys could have a very weak tendency towards short range order rather than clustering.

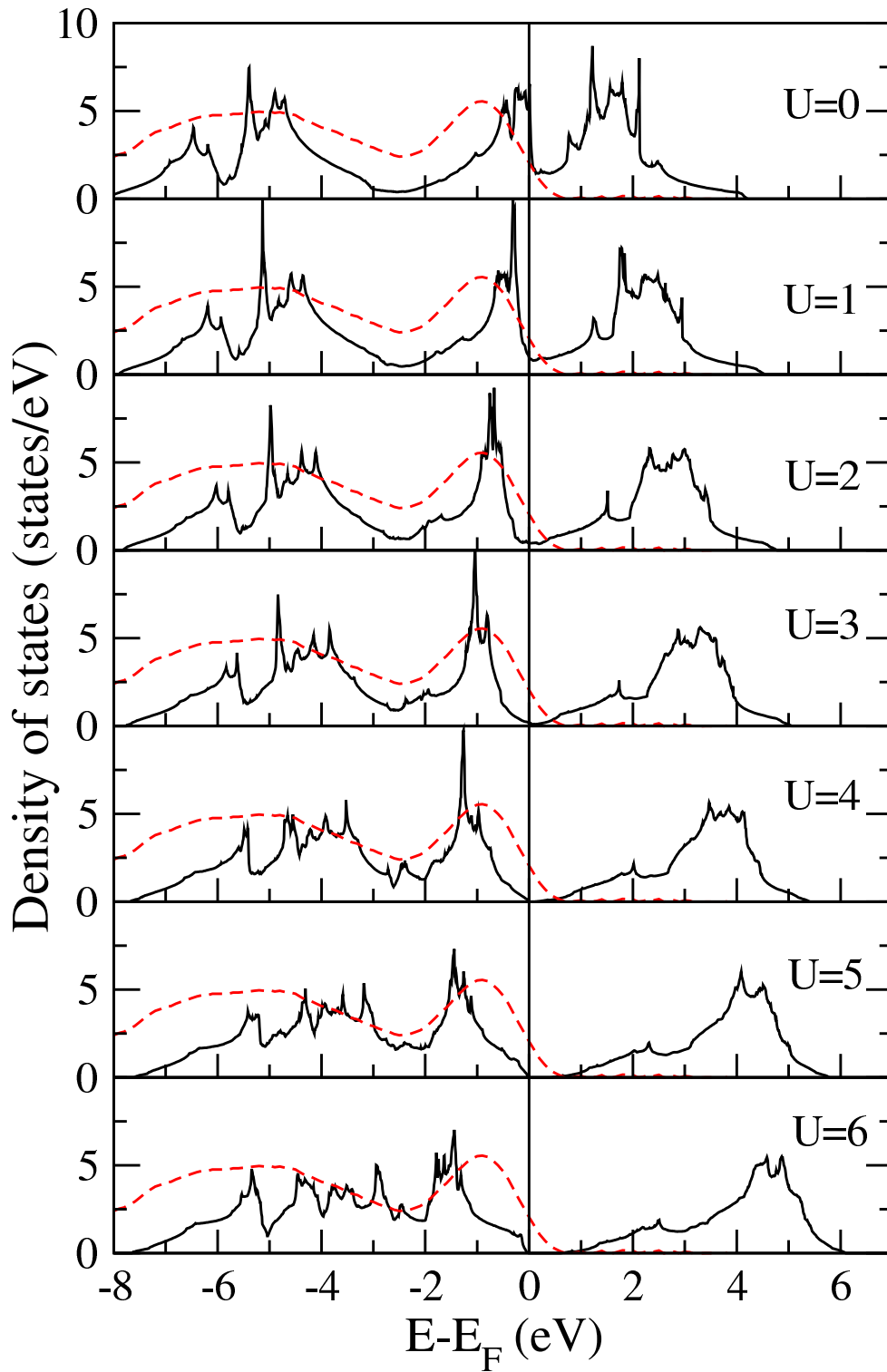


Figure 5.8: The electronic density of states of 001-oriented antiferromagnetic CrN as calculated with the LDA+U method for different values of U in eV (solid line). The experimental lattice spacing is used. For comparison the room temperature XPS-value redrawn from Ref. [16] is shown (dashed line).

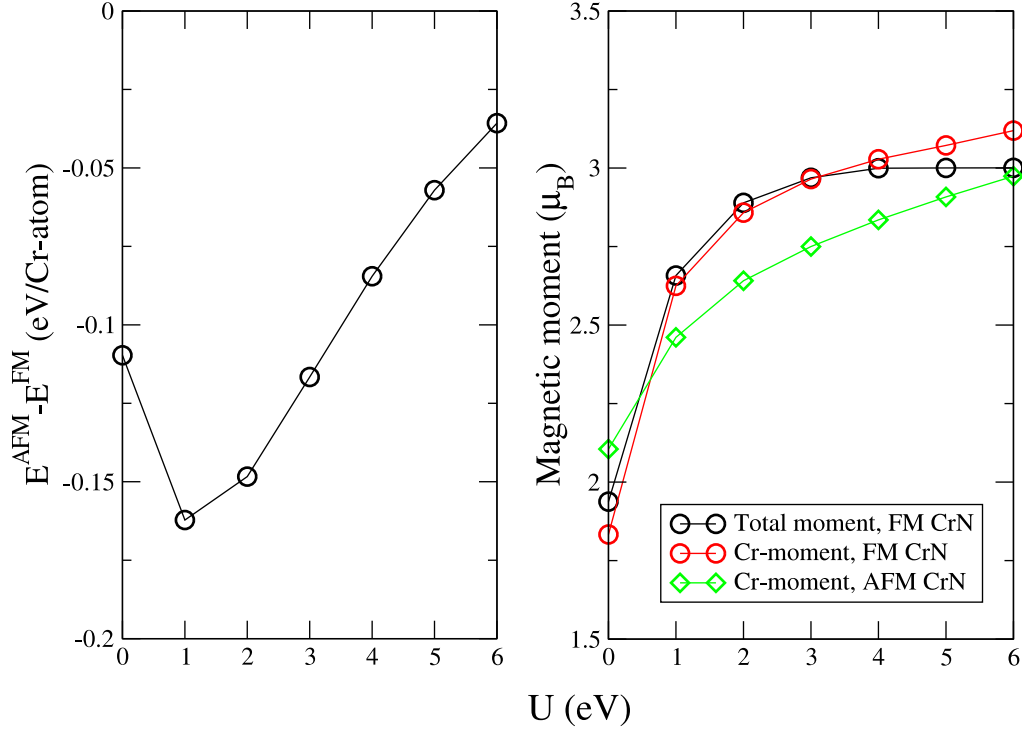


Figure 5.9: Left panel: The energy difference between 001-oriented AFM CrN and FM CrN as a function of U in the LDA+ U framework. Right panel: The magnetic moments of FM and AFM CrN as a function of U . Both total moment and local Cr-moments are shown for the FM configuration. Experimental value of the lattice spacing is used.

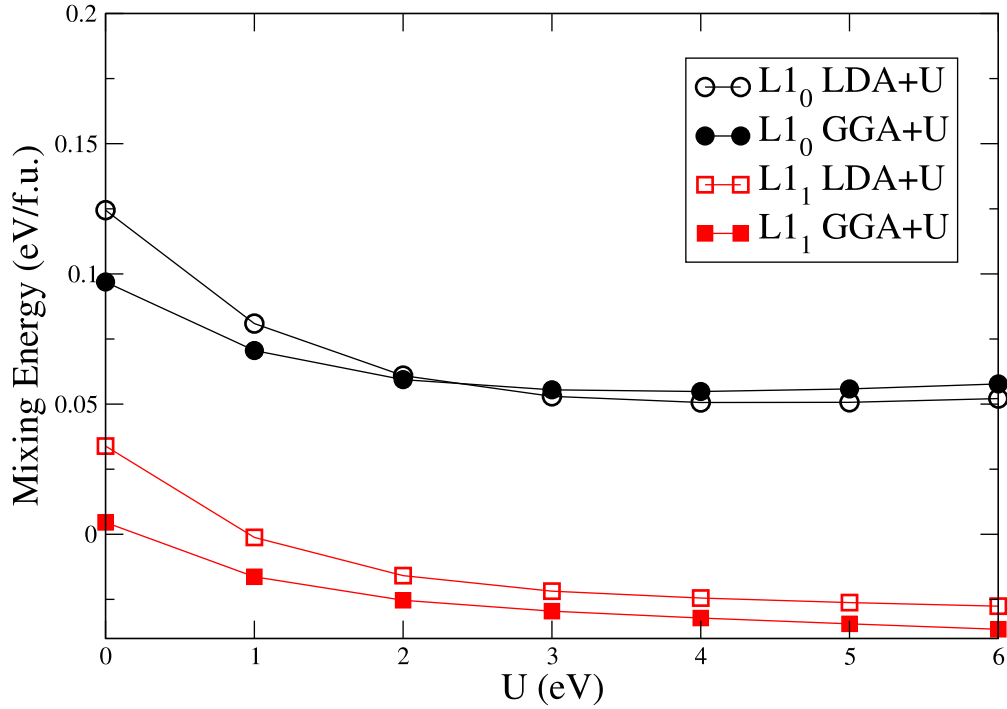


Figure 5.10: Calculated mixing energies of two ordered and antiferromagnetic $\text{Cr}_{0.5}\text{Al}_{0.5}\text{N}$ compounds with respect to antiferromagnetic CrN and c-AlN as a function of the value of U in the LDA+ U and GGA+ U approach. Experimental lattice parameters are used.

Chapter 6

Point defects and off-stoichiometry

In the previous chapters the investigation of various properties of $M_{1-x}Al_xN$ systems revealed the effects of choosing different transition metal nitrides as alloying material with AlN. In all calculations a perfect 1:1 stoichiometry between transition metal + aluminium and nitrogen has been assumed, as well as vacancy free sublattices. Although being a very reasonable starting point in those systems, since most experimental measurements indicates a metal to nitrogen ratio rather close to one, the possibility for a considerable deviation from this value, as well as the presence of vacancies and other point defects should be kept in mind. For instance, pure TiN_x is thermodynamically stable in the B1 structure for a substantial amount of nitrogen vacancies (V_N) up to a composition of $TiN_{0.67}$ ¹ at temperatures just above 1000 °C as can be seen in the phase diagram of Fig. 1.6. In non-equilibrium systems such as thin films the possible deviations from stoichiometry are likely to be larger compared to equilibrium situations. Furthermore the accuracy of the measurements of light element compositions using Rutherford backscattering spectroscopy (RBS) or elastic recoil detection analysis (ERDA) are often in the order of a few percent of the sublattice occupancy [15, 16, 46, 50] giving a small uncertainty to this degree of freedom in all experiments. Finally, even though it might be possible in principle to synthesize B1 structures with very close to 1:1 stoichiometry, it could be of interest to deliberately introduce off-stoichiometry, for instance by reducing the nitrogen pressure in the deposition chamber, in order to achieve certain effects. For instance nitrogen vacancies was suggested to increase hardness in Ref. [10]. In this chapter the energetics of nitrogen sub-stoichiometry is investigated. First the formation energies of nitrogen vacancies in the TiN, ScN, HfN, CrN and c-AlN binaries are studied. Then an investigation of the effect of local environment on the V_N energies in c- $Ti_{0.5}Al_{0.5}N$ is performed followed by a systematic study of the coupling between nitrogen sublattice occupancy and the tendency for isostructural coherent decomposition in the c- $Ti_{1-x}Al_xN_{1-y}$ system.

6.1 Vacancy formation energies in binary nitrides

The formation energy of a single nitrogen vacancy was calculated using the formula

¹This is the resulting sublattice occupation if the composition of 0.6 atomic parts Ti is balanced only with nitrogen vacancies which it is believed to be in this system.

$$E_f^{VN} = E^{def} - E^{ideal} + \frac{1}{2}E^{N_2} \quad (6.1)$$

where E^{def} is the energy of the supercell containing the defect, E^{ideal} is the supercell without defect and E^{N_2} is the energy of a nitrogen molecule in vacuum. The vacancy formation energy in the nitrides was calculated for the five binary nitrides TiN, ScN, HfN, c-AlN, and CrN using the PAW method. In the first four cases a supercell consisting of 3x3x3 conventional unitcells with 108 metal atoms and 107 nitrogen atoms was used. In the case of CrN, due to the increased computational cost due to magnetism, a supercell consisting of 2x2x2 conventional unit cells with 32 metal atoms and 31 nitrogen atoms was used. The effect of using a smaller supercell in this case is not expected to be large. In the case of the four other nitrides, the largest difference in E_f^{VN} between using a 215 atoms and a 63 atoms supercell was 0.28 eV (ScN). The values of the formation energies are tabulated in Tab. 6.1. The semiconductor c-AlN shows the clearly highest formation energy, 6.39 eV showing the high energy cost for braking the balance of valence in this system. It should be noted that charged defects, often present in semiconductors are not considered in this work. E_f^{VN} in HfN is calculated to 3.21 eV which is similar but not identical to the value in Ref. [84], 3.51 eV. The formation energies given in Ref. [84] are calculated using a less dense k-mesh and stated to be converged only to about 0.1 eV which possibly contributes to the difference with the present result. The value for ScN is lower, 2.87 eV. ScN is a zero bandgap semiconductor in the present calculations. In experiments the bandgap is measured to be larger 1.3 eV [154]. It is not clear if the formation energies of the nitrogen vacancies would change if a calculational procedure where used where the bandgap was reproduced correctly. However, it seems clear that the presence of unoccupied 3d non-bonding states at least reduces the formation energy of V_N in ScN with respect to the wide-bandgap semiconductor c-AlN.

In TiN E_f^{VN} is calculated to 2.41 eV which is identical to the value in Ref. [84]. E_f^{VN} in CrN, as calculated within the 001-oriented AFM magnetic state and the GGA equilibrium lattice parameter 4.14 Å, is considerably lower than in all the other systems, only 1.10 eV. If instead the calculation is done for the room temperature experimental lattice spacing 4.162 the value is not changed more than slightly: 1.17 eV. This is a clear indication that out of the systems considered in this work, CrN is the by far most likely candidate to start to lose nitrogen to the atmosphere or vacuum upon heat treatment. One should realise that the equation 6.1 is considering the 0K situation and that the gas phase will be much more favourable relative to the solid phase at finite temperatures due to entropy considerations. This prediction is clearly in line with the experimental reports of initiated nitrogen loss of CrN thin films and subsequent phase transformation to nitrogen poor phases, at temperatures around 800 °C [37]. Further more, by just comparing the values for E_f^{VN} in the binary nitrides in table 6.1 one can realise that the substitution of a part of the Cr atoms with Al forming CrAlN coatings is very likely to reduce this tendency, also in line with experimental reports [37].

All four transition metal nitrides considered here show a certain outward relaxation of the metal atoms neighbouring the vacancy. This is in line with what has been reported previously for TiN, ZrN and HfN [84]. In ScN, the Sc atoms closest to the vacancy position increase the distance from 2.26 Å, to 2.37 Å. In CrN the relaxations are smaller, the Cr atoms coordinating the vacancy increase their distance from this position from 2.07 Å to 2.09 Å. Once again, the small value is not due to the use of a smaller supercell since the

relaxation around the vacancy in ScN is very similar when calculated with the smaller cell. In c-AlN on the other hand, the introduction of a vacancy does not give rise to any considerable distortions in the lattice. The Al atoms closest to the vacancy only moves about 0.001 Å in the direction of the vacancy.

Table 6.1: Calculated formation energies of an uncharged nitrogen vacancy in pure nitrides.

Systems	$E_f^{V_N}$ [eV/f.u.]
c-AlN	6.39
HfN	3.21
ScN	2.87
TiN	2.42
CrN (AFM)	1.10

6.2 Local environment effects for V_N in $Ti_{0.5}Al_{0.5}N$

In the pure binary nitrides, the formation energy of a nitrogen vacancy, at least in the dilute regime, is unique. However, in the case of a solid solution ternary system such as $Ti_{1-x}Al_xN$ this is not the case. Instead the vacancy formation energy will depend on the local chemical environment of each potentially vacant site. We have already seen above in Fig. 4.6 that the nearest neighbour M-N and Al-N bond lengths show a considerable spread in $Ti_{0.75}Al_{0.25}N$, $Ti_{0.5}Al_{0.5}N$, and $Ti_{0.25}Al_{0.75}N$. It is likely that there is a corresponding spread in formation energies for the vacancies.

In order to investigate this we have calculated the formation energies of one V_N defect in a $Ti_{0.5}Al_{0.5}N$ SQS supercell with the 2x2x2 conventional unit cell format. This is different from the SQS supercells used above for calculation mixing enthalpies and is actually not a convenient geometry for optimising short range order between Ti and Al. However for this 16+16+32 atom supercell and this particular composition it is still possible to generate short range order parameters close to zero for the first seven coordination shells. The reason for using this geometry is that it is desirable to increase the shortest vacancy-vacancy distance in order to minimise the vacancy self-interaction. As was stated above the change in vacancy formation energies when increasing the cell further is rather small. In the case of c-AlN it is 0.16 eV and in the case of TiN it is 0.05 eV. In this supercell all possible 32 nitrogen vacancies were considered and the resulting $E_f^{V_N}$ are plotted in Fig. 6.1 as a function of the number of nearest neighbouring Al atoms coordinating the vacancy. It is seen that the substitution of half of the Ti with Al is shifting the formation energies to higher values, the value for pure TiN is shown with a filled square for reference. However there is still a huge difference up to the value of c-AlN, shown with a filled triangle.

There is as expected a considerable spread in formation energies of the vacancies. Interestingly both the maximum value (3.73 eV) and minimum value (2.93 eV) is calculated for nitrogen sites with the same number of Al nearest neighbours (2). Even though one might trace a weak tendency for lower formation energies for the nitrogen sites with more Ti neighbours, one might need to look for other and more complicated configura-

tional patterns in order to clarify the reason behind the rather large difference in $E_f^{V_N}$ for different nitrogen sites in $\text{Ti}_{0.5}\text{Al}_{0.5}\text{N}$.

The spread in formation energies have consequences. First of all the formation energy in the thermodynamic sense becomes temperature dependent. This is so since for low temperatures only the lowest energy states could be populated, while at increasing temperature also states with higher energy could. Thus it is slightly complicated to give an exact value for $E_f^{V_N}$ in $\text{Ti}_{0.5}\text{Al}_{0.5}\text{N}$ to be compared with the values in Tab. 6.1. It is clear however that the addition of Al into TiN increases the formation energy of nitrogen vacancies, decreasing the tendency for sub-stoichiometry given that all other relevant parameters could be kept constant. Alternatively one could say that a forced introduction of vacancies would give an additional driving force for decomposition into TiN and c-AlN since the vacancy formation energy would be smaller in the phase separated case, given that they tend to TiN of course. This point will be investigated in details in the next section.

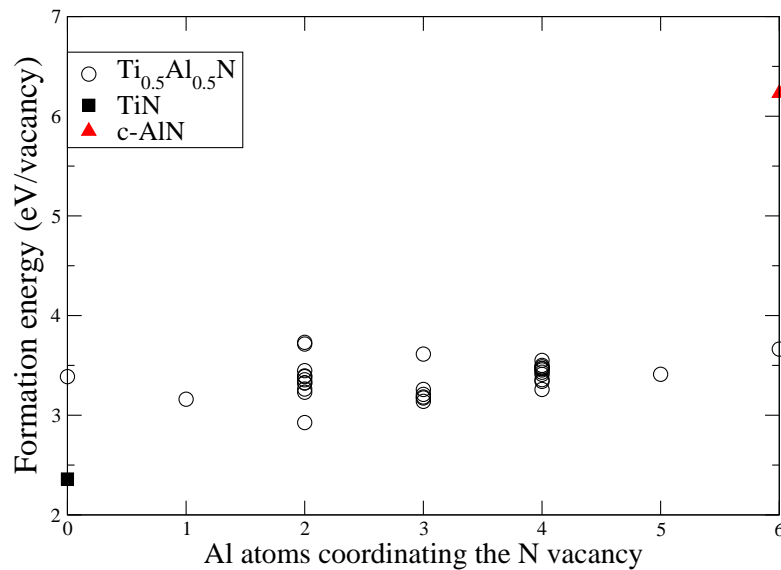


Figure 6.1: The calculated formation energies of nitrogen vacancies in $\text{Ti}_{0.5}\text{Al}_{0.5}\text{N}$ as a function of the number of nearest neighbouring Al atoms coordinating the vacancy. For comparison the formation energy in TiN (solid square) and c-AlN (solid triangle) is shown.

Secondly the spread in formation energies also influences diffusion of V_N in the lattice. If a nitrogen site corresponding to a low vacancy formation energy is empty, the additional barrier due to the spread in formation energies might prevent neighbouring nitrogen atoms to fill it. This could slow down diffusion of nitrogen or non-metal impurities like oxygen possibly present on the nitrogen sublattice. The very slow oxygen diffusion in TiAlN as compared to both TiN and AlN [27] might in fact be due not only to the formation of a protective Al_2O_3 layer but also due to decreased nitrogen and possibly oxygen diffusion rates within the nitride phase due to the results found above.

6.3 Nitrogen sub-stoichiometry in $c\text{-Ti}_{1-x}\text{Al}_x\text{N}_{1-y}$

We now turn to study if a possible nitrogen sub-stoichiometry influences the tendency for phase separation on the metal sublattice as was seen in Chapter 4.

We have calculated the total energy of the random solid solution $c\text{-Ti}_{1-x}\text{Al}_x\text{N}_{1-y}$ for the whole range $0 \leq x, y \leq 1$ with steps of $\Delta x, y = 0.125$ giving a mesh of 81 different compositions. Even though such solutions in the NaCl structure are thermodynamically unstable over a wide range of compositions, e.g. ground state AlN has the wurtzite structure and pure Ti crystalizes in the hcp structure, the scope is relevant for two reasons. Firstly, thin film deposition techniques can be employed to synthesize metastable systems far away from thermodynamic equilibrium and allow studies of coherent isostructural decomposition. Secondly, general trends might be observed which are useful for better physical understanding of the TiAlN system including in a common framework, important materials systems such as $\text{Ti}_{1-x}\text{Al}_x\text{N}$, MAX-phases [155] and Ti-Al intermetallics.

We have used the Order-N, Locally-self-consistent Green's function method (LSGF) [112, 113] described above, together with the Generalized Gradient Approximation (GGA) [97] for the exchange-correlation functional to solve the electronic structure problem for the solid solutions. The local interaction zone for the LSGF calculations included two nearest neighbour shells. Local relaxation of the N atoms were considered using the independent sublattice model while the small relaxation of the metal atoms were neglected. Each supercell, consisting of 648 metal atom sites and 648 nitrogen/ V_N sites, were created in order to mimick a completely random distribution in the solution phase [77]. The calculations of formation energies for the entire concentration grid was performed with respect to fcc-Al, fcc-Ti and N_2 molecules ².

Panel (a) of Fig. 6.2 shows the calculated mixing enthalpies of $\text{Ti}_{1-x}\text{Al}_x\text{N}_{1-y}$ with respect to TiN_{1-y} and AlN_{1-y} (Ti-Al mixing) at fixed levels of V_N . Panel (b) shows the mixing enthalpies with respect to $\text{Ti}_{1-x}\text{Al}_x\text{N}$ and $\text{Ti}_{1-x}\text{Al}_x(\text{N}-V_N)$ (N- V_N mixing) at different fixed Ti-to-Al ratios. The mixing enthalpy of stoichiometric $\text{Ti}_{1-x}\text{Al}_x\text{N}$ is in quantitative agreement with the calculations using EMTO-CPA-ISM presented above. The N-free, Ti-Al mixing enthalpy is in qualitative agreement with calculations for the fcc-Ti-Al mixing enthalpies in Ref. [156]. Our value at equiatomic concentrations, -0.211 eV/f.u. is ≈ 0.08 eV/f.u. less negative. The enthalpy of a relaxed fcc- $\text{Ti}_{0.5}\text{Al}_{0.5}$ SQS supercell used for comparison, -0.276 eV/f.u., lies in between the LSGF values and the ones in Ref. [156]. The difference between our LSGF and our PAW calculation is believed to be due to the neglect, in the former case, of local relaxations of metal atoms and the presence of an empty nitrogen sublattice which gives a slight artificial decrease in metal-metal interactions. The errors due to both those two sources are largest on the nitrogen free border and we thus have an estimate of their maximum value, and they are not believed to interfere with the conclusions made in this chapter.

Panel (a) of Fig. 6.2 shows a transition from large positive mixing enthalpies for the nitride system towards large negative mixing enthalpies for the transition metal alloy. In the nitride case, the positive mixing enthalpy and its non-symmetric shape is explained by the electronic mismatch between TiN and AlN leading to an unfavourable localisation of Ti non-bonding states described above. When the N is removed, the physics is

²A combination of the LSGF values for the energy of TiN and fcc Ti was used together with the PAW formation energy of TiN to get the value of $E(\text{N}_2)$.

gradually changing to the metallic bonding situation of the Ti-Al intermetallics which forms stable compounds. Panel (b) shows a transition from negative mixing enthalpies in TiN_{1-y} towards the large positive mixing enthalpies in AlN_{1-y} . TiN is a very stable compound due to the N p-Ti d hybridization. However, the system is tolerant for off stoichiometry due to flexibility of the metallic states around the Fermi level to incorporate V_N states, leading to a negative mixing enthalpy. The B1 AlN considered in this work is a semiconductor and any V_N will disturb the balance of valance and cost energy, leading to a high mixing enthalpy in line with the discussion of nitrogen vacancies above. Knowing the shape of the "pseudo-binary" mixing enthalpy curves is, however, not enough to determine preferred decomposition patterns in the two dimensional composition space of $\text{Ti}_{1-x}\text{Al}_x\text{N}_{1-y}$. One has to consider also the possibility for an inter-sublattice coupling. We have thus considered our total energies as a function of two independent concentration variables x and y .

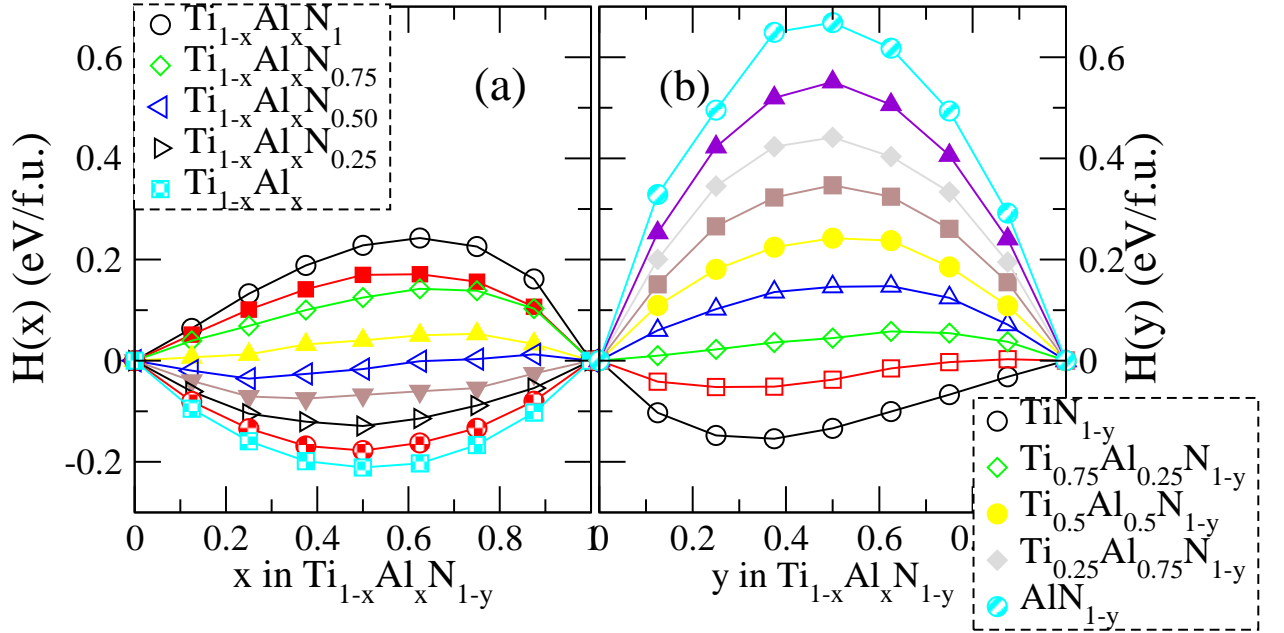


Figure 6.2: (a) Mixing enthalpy of $\text{Ti}_{1-x}\text{Al}_x\text{N}_{1-y}$ as a function of Al content x for different fixed fractions of N between $y=0$ and $y=1$, relative to TiN_{1-y} and AlN_{1-y} . (b) Mixing enthalpy of $\text{Ti}_{1-x}\text{Al}_x\text{N}_{1-y}$ as a function of N content ($1-y$) for different fixed Ti-to-Al ratios, relative to $\text{Ti}_{1-x}\text{Al}_x\text{N}_1$ and $\text{Ti}_{1-x}\text{Al}_x$.

In Fig. 6.3 the formation energy of $\text{Ti}_{1-x}\text{Al}_x\text{N}_{1-y}$ is shown as a function of x and y . It reveals that a simultaneous consideration of the x and y degrees of compositional freedom gives rise to a complicated curvature of the energy surface. The energy gain or loss *per concentration change unit* by any spontaneous fluctuation in composition separating the system into two subsystems with compositions $x+\Delta x, y+\Delta y$ and $x-\Delta x, y-\Delta y$ (where Δx and Δy can be both negative and positive independent of each other) can be written as:

$$\Delta E = \frac{E(x+\Delta x, y+\Delta y) + E(x-\Delta x, y-\Delta y) - 2E(x, y)}{2(|\Delta x| + |\Delta y|)}. \quad (6.2)$$

We have calculated this quantity numerically using for each (x, y) point the values from the eight points $(x \pm 0.125, y)$, $(x, y \pm 0.125)$ and $(x \pm 0.125, y \pm 0.125)$ surrounding it (except for at the perimeters where only one dimension of separation is possible) thus giving a measure on the energy gained by a small fluctuation in four different directions (\hat{x} , \hat{y} , $\hat{x}+\hat{y}$ and $\hat{x}-\hat{y}$). Other directions, e.g. $2\hat{x}+\hat{y}$, were not studied since their numerical derivation would involve a larger compositional offset. Note that our purpose is to find the driving force for spontaneous decomposition, without nucleation processes. We identify that this driving force is strongest in the direction in which ΔE has the largest negative value. Fig. 6.4 shows the results where the arrows point in the preferred decomposition direction and their length is proportional to ΔE . At 0 K, the solid solution is unstable towards small fluctuations in the concentration over almost the entire range of x and y values. The transition metal line and the TiN_{1-y} line are the two exceptions. However, three major regimes of different preferred decomposition directions can be identified.

1) Close to the stoichiometric nitride case and particularly at the medium and high Al content, the V_N are accumulated in Ti-rich regions while N sticks to Al. This tendency can be explained following the argument above that formations of V_N in AlN is unfavourable due to the semiconducting character of its bonding, while TiN can accommodate them, as experimentally observed [10]. We predict that this effect works together with the decomposition mechanism of stoichiometric $\text{Ti}_{1-x}\text{Al}_x\text{N}$ and should enhance the tendency for coherent isostructural decomposition. This is indicated by the fact that the arrows on the row of compositions $y=0.125$ are longer than those in the stoichiometric case $y=0.00$. Decreasing the N content can thus not be used as a way of stabilizing solid solution $\text{Ti}_{1-x}\text{Al}_x\text{N}$ at high Al-content. It would instead be a way to enhance the decomposition tendency in situations where such behavior is desired.

2) In the N-poor, Ti-rich region N sticks to Ti while Al is accumulated in the V_N -rich regions eventually forming metallic Al or an Al-Ti alloy. The chemical driving force for this separation is strong even if one compares it with the nitride case of the same Ti-to-Al ratio. The fact that Ti binds stronger to nitrogen than Al under N-poor conditions is connected with the discussion of the nitride case: Al can form stoichiometric AlN but between such compounds and metallic Al, all compositions are unfavourable due to the drastic incompatibility of the electronic structure of free-electron like Al and the semiconducting structure of AlN. This suggests a partial reinterpretation of the findings in Ref. [157] where epitaxial thin film samples of the composition $\text{Ti}_{0.66}\text{Al}_{0.34}\text{N}_{0.49}$ ³ were found to decompose into what was inferred to be $\text{TiN}_{y'}$ and $\text{AlN}_{y''}$. We propose that these phases more likely have compositions close to $\text{TiN}_{0.82}$ and $\text{Ti}_{0.18}\text{Al}_{0.82}$, the later possibly with an ordering tendency towards the $\text{Ti}_{0.25}\text{Al}_{0.75}\text{DO}_{22}$ compound. Even though complex ordering is not included in this analysis one can see that the decomposition trend goes in the same direction regarding neighbour coordination as the ordered compounds of the cubic Ti_3AlN perovskite and the hexagonal Ti_2AlN and Ti_4AlN_3 MAX-phases. Also in these systems nitrogen neighbours only Ti atoms while Al has a N-free nearest

³This is the composition given separately for each sublattice (cmp. Ti_1N_1) assuming no metal site vacancies, the total composition given in Ref. [157] is $\text{Ti}_{0.44}\text{Al}_{0.23}\text{N}_{0.33}$.

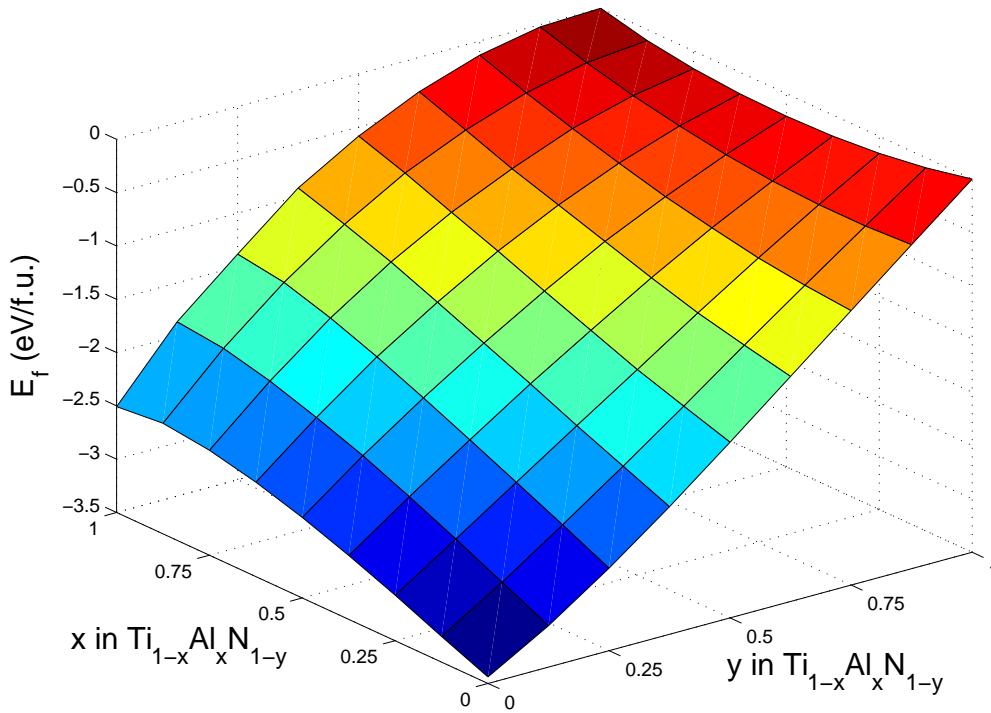


Figure 6.3: The calculated formation energy of $c\text{-Ti}_{1-x}\text{Al}_x\text{N}_{1-y}$ as a function of Al content x and nitrogen content $(1-y)$. Values are given relative to fcc-Al, fcc-Ti and N_2 molecules at 0K.

neighbour environment. The competition between for instance ordering in line with the Ti_3AlN perovskite and isostructural decomposition for situations like in the experiment above, deserves further analysis.

3) In between the N-rich and the N-poor/Ti-rich regimes, at high Al content, there is a region where the tendency for separation along the N-V_N direction is dominating. This region corresponds to the energetically most unstable compositions where no reports of synthesized stable or metastable phases exist.

In summary it has been shown that there exists a clear coupling between the composition and configuration of the metal sublattice with the nitrogen composition and the possibility of nitrogen vacancies on the nitrogen sublattice of cubic $\text{M}_{1-x}\text{Al}_x\text{N}_{1-y}$ systems. This coupling can explain both the increase of the onset temperature of nitrogen loss in $\text{Cr}_{1-x}\text{Al}_x\text{N}$ upon Al addition [37], and the decomposition pattern observed for heavily sub-stoichiometric $\text{Ti}_{0.66}\text{Al}_{0.34}\text{N}_{0.49}$ [157]. The diffusion of nitrogen or non-metal impurities on the nitrogen sublattice should be slower in $\text{Ti}_{0.5}\text{Al}_{0.5}\text{N}$ as compared to TiN due to local environment effects that create traps for vacancies. Further more a slight nitrogen sub-stoichiometry is likely to have an enhancing influence on the driving force for isostructural decomposition in $\text{Ti}_{1-x}\text{Al}_x\text{N}$ coatings.

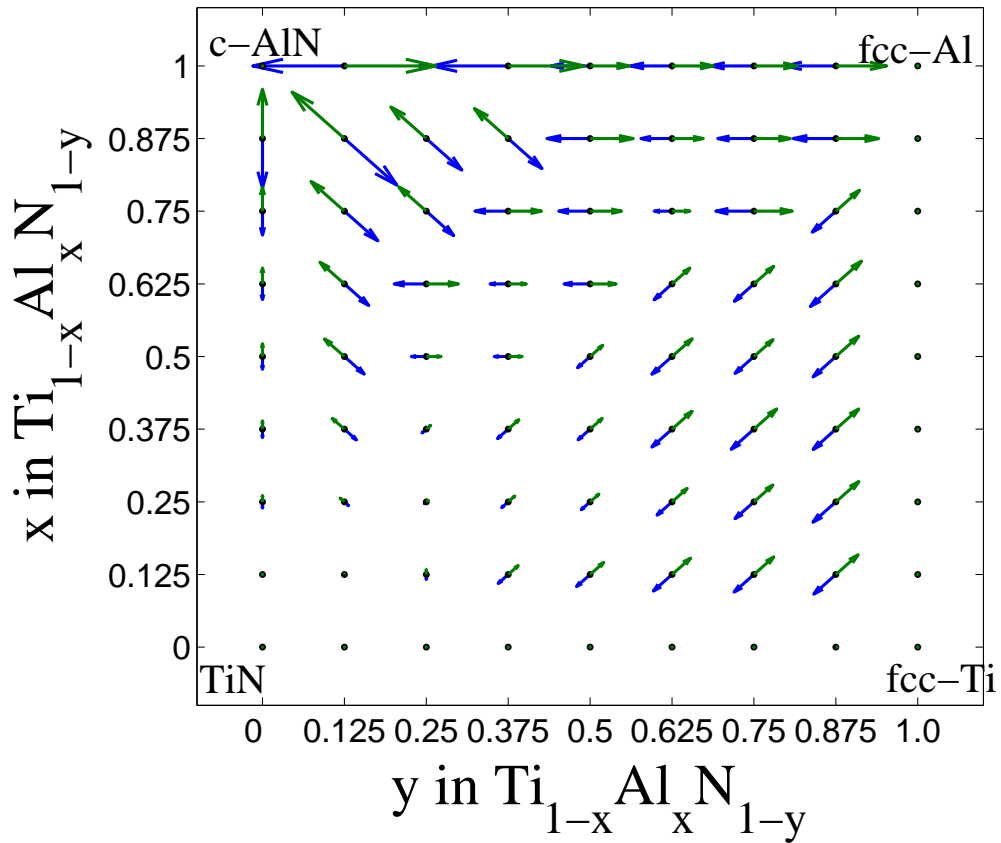


Figure 6.4: Energetically preferred decomposition pattern of $\text{Ti}_{1-x}\text{Al}_x\text{N}_{1-y}$ in x - y composition space. The arrows point in the direction in which a phase separation would be most energetically favorable. Their length indicate the magnitude of this energy. Just a dot indicates that there is no chemical driving force for nucleation-free phase separation. The directions of the arrows are approximate. The optimal direction can be in between the directions considered here.

Chapter 7

Discussion

Following the presentation of the results of this theoretical study in the chapters 3-6, a discussion is presented in this chapter focusing on two key issues. First a discussion about the methodological framework is performed. In the light of the previously presented results, especially for the $\text{Ti}_{1-x}\text{Al}_x\text{N}$ system, the strengths and the weaknesses of the different methods used can be analysed and a discussion on this topic is presented. Secondly the generality of the observed mixing and decomposition tendencies in different ternary $\text{M}_{1-x}\text{Al}_x\text{N}$ systems is discussed focusing on how the choice of transition metal influences the underlying driving force for and the process of decomposition.

7.1 Methodological discussion

The problem of treating the solid solution phases in $\text{M}_{1-x}\text{Al}_x\text{N}$ systems has been solved using two complementary methods, the special quasirandom structures (SQS) method and the coherent potential approximation (CPA). The SQS structures have been constructed for a series of compositions for the cubic B1 structure as well as for the hexagonal B4 structure in order to minimise the magnitude of the Warren-Cowley short range order parameters on the first seven nearest neighbour shells. This corresponds to designing the supercells so that they resemble the real solid solution system with respect to configurational correlation function parameters (Eq. 2.22) in the range where they are strongest. The price for this achievement, with comparison to e.g. random number generated structures, is of course that correlation functions for the longer ranged interactions are in worse agreement with the random state. In an alternative approach, the CPA method has been complemented by the introduction of the independent sublattice model (ISM) to treat the energetic effect of local lattice relaxations. The simultaneous application of two different methods, each with its own strengths and weaknesses allows a confidence in the results that could not have been reached with either of them alone. This is illustrated in Fig. 7.1 where the results of calculations of the isostructural mixing enthalpy of c- $\text{Ti}_{1-x}\text{Al}_x\text{N}$ calculated with the SQS and CPA-ISM methods are reiterated together with the results from methods used in two previous attempts [72, 73] to describe the mixing enthalpies of this system. Please note that in order to perform a completely fair comparison the enthalpies of the small ordered structures are recalculated with the GGA functional and are not the original LDA values from [72] which however are very similar. It is obvious that the state-of-the-art methods SQS and CPA-

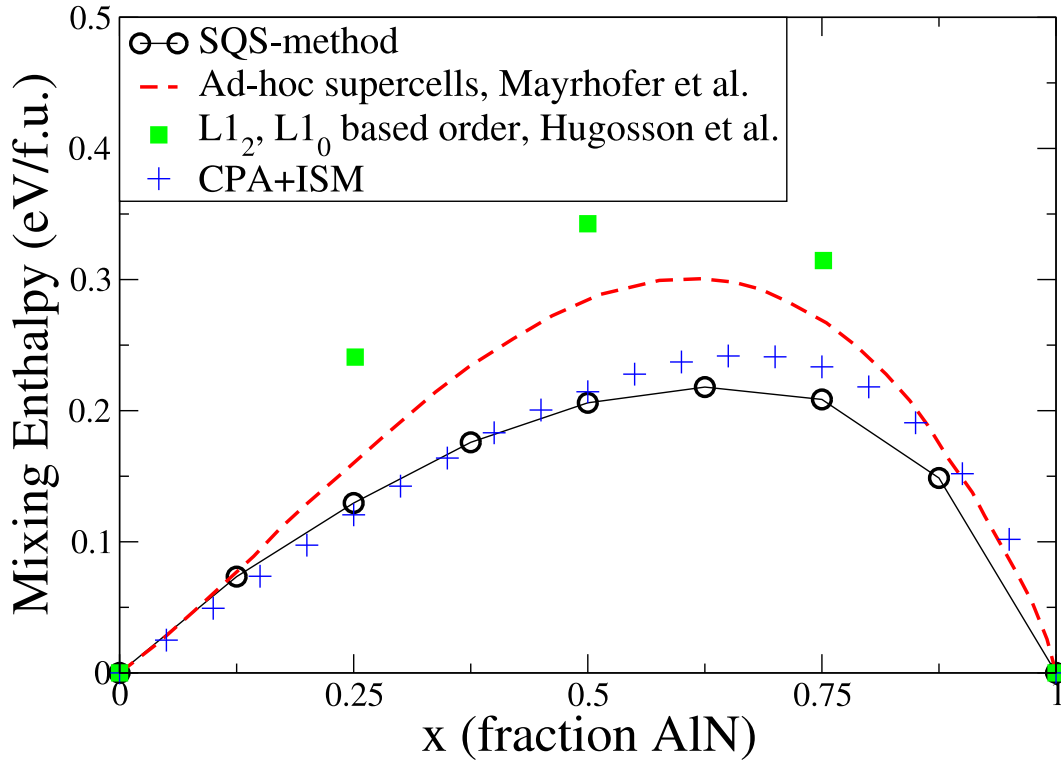


Figure 7.1: The calculated mixing enthalpy of $c\text{-Ti}_{1-x}\text{Al}_x\text{N}$ using the SQS-method, the CPA-ISM method, ad-hoc supercells and small ordered structures.

ISM give results in very good agreement with each other while the previously used methods significantly overestimate the enthalpies. This comparison clearly proves the absolute necessity to accurately consider the atomic configurational state when conclusions about physical properties of ternary nitrides hard coatings materials are to be drawn from first-principles calculations.

At this point one might object that perhaps the perfect random solid solution is not the correct system to analyse when trying to understand experimental thin films results. This is partly true in principle, in systems with a tendency for phase separation such as $\text{Ti}_{1-x}\text{Al}_x\text{N}$, one would expect some degree of short-range clustering also within as-deposited solid solutions. But the perfect random solid solution is the excellent starting point for any such analysis since it corresponds to, although ideal, well known and specified physical conditions. Further more, with the random distribution as starting point one can derive the driving forces in terms of mixing enthalpies or effective cluster interactions which will work towards a separation in the system for instance during cutting tools operations. Such an approach, for instance further developing the procedure in section 4.5, can then predict the amount of clustering tendency at a given temperature. However, if the exact distribution of atoms in as-deposited thin films materials is desired from pure first-principles calculations, one has to perform a study involving surface mobility and bulk-surface interactions. Such an interesting and comprehensive study would require the knowledge of the bulk processes taking place within the grains. On the other hand, if short ranged clustered structures are chosen ad-hoc one gets once again uncontrolled results which can not be directly compared for different compositions

or structures, pretty much like the problematic approach in Ref. [73], although those supercells, judging from the energetics, are likely to show short-range order rather than clustering. If however information is desired regarding some properties of a material in a specific experiment where SRO-parameters have been obtained experimentally, one should create SQS supercells corresponding to those known parameters. But that is an objective quite far from the one of this work.

The supercell based SQS method has some obvious benefits. When the problems of the creation of the structures, random-like or with SRO, have been solved, normal fast parallelised supercell methods can be used to derive total energies, geometry optimisation, electronic structure and other physical properties within a single framework without having to include any additional models or corrections.

The main disadvantage with the SQS method is that it is not *a priori* known which effective interactions in Eq. 2.27 that are strong enough to give a non-negligible contribution to the total energy. Although it is generally true that the strongest interactions are short-ranged pair interactions the number needed for quantitative predictions are system dependent. The problem of obtaining extremely high accuracy of the total energy is illustrated in Fig. 2.4. In some systems also larger sized cluster interactions, like three and four-sites clusters, are important. However, in principle and using big enough supercells, also multi-site correlation functions can be controlled in the SQS creation procedure. The ongoing development of increasing computational resources also works in favour of the SQS method which after all can be considered as an intelligent "brute force"-method.

The CPA method also has its benefits. First of all, it gives by its very nature a direct access to the physics of the ideally random alloy state. No worries are needed for artificial effects originating from supercell periodicity or uncontrolled correlation functions. Physical properties e.g. the total energy of any particular alloy composition can be calculated with equal ease and with identical accuracy making it possible to derive concentration derivatives of them. It also allows the study of effects that might be connected to delicate concentration dependent bandstructure effects of which the present work has a clear example in Fig. 4.8. The implementation of the disordered local moments method allows for the treatment of magnetically disordered phases like $\text{Cr}_{1-x}\text{Al}_x\text{N}$. Further more the single site nature of the method typically reduces computational cost as compared to the calculation of big supercells. Especially if multi-component alloys are to be considered such as $\text{c-Ti}_{1-x-y}\text{Cr}_x\text{Al}_y\text{N}$, the supercells needed to accurately describe relevant correlation functions becomes huge while the CPA works almost as fast as for two component calculations. The SGPM method relying on the CPA effective medium can be used to derive effective interactions. Although it was shown in section 4.5.3 that the usage of concentration dependent interactions for the study of phase separation temperatures are very problematic, such parameters can be directly used as control of which correlation functions that needs to be close to zero in a design of SQS supercells. This was in fact done already for the case of $\text{c-Ti}_{1-x}\text{Al}_x\text{N}$ in Ref. [77] which verified the presently used B1 SQS-structures for that system.

Of course there are problems with the CPA approach. Of highest relevance for the systems treated in this work is the problem with local lattice relaxations. In the system $\text{c-Ti}_{1-x}\text{Al}_x\text{N}$, the relaxation energies corresponds to roughly one third of the total mixing enthalpies as can be seen in Fig. 4.2. Without the usage of an accurate model for

the additional treatment of local lattice relaxations, the CPA would not be useful for energetic properties of $\text{Ti}_{1-x}\text{Al}_x\text{N}$. The independent sublattice model as introduced in chapter 2 and successfully tested and applied in chapter 4 is an important improvement on previous models for lattice relaxations e.g. the effective tetrahedron model [126], since it points at a scheme for treating lattice relaxations in systems with more than one sublattice. Although most likely rather accurate also for other systems with the B1 structure, it remains to be seen if it could work also for the wurtzite structure in e.g. $\text{h-Ti}_{1-x}\text{Al}_x\text{N}$. In that structure there are three independent lattice parameters already in the pure nitrides, a , c/a and u , to compare to the single one in the B1 structure which might give rise to problems. Further more one should be aware that even if the model works well for the energy, it does not capture coupling between local relaxations and other properties such as electronic structure or bulk modulus if they should be of interest.

The results of this work taken together clearly shows the potential of a simultaneous usage of the SQS and the CPA frameworks for studying disordered systems. With the knowledge of respective methods strengths and weaknesses, or even explicit combinations of them such as the LSGF-investigation in chapter 6, one can perform theoretical studies able to explain and even predict a long range of different properties of relevance for hard coatings materials.

Finally, a few words of a method that has not been used, the Connolly-Williams method [158]. This method, in which the energies of a series of ordered structures with known correlation functions are mapped to the effective cluster interactions of Eq. 2.27, is in fact the basis of a majority of alloy theory works these days, for instance in Ref. [67]. The choice of not using this methodological framework was done partly because the direct access to the electronic structure, as well as other properties, of the random alloys was desired without the need for a separate cluster expansion for every property. Further more, it was shown in Ref. [98] that even an excellent description of the energies of ordered structures does not guarantee that the description of high temperature disordered phases are accurate. Finally the consideration of a magnetically disordered state like the $\text{Cr}_{1-x}\text{Al}_x\text{N}$ case is problematic within the present day implementations of the Connolly-Williams scheme. However, considering the problems encountered in Chapter 4.4.3, one should not exclude the option to use this method to derive concentration independent effective cluster interactions in the $\text{Ti}_{1-x}\text{Al}_x\text{N}$ system. In such a case, the knowledge gained in the present study, in terms of energetics of disordered phases as well as the physical origin and range of effective cluster interactions, would be invaluable to accurately describe the disordered parts of phase space as well as the asymmetric concentration dependence of the mixing and decomposition thermodynamics.

7.2 The effects of alloying elements

In this work four different ternary $\text{M}_{1-x}\text{Al}_x\text{N}$ solid solution systems have been considered: $\text{Ti}_{1-x}\text{Al}_x\text{N}$, $\text{Cr}_{1-x}\text{Al}_x\text{N}$, $\text{Sc}_{1-x}\text{Al}_x\text{N}$, and $\text{Hf}_{1-x}\text{Al}_x\text{N}$. The reason for the choice of four different system has been to be able to reveal the general underlying physics governing these related but different systems. Especially the four transition metal nitrides TiN , CrN , ScN , and HfN differ in terms of valence electron number, lattice parameters,

and formation energies. The large lattice spacing difference between ScN and HfN on one hand and c-AlN on the other was demonstrated in chapter 3 together with the consequences for deviation from Vegard's rule and bulk modulus. The importance of an electronic bandstructure effect in the $\text{Ti}_{1-x}\text{Al}_x\text{N}$ system was clearly shown in chapter 4. In order to relate and compare these two effects Fig. 7.2 shows the calculated isostructural mixing enthalpies, derived analogous to Eq. 4.1 for the B1 systems $\text{Ti}_{1-x}\text{Al}_x\text{N}$, $\text{Cr}_{1-x}\text{Al}_x\text{N}$, $\text{Sc}_{1-x}\text{Al}_x\text{N}$, and $\text{Hf}_{1-x}\text{Al}_x\text{N}$.

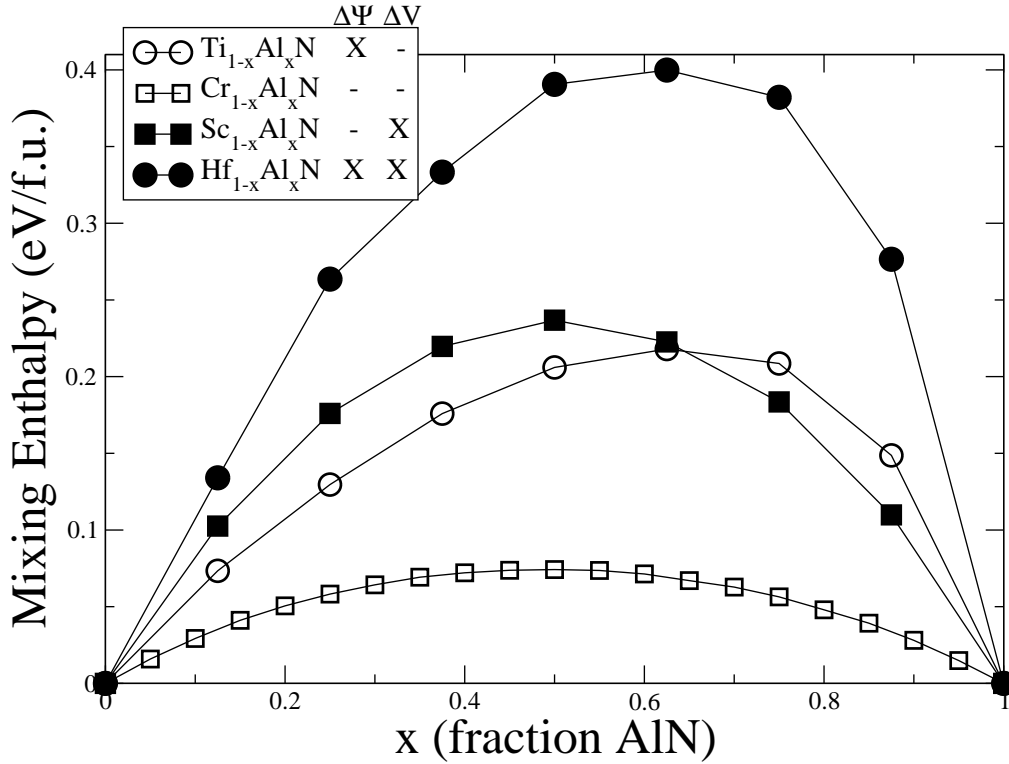


Figure 7.2: The calculated mixing enthalpy of c- $\text{Ti}_{1-x}\text{Al}_x\text{N}$, $\text{Sc}_{1-x}\text{Al}_x\text{N}$, and $\text{Hf}_{1-x}\text{Al}_x\text{N}$ using the SQS-method and for c- $\text{Cr}_{1-x}\text{Al}_x\text{N}$ using the CPA-ISM method. The legends indicate which system that has a large volume mismatch (ΔV) between the components and which systems that show an impact of electronic structure mismatch ($\Delta\Psi$).

Considering the big volume mismatch between HfN and c-AlN seen in e.g. Fig. 3.3, it is not surprising that $\text{Hf}_{1-x}\text{Al}_x\text{N}$ shows a huge mixing enthalpy. However, in the system $\text{Sc}_{1-x}\text{Al}_x\text{N}$, where the volume mismatch is almost as big, the enthalpies are much lower, more comparable to the values of $\text{Ti}_{1-x}\text{Al}_x\text{N}$. The picture becomes more clear when also the electronic structure is considered. In Fig. 7.3 the electronic density of states for the transition metal site is shown both for pure MN and in $\text{M}_{0.25}\text{Al}_{0.75}\text{N}$ for all the four systems under consideration. The calculations are done with the KKR-ASA-CPA method. The $\text{Ti}_{1-x}\text{Al}_x\text{N}$ system (top left panel) shows the now familiar sharpening of the 3d non-bonding state and the disappearance of the low energy shoulder in the $\text{Ti}_{0.25}\text{Al}_{0.75}\text{N}$ alloy. In the case of $\text{Cr}_{1-x}\text{Al}_x\text{N}$ (top right panel) the magnetic split of the non-bonding 3d state can be seen right at the Fermi level but the sharpening of the non-bonding states are also visible. In $\text{Sc}_{1-x}\text{Al}_x\text{N}$ (lower left panel), having one less valence electron per transition metal as compared to $\text{Ti}_{1-x}\text{Al}_x\text{N}$, the non-bonding 3d-state is above the Fermi level already in pure ScN. However, as Al is added the

qualitatively same development as in $\text{Ti}_{1-x}\text{Al}_x\text{N}$ can be seen for the non-bonding state but now above the Fermi level. The calculations for $\text{Hf}_{1-x}\text{Al}_x\text{N}$ is shown in the lower right panel. For this system the very sharp and localised 4f-states are visible at about 12 eV below the Fermi level, but they are not taking any relevant part in the bonding in the system. Another difference from the three other systems is that the 5d valence states of Hf are considerably broader as compared to the 3d states of Sc, Ti, and Cr. When AlN is added to HfN the trend is similar as $\text{Ti}_{1-x}\text{Al}_x\text{N}$. The low energy shoulder of the 5d non-bonding state is removed in $\text{Hf}_{0.25}\text{Al}_{0.75}\text{N}$ and the Fermi level is forced up onto a sharper state. It is worth noting that in the cases $\text{Sc}_{1-x}\text{Al}_x\text{N}$ and $\text{Hf}_{1-x}\text{Al}_x\text{N}$, the sharpening of the non-bonding state is partially countered by the broadening that is the result of the decreased lattice spacing in AlN-rich samples.

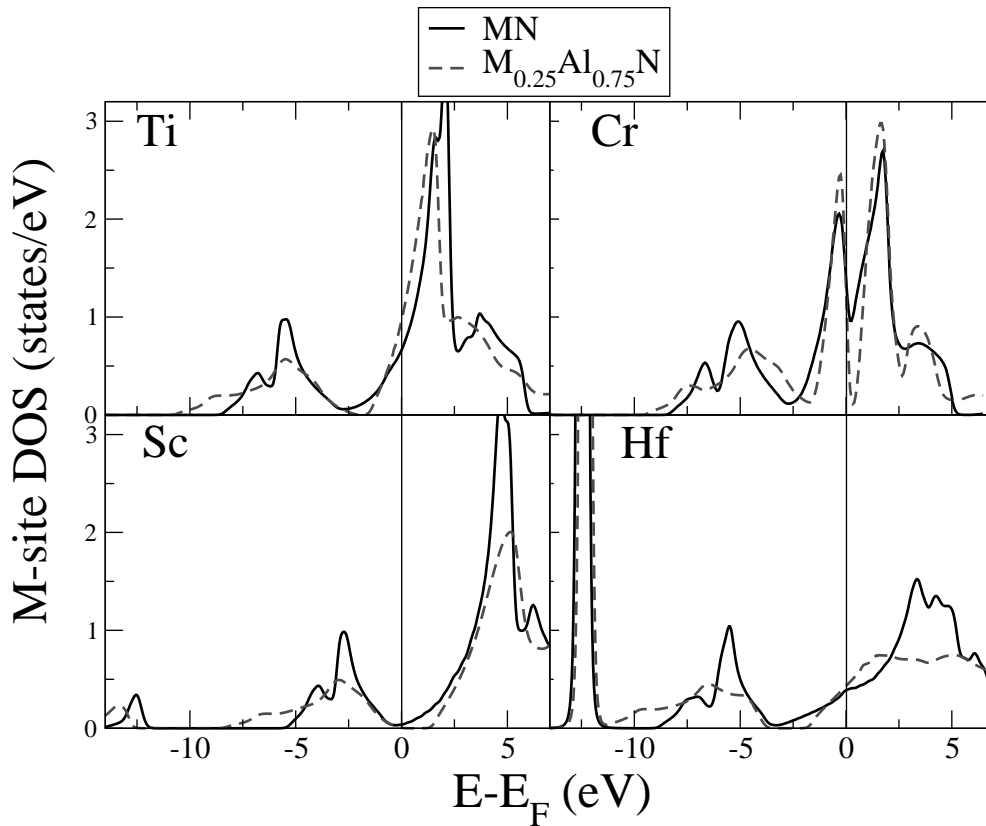


Figure 7.3: The calculated site projected density of states for the different transition metals in both pure MN and in a $\text{M}_{0.25}\text{Al}_{0.75}\text{N}$ alloy. The calculations are done using the KKR-ASA-CPA method.

Thus one can conclude that the development of the non-bonding d-state is similar for all treated systems when AlN is added. However the valence electron concentration and the consequent position of the Fermi level decides whether or not this development affects the energetics and mixing enthalpies. In the case $\text{Sc}_{1-x}\text{Al}_x\text{N}$ it has no effect and it is instead the large volume mismatch between ScN and c-AlN that gives rise to a large and symmetric mixing enthalpy. In $\text{Ti}_{1-x}\text{Al}_x\text{N}$ it is the electronic structure effect that is dominating giving rise to a strongly asymmetric shape of the enthalpy curve. In $\text{Hf}_{1-x}\text{Al}_x\text{N}$ both effects are present giving rise to a very high mixing enthalpy and thus a huge energetic driving force for decomposition. In $\text{Cr}_{1-x}\text{Al}_x\text{N}$ the difference in volume

is very small and the magnetic splitting of the Cr non-bonding 3d state disarms the electronic structure mismatch. Thus the latter system shows a small mixing enthalpy in comparison with the other systems. In the legends of Fig. 7.2 an X indicates which systems that show an impact from respectively effects.

The electronic mismatch is not only affecting the mixing enthalpy. There is also an impact on the bond length distribution. This can be seen from the comparison of the nearest-neighbour bond length distributions in the two systems $\text{Sc}_{0.5}\text{Al}_{0.5}\text{N}$ and $\text{Hf}_{0.5}\text{Al}_{0.5}\text{N}$ shown in Fig. 7.4.

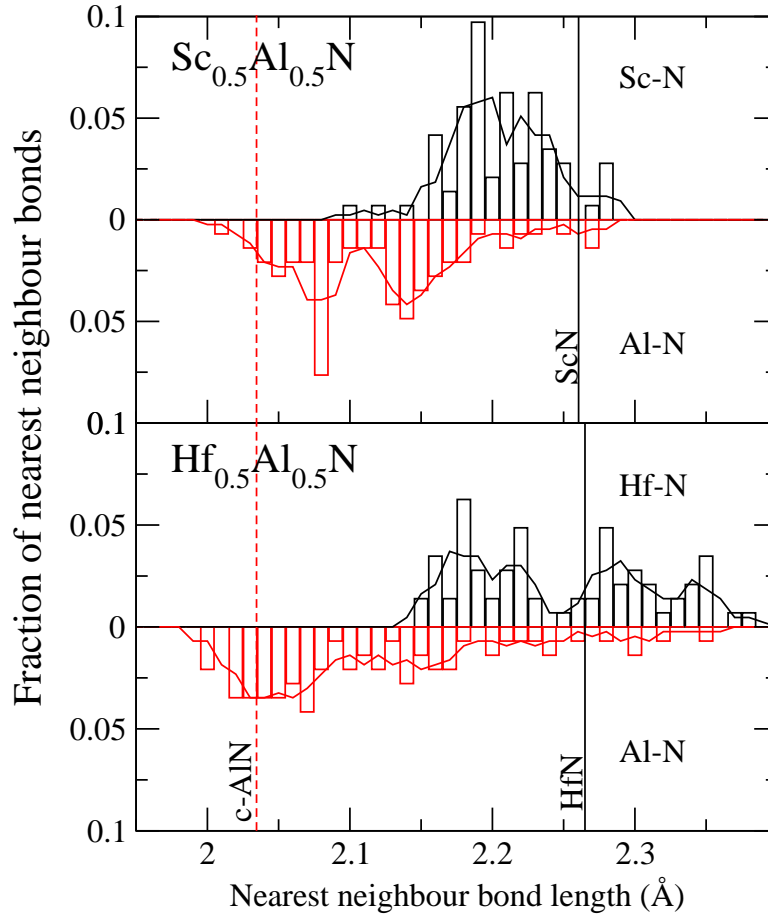


Figure 7.4: The calculated nearest neighbour distance (M-N and Al-N) for the two systems $\text{Hf}_{0.5}\text{Al}_{0.5}\text{N}$ and $\text{Sc}_{0.5}\text{Al}_{0.5}\text{N}$. The bars show the fraction of bonds that are rounded to each 0.01 Å while the lines are running averages over 0.03 Å.

Since the volume difference between the components are similar in these two alloy systems, one could expect that the bond-length distributions would look similar. However, as can be seen, this is not the case. The top panel, showing the distribution in the $\text{Sc}_{0.5}\text{Al}_{0.5}\text{N}$ system, is close to what one could expect. The Al-N bonds are stretched while the Sc-N bonds are compressed without a huge spread in values. In the $\text{Hf}_{0.5}\text{Al}_{0.5}\text{N}$ case shown in the lower panel on the other hand, the spread is huge. The Al-N bonds are not as stretched in average as in the previous system but the spread in values is huge. The Hf-N bonds are both stretched and compressed. This is an indication that solid solution hardening can depend on electronic structure effects as much as on lattice mismatch.

This work has revealed an electronic band structure effect which has as large an impact on the mixing enthalpies in $\text{Ti}_{1-x}\text{Al}_x\text{N}$ and $\text{Hf}_{1-x}\text{Al}_x\text{N}$ as the effect of a volume difference in a heavily mismatched systems such as $\text{Sc}_{1-x}\text{Al}_x\text{N}$. The question if these two different driving forces for decomposition are likely to give rise to similar or different decomposition behaviour. In order to answer this question, one should keep in mind that the mixing enthalpies are calculated for the equilibrium volume for each composition, including the pure binary nitrides. This is important to consider if one is interested in the situation in coherent grains of mixed nitrides. In such a situation a phase separation would not result in pure nitrides at their respectively optimal lattice spacing, but rather domains that are strained to match each other on the phase boundary. In such a situation the decomposition relying on volume mismatch as driving force would be considerably hampered. This was demonstrated clearly in the semiconductor nitride system B3 (Ga,In)N [67] where decomposition temperatures for coherent bulk situations was decreased by a factor of 3 as compared to the incoherent situation actually resulting in a superstructure ordering rather than clustering. In our case the system $\text{Sc}_{1-x}\text{Al}_x\text{N}$ is likely to show a similar behaviour. On the other hand, in AlN-rich $\text{Ti}_{1-x}\text{Al}_x\text{N}$ systems where the main driving force for decomposition is the electronic mismatch, the impact of coherency strain would be weak in this aspect. One can conclude that it is the electronic mismatch that is the key for obtaining coherent isostructural decomposition, such as spinodal decomposition, in the typical polycrystalline phases of multinary nitrides hard coatings materials. A volume mismatch between the components will instead promote nucleation and growth of either isostructural or non-isostructural phases. A schematic illustration of this discussion is made in Fig. 7.5.

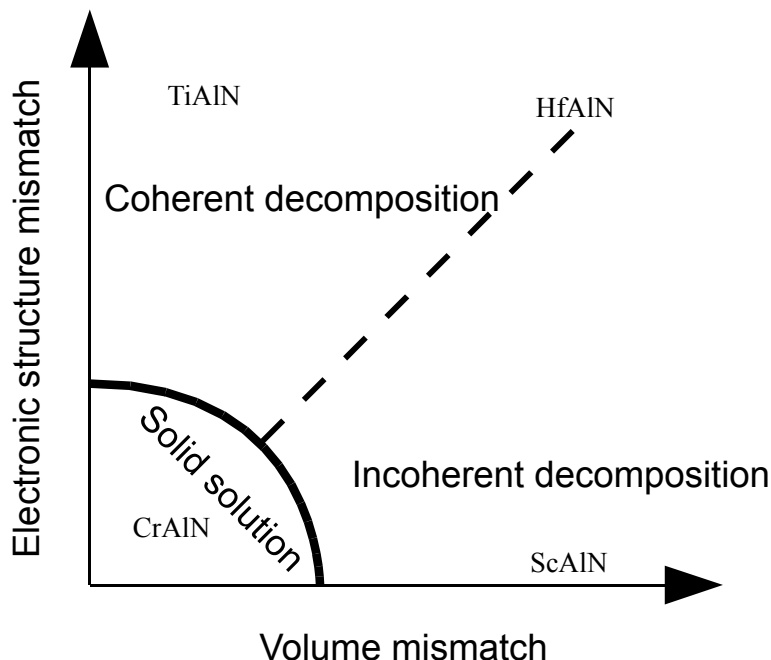


Figure 7.5: A schematic illustration of the effects of electronic structure mismatch and volume mismatch when metastable $\text{M}_{1-x}\text{Al}_x\text{N}$ solid solution coatings are subject to high temperatures.

Chapter 8

Conclusions

In this work a systematic theoretical investigation from first-principles has been performed on four important multinary nitrides hard coatings materials systems: TiAlN, CrAlN, ScAlN, and HfAlN. The study has been focused on the properties of disordered metastable solid solution phases in the cubic B1 structure which has also been the major focus of experimental research and industrial applications. The study, aimed at reducing the knowledge gap between the observed performance of different coatings in cutting tools applications and the fundamental quantum mechanic and thermodynamic physics governing this behaviour, has resulted in a number of important conclusions.

- First of all it was found that the simultaneous usage of both the special quasirandom structures (SQS) method, and the coherent potential approximation (CPA) method to treat the disordered phases made it possible to calculate a long range of properties with an accuracy and confidence that would not have been possible with either of the methods alone. The suggested independent sublattice model for local lattice relaxations was found to work well as a complement to CPA calculations in mixed nitrides with the B1 structure.
- All four studied systems, B1 $\text{Ti}_{1-x}\text{Al}_x\text{N}$, $\text{Cr}_{1-x}\text{Al}_x\text{N}$, $\text{Sc}_{1-x}\text{Al}_x\text{N}$, and $\text{Hf}_{1-x}\text{Al}_x\text{N}$, have been shown to have lattice parameters exhibiting a systematic positive deviation from Vegard's rule as a function of composition. This behaviour is the consequence of the fact that no new nearest neighbour bonds are introduced in the alloys as compared to the M-N and Al-N bonds in the binary nitrides. Instead it is the anharmonic behaviour of these bonds, making it more favourable to extend the Al-N bonds as compared to compress the M-N bonds, that gives a positive deviation. A modified Vegard's rule where proposed taking these results into consideration, predicting that the lattice parameter of an alloy is equal to the minimum point of the concentration weighted average of the whole equation of states of the included components. The possible deviations of real systems from this prediction is more likely to indicate a change in the bonding picture as compared to a deviations from the original Vegard's rule.
- In the system $\text{Ti}_{1-x}\text{Al}_x\text{N}$, it was shown that the cubic B1 structure is lower in energy as compared to the hexagonal B4 structure for $x \leq 0.71$. The hypothetical hexagonal B4' phase with a small c/a value, was shown to have higher energy as compared to either the B1 ($x \leq 0.71$) or B4 ($x \geq 0.71$) phases. These energy

relations are parts of the explanation of why the cubic phase is preferably formed during PVD synthesis over a large range of compositions in this system, however also growth parameters and the structure of the substrate are likely to influence the structure of as-deposited samples.

- In the B1 $c\text{-Ti}_{1-x}\text{Al}_x\text{N}$ system, a peculiar development of the electronic structure was found to occur with increasing AlN content. Especially, the non-bonding 3d state of Ti developed into an atomic like sharp state at the Fermi level in AlN-rich samples. This band structure effect was shown to have a direct impact on the mixing enthalpy and thus on the driving force for decomposition in this system. Especially in samples with high AlN-content the driving force for isostructural decomposition was found to be huge. The tendency for isostructural decomposition is highly likely to be the limiting factor in attempts to solve high amounts of AlN in the cubic phase of $\text{Ti}_{1-x}\text{Al}_x\text{N}$. The isostructural phase diagram of $c\text{-Ti}_{1-x}\text{Al}_x\text{N}$ was derived using the mean field approximation for temperature effects. It showed through the asymmetric shape of the miscibility gap as well as the spinodal region a clear impact of the electronic structure effect reported above. At 1000°C the spinodal region was predicted to be $0.25 \leq x \leq 0.99$. The experimental observation of isostructural spinodal decomposition in AlN-rich $c\text{-Ti}_{1-x}\text{Al}_x\text{N}$ has thus been explained. In order to go beyond the mean field approximation effective cluster interactions (ECI) for the configurational Hamiltonian was derived using the screened generalized perturbation method (SGPM). Important knowledge regarding the range of ECIs and the local configurational impact of the electronic structure was gained. Specifically a prediction was done of a possible metastable phase consisting of alternating (111) bi-layers of AlN and TiN in Ti-rich samples, especially under conditions of limited bulk diffusion.
- In $\text{Cr}_{1-x}\text{Al}_x\text{N}$ the utmost importance of allowing for magnetisation of Cr atoms in the theoretical description also above the Néel temperature, was demonstrated. Due to the magnetic split of the Cr 3d non-bonding states for all compositions in $\text{Cr}_{1-x}\text{Al}_x\text{N}$, the electronic structure discussed above for $\text{Ti}_{1-x}\text{Al}_x\text{N}$, gives only a weak or possibly no effect on the mixing energetics of the $\text{Cr}_{1-x}\text{Al}_x\text{N}$ system which shows in comparison small positive values of the mixing enthalpy. This explains the experimentally observed possibility to solve higher amounts of AlN in the metastable cubic phase of $\text{Cr}_{1-x}\text{Al}_x\text{N}$ as compared to $\text{Ti}_{1-x}\text{Al}_x\text{N}$. If strong electron correlation, which might have a certain importance in this particular nitride system, is taken into account, the tendency for isostructural decomposition in the $\text{Cr}_{1-x}\text{Al}_x\text{N}$ system is further diminished.
- The formation energy of nitrogen vacancies was calculated for the cubic binary nitrides TiN, HfN, ScN, CrN, and $c\text{-AlN}$. These calculations revealed that vacancies are readily formed in CrN, explaining the experimental observation of onset of decomposition through nitrogen loss of CrN thin films at rather low temperatures. In contrast, $c\text{-AlN}$ shows a huge formation energy for vacancies. The combination of these two results explains the shift to higher onset temperatures of nitrogen loss in $\text{Cr}_{1-x}\text{Al}_x\text{N}$ samples upon AlN addition. Nitrogen vacancies in the $\text{Ti}_{1-x}\text{Al}_x\text{N}$ system were studied in detail and two main conclusions were drawn: If a small amount of nitrogen vacancies are present in $\text{Ti}_{1-x}\text{Al}_x\text{N}$ samples they

enhances the tendency for isostructural decomposition as they cluster in Ti-rich regions while AlN-rich regions tends to be vacancy free. On the other hand in heavily substoichiometric composition nitrogen tends to Ti-rich regions while Al forms nitrogen free AlTi alloys.

- In order to compare the effects of electronic mismatch and volume mismatch on the driving force for decomposition, the mixing enthalpies of the $\text{Sc}_{1-x}\text{Al}_x\text{N}$ and $\text{Hf}_{1-x}\text{Al}_x\text{N}$ systems were also studied. It was found that the large lattice misfit, between ScN and HfN on one hand and c-AlN on the other, gave rise to a large and symmetric contribution to the mixing enthalpies in these systems. $\text{Hf}_{1-x}\text{Al}_x\text{N}$ displayed also the impact of electronic mismatch while $\text{Sc}_{1-x}\text{Al}_x\text{N}$ did not. It was concluded that due to the resulting strain in decomposed but coherent samples, the volume mismatch is not an optimal driving force for coherent decomposition. The electronic structure mismatch on the other hand is the key property to look for when isostructural coherent decomposition, such as spinodal decomposition is desired.
- The study of disordered phases revealed some important features related to the fact that different atoms have different chemical environments. The bond strengths within the mixed systems differs substantially manifesting itself through a spread in equilibrium bond lengths in e.g. $\text{Ti}_{1-x}\text{Al}_x\text{N}$ and $\text{Hf}_{1-x}\text{Al}_x\text{N}$. This gives rise to solid solution hardening. It was shown that electronic structure mismatch gave at least as large impact on this spread as compared to volume mismatch. Further more the vacancy formation energies in $\text{Ti}_{1-x}\text{Al}_x\text{N}$ depends on the local environment of the vacant site. This creates traps for vacancies and are likely to slow down diffusion of nitrogen or oxygen impurities on the nitrogen sublattice in this system.

Perspectives

All studies are limited in extent and so is this one. However, certain questions remains to be solved and some new ones has been raised during these years. Here follow some suggestions of possible continuations of the present work.

- First of all the bulk thermodynamics of the $\text{Ti}_{1-x}\text{Al}_x\text{N}$ system is not yet fully understood. The problem origins in the fact that the effective cluster interactions as derived from the random alloy as reference state are strongly concentration dependent. At the same time, standard thermodynamic simulation methods do not take into account that in clustering systems, the local concentration changes during the simulation. To solve this problem one needs to either map the concentration dependence of the ECIs onto multi-body interactions of concentration independent ECIs or develop a Monte Carlo scheme which uses a local definition of the concentration and updates the ECIs accordingly.
- The thermodynamics relations are only one part of the story in metastable thin films materials. The kinetics relations are in many cases as important in order to explain physical properties. Thus an extension of the present work including

kinetic barriers for bulk and surface diffusion in multinary nitrides followed by a kinetic Monte Carlo simulation would be of extreme importance.

- Since the development within hard coatings applications is going in the direction of nanocomposites such as TiN/SiN_x and $\text{Cr}_{1-x}\text{Al}_x\text{N}/\text{SiN}_y$ the interactions between the materials system studied in this work and SiN_x phases at interfaces would be of interest. Also of interest would be a theoretical study of the process of oxidation of mixed nitrides.
- This is just a few examples of possible tracks of further theoretical studies in the field of multinary nitrides hard coatings materials. It would also be of great importance if certain experimental investigations were performed in order to try to confirm or falsify the predictions of this work, for example detailed XPS measurements of the development of Ti 3d states as a function of AlN content in $\text{Ti}_{1-x}\text{Al}_x\text{N}$.

Bibliography

- [1] I. Manning. Transport-theory approach to ion-beam mixing and recoil implantation. *Physical Review B*, 42:9853, 1990.
- [2] H. Holleck. Metastable coatings - prediction of composition and structure. *Surface and coatings technology*, 36:151, 1988.
- [3] T.B. Massalski, editor. *Binary Alloy Phase Diagrams*, volume 1 and 2. American Society for Metals, 1986.
- [4] S.-H. Jhi, J. Ihm, S.G. Louie, and M.L. Cohen. Electronic mechanism of hardness enhancement in transition-metal carbonitrides. *Nature*, 399:132–134, 1999.
- [5] C. Y. Ting. TiN formed by evaporation as a diffusion barrier between Al and Si. *Journal of Vacuum Science and Technology*, 21:14, 1982.
- [6] S.-K. Rha, S.-Y. Lee, W.-J. Lee, Y.-S. Hwang, C.-O. Park, D.-W. Kim, Y.-S. Lee, and C.-N. Whang. Characterization of TiN barriers against Cu diffusion by capacitance-voltage measurement. *Journal of Vacuum Science and Technology B*, 16:2019, 1998.
- [7] P. Roquiny, F. Bodart, and G. Terwagne. Colour control of titanium nitride coatings produced by reactive magnetron sputtering at temperature less than 100°C. *Surface and Coatings Technology*, 116-119:278–283, 1999.
- [8] J. S. Zabinski and A. A. Voevodin. Recent development in the design, deposition, and processing of hard coatings. *Journal of Vacuum Science and Technology A*, 16(3):1890, 1998.
- [9] H. A. Wriedt and J. L. Murray. The N-Ti (Nitrogen-Titanium) System. *Bulletin of Alloy Phase Diagrams*, 8:378, 1987.
- [10] C. S. Shin, D. Gall, N. Hellgren, J. Patscheider, I. Petrov, and J. E. Greene. Vacancy hardening in single-crystal $\text{TiN}_x(001)$ layers. *Journal of Applied Physics*, 93:6025, 2003.
- [11] J. Vetter. Vacuum arc coatings for tools: potentials and application. *Surface and Coatings Technology*, 76-77:719–724, 1995.
- [12] A. Persson, J. Bergström, C. Burman, and S. Hogmark. Influence of deposition temperature and time during PVD coating of CrN on corrosive wear in liquid aluminium. *Surface and Coatings Technology*, 146-147:42–47, 2001.

- [13] L. M. Corliss, N. Elliott, and J. M. Hastings. Antiferromagnetic structure of CrN. *Physical Review*, 117(4):929, 1960.
- [14] R. M. Ibberson and R. Cywinski. The magnetic and structural transitions in CrN and (Cr,Mo)N. *Physica B*, 180-181:329, 1992.
- [15] D. Gall, C. S. Shin, R. T. Haasch I. Petrov., and J. E. Greene. Band gap in epitaxial NaCl-structure CrN(001) layers. *Journal of Applied Physics*, 91(9):5882, 2002.
- [16] R. Sanjinés, O. Banakh, C. Rojas, P. E. Schmid, and F. Lévy. Electronic properties of $\text{Cr}_{1-x}\text{Al}_x\text{N}$ thin films deposited by reactive magnetron sputtering. *Thin Solid Films*, 420-421:312, 2002.
- [17] H. Vollstädt, E. Ito, M. Akaishi, S. Akimoto, and O. Fukunaga. High pressure synthesis of rocksalt type AlN. *Proceedings of the Japanese Academy B*, 66:7, 1990.
- [18] Z. M. Ren, Y. F. Lu, H. Q. Ni, T. Y. F. Liew, B. A. Cheong, S. K. Chow, M. L. Ng, and J. P. Wang. Room temperature synthesis of c-AlN thin films by nitrogen-ion-assisted pulsed laser deposition. *Journal of Applied Physics*, 88:7346, 2000.
- [19] I. Petrov, E. Mojab, R. C. Powell, J. E. Greene, L. Hultman, and J.-E. Sundgren. Synthesis of metastable epitaxial zinc-blende-structure AlN. *Applied Physics Letters*, 60:2491, 1992.
- [20] G. Beensh-Marchwicka, L. Król-Stepniewska, and W. Posadowski. Structure of thin films prepared by the cosputtering of titanium and aluminium or titanium and silicon. *Thin Solid Films*, 82:313–320, 1981.
- [21] O. Knotek, M. Böhmer, and T. Leyendecker. On structure and properties of sputtered Ti and Al based hard compound films. *Journal of Vacuum Science and Technology A*, 4:2695, 1986.
- [22] W. D. Münz. Titanium aluminium nitride films: A new alternative to TiN coatings. *Journal of Vacuum Science and Technology A*, 4:2717, 1986.
- [23] H. A. Jehn, S. Hofmann, and V. E. Rückborn. Morphology and properties of sputtered (Ti,Al)N layers on high speed steel substrate as a function of deposition temperature and sputtering atmosphere. *Journal of Vacuum Science and Technology A*, 4:2701, 1986.
- [24] O. Knotek, W. D. Münz, and T. Leyendecker. Industrial deposition of binary, ternary, and quaternary nitrides of titanium, zirconium, and aluminum. *Journal of Vacuum Science and Technology A*, 5:2173, 1987.
- [25] T. Ikeda and H. Satoh. Phase formation and characterization of hard coatings in the Ti-Al-N system prepared by the cathodic arc ion plating method. *Thin Solid Films*, 195:99–110, 1991.
- [26] A. Hörling, L. Hultman, M. Oden J. Sjölen, and L. Karlsson. Mechanical properties and machining performance of $\text{Ti}_{1-x}\text{Al}_x\text{N}$ -coated cutting tools. *Surface and Coatings Technology*, 191:384, 2005.

-
- [27] D. McIntyre, J. E. Greene, G. Håkansson, J. E. Sundgren, and W.-D. Münz. Oxidation of metastable single-phase polycrystalline $\text{Ti}_{0.5}\text{Al}_{0.5}\text{N}$ films: Kinetics and mechanisms. *Journal of Applied Physics*, 67:1542, 1990.
- [28] S. Hofmann and H. A. Jehn. Selective oxidation and chemical state of Al and Ti in (Ti,Al)N coatings. *Surface and Interface Analysis*, 12:329–333, 1988.
- [29] A. E. Santana, A. Karimi, V. H. Derflinger, and A. Schutze. Thermal treatment effects on microstructure and mechanical properties of TiAlN thin films. *Tribology Letters*, 17:689, 2004.
- [30] H. Ljungcrantz, M. Odén, L. Hultman, J. E. Greene, and J.-E. Sundgren. Nanoin-dentation studies of single-crystal (001)-, (011)-, and (111)-oriented TiN layers on MgO. *Journal of Applied Physics*, 80:6725, 1996.
- [31] S. PalDey and S.C. Deevi. Single layer and multilayer wear resistant coatings of (Ti,Al)N: a review. *Materials Science and Engineering A*, 342:58–79, 2003.
- [32] P. H. Mayrhofer, A. Hörling, L. Karlsson, J. Sjöln, T. Larsson, C. Mitterer, and L. Hultman. Self-organized nanostructures in the Ti-Al-N system. *Applied Physics Letters*, 83:2049, 2003.
- [33] L. Karlsson, A. Hörling, M. P. Johansson, L. Hultman, and G. Ramanath. The influence of thermal annealing on residual stresses and mechanical properties of arc-evaporated $\text{TiC}_x\text{N}_{1-x}$ ($x = 0, 0.15$ and 0.45) thin films. *Acta Materialia*, 50:5103–5114, 2002.
- [34] A. Hörling. *Thermal Stability and Age Hardening of TiN-based Thin Films*. PhD thesis, Linköping University, 2005.
- [35] A. Sugishima, H. Kajioka, and Y. Makino. Phase transition of pseudobinary Cr-Al-N films deposited by magnetron sputtering method. *Surface and Coatings Technology*, 97:590–594, 1997.
- [36] Y. Makino and K. Nogi. Synthesis of pseudobinary Cr-Al-N films with B1 structure by rf-assisted magnetron sputtering method. *Surf. Coat. Technol.*, 98:1008, 1998.
- [37] A. E. Reiter, V. H. Derflinger, B. Hanselmann, T. Bachmann, and B. Sartory. Investigation of the properties of $\text{Al}_{1-x}\text{Cr}_x\text{N}$ coatings prepared by cathodic arc evaporation. *Surface and Coatings Technology*, 200:2114, 2005.
- [38] H. Willmann, P. H. Mayrhofer, P.O.Å. Persson, A. E. Reiter, L. Hultman, and C. Mitterer. Thermal stability of Al-Cr-N hard coatings. *Scripta Materialia*, 54:1847, 2006.
- [39] O. Knotek, M. Atzor, A. Barimani, and F. Jungblut. Development of low temperature ternary coatings for high wear resistance. *Surface and Coatings Technology*, 42:21–28, 1990.
- [40] O. Knotek, F. Löffler, and H.-J. Scholl. Properties of arc-evaporated CrN and (Cr,Al)N coatings. *Surface and Coatings Technology*, 45:53–58, 1991.

- [41] F.-H. Lu and H.-Y. Chen. Phase changes of CrN films annealed at high temperature under controlled atmosphere. *Thin Solid Films*, 398-399:368–373, 2001.
- [42] M. Beckers, H. Willmann, P. Mayrhofer, C. Mitterer, and L. Hultman. (in press), 2009.
- [43] F. Lévy, P. Hones, P. E. Schmid, R. Sanjinés, M. Diserens, and C. Wiemer. Electronic states and mechanical properties in transition metal nitrides. *Surface and Coatings Technology*, 120:284, 1999.
- [44] R. Lamni, R. Sanjines, M. Parlinska-Wojtan, A. Karimi, and F. Levy. Microstructure and nanohardness properties of Zr-Al-N and Zr-Cr-N thin films. *Journal of Vacuum Science and Technology A: Vacuum, Surfaces, and Films*, 23(4):593–598, 2005.
- [45] R. Sanjinés, C. S. Sandu, R. Lamni, and F. Lévy. Thermal decomposition of $\text{Zr}_{1-x}\text{Al}_x\text{N}$ thin films deposited by magnetron sputtering. *Surface and Coatings Technology*, 200:6308, 2006.
- [46] B. Howe, J. Bareño, M. Sardela, J. G. Wen, J. E. Greene, L. Hultman, A. A. Voevodin, and I. Petrov. Growth and physical properties of epitaxial metastable $\text{Hf}_{1-x}\text{Al}_x\text{N}$ alloys deposited on $\text{MgO}(001)$ by ultrahigh vacuum reactive magnetron sputtering. *Surf. Coat. Technol.*, 202:809, 2007.
- [47] M. Pfeiler, K. Kutschej, M. Penoy, C. Michotte, C Mitterer, and M. Kathrein. The influence of bias voltage on structure and mechanical/tribological properties of arc evaporated Ti-Al-V-N coatings. *Surface and Coatings Technology*, 202:1050–1054, 2007.
- [48] A. E. Santana, A. Karimi, V. H. Derflinger, and A. Schütze. Microstructure and mechanical behavior of TiAlCrN multilayer thin films. *Surface and Coatings Technology*, 177-178:334–340, 2004.
- [49] P. Schwarzkopf and R. Kieffer. *Refractory Hard Metals*. The MacMillan Company, 1 edition, 1953.
- [50] C. Höglund, J. Barenó, J. Birch, B. Alling, Z. Czigány, and L. Hultman. (in press), 2009.
- [51] S. Veprek and S. Reiprich. A concept for the design of novel superhard coatings. *Thin Solid Films*, 268:64, 1995.
- [52] S. Veprek, M. G. J. Veprek-Heijman, P. Karvankova, and J. Prochazka. Different approaches to superhard coatings and nanocomposites. *Thin Solid Films*, 476:1, 2005.
- [53] Jr C. D. Gelatt, A. R. Williams, and V. L. Moruzzi. Theory of bonding of transition metals to nontransition metals. *Physical Review B*, 27:2005, 1983.
- [54] D. L. Price and B. R. Cooper. Total energies and bonding for crystallographic structures in titanium-carbon and tungsten-carbon systems. *Physical Review B*, 39:4945, 1989.

-
- [55] J. Häglund, A. Fernande Guillermet, G. Grimvall, and M. Körling. Theory of bonding in transition-metal carbides and nitrides. *Physical Review B*, 48:11685, 1993.
- [56] S. H. Jhi and J. Ihm. Electronic structure and structural stability of $\text{TiC}_x\text{N}_{1-x}$. *Physical Review B*, 56:13826, 1997.
- [57] C. Stampfl, W. Mannstadt, R. Asahi, and A. J. Freeman. Electronic structure and physical properties of early transition metal mononitrides: Density-functional theory LDA, GGA, and screened-exchange LDA FLAPW calculations. *Physical Review B*, 63:155106, 2001.
- [58] W. Y. Ching and B. N. Harmon. Electronic structure of AlN. *Physical Review B*, 34(8):5305, 1986.
- [59] Yong-Nian Xu and W. Y. Ching. Electronic, optical, and structural properties of some wurtzite crystals. *Physical Review B*, 48:4335, 1993.
- [60] N. E. Christensen and I. Gorzyca. and structural properties of III-V nitrides under pressure. *Physical Review B*, 50:4397, 1994.
- [61] Chin-Yu Yeh, Z. W. Lu, S. Froyen, and Alex Zunger. Zinc-blende - wurtzite polytypism in semiconductors. *Physical Review B*, 46(16):10086, 1992.
- [62] R. F. Zhang, S. H. Sheng, and S. Veprek. Mechanism of the $B3$ to $B1$ transformation in cubic AlN under uniaxial stress. *Physical Review B*, 76:075208, 2007.
- [63] K. Miwa and A. Fukumoto. First-principles calculations of the structural, electronic, and vibrational properties of gallium nitride and aluminium nitride. *Physical Review B*, 48:7897, 1993.
- [64] A. Siegel, K. Parlinski, and U. D. Wdowik. *Ab initio* calculation of structural phase transitions in AlN crystal. *Physical Review B*, 74:104116, 2006.
- [65] P. R. C. Kent and A. Zunger. *Physics and Applications of Dilute Nitrides*, chapter 1, pages 1–22. Taylor & Francis, New York, 2004.
- [66] V. Popescu, G. Bester, M. C. Hanna, A. G. Norman, and A. Zunger. Theoretical and experimental examination of the intermediate-band concept for strain-balanced (In,Ga)As/Ga(As,P) quantum dot solar cells. *Physical Review B*, 78:205321, 2008.
- [67] J. Z. Liu and A. Zunger. Thermodynamic states and phase diagrams for bulk-incoherent, bulk-coherent, and epitaxially-coherent semiconductor alloys: Application to cubic (Ga,In)N. *Physical Review B*, 77:205201, 2008.
- [68] J. Petrá, J. Klíma, and P. Hertzog. A KKR-CPA study of the electronic states in $\text{Ti}_{0.75}\text{Al}_{0.25}\text{N}$. *Zeitschrift für Physik B - Condensed matter*, 76:483, 1989.
- [69] D. Vogtenhuber-Pawelczak, P. Hertzog, and J. Klíma. A theoretical investigation of titanium aluminium nitrides, (Ti,Al)N: electronic structure and chemical bonding. *Zeitschrift für Physik B - Condensed matter*, 84:211–219, 1991.

- [70] L. Szunyogh, J. Klima, D. Vogtenhuber-Pawelczak, P. Hertzog, and P. Weinberger. Theoretical spectroscopy of random $\text{Ti}_x\text{Al}_{1-x}\text{N}$. *Zeitschrift für Physik B - Condensed matter*, 85:281–284, 1991.
- [71] A. L. Ivanovsky, N. I. Medvedeva, G. P. Shveikin, and V. M. Zhukovsky. Electronic Properties of Al, Si-containing solid solutions based on B1-TiN, TiC Determined by LMTO band structure calculations. *Physica status solidi B*, 195:195, 1996.
- [72] H. Hugosson, H. Högberg, M. Algren, M. Rodmar, and T. I. Selinder. Theory of the effects of substitutions on the phase stabilities of $\text{Ti}_{1-x}\text{Al}_x\text{N}$. *Journal of Applied Physics*, 93:4505, 2003.
- [73] P. H. Mayrhofer, D. Music, and J. M. Schneider. *Ab initio* calculated binodal and spinodal of cubic $\text{Ti}_{1-x}\text{Al}_x\text{N}$. *Applied Physics Letters*, 88:071922, 2006.
- [74] P. H. Mayrhofer, D. Music, and J. Schneider. Influence of the Al distribution on the structure, elastic properties, and phase stability of supersaturated $\text{Ti}_{1-x}\text{Al}_x\text{N}$. *Journal of Applied Physics*, 100:094906, 2006.
- [75] P. H. Mayrhofer, D. Music, and J. M. Schneider. Erratum: " *Ab initio* calculated binodal and spinodal of cubic $\text{Ti}_{1-x}\text{Al}_x\text{N}$ ". *Applied Physics Letters*, 90:029902, 2007.
- [76] R. F. Zhang and S. Veprek. Metastable phases and spinodal decomposition in $\text{Ti}_{1-x}\text{Al}_x\text{N}$ system studied by ab initio and thermodynamic modeling, a comparison with the TiN– Si_3N_4 system. *Materials Science and Engineering A*, 448:111–119, 2007.
- [77] B. Alling, A. V. Ruban, A. Karimi, O. E. Peil, S. I. Simak, L. Hultman, and I. A. Abrikosov. Mixing and decomposition thermodynamics of c- $\text{Ti}_{1-x}\text{Al}_x\text{N}$ from first-principles calculations. *Physical Review B*, 75:045123, 2007.
- [78] P. H. Mayrhofer, F. D. Fischer, H. J. Böhm, C. Mitterer, and J. M. Schneider. Energetic balance and kinetics for the decomposition of supersaturated $\text{Ti}_{1-x}\text{Al}_x\text{N}$. *Acta Materialia*, 55:1441–1446, 2007.
- [79] B. Alling, T. Marten, I. A. Abrikosov, and A. Karimi. Comparison of thermodynamic properties of cubic $\text{Cr}_{1-x}\text{Al}_x\text{N}$ and $\text{Ti}_{1-x}\text{Al}_x\text{N}$ from first-principles calculations. *Journal of Applied Physics*, 102:044314, 2007.
- [80] R. F. Zhang and S. Veprek. Phase stabilities and spinodal decomposition in the $\text{Cr}_{1-x}\text{Al}_x\text{N}$ system studied by ab initio LDA and thermodynamic modeling: Comparison with the $\text{Ti}_{1-x}\text{Al}_x\text{N}$ and TiN/ Si_3N_4 systems. *Acta Materialia*, 55:4615–4624, 2007.
- [81] S. H. Sheng, R. F. Zhang, and S. Veprek. Phase stability and thermal decomposition in the $\text{Zr}_{1-x}\text{Al}_x\text{N}$ system studied by ab initio calculation and thermodynamic modeling. *Acta Materialia*, 56:968–976, 2008.
- [82] B. Alling, A. Karimi, and I. A. Abrikosov. Electronic origin of the isostructural decomposition in cubic $\text{M}_{1-x}\text{Al}_x\text{N}$ (M=Ti, Cr, Sc, Hf): A first-principles study. *Surface and Coatings Technology*, 203:883–886, 2008.

-
- [83] L. Tsetseris, N. Kalfagiannis, S. Logothetidis, and S. T. Pantelides. Role of N defects on thermally induced atomic scale structural changes in transition-metal nitrides. *Phys. Rev. Lett.*, 99:125503, 2007.
- [84] L. Tsetseris, N. Kalfagiannis, S. Logothetidis, and S. T. Pantelides. Structure and interaction of point defects in transition-metal nitrides. *Physical Review B*, 76:224107, 2007.
- [85] B. Alling, A. Karimi, L. Hultman, and I. A. Abrikosov. First-principles study of the effect of nitrogen vacancies on the decomposition pattern in cubic $\text{Ti}_{1-x}\text{Al}_x\text{N}_{1-y}$. *Appl. Phys. Lett.*, 92:071903, 2008.
- [86] F. Bloch. Über die Quantenmechanik der Elektronen in Kristallgittern. *Zeitschrift für Physik*, 52:555, 1928.
- [87] L. H. Thomas. The calculation of atomic fields. *Mathematical Proceedings of the Cambridge Philosophical Society*, 23(05):542–548, 1927.
- [88] E. Fermi. Un metodo statistico per la determinazione di alcune priorieta dell’atome. *Accad. Naz. Lincei*, 71:1253–1266, 1927.
- [89] P. Hohenberg and W. Kohn. Inhomogeneous electron gas. *Physical Review*, 136(3B):B864–B871, 1964.
- [90] W. Kohn and L. J. Sham. Self-consistent equations including exchange and correlation effects. *Physical Review*, 140(4A):A1133–A1138, 1965.
- [91] D. M. Ceperley and B. J. Alder. Ground state of the electron gas by a stochastic method. *Physical Review Letters*, 45:566–569, 1980.
- [92] S. H. Vosko, L. Wilk, and M. Nusair. Accurate spin-dependent electron liquid correlation energies for local spin density calculations: a critical analysis. *Can. J. Phys*, 58:1200, 1980.
- [93] J. P. Perdew and A. Zunger. Self-interaction correction to densityfunctional approximations for many-electron systems. *Physical Review B*, 23:5048, 1981.
- [94] R. M. Martin. *Electronic structure, basic theory and practical methods*. Cambridge University Press, 2004.
- [95] A. D. Becke. Density functional exchange-energy approximation with correct asymptotic behaviour. *Physical Review A*, 38:3098, 1988.
- [96] Y. Wang and J. P. Perdew. Correlation hole of the spin-polarized electron gas, with exact small-wave-vector and highdensity scaling. *Physical Review B*, 44:13298, 1991.
- [97] J. P. Perdew, K. Burke, and M. Ernzerhof. Generalized gradient approximation made simple. *Physical Review Letters*, 77:3865, 1996.
- [98] A. V. Ruban and I. A. Abrikosov. Configurational thermodynamics of alloys from first principles: effective cluster interactions. *Repports on Progress in Physics*, 71:046501, 2008.

- [99] S. L. Dudarev, G. A. Botton, S. Y. Savrasov, C. J. Humphreys, and A. P. Sutton. Electron-energy-loss spectra and the structural stability of nickel oxide: An LSDA+U study. *Physical Review B*, 57:1505, 1998.
- [100] P. E. Blöchl. Generalized separable potentials for electronic-structure calculations. *Physical Review B*, 41:5414, 1990.
- [101] D. Vanderbilt. Soft self-consistent pseudopotentials in a generalized eigenvalue formalism. *Phys. Rev. B*, 41:7892, 1990.
- [102] P. E. Blöchl. Projector augmented-wave method. *Physical Review B*, 50:17953, 1994.
- [103] G. Kresse and J. Hafner. *Ab initio* molecular dynamics for open-shell transition metals. *Physical Review B*, 48:13115, 1993.
- [104] G. Kresse and D. Joubert. From ultrasoft pseudopotentials to the projector augmented-wave method. *Physical Review B*, 59:1758, 1999.
- [105] J. Korringa. On the calculation of the energy of a Bloch wave in a metal. *Physica*, 13:392, 1947.
- [106] W. Kohn and N. Rostoker. Solution of the Schrödinger equation in periodic lattices with an application to metallic lithium. *Physical Review*, 94:1111, 1954.
- [107] O. K. Andersen. Linear methods in band theory. *Physical Review B*, 12:3060, 1975.
- [108] O. K. Andersen and O. Jepsen. Explicit, first-principles tight-binding theory. *Physical Review Letters*, 53:2571, 1984.
- [109] H. L. Skriver and N. M. Rosengaard. Self-consistent Green's-function technique for surfaces and interfaces. *Physical Review B*, 43:9538, 1991.
- [110] I. A. Abrikosov and H. L. Skriver. Self-consistent linear-muffin-tin-orbitals coherent-potential technique for bulk and surface calculations: Cu-Ni, Ag-Pd, and Au-Pt random alloys. *Physical Review B*, 47:16532, 1993.
- [111] A. V. Ruban and H. L. Skriver. Calculated surface segregation in transition metal alloys. *Computational Materials Science*, 15:119, 1999.
- [112] I. A. Abrikosov, A. M. N. Niklasson, S. I. Simak, B. Johansson, A. V. Ruban, and H. L. Skriver. Order-N Green's function technique for local environment effects in alloys. *Physical Review Letters*, 76:4203, 1996.
- [113] I. A. Abrikosov, S. I. Simak, B. Johansson, A. V. Ruban, and H. L. Skriver. Locally self-consistent Green's function approach to the electronic structure problem. *Physical Review B*, 56:9319, 1997.
- [114] L. Vitos. Total-energy method based on the exact muffin-tin orbitals theory. *Physical Review B*, 64:014107, 2001.

- [115] L. Vitos, I.A. Abrikosov, and B. Johansson. Anisotropic lattice distortions in random alloys from first-principles theory. *Physical Review Letters*, 87:156401, 2001.
- [116] J. M. Sanchez, F. Ducastelle, and D. Gratias. Generalized cluster description of multicomponent systems. *Physica A: Statistical and Theoretical Physics*, 128(1-2):334 – 350, 1984.
- [117] A. Zunger, S. H. Wei, L. G. Ferreira, and J. E. Bernard. Special quasirandom structures. *Physical Review Letters*, 65:353, 1990.
- [118] A. V. Ruban, S. Shallcross, S. I. Simak, and H. L. Skriver. Atomic and magnetic configurational energetics by the generalized perturbation method. *Physical Review B*, 70:125115, 2004.
- [119] S. I. Simak, P. A. Korzhavyi, and A. V. Ruban. (unpublished).
- [120] P. Soven. Coherent potential model of substitutional disordered alloys. *Physical Review*, 156:809, 1967.
- [121] B. L. Györffy. Coherent-potential approximation for a nonoverlapping-muffin-tin-potential model of random substitutional alloys. *Physical Review B*, 5:2382, 1972.
- [122] B. L. Györffy, A. J. Pindor, J. Staunton, G. M. Stocks, and H. Winter. A first-principles theory of ferromagnetic phase transitions in metals. *Journal of Physics F: Metal Physics*, 15:1337, 1985.
- [123] I. A. Abrikosov, A. E. Kissavos, F. Liot, B. Alling, S. I. Simak, O. Peil, and A. V. Ruban. Competition between magnetic structures in the Fe rich fcc FeNi alloys. *Physical Review B*, 76:014434, 2007.
- [124] A. V. Ruban and H. L. Skriver. Screened Coulomb interactions in metallic alloys. I. Universal screening in the atomic-sphere approximation. *Physical Review B*, 66:024201, 2002.
- [125] A. V. Ruban, S. I. Simak, P. A. Korzhavyi, and H. L. Skriver. Screened Coulomb interactions in metallic alloys. II. Screening beyond the single-site and atomic-sphere approximations. *Physical Review B*, 66:024202, 2002.
- [126] A. V. Ruban, S. I. Simak, S. Shallcross, and H. L. Skriver. Local lattice relaxations in random metallic alloys: Effective tetrahedron model and supercell approach. *Physical Review B*, 67:214302, 2003.
- [127] F. Ducastelle and F. Gautier. Generalized perturbation theory in disordered transitional alloys - applications to the calculation of ordering energies. *Journal of Physics F: Metal Physics*, 6:2039, 1976.
- [128] F. Ducastelle. *Order and phase stability in Alloys*. North-Holland, Amsterdam, 1991.
- [129] H. Schulz and K. Thielmann. Crystal structure refinement of AlN and GaN. *Solid State Communications*, 23:815, 1977.

- [130] P. Villars and L. D. Calvet. *Pearson's Handbook of Crystallographic Data for Intermetallic Phases*. American Society for Metals, Metals Park, OH, 1985.
- [131] W. Lengauer. Investigations in the Scandium-Nitrogen System. *Journal of Solid State Chemistry*, 76:412, 1988.
- [132] F. Adibi, I. Petrov, J.E. Greene, U. Wahlström, and J.E. Sundgren. Design and characterization of a compact two-target ultrahigh vacuum magnetron sputter deposition system: Application to the growth of epitaxial $\text{Ti}_{1-x}\text{Al}_x\text{N}$ alloys and $\text{TiN}/\text{Ti}_{1-x}\text{Al}_x\text{N}$ superlattices. *Journal of Vacuum Science and Technology A*, 11:136, 1993.
- [133] U. Wahlström, L. Hultman, J. E. Sundgren, F. Adibi, I. Petrov, and J. E. Greene. Crystal growth and microstructure of polycrystalline $\text{Ti}_{1-x}\text{Al}_x\text{N}$ alloy films deposited by ultra-high-vacuum dual target magnetron sputtering. *Thin Solid Films*, 235:62, 1993.
- [134] A. Kimura, M. Kawate, H. Hasegawa, and T. Suzuki. Anisotropic lattice expansion and shrinkage of hexagonal TiAlN and CrAlN films. *Surface and Coatings Technology*, 169-170:367, 2003.
- [135] *Powder Diffraction File c-AlN: [25-1495]*, JCPDC International Center for Powder Diffraction Data Swarthmore, PA, 1994.
- [136] L. Vegard. Die konstitution der mischkristalle und die raumfüllung der atome. *Zeitschrift für Physik*, 5(1), January 1921.
- [137] V. L. Moruzzi, J. F. Janak, and K. Schwarz. Calculated thermal properties of metals. *Physical Review B*, 37:790, 1988.
- [138] J. O. Kim, D. Achenbach, P. B. Mirkarimi, M. Shinn, and S. A. Barnett. Elastic constants of single-crystal transition-metal nitride films measured by line-focus acoustic microscopy. *Journal of Applied Physics*, 72:1805, 1992.
- [139] X.-J. Chen *et. al.* Hard superconducting nitrides. *Proceedings of the National Academy of Sciences of the the United States of America*, 102:3198, 2005.
- [140] E. I. Isaev, S. I. Simak, I. A. Abrikosov, R. Ahuja, Yu. Kh. Vekilov, M. I. Katsnelson, A. I. Lichtenstein, and B. Johansson. Phonon related properties of transition metals, their carbides, and nitrides: A first-principles study. *J. Appl. Phys.*, 101:123519, 2007.
- [141] P. H. Mayrhofer, D. Music, Th. Reeswinkel, H.-G. Fuss, and J. M. Schneider. Structure, elastic propertis and phase stability of $\text{Cr}_{1-x}\text{Al}_x\text{N}$. *Acta Materialia*, 56:2469–2475, 2008.
- [142] E. K. Tentardini, C. Kwietniewski, F. Perini, E. Blando, R. Hübler, and I. J. R. Baumvol. Deposition and characterization of non-isosstructural $(\text{Ti}_{0.7}\text{Al}_{0.3}\text{N}/(\text{Ti}_{0.3}\text{Al}_{0.7}\text{N}))$. *Surface and Coatings Technology*, 203:1176–1181, 2009.

-
- [143] A. Flink, J. M. Andersson, B. Alling, R. Daniel, J. Sjöln, L. Karlsson, and L. Hultman. Structure and thermal stability of arc evaporated $(\text{Ti}_{0.33}\text{Al}_{0.67})_{1-x}\text{Si}_x\text{N}$ thin films. *Thin Solid Films*, 517:714–721, 2008.
- [144] N. Farrer and L. Bellaiche. Properties of hexagonal ScN versus wurtzite GaN and InN. *Physical Review B*, 66:201203(R), 2002.
- [145] B. Alling. Local lattice relaxations in the fcc-AgAu system. (unpublished).
- [146] P.E. Van Camp, V. E. Van Doren, and J. T. Devreese. High-pressure properties of wurtzite- and rocksalt-type aluminum nitride. *Physical Review B*, 44:9056, 1991.
- [147] S. Strite and H. Morkoc. GaN, AlN, and InN: A review. *Journal of Vacuum Science and Technology B*, 10:1237, 1992.
- [148] E. A. Smirnova, P. A. Korzhavyi, Yu. Kh. Vekilov, B. Johansson, and I. A. Abrikosov. Origin of the asymmetric spinodal decomposition in the Al-Zn system. *Physical Review B (Condensed Matter and Materials Physics)*, 64(2):020101, 2001.
- [149] A. Filippetti, W. E. Pickett, and B. M. Klein. Competition between magnetic and structural transitions in CrN. *Physical Review B*, 59(10):7043, 1999.
- [150] P. Olsson, I. A. Abrikosov, L. Vitos, and J. Wallenius. Ab initio formation energies of Fe-Cr alloys. *Journal of Nuclear Materials*, 321:84, 2003.
- [151] A. E. Kissavos, S. I. Simak, P. Olsson, L. Vitos, and I. A. Abrikosov. Total energy calculations for systems with magnetic and chemical disorder. *Computational Materials Science*, 35:1–5, 2006.
- [152] A. V. Ruban, M. I. Katsnelson, W. Olovsson, S. I. Simak, and I. A. Abrikosov. Origin of magnetic frustrations in Fe-Ni Invar alloys. *Physical Review B*, 71:054402, 2005.
- [153] I. A. Abrikosov, F. Liot, T. Marten, and E. A. Smirnova. Magnetism in systems with reduced dimensionality and chemical disorder: The local environment effects. *Journal of Magnetism and Magnetic Materials*, 300:211–215, 2006.
- [154] D. Gall, M. Städele, K. Järrendahl, I. Petrov, P. Desjardins, R. T. Haasch, T. Y. Lee, and J. E. Greene. Electronic structure of ScN determined using optical spectroscopy, photoemission, and *ab initio* calculations. *Phys. Rev. B*, 63(125119), 2001.
- [155] M. W. Barsoum. The $\text{M}_{N+1}\text{AX}_N$ phases: A new class of solids; Thermodynamically stable nanolaminates. *Progress in Solid State Chemistry*, 28:201–281, 2000.
- [156] M. Asta, D. de Fontaine, M. van Schilfgaarde, M. Sluiter, and M. Methfessel. First-principles phase-stability study of fcc alloys in the Ti-Al system. *Physical Review B*, 46:5055, 1992.

- [157] M. Beckers, N. Schell, R. M. S. Martins, A. Mücklich, W. Möller, and L. Hultman. Nucleation and growth of Ti_2AlN thin films deposited by reactive magnetron sputtering onto $\text{MgO}(111)$. *Journal of Applied Physics*, 102:074916, 2007.
- [158] J. W. D. Connolly and A. R. Williams. Density-functional theory applied to phase transformations in transition-metal alloys. *Phys. Rev. B*, 27:5169, 1983.

Acknowledgements

Three and a half years have past since I started the work leading up to this thesis. It has been a lot of time of thinking about physics, some periods of really hard work and some periods with a rather easy pace. Regardless of which, most of the time I have truly enjoyed it. And many people have contributed to making these years into what they have been.

First of all I would like to thank my supervisor Dr. Ayat Karimi for making this work possible by inviting me to work in his group in Lausanne as well as for all encouragement, friendly guidance and expertise in the field of nitrides hard coatings materials. Moreover, I would like to thank my second supervisor Prof. Igor Abrikosov for his support, guidance, inspiration, motivation and for believing in my ideas.

Dr. Andrei Ruban has helped me so many times along this way with sorting out problems ranging from the intricate physics of cluster expansions to modifying computer codes, and I am most grateful. Prof. Lars Hultman has his important role in starting this collaboration between the Linköping University and the EPFL of which this thesis work is one result. I am also thankful for his inspiration and expertise on thin films materials. Dr. Sergei Simak is acknowledged for introducing me into the art of SQS generation and for the jokes on the Monday meetings. Dr. Daniele Mari is acknowledged for numerous instructive discussions about hard materials, a couple of well needed advices about how things work in Switzerland, and for accepting in our common office the results of the fact that my research on disorder has not been of purely theoretical character. Dr. Eyvaz Isaev is gratefully acknowledged for introducing me to phonons and for his cheerful mode.

I am grateful to my current and past fellow PhD-students as well as the post-docs in the theory and modelling groups in Linköping for their contribution to these years of physics, fun, and hard work. Tobias Marten is acknowledged for being a perfect office neighbour, Johan Böhlén for the jokes, coffee breaks and for coming back to physics, Andreas Kissavos for the chess games, Christian Asker for his cheerful spirit, Marcus Ekholm for his love of cats, Peter Steneteg for his powerful voice, Francois Liot for his logic, Mattias Jakobsson for joining in for lunch, Arkady Mikhaylushkin for his skills in putting things under pressure, Ferenc Tasnadi for asking the the critical questions, and Olle Hellman and Olga Vekilova for looking after my very first office.

I am thankful to my experimental colleagues in the Thin Films group in Linköping. Axel Flink is acknowledged for introducing me to silicon nitride, Carina Höglund for actually trying out one of my ideas in the vacuum chamber, Javier Bareño for keeping up my interest in hafnium, Manfred Beckers for making me realise the importance of vacancies, and Martin Dahlqvist for his thoroughness. It has been instructive to work

ACKNOWLEDGEMENTS

with you and I am looking forward to future collaborations.

To all the people which I have met and worked with in Lausanne (and nearby), thank you for making my visits here into pleasant and valuable times. Monique Bettinger is acknowledged for helping me out with all kinds of Swiss bureaucracy, Dr. Marcus Morstein for giving me an industries point of view, prof. Eric Bergmann for his efforts to start this collaboation, and Zlatko Mickovic for keeping up the good mood among the PhD students.

I have worked together also with many others during these years, Dr. Oleg Peil, Oscar Grånäs, Dr. David Andersson, and Dr. Sam Shallcross. Thank you all for interesting discussions and valuable knowledge gained.

I am thankful to all my friends for making me think of other things than physics. I am thankful to Anna Morvall for reminding me that science is more than physics, for all good times, and a few hours together in jail, and Conny Olsson for keeping me company on Skype, (handshake).

My parents and my sister have always supported me and encouraged me in all possible ways. I would not have come this far without their support.

Finally and most importantly: Thank you Malin. For everything.

Björn Alling

Lausanne, March 2009

Curriculum vitæ

Björn Alling

Storgården 7

SE-586 44 Linköping

SWEDEN

Born: 22:nd October 1980

Education

- 2006-2009: PhD-studies in material physics, Ecole Polytechnique Fédérale de Lausanne (EPFL), Lausanne, Switzerland
- 2005-2009: PhD-studies in theoretical physics, Linköping University, Linköping, Sweden
- 1999-2005: Master of science, applied physics and electrical engineering, Linköping University, Linköping, Sweden

Employment record

- 2006-2009: Ecole Polytechnique Fédérale de Lausanne (EPFL), Lausanne, Switzerland: PhD-student
- 2005-2009: Linköping University, Linköping, Sweden: PhD-student

Scientific publications

Publications directly related to the thesis

Electronic origin of the isostructural decomposition in cubic $M_{1-x}Al_xN$ ($M = Ti, Cr, Sc, Hf$) - A first-principles study
B. Alling, A. Karimi, and I. A. Abrikosov
Surface & Coatings Technology **203** 883-886 (2008)

First-principles study of the effect of nitrogen vacancies on the decomposition pattern in cubic $Ti_{1-x}Al_xN_{1-y}$
B. Alling, A. Karimi, L. Hultman, and I. A. Abrikosov
Applied Physics Letters **92**, 071903 (2008)

Comparison of thermodynamic properties of cubic $Cr_{1-x}Al_xN$ and $Ti_{1-x}Al_xN$ from first-principles calculations
B. Alling, T. Marten, I. A. Abrikosov and A. Karimi
Journal of Applied Physics **102**, 044314 (2007)

Mixing and decomposition thermodynamics of c - $Ti_{1-x}Al_xN$ from first-principles calculations
B. Alling, A. V. Ruban, A. Karimi, O. E. Peil, S. I. Simak, L. Hultman, and I. A. Abrikosov
Physical Review B **75** (2007)

Publications on adjacent topics

Stability of the ternary perovskites Sc_3EN ($E = B, Al, Ga, In$) from first principles
A. S. Mikhaylushkin, C. Höglund, J. Birch, Zs. Czigány, L. Hultman, S. I. Simak, B. Alling, F. Tasnadi, and I. A. Abrikosov
Physical Review B **79**, 134107 (2009)

Structure and thermal stability of arc evaporated $(Ti_{0.33}Al_{0.67})_{1-x}Si_xN$ thin films
A. Flink, J. M. Andersson, B. Alling, R. Daniel, J. Sjöln, L. Karlsson, and L. Hultman
Thin Solid Films **517**, 714-721 (2008)

Metastability of fcc-related Si-N phases
B. Alling, E. I. Isaev, A. Flink, L. Hultman, and I. A. Abrikosov
Physical Review B **78**, 132103 (2008)

Sc_3AlN - A new Perovskite
C. Höglund, J. Birch, M. Beckers, B. Alling, Z. Czigány, A. Mücklich, and L. Hultman
European Journal of Inorganic Chemistry 2008 1193-1195

Other publications

Effect of thermal expansion, electronic excitations, and disorder on the Curie temperature of $Ni_{1-x}Cu_xMnSb$ alloys

B. Alling, A. V. Ruban, and I. A. Abriksov

Physical Review B **79**, 134417 (2009)

Energetics and magnetic impact of 3d-metal doping of the half-metallic ferromagnet $NiMnSb$

B. Alling, M. Ekholm, and I. A. Abriksov

Physical Review B **77**, 144414 (2008)

Competition between magnetic structures in Fe rich fcc $FeNi$ alloys

I. A. Abrikosov, A. E. Kissavos, F. Liot, B. Alling, S. I. Simak, O. Peil, and A. V. Ruban

Physical Review B **77**, 014434 (2007)

Role of stoichiometric and nonstoichiometric defects on the magnetic properties of the half-metallic ferromagnet $NiMnSb$

B. Alling, S. Shallcross, and I. A. Abriksov

Physical Review B **73**, 064418 (2006)